NUREG-1864

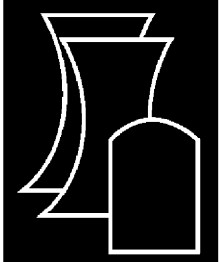

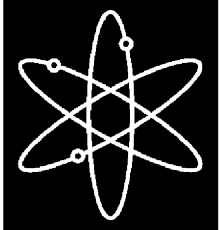

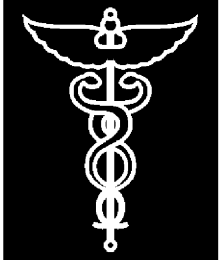

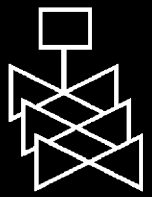

A Pilot Probabilistic Risk Assessment Of a Dry Cask Storage System At a Nuclear Power Plant

U.S. Nuclear Regulatory Commission
Office of Nuclear Regulatory Research
Washington, DC 20555-0001

AVAILABILITY OF REFERENCE MATERIALS IN NRC PUBLICATIONS

NRC Reference Material

As of November 1999, you may electronically access NUREG-series publications and other NRC records at NRC's Public Electronic Reading Room at http://www.nrc.gov/reading-rm.html.

Publicly released records include, to name a few, NUREG-series publications; *Federal Register* notices; applicant, licensee, and vendor documents and correspondence; NRC correspondence and internal memoranda; bulletins and information notices; inspection and investigative reports; licensee event reports; and Commission papers and their attachments.

NRC publications in the NUREG series, NRC regulations, and Title 10, Energy, in the *Code of Federal Regulations* may also be purchased from one of these two sources:

1. The Superintendent of Documents
   U.S. Government Printing Office
   Mail Stop SSOP
   Washington, DC 20402–0001
   Internet: bookstore.gpo.gov
   Telephone: 202-512-1800
   Fax: 202-512-2250
2. The National Technical Information Service
   Springfield, VA 22161–0002
   www.ntis.gov
   1–800–553–6847 or, locally, 703–605–6000

A single copy of each NRC draft report for comment is available free, to the extent of supply, upon written request as follows:

Address: Office of the Chief Information Officer
Reproduction and Distribution
Services Section
U.S. Nuclear Regulatory Commission
Washington, DC 20555-0001
Email: DISTRIBUTION@nrc.gov
Facsimile: 301–415–2289

Some publications in the NUREG series that are posted at NRC's Web site address http://www.nrc.gov/reading-rm/doc-collections/nuregs are updated periodically and may differ from the last printed version. Although references to material found on a Web site bear the date the material was accessed, the material available on the date cited may subsequently be removed from the site.

Non-NRC Reference Material

Documents available from public and special technical libraries include all open literature items, such as books, journal articles, and transactions, *Federal Register* notices, Federal and State legislation, and Congressional reports. Such documents as theses, dissertations, foreign reports and translations, and non-NRC conference proceedings may be purchased from their sponsoring organization.

Copies of industry codes and standards used in a substantive manner in the NRC regulatory process are maintained at—

The NRC Technical Library
Two White Flint North
11545 Rockville Pike
Rockville, MD 20852–2738

These standards are available in the library for reference use by the public. Codes and standards are usually copyrighted and may be purchased from the originating organization or, if they are American National Standards, from—

American National Standards Institute
11 West 42nd Street
New York, NY 10036–8002
www.ansi.org
212–642–4900

Legally binding regulatory requirements are stated only in laws; NRC regulations; licenses, including technical specifications; or orders, not in NUREG-series publications. The views expressed in contractor-prepared publications in this series are not necessarily those of the NRC.

The NUREG series comprises (1) technical and administrative reports and books prepared by the staff (NUREG–XXXX) or agency contractors (NUREG/CR–XXXX), (2) proceedings of conferences (NUREG/CP–XXXX), (3) reports resulting from international agreements (NUREG/IA–XXXX), (4) brochures (NUREG/BR–XXXX), and (5) compilations of legal decisions and orders of the Commission and Atomic and Safety Licensing Boards and of Directors' decisions under Section 2.206 of NRC's regulations (NUREG–0750).

NUREG-1864

A Pilot Probabilistic Risk Assessment Of a Dry Cask Storage System At a Nuclear Power Plant

Manuscript Completed: June 2006
Date Published: March 2007

A. Malliakos, NRC Project Manager

Division of Risk Assessment and Special Projects
Office of Nuclear Regulatory Research
U.S. Nuclear Regulatory Commission
Washington, DC 20555-0001

Spent Fuel Project Office
Office of Nuclear Material Safety and Safeguards
U.S. Nuclear Regulatory Commission
Washington, DC 20555-0001

ABSTRACT

In response to a request from the U.S. Nuclear Regulatory Commission (NRC), Office of Nuclear Material Safety and Safeguards (NMSS), the Office of Nuclear Regulatory Research (RES) and the NMSS Spent Fuel Project Office (SFPO) have jointly developed and applied a methodology for performing a pilot probabilistic risk assessment (PRA) of a dry cask storage system at a nuclear power plant site (i.e., an independent spent fuel storage installation). This RES/NMSS report documents the pilot PRA for a specific dry cask system (Holtec International HI-STORM 100) at a specific boiling-water reactor (BWR) site. The methodology developed can serve as a guide for performing similar PRAs in the future. The pilot study can provide guidance for assessing the risk to the public and identifying the dominant contributors to that risk. The cask system consists of a multipurpose canister (MPC) that confines the fuel, a transfer overpack that shields workers from radiation while the cask is being prepared for storage, and a storage overpack that shields people from radiation and mechanically protects the MPC during storage. The study covers various phases of the dry cask storage process, from loading fuel from the spent fuel pool, preparing the cask for storage and transferring it outside the reactor building, moving the cask from the reactor building to the storage pad, and storing the cask for 20 years on the storage pad.

The study develops and assesses a comprehensive list of initiating events, including dropping the cask during handling and external events during onsite storage (such as earthquakes, floods, high winds, lightning strikes, accidental aircraft crashes, and pipeline explosions). Potential cask failures from mechanical and thermal loads are modeled. The study estimates the annual risk for one cask in terms of the individual probability of a prompt fatality within 1.6 km (1 mile) and a latent cancer fatality within 16 km (10 miles) of the site.

This page intentionally left blank

FOREWORD

The spent fuel pools of commercial nuclear power plants are becoming filled with spent fuel assemblies and many utilities have been removing older fuel and storing it onsite in dry casks. For this purpose, the fuel first is loaded from the spent fuel pool into a cask which is then prepared for storage. Then the cask is transferred to and stored on the storage pad. Given the increasing trend to onsite storage, it is necessary to assess the risk to the public and to identify the dominant contributors to that risk from this operation. For this reason, the U.S. Nuclear Regulatory Commission (NRC), Office of Nuclear Regulatory Research (RES), has developed and applied a methodology for performing a pilot probabilistic risk assessment (PRA) of a dry cask storage system. On that basis, RES and the NRC's Office of Nuclear Material Safety and Safeguards (NMSS) have jointly performed the pilot PRA as documented in this report, for a specific cask system at a specific boiling-water reactor site.

To analyze the risk in this report, the staff developed a comprehensive list of initiating events, and evaluated the risk associated with each initiating event. Initiating events considered include dropping the cask inside the secondary containment building during transfer operations, as well as external events during onsite storage (such as earthquakes, floods, high winds, lightning strikes, accidental aircraft crashes, and pipeline explosions). Potential cask failures from mechanical and thermal loads, including thermal loads caused by mis-loading events, were modeled. In the event of a cask failure/breach, the fuel inventory available for release was based on 10-year-old fuel. Weather conditions and the population distribution in the vicinity of the site were also considered.

The risk to the public is measured in terms of the individual probabilities of a prompt fatality within 1.6 km (1 mi) and a latent cancer fatality within 16 km (10 mi) of the site. No prompt fatalities are expected. The resulting calculated risk is extremely small, with an individual probability of a latent cancer fatality of 1.8×10^{-12} during the first year of service, and 3.2×10^{-14} per year during subsequent years of storage.

The methodology developed in this study can be used as a guide for performing other similar PRAs. Moreover, the results of this study can be used in conjunction with the methodology selected to determine the need for other PRAs, improvements in data gathering and analysis, and additional engineering design analysis. It should be noted that the focus of this pilot study was solely on the methodology and its limited (i.e., case-specific) application. Thus, no inferences or conclusions should be drawn with regard to the study's regulatory implications.

Brian W. Sheron, Director
Office of Nuclear Regulatory Research
U.S. Nuclear Regulatory Commission

This page intentionally left blank

CONTENTS

Appendices

Figures

Tables

EXECUTIVE SUMMARY

The spent fuel pools of commercial nuclear power plants are becoming filled with spent fuel assemblies. To avoid having to cease operations when the pools are full, many utilities have been removing older fuel from the pools and storing it onsite in dry casks. In this study, sponsored by the U.S. Nuclear Regulatory Commission (NRC), the Office of Nuclear Regulatory Research (RES) and the Spent Fuel Project Office (SFPO) in the Office of Nuclear Material Safety and Safeguards (NMSS) have jointly developed a methodology for performing a probabilistic risk assessment (PRA) of a dry cask storage system and applied the methodology by performing a pilot PRA of a specific cask system at a specific boiling-water reactor (BWR) site. Although the study results do not necessarily apply to other cask systems or sites, the methodology can serve as a guide for performing other such PRAs. Nonetheless, it should be noted that the focus of this pilot study is on the methodology and its limited (i.e., case-specific) application. Consequently, no inferences or conclusions should be drawn with regard to the regulatory implications of this study.

The pilot PRA assesses the risk to the public and identifies the dominant contributors to risk associated with dry cask storage involving a single cask at a specific BWR site. Among the items that were beyond the scope of the study were subsequent versions of the specific cask studied in this report, unloading of the cask, offsite transportation, repository storage, uncertainty analysis, worker risk, human reliability, fabrication errors, mis-loading of spent nuclear fuel, aging effects, and combinations of factors that could impact the probability of MPC failure.

The cask system analyzed is the Holtec International HI-STORM 100. This cask system, which is used for onsite storage only, consists of three major components, including a multipurpose canister (MPC), a transfer overpack, and a storage overpack. The MPC confines spent fuel assemblies for the duration of the storage period (typically 20 years). While the MPC is loaded with spent fuel assemblies from the spent fuel pool and is prepared for storage, it is inside the transfer overpack to shield workers from radiation. During onsite storage, the storage overpack shields people from radiation, provides a path to cool the MPC by convection though vents, and protects the MPC during storage. In this study, the transfer overpack containing the MPC is referred to as the transfer cask, and the storage overpack containing the MPC is referred to as the storage cask.

The dry cask storage operation is divided into the three phases of handling, transfer, and storage. During the handling phase, spent fuel assemblies are placed into the MPC within a transfer overpack. After the MPC is dried, inerted with helium, and sealed, it is removed from the transfer cask and placed in the storage overpack. The transfer phase takes place when the storage cask is moved out of the secondary containment to the storage pad. The storage phase takes place after the storage cask is set down on the storage pad. To analyze the risk of the dry cask storage operation, the phases are divided into 34 stages. A stage is defined as a discrete part of the operation that is convenient for the risk analysis. For example, because the height at which the cask is moved and the composition of the surface over which it is moved determine the mechanical load on the MPC if it were dropped, these aspects of the operation are used to define some of the stages.

A comprehensive list of initiating events is developed, and the risk associated with each initiating event is evaluated. Analyses are performed to determine the cask's response to the mechanical and thermal loads imposed by the initiating events. For example, the following analyses evaluate the consequences of dropping the transfer cask during the handling phase:

- A mechanical load analysis determines the stresses on the fuel cladding and MPC as a function of drop height.
- Given the stress on the fuel cladding and MPC from dropping the transfer cask or MPC, failure analyses determine the probability of the fuel cladding and MPC failing.
- Source term analysis is used to determine the releases from the fuel cladding and the MPC.
- An engineering analysis determines the reliability of the secondary containment to isolate if there is an accidental release of radioactivity inside the secondary containment.

To quantify the risk, the study uses "best available" point estimates. When there is insufficient information or data, conservative bounding assumptions or estimates are used. Because no uncertainty analysis was performed, the identification of the dominant contributors was based on the point estimates developed by the study. The dominant contributors might possibly change if uncertainty is considered. The study measures the risk to the public in terms of the individual probabilities of a prompt fatality and a latent cancer fatality within 16 km (10 mi) of the site. In calculating the risks, the study also considers weather conditions and the population distribution in the vicinity of the site.

The results of this analysis indicate that the risk is solely from latent cancer fatalities, and no prompt fatalities are expected. The risk is dominated by accident sequences occurring in three stages of the handling phase. These involve the drop of the transfer cask through the equipment hatch (Stage 18) and drops of the MPC into the storage overpack (Stages 20 and 21). The aggregated risk values are quite low. Some of the scenarios have zero risk because either their initiating events cannot occur at the subject plant or no radioactive release will result. The overall risk of dry cask storage was found to be extremely low. That is, the estimated aggregate risk is an individual probability of a latent cancer fatality of 1.8×10^{-12} during the first year of service, and 3.2×10^{-14} per year during subsequent years of storage. Questions pertinent to this study may arise from the public. Thus, a list of potential questions and their answers as related to this study has been prepared and is presented in Appendix F.

ACKNOWLEDGMENTS

Team Members	Contributions
U.S. Nuclear Regulatory Commission	
Ronaldo Jenkins	Overall management
Alan Rubin	Overall management and technical oversight (through March 2006)
Edward Rodrick	Team Leader (through September 2001)
Lee Abramson	Team Leader, data analysis, technical review, report editing (through September 2004)
John Thorp	Team Leader, technical review, report editing (through August 2005)
Asimios Malliakos	Team Leader and final risk assessment calculations, technical review, and report editing
Christopher Ryder	Technical coordination among technical disciplines, report compilation, and review; flooding analysis and project management of secondary containment analyses at Lawrence Livermore National Laboratory; and peer review at Sandia National Laboratories (through September 2003)
Christina Antonescu	Effects of lightning, and project management of lightning analysis at Oak Ridge National Laboratory
Gordon Bjorkman	Structural mechanics, stress analysis and buckling, LS-DYNA model modifications and analyses, weld failure methodology, MPC integrity evaluation and failure probability, fuel rod integrity methodology and analyses, and aircraft impact analysis
Kim Hardin	SFPO Team Leader, coordination among SFPO technical disciplines, technical review, and interface with RES (2004–2005)
Tze-Jer Chuang	SFPO Team Leader, coordination among SFPO technical disciplines, technical review and report editing, and interface with RES (2005–2006)
Robert Einziger	Source term methodology and source term estimates
Jason Piotter	Implemented LS-DYNA model modifications and LS-DYNA analyses (March 2006 to February 2006)
Monideep Dey	Fires (through November 2004)
Brad Hardin	Frequencies of aircraft crashes and natural events
Douglas Kalinousky	Failure analysis
Jocelyn Mitchell	Consequences
Carlos Navarro	Consequences
Cayatano Santos	Failure analysis
Shah Malik	Failure analysis
Jason Schaperow	Source term and consequences
Syed Shaukat	Structural mechanics and project management of structural analyses at Brookhaven National Laboratory
Ghani Zigh	Thermal-hydraulic analyses of fires and blocked vents
Tony Ulses	Criticality analysis

Team Members	Contributions
Brookhaven National Laboratory	
Joseph Braverman	Mechanical load calculations
Charles Hofmayer	Mechanical load calculations
Charles Miller	Mechanical load calculations
Richard Morante	Mechanical load calculations
Jim Xu	Mechanical load calculations
Jinsuo Nie	Mechanical load calculations
Nikolaos Simos	Mechanical load calculations
Lawrence Livermore National Laboratory	
Peter Prassinos	Reliability of secondary containment isolation
Oak Ridge National Laboratory	
James Yugo	Electromagnetic analysis of lightning effects on dry cask
Sandia National Laboratories	
Douglas Ammerman	Cask and fuel rod response for source term estimates
Robert Kalan	Cask and fuel rod response for source term estimates
Vincent Luk	Seismic load calculations
Jeremy Sprung	Source term estimates

Comment Review Group	Group Leaders
SFPO Thermal Group	Jorge Solis
SFPO Structural Group	Gordon Bjorkman, Henry Lee, Bob Tripathi, Jason Piotter, and David Tang
SFPO Materials Group	Robert Einziger, Tze-Jer Chuang, and Chuck Interrante
SFPO Criticality Group	Carl Withee, Kim Hardin, and Bernie White
SFPO Containment and Radiation Protection	Kim Hardin, Steve Baggett, Mike Waters, Michel Call
Transportation and Storage Safety & Inspection Section	Rob Temps
Spent Fuel Licensing Section	Steve O'Connor
NMSS Risk Task Group (no longer in existence)	Bret Leslie
Specialists	Dennis Damon and Robert Einziger

ABBREVIATIONS

ASME	American Society of Mechanical Engineers
BNL	Brookhaven National Laboratory
BWR	boiling-water reactor
CFD	computational fluid dynamics
CRUD	Chalk River unidentified deposits
CFR	Code of Federal Regulations
DBE	design-basis earthquake
DCF	dose conversion factor
EAB	exclusion area boundary
EPS	effective plastic strain
FAA	Federal Aviation Administration
FEM	finite element model
FSAR	final safety analysis report
GFD	ground flash density
HI-STORM	Holtec International Storage and Transfer Operation Reenforced Module
HI-TRAC	Holtec International Transfer Cask
HRA	human reliability analysis
HVAC	heating, ventilation, and air conditioning
IFT	isolation failure type
ISFSI	independent spent fuel storage installation
KE	kinetic energy
LWR	light-water reactor
MACCS2	MELCOR Accident Consequence Code System
MPC	multipurpose canister
NG	noble gases
NLDN	National Lightning Detection Network
NMSS	Office of Nuclear Material Safety and Safeguards (NRC)
NRC	U.S. Nuclear Regulatory Commission
NSSS	nuclear steam supply system
ORNL	Oak Ridge National Laboratory
OT	other than noble gases

PE	potential energy
PMP	probable maximum precipitation
PRA	probabilistic risk assessment
PT	dye penetrant (test) examination
PWR	pressurized-water reactor
Ref	reference
RES	Office of Nuclear Regulatory Research (NRC)
RT	radiographic (test) examination
SA	submerged arc (weld)
SGTS	standby gas treatment system
SIMPLE	Semi-Implicit Method for Pressure-Linked Equations
SME	seismic margin earthquake
SNL	Sandia National Laboratories
SRP	Standard Review Plan
TIG	tungsten-inert-gas (process)
TO	transfer overpack
UT	ultrasonic testing (nondestructive test process)

SYMBOLS

atm	atmospheric pressure
C	Centigrade/Celsius
cfm	cubic feet per minute
cm	centimeter
F	Fahrenheit
ft	feet
g	gravitational constant
hr	hour
in.	inch
kg	kilogram
km	kilometer
kPa	kilo-Pascal
kW	kilowatt
lb	pound
m	meter
MPa	mega-Pascal
mi	mile
min	minute
mph	miles per hour
MW	megawatts
MWd/MTU	megawatt-days per metric ton
psi	pound per square inch
s	second
yr	year

This page intentionally left blank

GLOSSARY OF SELECTED TERMS

Probabilistic Risk Assessment (PRA): A systematic method for addressing the risk triplet, as it relates to the performance of a complex system, to understand likely outcomes, sensitivities, areas of importance, system interactions, and areas of uncertainty. The risk triplet is the set of three questions that the NRC uses to define "risk": (1) what can go wrong? (2) how likely is it? and (3) what are the consequences? The NRC identifies important scenarios from such an assessment [from "Staff Requirements — SECY 98-144 — White Paper on Risk-Informed and Performance-Based Regulation" (Reference 1)].

Storage Cask: A Holtec International Storage and Transfer Operation Reenforced Module (HI-STORM) containing a multipurpose canister (MPC) loaded with fuel assemblies.

Storage (HI-STORM) Overpack: The long-term storage container designed and fabricated to allow safe movement of an MPC containing spent fuel assemblies to a storage pad and to provide shielded, safe storage of the MPC in the independent spent fuel storage installation (ISFSI). When the MPC containing fuel assemblies is transferred into the storage overpack, it is referred to as the "storage cask."

Transfer Cask: A Holtec International Transfer Cask (HI-TRAC) containing an MPC loaded with fuel assemblies.

Transfer (HI-TRAC) Overpack: The shielded container designed and fabricated to allow safe loading of fuel assemblies into the MPC, preparation of the MPC for storage, and transfer of the MPC into the storage (HI-STORM) overpack. When the transfer overpack has been loaded with an MPC and associated spent fuel assemblies, it is referred to as the "transfer cask."

This page intentionally left blank

1. INTRODUCTION

The spent fuel pools of commercial nuclear power plants are becoming filled with spent fuel assemblies. To avoid having to cease operations when the pools are full, many utilities have been removing older fuel from the pools and storing it in dry casks in an onsite independent spent fuel storage installation (ISFSI). In this study, a methodology for performing a probabilistic risk assessment (PRA) of a dry cask storage system was developed and applied by performing a pilot PRA of a specific cask system at a specific boiling-water reactor (BWR) site. Although the study results do not necessarily apply to other cask systems or sites, the methodology can serve as a guide for performing other such PRAs. Nonetheless, it should be noted that this study does not endorse the use (or non-use) of a dry cask storage system at any particular site.

The U.S. Nuclear Regulatory Commission (NRC), Office of Nuclear Regulatory Research (RES), jointly with the Spent Fuel Project Office (SFPO), performed this study in response to a request by the NRC's Office of Nuclear Material Safety and Safeguards (NMSS), to support its efforts to risk-inform NMSS-regulated activities. It is expected that NMSS will use the results of this study in conjunction with the methodology to develop a basis to determine the need for other PRAs, improvements in data gathering and analysis, and additional engineering design analysis, and to identify general program areas that may be candidates for increased or decreased staff review or inspection focus. Because the focus of this pilot study is solely on the methodology and its limited (i.e., case specific) application, no inferences or conclusions should be drawn with regard to the regulatory implications of this study.

1.1 Purpose

The purpose of this study is to develop and apply a methodology for performing a PRA to assess the risk to the public and to identify the dominant contributors to risk associated with dry cask storage involving a single cask at a specific site. The risk is evaluated using "best available" point estimates; when there is insufficient information or data, conservative bounding assumptions or estimates are used. The results of this study can be helpful for future studies to determine the extent and depth of any uncertainty analysis that may be needed. Similar to PRAs for nuclear power plants, this PRA includes a list of initiating events, response of system (i.e., dry cask) to initiating events, secondary containment analysis, and consequence analysis. Contrary to PRAs for nuclear power plants, this PRA did not include a human reliability analysis (HRA).

1.2 Scope

1.2.1 Issues Within the Scope

The cask system analyzed is the Holtec International Storage and Transfer Operation Reinforced Module (HI-STORM) 100 (Reference 2). This cask system, which is used for onsite storage only, consists of three major components, including a multipurpose canister (MPC), a Holtec International Transfer Cask (HI-TRAC overpack) which in this report is called a "transfer overpack," and a HI-STORM (overpack) called the "storage overpack." The MPC confines spent fuel assemblies for the duration of the storage period (typically 20 years). When the MPC is removed from the spent fuel pool and prepared for storage, it is already inside the transfer overpack to shield workers from radiation.

In this study, the transfer overpack containing the MPC is referred to as the "transfer cask," and the storage overpack containing the MPC is referred to as the "storage cask." During onsite storage, the storage cask shields people from radiation, provides a path to cool the MPC by convection through vents, and mechanically protects the MPC.

The study's assessment begins when spent nuclear fuel assemblies are loaded into the MPC, within the transfer overpack. The transfer cask is then moved to an area on the refueling floor, where the MPC is prepared for storage. The transfer cask is lowered through the equipment hatch to the storage overpack on the ground level, where the MPC is moved from the transfer cask into the storage overpack. The loaded storage cask is then moved to the ISFSI, where it is set on a concrete pad.

For source term and release fractions, this study considered spent BWR fuel. The fuel considered is high-burnup, having been stored and cooled for 10 years, respectively, in the spent fuel pool.

1.2.2 Issues Beyond the Scope

1.2.2.1 Version of the Cask

The version of the cask used in this study is that documented in Reference 2. Any subsequent changes to the design, documented as amendments or performed in accordance with Title 10, Section 72.48, of the *Code of Federal Regulations* (10 CFR 72.48), are beyond the scope. Nonetheless, changes to the cask would have to be fairly significant to impact the main conclusion of this report (that the overall risk is extremely low).

1.2.2.2 Unloading, Offsite Transportation, and Repository Storage

A storage cask may have to be unloaded. The storage overpack is designed for onsite transfer and storage; it cannot be moved offsite. If spent fuel is moved to a permanent repository, at a minimum, the MPC would have to be removed from the storage overpack and placed in a transport overpack. If, for some reason, the spent fuel needed to be reconfigured (e.g., because incorrect assemblies were mistakenly loaded), the MPC would need to be opened. Neither circumstance is analyzed in this study. The storage overpack is designed for onsite transportation and storage. Thus, offsite transportation and repository storage are not analyzed in this study.

1.2.2.3 Damage to the Plant

The effects of dropping the transfer cask on the floors of the load path from the cask pit (the alcove of the spent fuel pool where the transfer cask is loaded) to the equipment hatch were estimated where details of the floors were obtained. Any damage to underlying plant systems, equipment, and components, or capabilities to shut down the reactor were not analyzed and are beyond the scope of this study. Where the floor has supporting beams, girders, or concrete walls located underneath, the floor is expected to hold the cask, were it to drop from a distance typical of the height to which it is lifted while being moved. It is important to note that the crane carrying the transfer cask along the load path between the cask pit and equipment hatch is single-failure-proof.

1.2.2.4 Uncertainty

Although there are inherent uncertainties in the initiating event frequencies, conditional probabilities, and consequences used to calculate the risk, this study does not consider those uncertainties. This is because the purpose and scope of this study were limited, as were the resources for developing and applying a methodology to assess the risk to the public and to identify the dominant contributors to risk associated with dry cask storage involving a single cask at a specific site. An essential element of an uncertainty analysis is a sensitivity analysis whereby the possible ranges of the input variables are determined and their effects on the output measures are systematically evaluated. With a few exceptions, this study did not involve a sensitivity analysis of its input variables. This study uses best available point estimates, when available; conservative or bounding assumptions are used when best estimates are not available. However, because no uncertainty analysis is performed, the degree of conservatism in the risk estimates cannot be determined.

1.2.2.5 Worker Risk

The PRA methodology developed in this study is patterned after that used for nuclear power plants, which considers public risk. PRAs for reactors, such as those in Reference 3, were performed, in part, to evaluate the extent to which five plants met the NRC's safety goals (Reference 4) for risk to the public. Like PRAs for reactors, this study does not consider worker risk.

1.2.2.6 Human Reliability

A human reliability analysis (HRA) of loading spent fuel into the MPC, lifting the transfer cask during the handling phase, and welding the MPC when preparing it for storage, was not incorporated into this pilot PRA.

1.2.2.7 Fabrication of the MPC, Transfer Overpack, and Storage Overpack

This study assumes that the cask is fabricated as designed (Reference 2).

- Assumption: The MPC, transfer overpack, and storage overpack are constructed as designed.

Fabrication includes manufacturing and assembly of cask components. While fabrication errors could be modeled and analyzed, this was not done in this study.

Welds made according to accepted standards inherently contain small flaws that depend on the material being welded, the welding materials, and the welding process. Although this study does not consider fabrication errors, the weld failure evaluation of the MPC does take into account normal flaws that exist in weld-deposited austenitic stainless steel. Statistical distributions describing the densities and sizes of flaws were obtained from results documented in Reference 5.

1.2.2.8 Mis-Loading Spent Nuclear Fuel

An HRA to determine the probability of mis-loading spent nuclear fuel into the MPC is beyond the scope of this study for the reasons discussed in Section 1.2.2.6. Even though the frequency of mis-loading is not estimated, deterministic calculations were performed to investigate the effects of mis-loading on thermal loads, the failure probability of the MPC (Section 8.1), and the possibility for criticality (Section 8.2).

1.2.2.9 Aging Effects

To evaluate possible aging effects, a CASTOR-V/21 dry storage cask was examined for degradation (Reference 6). This cask was produced for use in testing aging effects on long-term dry cask storage. (This cask design was not put into production.) The examination consisted of remote indirect visual examination [cask internal, lid seals, and pressurized-water reactor (PWR) spent fuel assemblies] and temperature measurements of selected spent fuel assemblies. Interior crud samples were taken, and surface gamma and neutron dose rates were measured. Selected fuel rod assemblies were removed from one assembly, visually examined, and subjected to nondestructive, destructive, and mechanical examination. The helium inerting gas was sampled for analysis.

After 14 years of storage, no evidence of degradation that would affect the performance of the cask or integrity of the fuel was evident. The fuel was intact; there was no evidence of creep or rod bow. Crud found on the fuel rods was attributed to oxidized steel while the fuel was in the reactor; none of the oxidation is attributed to dry storage. Of 16 stitch welds that attached borated plates to the basket, 15 were cracked. The stitch weld cracking was attributed to the tight fit of the assemblies in the basket, not to storage. Small amounts of air mixed in with the helium were attributed to the process of inerting the cask.

While the results for the CASTOR-V/21 dry cask suggest that there will be no significant aging effects for the subject cask, it is unclear whether the two casks experience similar conditions. Accordingly, except for possible cask and fuel corrosion (see Section 8.3), aging effects are beyond the scope of this study.

1.2.2.10 Combinations of Factors That Could Impact the Probability of MPC Failure

Section 8 discusses several factors that can influence the probability of MPC failure. Individual factors are investigated one at a time with sensitivity studies. It is not expected that combinations of factors will significantly impact the risk estimates.

1.2.2.11 Military Missiles, Sabotage, and Terrorism

The impact of military missiles, sabotage, and terrorism was not incorporated into this pilot PRA.

1.3 Overview of the Risk Calculations

The structure of the risk calculations, as illustrated in Figure 1, closely mirrors the structure of this report. In the figure, boxes indicate analyses, models, and results. The associated section numbers indicate where this report discusses the results needed to estimate risk. Circled numbers are keyed to the discussion below.

The system that is to be modeled consists of the dry cask (MPC, transfer overpack, storage overpack) and the plant layout (load path, floor structure, crane). The structure of the dry cask components is determined from engineering drawings and cask specifications (1). The next step is to describe the secondary containment isolation system (2).

Challenges to the transfer cask and the storage cask are determined from other studies (3), such as Reference 7. The list of initiating events in Reference 7 is a general list that was developed for risk assessments of commercial nuclear power plants. Along with information about the cask system (1) and the subject plant (2), the initiating events are evaluated (4) to derive a list of initiating events (5) that is relevant to the subject cask at the subject site. The frequency of each initiating event in the list is then determined (6) from other reference information (3).

With information about the cask system (1), and information about the plant layout (2), engineering analyses (7) are performed to determine the mechanical loads (8) on the cask that result from initiating events that can occur at the subject site and affect the cask. A mechanical load model (9) is developed with engineering analyses (7). With the mechanical loads for each initiating event, the mechanical load model is used to determine the mechanical stresses (10) in the MPC. The mechanical stresses are then used in a failure model of the MPC (11) to assess the probability of MPC failure (12). The mechanical loads are also used in the fuel failure model (16) to determine the fraction of fuel rods that fail (17).

With information about the cask system (1) and a list of initiating events (5) that can occur at the subject site and affect the cask, engineering analyses (7) are performed to determine the thermal loads (13). A thermal load model (14) is developed with engineering analyses (7). Given the thermal loads (13), the thermal load model is used to determine the thermal stresses (15) on the MPC and the fuel rods. The thermal stresses are then used in the failure model of the MPC (11) to assess the probability of MPC failure (12), and in the fuel failure model (16) to determine the fraction of fuel rods that fail (17).

From the plant information (2), engineering analyses (7) are performed to assess the systems reliability to isolate the secondary containment in the event of a release of radioactive material inside the secondary containment. A reliability model (18) is then used to determine the conditional probability that the secondary containment will fail to isolate (19) if the MPC is dropped, fails, and releases radioactive material into the secondary containment.

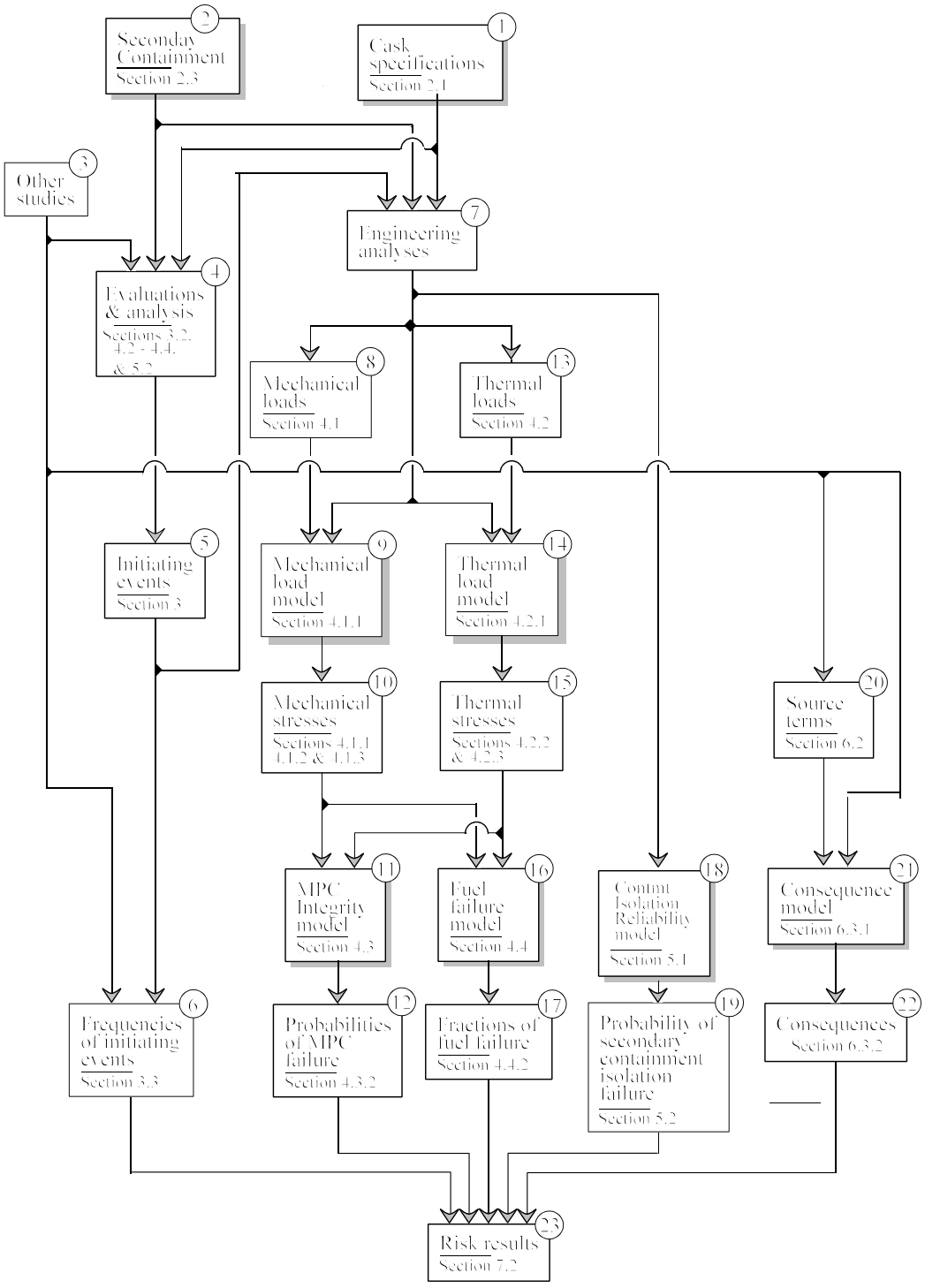

Figure 1. Structure of the Risk Calculations and Organization of the Report

From other studies (3), source terms (20) are determined. The source terms, adjusted to account for the inventory of radionuclides in the MPC and other information (3) about the plant site (e.g., population distribution), are then used in a consequence model (21) to estimate the consequences (22) of an accident.

The values needed to assess risk (23) are the frequencies of the initiating events (6), the probability of MPC failure (12), the fractions of fuel rods that fail (17), the probability that the secondary containment will fail to isolate (19), and the consequences (22). These five values are combined to calculate the risk to the public. To quantify the risk, best available point estimates are used. When there is insufficient information or data, conservative bounding assumptions or estimates are used.

1.4 Elements of the PRA

The dry cask storage operation is divided into the three phases of handling, transfer, and storage. During the handling phase, spent fuel assemblies are placed into the MPC within the transfer cask. After the MPC is dried, inerted with helium, and sealed, the transfer cask is lowered through the equipment hatch to the storage overpack on the ground level. The MPC is then moved from the transfer cask into the storage overpack. The transfer phase takes place when the storage cask is moved out of the secondary containment to the storage pad. The storage phase takes place after the storage cask is set down on the storage pad. To analyze the risk of the dry cask storage operation, the phases are divided into 34 stages. A stage is defined as a discrete part of the operation that is convenient for the risk analysis. For example, because the height at which the cask is moved and the composition of the surface over which it is moved determine the mechanical load on the MPC if it were dropped, these aspects are used to define some of the stages.

A comprehensive list of initiating events is developed, and the risk associated with each initiating event is evaluated. Analyses are performed to determine the cask's response to the mechanical and thermal loads imposed by the initiating events. For example, the following analyses evaluate the consequences of dropping the transfer cask during the handling phase:

- A mechanical load analysis determines the stresses on the fuel cladding and MPC as a function of drop height.
- Given the stress on the fuel cladding and MPC from dropping the transfer cask or MPC, failure analyses determine the probability of the fuel cladding and MPC failing.
- Source term analysis is used to determine the releases from the fuel cladding and the MPC.
- An engineering analysis determines the reliability of the secondary containment to isolate if there is an accidental release of radioactivity inside the secondary containment.

The annual risk to the public of handling, transfer, and storage of a single cask is estimated. The risk measures are the individual probabilities of a prompt fatality within 1.6 km (1.0 mi) and a latent cancer fatality within 16 km (10 mi) of the site. In calculating the annual risks, the PRA considers weather conditions and population distribution in the vicinity of the site. (Appendix E to this report provides more detailed discussion and basis for emergency planning assumptions.) These are the consequence measures that are typically calculated in the risk assessments of nuclear power plants (e.g., Reference 4). Risks to the environment and property are not typically calculated in reactor PRAs and were not considered in this study.

This page intentionally left blank

2. DRY CASK AND SECONDARY CONTAINMENT SYSTEMS

2.1 Dry Cask System

The Holtec HI-STORM 100 dry cask system consists of an MPC that confines the fuel, a transfer overpack that shields workers from radiation while the cask is being prepared for storage, and a storage overpack that shields people from radiation and protects the MPC during storage. When the transfer overpack contains the MPC, the unit is referred to as the transfer cask. When the storage overpack contains the MPC, the unit is referred to as the storage cask. Details of the cask system are illustrated in Figures 2 and 3. These and other figures are based on drawings in Sections 1 and 8 of Reference 2.

Figure 2 is a composite sketch of the MPC and transfer overpack. The MPC is 4.8 m (15.8 feet) high and 1.73 meter (5.7 feet) in diameter. When loaded with BWR fuel assemblies, it weighs 36 metric tons (40 tons). The transfer cask is 5.0 meters (16.4 feet) high and 2.3 meters (7.6 feet) in diameter. When loaded with BWR fuel assemblies, it weighs 91 metric tons (100 tons). The fuel basket is free standing, but held in position inside the MPC by basket supports. Boral plates along the walls of each cell prevent the spent fuel from becoming critical, while upper and lower fuel spacers keep the fuel assemblies vertically positioned in the basket. Except for the boral plates and heat conduction elements, all MPC components are made of stainless steel. The transfer overpack consists of an inner steel shell, lead shield, and outer steel shell, and a water jacket provides additional shielding. The pool lid at the bottom of the transfer overpack seals the inner cavity, thereby retaining clean demineralized water to prevent the exterior of the MPC from being contaminated. A lift yoke (not shown) attaches to lift trunnions on the transfer overpack.

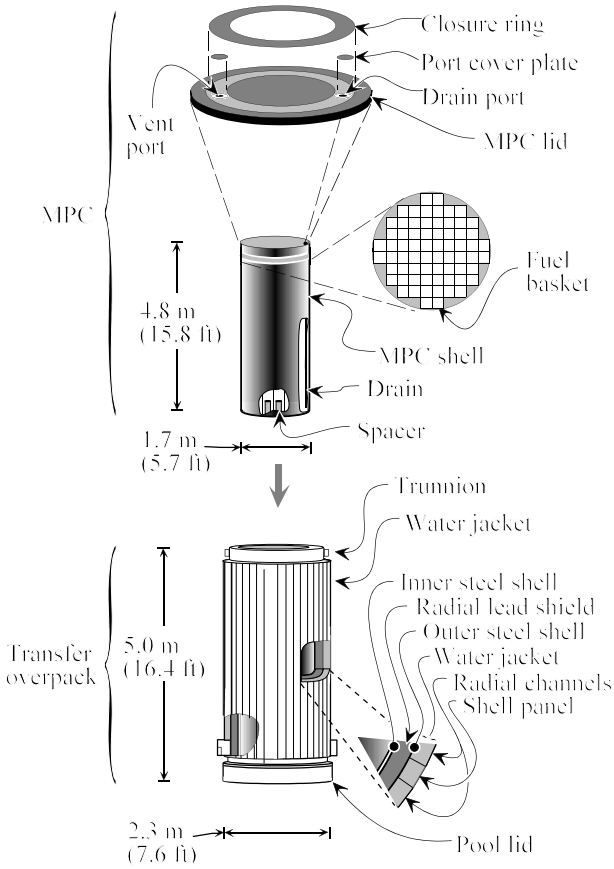

Figure 2. MPC and Transfer Overpack

Figure 3 is a composite sketch of the storage cask with the MPC partially inserted. The overpack consists of inner and outer steel shells connected by full-length steel radial plates that extend from the bottom to the top. The volume between the shells is filled with unreinforced concrete. The shells and the radial plates form the structural member. The concrete is for radiation shielding. The lid is bolted to the overpack at anchor blocks, which are attached to the radial plates.

Channels between the overpack and the MPC allow air to circulate, entering the inlet vent at the bottom of the overpack and exiting the outlet vent at the top of the overpack. The channels are designed to progressively collapse during a severe impact, absorbing some of the impact that could be transmitted to the MPC. Shield cross-plates reduce radiation streaming through the vents. Screen covers prevent insects, birds, and animals from entering the vents to build nests that might block the vents.

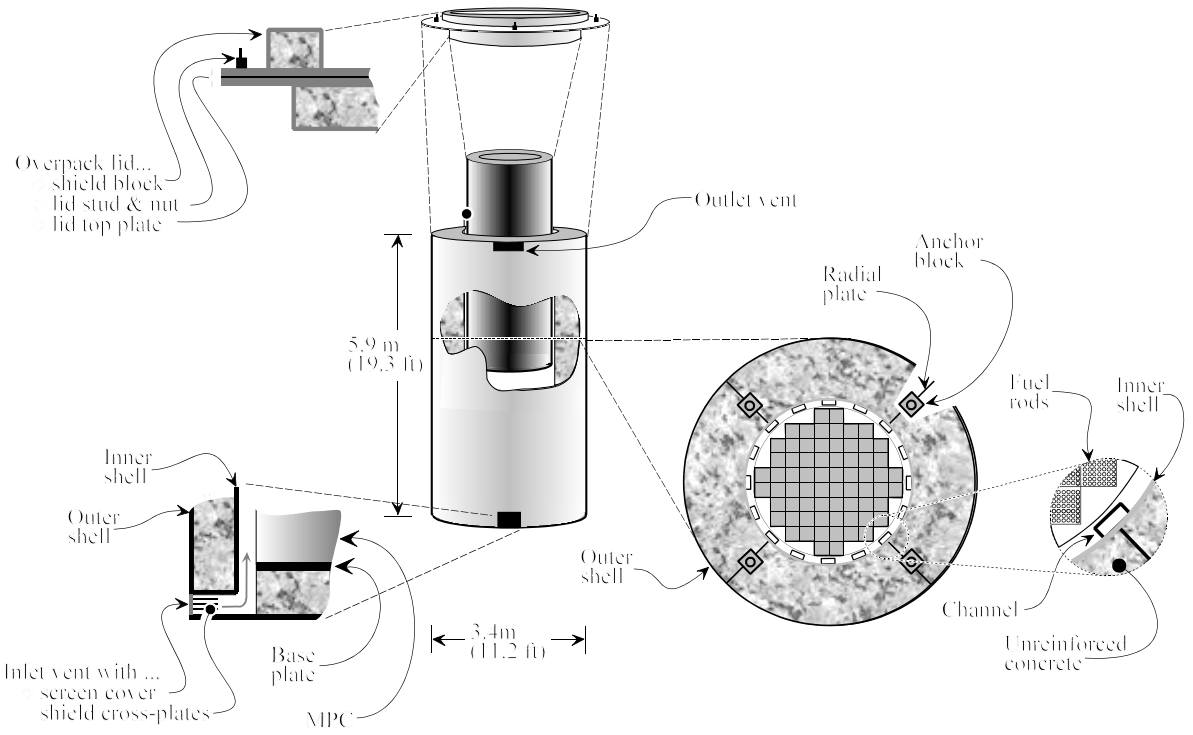

Figure 3. MPC and Storage Overpack

2.2 Stages of the Dry Cask Storage Operation

As previously noted, the dry cask storage operation is divided into the three phases of handling, transfer, and storage:

(1) During the handling phase, activities take place on the refueling floor and ground level. From the refueling floor, about 29.9 meters (98.1 feet) above ground level, the transfer cask is lowered about 13 meters (42.7 feet) to the bottom of the cask pit next to the spent fuel pool. There, the dry cask storage operation begins when spent fuel assemblies are loaded into the MPC. After the MPC basket is full, the lid is installed and the transfer cask is lifted out of the spent fuel pool and moved to a preparation area on the refueling floor, where the MPC is drained, dried, inerted, and sealed. Additional preparations are made, and the transfer cask is lowered to the storage cask, still inside the secondary containment. The MPC is then lowered from the transfer cask to the storage cask.

(2) After the Kevlar stays and the alignment device are removed, the storage cask (with the MPC inside) is moved through an airlock to outside the secondary containment to begin the transfer phase. The storage cask is moved away from the secondary containment, where final preparations are made before moving the storage cask to the storage pad with a specially designed tractor, called an overpack (cask) transporter. There, the storage cask is set down in a predetermined location (footprint), which is indicated by paint marks on the storage pad. This predetermined storage footprint ensures that the storage casks are adequately spaced and their weight is properly distributed over the storage pad.

(3) During the storage phase, storage casks remain on the storage pad for 20 years. The storage cask does not have (and does not require) instruments or other mechanisms to detect heat loads or leaks in the MPC. Routine surveillance ensures that the vents remain unblocked.

The handling, transfer, and storage phases of the dry cask storage operation are divided into 34 stages, as listed in Table 1. Figure 4 is a schematic diagram illustrating the movement of the transfer cask and storage cask through the stages in Table 1 as the MPC is moved from the spent fuel pool to the ISFSI, where the storage pads are located. The numbers along the paths in Figure 4 correspond to the stages in Table 1.

A stage is defined as a discrete part of the operation that is convenient for risk analysis. Factors used to define the various stages include the following examples:

- height at which the cask is carried
- direction in which the cask is moved
- rigging of the cask
- surface (e.g., concrete, asphalt, gravel) over which the cask is moved

The phases described above reflect the process used at the particular plant site that served as the basis for this study. Terminology may vary to some extent from plant to plant, so in such cases, the reader is advised to compare the given plant's terminology with the way the terms are used in this report.

Table 1. Stages of the Dry Cask Storage Operation

Stages		Height [A] m	Height [A] ft
1	Loading fuel assemblies into the MPC [B]	4.8	16
2	Placing the MPC lid onto the MPC and engaging the lift yoke on the transfer cask [C]	0	0
3	Lifting the transfer cask out of the cask pit	13	42.5
4	Moving the transfer cask over a railing of the spent fuel pool	0.9	3
5	Moving the transfer cask to the preparation area (1st segment)	0.3	1
6	Moving the transfer cask to the preparation area (2nd segment)	0.3	1
7	Moving the transfer cask to the preparation area (3rd segment)	0.3	1
8	Lowering the transfer cask onto the preparation area [D]	0.3	1
9	Preparing (draining, drying, inerting, and sealing) the MPC for storage	0	0
10	Installing the short stays and attaching the lift yoke [D]	0	0
11	Lifting the transfer cask	0.6	2
12	Moving the transfer cask to exchange bottom lids of the transfer cask (1st segment)	0.6	2
13	Moving the transfer cask to exchange bottom lids of the transfer cask (2nd segment)	0.6	2
14	Replacing the pool lid with the transfer lid	0.1	0.25
15	Moving the transfer cask near the equipment hatch	0.6	2
16	Holding the transfer cask	0.6	2
17	Moving the transfer cask to the equipment hatch	0.6	2
18	Lowering the transfer cask to the overpack through the equipment hatch	24.4	80
19	Preparing (remove short stays, disengage lift yoke, attach long stays) to lower the MPC	0	0
20	Lifting the MPC and opening doors of transfer lid	5.8	19
21	Lowering the MPC through the transfer cask into the storage cask	5.8	19
22	Moving the storage cask into the airlock on Helman rollers	0	0
23	Moving the storage cask out of the airlock on Helman rollers	0	0
24	Moving the storage cask away from the secondary containment on Helman rollers	0	0
25	Preparing (installing lid, vent shield cross-plates, vent screens) the storage cask for storage	0	0
26	Lifting the storage cask above the Helman rollers with the overpack transporter	0.1	0.25
27	Moving the storage cask above a cushion on the preparation area	<0.1	<0.25
28	Holding the storage cask above the cushion while attaching a Kevlar belt	<0.1	<0.25
29	Moving the storage cask above the concrete surface of the preparation area	0.3	1
30	Moving the storage cask above the asphalt road	0.3	1
31	Moving the storage cask above the gravel surface around the storage pads	0.3	1
32	Moving the storage cask above the concrete storage pad	0.3	1
33	Lowering the storage cask onto the storage pad	0.3	1
34	Storing the storage cask on the storage pad for 20 years	0	0

[A] Height is the distance the cask would fall if the support system failed.

[B] Prior to Stage 1, the MPC is inserted into the transfer cask, and after other preparations, lowered into the cask pit. The storage overpack is placed on Helman rollers and moved under the equipment hatch.

[C] The lift yoke attaches to the trunnions of the transfer cask.

[D] Stays attach to the lift yoke on one end and cleats of the MPC on the other end.

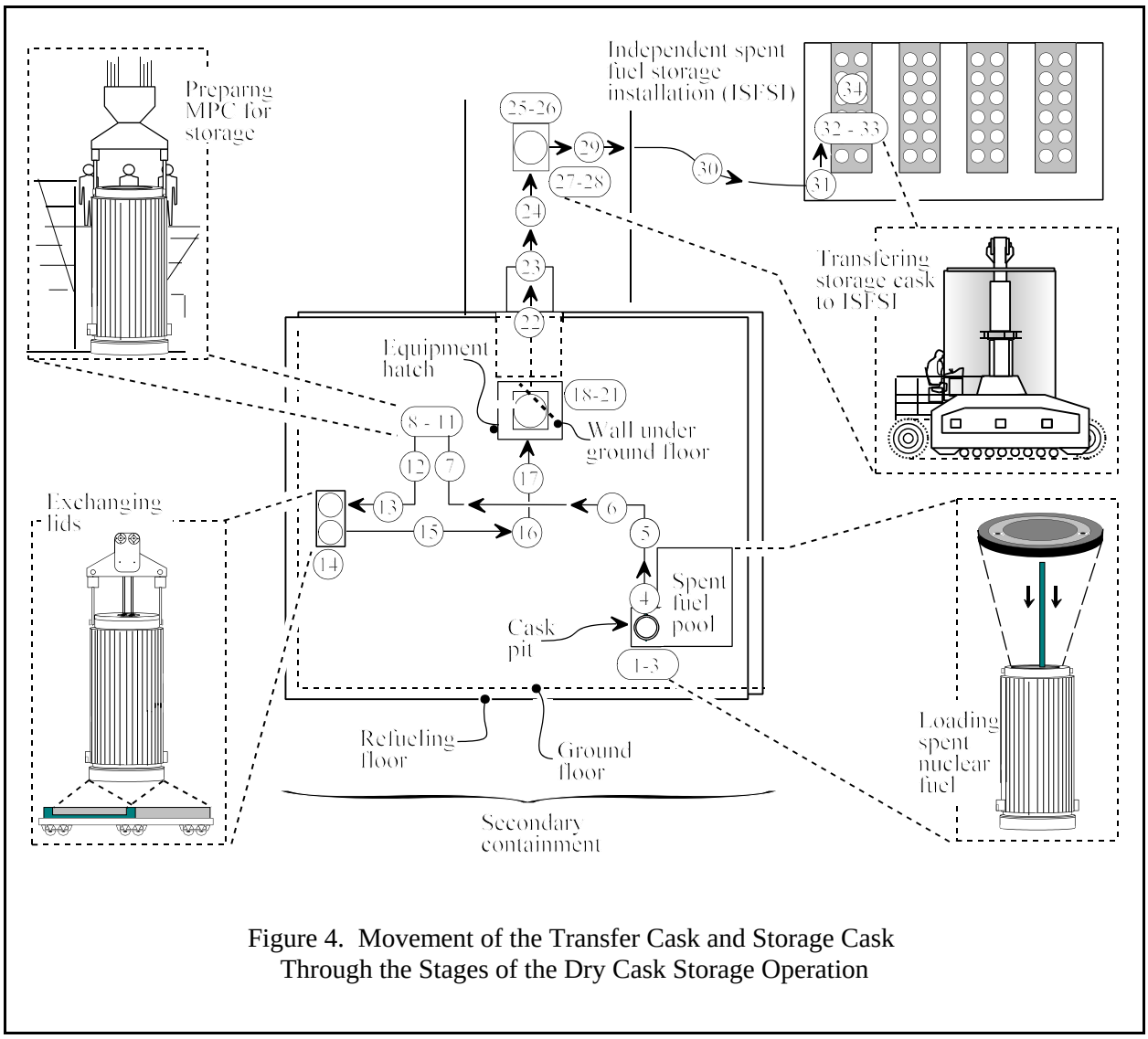

Figure 4. Movement of the Transfer Cask and Storage Cask Through the Stages of the Dry Cask Storage Operation

Figure 5 shows a vertical view of stages where the transfer cask is in the equipment hatch. Except for the floor thicknesses, the vertical axis is drawn to scale; the inset shows the wall supporting the overpack at ground level. The steel beams and concrete walls supporting the refueling floor along the path where the transfer cask is carried are not shown. The lift height is kept to the minimum necessary to clear obstacles on the floor (such as railings, pipes, and raised edges of floors).

Variations in the lift height and path over which the transfer cask and storage cask are normally carried are considered uncertainties. Uncertainty is beyond the scope of this study (see Section 1.2.2.4).

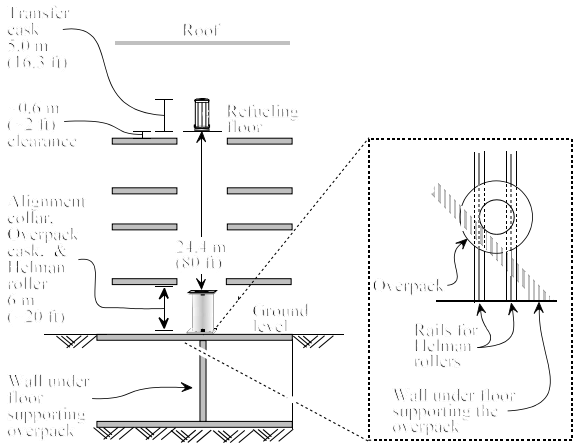

Figure 5. Vertical View of the Equipment Hatch

Pre-stage conditions and preparations prior to Stage 1

The secondary containment is closed because the reactor is at full power. The normal slightly negative pressure inside the secondary containment is established.

The storage overpack is on Helman rollers on the ground floor underneath the equipment hatch.

The MPC is inserted into the transfer overpack (transfer cask). After the MPC is filled with water, the transfer cask is lowered into the cask pit (an alcove of the spent fuel pool).

Gates between the spent fuel pool and cask pit, above the level of the fuel, have been removed to allow movement of spent fuel assemblies from the spent fuel pool into the MPC inside the empty transfer cask in the cask pit. After the MPC is filled with 68 spent fuel assemblies, the gates are replaced and the lid is placed on the MPC.

The analysis uses the following assumptions:

- The secondary containment remains closed during the handling phase.
- The transfer cask and storage cask are carried at the heights specified in the formal procedures (see Table 1).
- The transfer cask is carried along the load path over the refueling floor of the secondary containment.
- The storage cask is carried along the designated route to its placement on the storage pad in the ISFSI.

Stages 1–3

In Stage 1, fuel assemblies are placed inside the MPC basket. Specific assemblies are loaded into specific spaces of the basket to take advantage of the shielding, criticality control, and heat rejection capabilities of the cask system. After the MPC is loaded with spent fuel assemblies, the lid is installed to shield workers from radiation emanating from the top (the transfer cask shields workers from radiation emanating from the sides and bottom). The lift yoke is engaged on the trunnions of the transfer cask (Stage 2). The transfer cask is lifted out of the cask pit to about 13 meters (43 feet) above the bottom of the cask pit, where it is rinsed with clean water (Stage 3).

Stages 4–7

The transfer cask is moved over the cask pit to clear a railing and a pipe (Stage 4), then lowered to about 0.3 meters (1 foot) as it is moved along a predetermined path to the preparation area. The load path of the refueling floor is supported by steel beams and walls such that it can hold a static load of 127 metric tons (125 tons). The load path to the preparation area consists of three perpendicular segments.

Stages 8–13

At the preparation area, the transfer cask is lowered to the refueling floor (Stage 8) where the MPC is partially drained and prepared for storage (Stage 9). After the lid is welded to the shell of the MPC, the MPC is filled with water to hydrostatically test the weld. After the water is drained, the MPC is dried, purged, and filled with helium. A port cover and drain cover are then welded to the lid, and the closure ring is welded to the lid and the shell for redundant sealing. The top lid of the transfer cask is then installed and bolted to the transfer overpack.

After the MPC is prepared, the transfer cask is rigged to move (Stage 10). While the yoke is over the cask with the holes of the arms below the trunnions, rigging personnel on scaffolds install the short Kevlar support stays, which are attached from the lift yoke through an access hole in the top lid of the transfer cask to cleats on the MPC. In Figure 6, the body of the yoke is close to the transfer cask so the stays are slack while being attached to the cleats. As the yoke is raised, the stays become taut, lifting the MPC off of the pool lid. When the holes of the arms are next to the trunnions, the yoke arms are placed over the trunnions, and the lift yoke is attached. The transfer cask is then lifted about 0.6 meters (2 feet) above the refueling floor (Stage 11), and is moved along a load path to another area of the refueling floor (Stages 12 and 13).

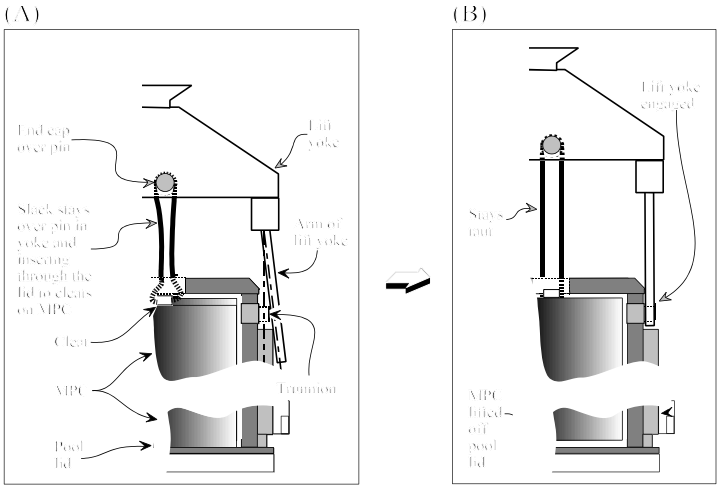

Figure 6. Lift Yoke with Stays Attached (A) Prior to and (B) after Engaging the Yoke Arms on the Trunnions

Stages 14–22

The pool lid at the bottom of the transfer cask is replaced by a transfer lid (Stage 14) for use in Stage 20. The transfer lid is on a carriage. Short stays hold the MPC above the pool lid inside the transfer cask. The transfer cask is set down in the empty side of the carriage. The pool lid is unbolted. The transfer cask is then raised slightly, and the carriage is moved to bring the transfer lid underneath the transfer cask. The transfer cask is lowered and the transfer lid is bolted to the transfer cask shell. The bottom lid exchange is illustrated in Figure 7. With the transfer lid attached, the transfer cask is lifted to a height of about 0.6 meters (2 feet) above the refueling floor and moved (Stage 15) to a holding area near the equipment hatch (Stage 16).

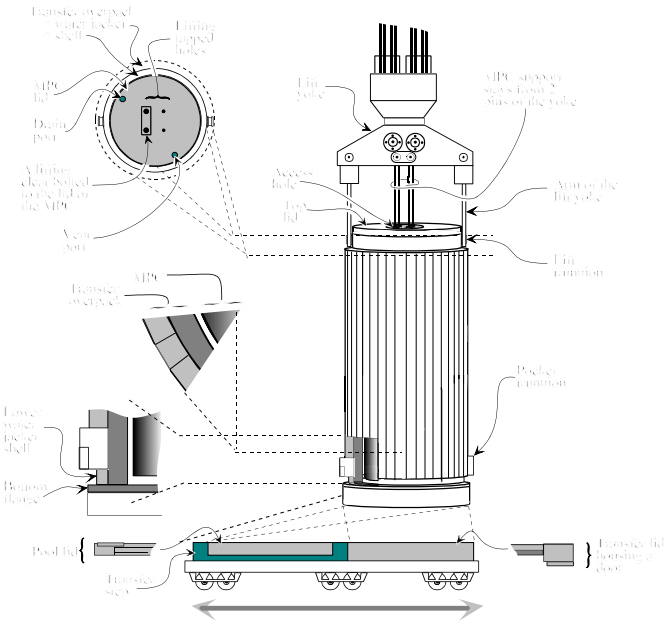

Figure 7. Replacing the Pool Lid with the Transfer Lid

The transfer cask is held while preparations are made on the ground floor to receive the transfer cask. The transfer cask is then moved to the equipment hatch (Stage 17). The height is sufficient to clear a raised lip around the hatch on the refueling floor. The transfer cask is then lowered through the equipment hatch of the refueling floor, 24.4 meters (80 feet) to the top of the storage overpack (storage cask) at ground level (Stage 18). Two workers assist in guiding the transfer cask onto the storage cask. An alignment device (i.e., collar on the storage cask) has receptacles that determine the correct position of the transfer cask on the storage cask. The lift yoke is removed and the short stays are replaced with long stays, which are used to lift the MPC off the transfer lid (Stage 19). After the MPC is lifted several inches off the transfer door by the Kevlar stays (Stage 20), the transfer doors are opened, and the MPC is lowered into the storage cask (Stage 21). As it is lowered, the MPC is guided by the transfer cask and, when in the storage cask, by channels in the storage cask. Once lowered, the MPC comes to rest on the pedestal inside the storage cask. The storage cask is moved along tracks on Helman rollers into the airlock of the secondary containment (Stage 22). The movement is accomplished by pulling the storage cask with a diesel-powered rail vehicle called the trackmobile. The airlock is needed to maintain the negative pressure inside the secondary containment, which is developed by the ventilation system.

Stages 23–28

The trackmobile continues to pull the storage cask from the airlock, outside the secondary containment (Stage 23). The storage cask is moved a short distance outside the secondary containment, still on the Helman rollers (Stage 24), to an area where it is prepared for storage (Stage 25). The storage cask lid is installed. Shield cross-plates are inserted into the vents on the top and bottom of the storage cask, and screens are installed over the vents. Cleats are bolted to the top of the storage cask. A transporter is moved up to the storage cask, and the lift yoke is attached to the cleats. The lift yoke is engaged and the storage cask is lifted about 0.3 meters (1 feet) above the ground (Stage 26). Four pins are inserted into the hydraulic lifting mechanism of the storage cask transporter to lock them. The hydraulic mechanism is deactivated, bringing the weight of the storage cask onto the four pins. The storage cask is moved over a cushion (Stage 27), where it is held (Stage 28) while a Kevlar belt is wrapped around the midline of the storage cask to keep it from swaying while being moved to the ISFSI.

Stages 29–33

The storage cask is moved by the transporter about 0.6 km (about 0.4 mi) from the reactor building at a speed of about 0.64 km/hr (0.4 mph). This travel begins on concrete (Stage 29), but the road from the preparation area to the ISFSI is asphalt (Stage 30), and the road between the storage pads inside the ISFSI is gravel (Stage 31). The transporter travels along the gravel road and pivots next to the place on the storage pad where the storage cask will be placed. The storage cask is then moved onto the concrete storage pad (Stage 32), where it is set down in a predetermined location (Stage 33).

Stage 34

Storage casks are kept in the ISFSI. The ISFSI of the subject plant has four concrete pads, and each pad holds 12 storage casks. Storage casks are placed on the pads in a pattern that distributes their weight. Paint marks on the concrete indicate where each storage cask is to be placed.

2.3 Secondary Containment Isolation System

Stages 1–22 (Table 1) occur inside the secondary containment, which is a large concrete structure that encloses the refueling and spent fuel pool areas, both reactor units, and associated equipment rooms and areas. The secondary containment has a total free volume of approximately 84,951 m^3 (3×10^6 ft^3). The atmosphere inside is cooled by four heating, ventilation, and air conditioning (HVAC) systems.

If a release of radioactive material were to occur inside the secondary containment following a drop of the transfer cask, three distinct functions would occur to (1) detect radioactive material, (2) isolate the secondary containment, and (3) operate the standby gas treatment system (SGTS). Each of these functions is accomplished by redundant and independent trains of systems. The release of radioactive material is detected by one or more of six detector systems that signal the containment to isolate. Each of these detector systems consists of two trains, with each train having two detectors. Both detectors in a train must detect radiation to isolate the containment. Only one of the 12 trains is needed to isolate the secondary containment.

The radiological monitoring system for the secondary containment is part of the process radiation monitoring system. Table 2 shows the process and effluent radiological monitors of the secondary containment. This table provides a brief description of each radiological monitor in these systems.

Table 2. Detectors in the Secondary Containment System

Location	Purpose	Principal Radionuclides Detected
Reactor building ventilation stack	Monitor discharge to environment	Kr-85m, Kr-87, Kr-88, Xe-135
Main stack	Monitor discharge to environment	Ar-41, Xe-133
Reactor building ventilation exhaust	Isolate building and initiate SGTS	Kr-85m, Kr-87, Kr-88, Xe-135
Reactor building ventilation filter discharge	Monitor filter exhaust	Kr-85m, Kr-87, Kr-88, Xe-135
Refueling floor zone ventilation exhaust	Isolate building and initiate SGTS	Kr-85m, Kr-87, Kr-88, Xe-135
Refueling floor ventilation filter	Monitor filter exhaust	Kr-85m, Kr-87, Kr-88, Xe-135
Standby gas treatment system	Monitor process duct	Ar-41, Xe-133

Normally, the HVAC systems ventilate the secondary containment, maintaining a slight negative pressure inside with respect to the outside environment. If the containment is opened to atmosphere, fans will trip on overload as they throttle to maintain the negative pressure, and indicators will alarm in the control room. Table 3 shows that total exhaust flow rates are greater than total supply flow rates, to maintain a negative pressure in the secondary containment. The difference in the flow rates is attributable to leakage through cracks and joints into the secondary containment. The SGTS is normally in a standby mode. If a small amount of radioactive material is released into the accessible area (where people are working), the exhaust of this area isolates, and flow is redirected to the inaccessible area where it is filtered before being exhausted. This arrangement utilizes the more effective filters on the exhausts of the inaccessible area ventilation system and avoids isolating the entire secondary containment when small amounts of radioactive material are released in the secondary containment, as would be expected during normal plant operations. If a larger amount of radioactive material passes through the filter, radiation monitors signal the HVAC systems to isolate the entire secondary containment.

Table 3. Volumetric Flow Rates of Secondary Containment Ventilation

		HVAC					
		Supply		Exhaust		SGTS	
		m^3/min	ft^3/min	m^3/min	ft^3/min	m^3/min	ft^3/min
Unit 1	Refueling Area	850	30000	905	31970		
	Rx Bldg Accessible	1699	60000	850	30000	85	3000
	Rx Bldg Inaccessible			950	31970		
Unit 2	Refueling Area	850	30000	905	31970		
	Rx Building	170	6000	170	6000	113	4000
	Total:	3568	126000	3735	131910	198	7000

In the event of a breach of the MPC and release of radioactive material into the secondary containment building after a transfer cask drop, the HVAC system is designed to isolate the secondary containment to prevent the release of radioactive material to the environment. The containment is isolated by stopping the HVAC fans and closing one of two serial isolation valves located on each HVAC supply and exhaust duct. One isolation valve is located inside, and the other is located outside the secondary containment. While all HVAC fans receive an isolation signal, 6 of the 12 detector trains generate an isolation signal for the inside isolation valves, while the other 6 detector trains generate an isolation signal for the outside isolation valves. This arrangement allows for independence between the two serial isolation valves and their isolation trains.

Each SGTS consists of two trains of filters and exhaust fans. Both trains of both SGTSs receive a start signal from any of the 12 detector trains. While the capacity of both SGTSs is not enough to overcome the flow generated by a single operating HVAC fan (supply or exhaust), only one SGTS is needed to mitigate an uncontrolled and unfiltered release with all HVAC fans off. Even if the isolation valves fail to close, the containment effectively isolates if all fans are off and either SGTS operates.

This page intentionally left blank

3. INITIATING EVENTS

3.1 List of Initiating Events

An initiating event is a disturbance in the normal operation of the dry cask storage system, which could potentially lead to a release of radioactive material to the environment. For this study, a comprehensive list of initiating events was developed. Those initiating events that could not affect the subject plant, the transfer/storage cask(s), or the MPC were eliminated from further consideration. For the remaining initiating events, estimates of frequencies, probability of MPC failure, and consequences were developed.

Tables 4–6 list initiating events at the subject plant during the handling, transfer, and storage phases, respectively. These initiating events were identified from Reference 7, as well as design and operational data for the specific cask and plant being studied. Information concerning the cask system design was obtained from licensing documents (e.g., Reference 2). Analysts visited the subject plant to observe the operation and equipment used during the handling, transfer, and storage phases. Written descriptions of the procedures were also obtained and studied, and additional details were obtained through discussions with plant personnel.

The lists of initiating events were reviewed by NRC staff who had also reviewed and licensed the dry cask storage system. This review drew upon extensive knowledge and diverse perspectives regarding the cask system. Based on these reviews and the process used to construct the list, Tables 4–6 are believed to comprise a complete list of all initiating events that could conceivably affect the cask system.

The initiating events represent potential challenges to the cask's confinement function. They are grouped by operational phase (i.e., handling, transfer, storage) and type of load placed on the cask (i.e., mechanical and thermal).

In Tables 4–6, initiating events that are marked with an X in the status column have a risk of zero, because the frequency is zero for the subject site, the probability of MPC failure is zero, or the fraction of the fuel failing is zero. That is, the risk is zero if any one of these parameters is zero.

Table 4. Initiating Events During the Handling Phase and the Sections Where Frequency, MPC Failure, and Fuel Failure Are Discussed

Mechanical Events	Status	Frequency	MPC Failure	Fuel Failure
Drop of the Transfer Cask				
Into the cask pit		3.3.2	4.1.2.1	4.4
Cask tip-over		3.3.2	4.1.2.2	4.4
Onto storage overpack		3.3.2	4.1.2.3	4.4
Onto concrete floor		3.3.2	4.1.2.4	4.4
Onto refueling floor		3.3.2	4.1.2.5	4.4
Drop of the MPC into the storage overpack		3.3.2	4.1.2.6	4.4
Thermal Events				
Fire from diesel fuel in the trackmobile	X		4.2.1.2	

LEGEND: X indicates that the initiator does not affect the subject plant or does not breach the MPC.

Table 5. Initiating Events During the Transfer Phase and Section Where Frequency, MPC Failure, and Fuel Failure Are Discussed

Mechanical Events	Status	Frequency	MPC Failure	Fuel Failure
Drop of the Storage Cask				
On concrete	X		4.1.3.1	4.4
On asphalt	X		4.1.3.1	4.4
On gravel	X		4.1.3.1	4.4
Tip-over of the Storage Cask				
While the cask is being moved	X	4.1.3.1	4.1.3.2	4.4
Cask impacted by a vehicle	X	4.1.3.1	4.1.3.2	4.4
Thermal Events				
Fire from diesel fuel in trackmobile	X		4.2.1.2	
Fire from diesel fuel in cask transporter	X		4.2.1.2	

LEGEND: X indicates that the initiator does not affect the subject plant or does not breach the MPC.

Table 6. Initiating Events During the Storage Phase and Section Where Frequency, MPC Failure, and Fuel Failure Are Discussed

Mechanical Events	Status	Frequency	MPC Failure	Fuel Failure
Water currents during a flood	X	3.2.1		
Tsunamis	X	3.2.2		
Seismic events		3.3.3	4.1.3.2	
Volcanic activity	X	3.2.3		
High winds	X	3.3.4	4.1.3.2	
Soil erosion from intense precipitation	X	3.2.4		
Strikes from heavy objects				
Aircraft		3.3.7	4.1.3.3	
Wind-driven objects	X		4.1.3.3	
Heavy objects in flood waters	X	3.2.1		
Vehicle	X		4.1.3.3	
Meteorite		3.3.5	3.3.5	
Shockwaves from explosions				
Pipelines	X		4.1.3.4	
Nearby trucks and railcars	X		4.1.3.4	
Transformers	X	3.2.5		
Nearby barge	X	3.2.5		
Storage tanks	X	3.2.5		
Military missile	X	3.2.5		
Other facilities	X	3.2.5		
Thermal Events				
Vent Blockage				
Flood water over vents but below MPC	X	3.2.1		
Flood water over vents contacting MPC	X	3.2.1		
Flood water over vents submerging MPC	X	3.2.1		
Snow	X		4.2.1.2	
Ice	X		4.2.1.2	
Hail	X		4.2.1.2	
Intense precipitation	X		4.2.1.2	
Dirt & debris from winds	X		4.2.1.2	
Dirt from landslide due to heavy rains	X		4.2.1.2	
Dirt from landslide due to volcanic activity	X		4.2.1.2	
Volcanic ash deposits	X		4.2.1.2	
Accumulations or biological intrusions	X		4.2.1.2	
Lightning	X	3.3.6	4.2.2.2	
Fire causes pressurization or differential heating				
Fire from aircraft fuel	X	3.3.7	4.2.1.2	
Fire from burning barge contents	X		4.2.1.2	
Fire from site-specific materials	X		4.2.1.2	
Fire from a gas main	X		4.2.1.2	
Forest fire	X		4.2.1.2	

LEGEND: X indicates that the initiator does not affect the plant or does not breach the MPC.

The lists of initiating events exclude those that are not predicted to occur as a result of physical limitations. For example, water level from the hypothetically largest possible storm, along with three dams failing, and 35 mph winds causing waves, is not predicted to reach the ISFSI. Because this is the largest conceivable flood height, flooding is excluded as an initiating event.

A zero probability of MPC failure means that based on the weld failure data and methodology discussed in Appendix B, and the MPC maximum stress (strain) levels calculated in Appendix A, the probability of weld failure is less than $1x10^{-6}$ for the mechanical load event.

Reference 8 describes the modeling of the individual risk of "prompt fatality," using a two parameter Weibull function. In the model, zero probability of prompt fatality is typically assumed at doses below a threshold of 150 Rem to the red bone marrow and 500 Rem to the lungs. A prompt fatality can be described as any death that occurs as a result of a large acute total body exposure sufficient to cause one or more of three major classes of fatal syndromes (Reference 9) identified as cerebrovascular syndrome causing death within 30–50 hours from exposures of about 100 Gy (10,000 Rads), gastrointestinal syndrome causing death within about 9 days from exposures of about 10 Gy (1000 Rads), and hematopoietic syndrome (bone marrow death) causing death within several weeks from exposures of 2.5–8 Gy (250–800 Rads). While a single threshold value is not easily cited as the exposure below which there is zero probability of prompt fatality, the assumption discussed above is consistent with the findings discussed in Reference 9. The levels of exposure that could result from the events considered in this study do not approach those that would be of concern for prompt fatality.

Relative to the probability of latent cancer fatalities, two general models were considered. The linear threshold model predicts that doses below a specific threshold do not cause latent cancer fatality. By contrast, the linear no-threshold model predicts a probability of a latent cancer fatality that is proportional to dose. The current study used the linear no-threshold model.

If an uncertainty analysis were performed, some of the risks shown as zero in Tables 4–6, might become positive, but would still be extremely small. However, such an analysis is beyond the scope of this study.

The initiating events that can occur during the handling phase are shown in Table 4. When the cask is lifted out of the cask pit (Stage 3) and moved (Stages 4 through 8) to the preparation area, the MPC lid is on, but not welded. MPC failure is not an issue because the MPC is unsealed. Also, since the MPC is filled with water, for any fuel cladding failure that may occur during these stages, the fuel particulate would be scrubbed since the gap release passes through the water in the MPC. In addition, there is no cladding failure in a case of a tip-over. In Stage 8, the transfer cask is lowered to the preparation area where the MPC is prepared for storage (Stage 9). In Stages 11–18, the transfer cask is prepared and lowered to the storage overpack on the ground floor. In Stage 18, the drop height from the equipment hatch to the top of the storage cask is about 24.4 meters (80 feet). The probability of the MPC failing when the transfer cask is dropped from this height onto the storage overpack is 0.0002, based on a weld failure probability distribution and strain values produced by LS-DYNA analyses of drops from various heights. (See Appendix A for details.) In Stage 19, the transfer cask is resting on the storage cask, where the rigging is changed to lower the MPC into the storage cask. Notably, the transfer cask cannot be dropped while it is resting on the storage cask, and momentum calculations show that it cannot be tipped over.

After rigging, the MPC is lifted off the transfer lid doors (Stage 20) and lowered into the storage cask (Stage 21). The drop height is as high as 5.8 meters (19 feet), and the probability of MPC failure when dropped from this height into the storage cask is 0.28, based on a weld failure probability distribution and strain values produced by LS-DYNA analyses of drops from various heights. This drop of the MPC (by itself) into the storage overpack produces a much higher calculated probability of MPC failure compared to the 24.4-meter (80-foot) drop of the transfer cask containing the MPC; this difference indicates the protection that the transfer cask affords to the MPC during an accidental load drop. This protection derives from the fact that the mass and ruggedness of the transfer cask locally crushes any target it impacts. This crushing acts as an "impact limiter," which absorbs large amounts of kinetic energy and, in turn, significantly limits the strain levels in the MPC. By contrast, a drop of the MPC into the storage overpack is a very hard impact, in which virtually all of the MPC's kinetic energy is absorbed by its shell. This energy absorption results in the higher strains in the MPC and a higher probability of failure.

The storage cask is on rollers when it receives the MPC, and those rollers allow the storage cask to be moved inside an airlock of the secondary containment (Stage 22). The storage cask cannot be dropped during this process. Stage 22 is the last stage in the handling phase.

In assessing the risk from the dry cask storage operation, only one initiating event at a time is postulated to occur during an otherwise normal operation. That is, the assessment does not account for multiple initiating events, such as the following examples:

- aircraft crashes that might damage the secondary containment during an initiating event in the handling phase
- seismic events during the handling phase

Moreover, the analysis does not consider certain other circumstances, such as the following:

- The containment is normally closed (Section 5.1), and the analysis does not consider the effect of the containment inadvertently being opened.

Even though such simultaneous occurrences could increase the consequences, the incremental risk is negligible because of the minuscule incremental frequency of such events occurring simultaneously.

The initiating events during the transfer phase are shown in Table 5. Stage 23 begins the transfer phase when the storage cask is moved out of the secondary containment airlock and away from the secondary containment. As in Stage 22, the storage cask is on rollers and cannot be dropped. Similarly, in Stage 25, the storage cask is being prepared for storage before it is moved to the ISFSI. During Stages 26–32, the storage cask is lifted above the rollers, over a cushion, and then transferred over concrete, asphalt, and gravel surfaces before being set down on the concrete storage pad (Stage 33). The transfer phase ends in Stage 33 with the storage cask being set down on the storage pad. During the transfer phase, the cask is lifted no more than 0.3 meter (1 foot) above the surface level. At this height, the MPC has zero failure probability.

The initiating events that can occur during the storage phase are shown in Table 6. The storage phase comprises only one stage (Stage 34), but many postulated initiating events.

3.2 Initiating Events That Cannot Affect the Subject Plant

3.2.1 Floods

The flooding analysis at the subject plant is based on the probable maximum precipitation (PMP), which is defined as the "theoretically greatest depth of precipitation for a given duration that is physically possible over a particular drainage area at a certain time of the year." The National Weather Service determines the maximum precipitation by maximizing the parameters of a hypothetical storm over a drainage area. This maximum is called "probable" because there is a chance, albeit unknown, that a storm could be more severe. However, to the extent that the maximum can be determined, the PMP is the most severe case.

To obtain the PMP for the subject site, the rainfall from a hurricane that occurred in Florida during 1916 was considered to occur at the drainage basin at the subject site. The storm was analytically positioned within meteorological limits over the drainage basin in order to result in the maximum volume of precipitation at the subject site. The 48.3 centimeters (19 inches) of rain produced an estimated volumetric flow rate of 17,330 m^3/s (612,000 ft^3/s). A stage-discharge model was developed from the limited amount of data. From the models, a peak discharge of 17,330 m^3/s (612,000 ft^3/s) is expected to result in a flood stage of 32 meters (105 feet).

Hydrologists also determined the effects of winds to create waves. The maximum sustained wind was taken to be 72 km/hr (45 mph). From these winds, a maximum wave height of 2.0 meters (6.5 feet) (crest to trough) was predicted. The waves crests would add 1.0 m (3.3 feet) to the maximum flood stage of 32 meters (105 feet).

In the drainage basin, two dams are in series and a third dam is in parallel with the other two. A break of the lower serial dam would add about 2,832 m^3/s (100,000 ft^3/s) to the flood waters at the subject site. This would increase the water level by about 1.2 meter (4 feet). If both serial dams failed, the predicted wave would be 1.5 meters (5 feet). If the parallel dam failed instead, a wave of 0.3 meter (1 foot) is predicted. Combining all of these effects results in a maximum flood height of 35 meters (114 feet).

Reference 10 requires updating plants flood analyses using revised maximum precipitation estimates from Reference 11. The largest hypothetical storm in the drainage area for the subject site has a duration of 72 hours and produces 63.0 centimeters (24.8 inches) of rain. Given that a storm of 48.3 centimeters (19 inches) produced a volumetric flow rate of 17,330 m^3/s (612,000 ft^3/s), 63.0 centimeters (24.8 inches) of precipitation would produce a volumetric flow rate of 22,625 m^3/s (799,000 ft^3/s). According to the previously determined relation of flood stage to flow rate, a flood stage of 33 meters (110 feet) would result. Sustained winds of 28 km/hr (45 mph) would raise the flood stage by about 1 meter (3.3 feet), while dam failure would result in waves at the subject site of 0.3–1.5 meters (1–5 feet). Therefore, the maximum flood height is 36 meters (119 feet).

The ISFSI at the subject site is at an elevation of 38 meters (126 feet). Thus, the flood waters from a combined maximum storm, sustained winds, and dam failures would be insufficient to reach storage casks on the storage pad.

3.2.2 Tsunamis

Tsunamis, the large ocean waves resulting from earthquakes originating near or in the ocean, occur mainly in the Pacific Ocean where they can threaten shoreline areas such as the west coast of Washington, Oregon, and California in the United States. Historically, there have been some tsunamis in the Carribean, but none on the East Coast that could conceivably affect the subject storage site. The U.S. National Oceanic and Atmospheric Administration states that tsunamis typically lose their energy within 8.5 km (5 mi) as a result of frictional losses and impacts with trees, vertical land masses, and other structures. The subject plant is far enough inland that it will not be affected by a tsunami.

3.2.3 Volcanic Activity

According to the U.S. Geological Survey, volcanic regions are located in California, Oregon, Washington, Alaska, and Hawaii. The hazards from volcanoes are as follows:

- Lava flows are streams of molten rock from an erupting vent during either nonexplosive or explosive activity.
- Pyroclastic flows are high-density mixtures of hot, dry rock fragments and hot gases that move away from the erupting vent at high speeds. Most pyroclastic flows consist of a basal flow of coarse fragments that moves along the ground, and a turbulent cloud of ash that rises above the basal flow. Ash may fall from the cloud over a wide area downwind from the pyroclastic flow.
- Tephra are fragments of volcanic rock and lava that are blasted into the air by explosions or carried upward by hot gases in eruption columns or lava fountains. The fragments can be in the form of ash or large rocks. Large-sized tephra typically falls back to the ground close to the volcano, but ash can travel hundreds to thousands of kilometers downwind from a volcano.
- Lahar is a hot or cold mixture of water and rock fragments flowing down the slopes of a volcano or river valleys.
- Landslides are large masses of rock and soil that fall, slide, or flow rapidly under the force of gravity.
- Eruption-induced atmospheric shock waves are strong compressive waves driven by rapidly moving volcanic ejecta. Although most volcanic eruptions are not associated with such waves, examples are known. Air-shock waves can be sufficiently energetic to damage structures far from their source. Air shocks can couple to the ground strongly enough to cause damage to buildings at 100 km (62.1 miles) away from an eruption.
- Floods can be produced by melting snow and ice during eruptions of ice-clad volcanoes, by heavy rains that may accompany eruptions, and by transformation of lahars to stream flow. Floods caused by an eruption can occur suddenly and have a large volume if other flood conditions preexist.

The subject plant is far from these volcanic regions, and well out of the influence of volcanic activity.

3.2.4 Intense Precipitation

Intense precipitation can erode soil. However, the ISFSI is designed so that graded land and drains conduct water away from storage pads. Accordingly, intense precipitation will not affect the storage cask.

3.2.5 Storage Tanks, Transformers, Barges, Trucks, Railcars, and Nearby Industrial Facilities

- There are no storage tanks near the route of the storage cask to the storage pad.
- There are no transformers near the route of the storage cask to the storage pad.
- There is no commercial traffic on the nearby river in the vicinity of the site. The only barge traffic on the river in the vicinity of the storage pad is a snagging barge operated by the Army Corps of Engineers. This barge passes the site about two times per year, once going upstream, and the other time going downstream. The barge does not carry explosive or flammable materials.
- Other than a spur track from a railway line, there are no railway lines near the route of the storage cask from the reactor building to the storage pad or at the storage pad.
- Within a radius of 8 km (5 miles) of the subject plant, there are no manufacturing or chemical plants, refineries, storage facilities, mining operations, military bases, military bombing ranges, aircraft low-level flight patterns, missile sites, transportation facilities, oil or gas wells, or underground storage facilities. The area within this radius of the subject plant is mostly rural; the land is either residential or agricultural. The area is not expected to change significantly in the foreseeable future.

3.3 Frequencies of Initiating Events

3.3.1 Dropped Fuel Assembly

Data from 1968 – 2002 show that there have been 11 events in which reactor fuel assemblies have been dropped during movement of the assemblies either prior to loading into a reactor, during loading, or after removal as spent fuel (Reference 12). None of the 11 dropped fuel assemblies failed.

Data from the U.S. Department of Energy (Reference 13) for the same time period show that the projected number of permanently discharged spent fuel assemblies is approximately 159,600 (including both BWR and PWR fuel assemblies). Each permanently discharged fuel assembly has been moved at least twice during fuel loading and for storage in the spent fuel pool. Given the number of fuel assemblies typically found in the core of reactors (Reference 14) and the number of reactors in operation (Reference 15), the number of fuel assemblies in the reactor cores is at least 24,800. (It may be as large as 40,800, depending on how many assemblies are assumed in the reactors of Reference 14.) The assemblies in the cores have been lifted at least once. Thus, the total number of lifts is at least 344,000 during the subject time period (1968 – 2002). Therefore, the probability of a fuel assembly being dropped is estimated to be 11/344,000 or 3.2×10^{-5}.

3.3.2 Dropped Transfer Cask

The frequency of dropping the transfer cask depends on the number of lifts and the probability of dropping the transfer cask given a lift. There are two approaches to estimating the drop probability. The first approach is to perform a reliability analysis of the crane used to lift the transfer cask and an HRA of workers' actions to rig the cask and operate the crane. The second approach is to obtain an empirical estimate based on experience with lifting heavy loads. This study used the second approach.

Although the first approach provides more insight and is possibly more accurate, it is much more complex than the second approach. It must account for both the reliability of the lifting equipment (e.g., crane, yoke) and the reliability of workers to rig the transfer cask and operate the crane. A fault tree analysis of the crane equipment must be based on detailed design and operational information (e.g., lift heights, lift speeds, lift times, movements of the bridge, movements of the trolley). While the fault tree analysis can be performed with standard methods, the HRA requires further evaluation of human performance issues relevant to dry cask storage operations and, possibly, further development of HRA methods. For example, the kinds of actions that could result in dropping the transfer cask, such as the potential for human error in attaching the lift yoke to the trunnions at the subject plant, are not well understood, and not every erroneous action would necessarily cause the transfer cask to fall.

The probability of dropping the transfer cask can be estimated from data on lifts of very heavy loads at U.S. nuclear power plants. A very heavy load is defined as weighing 27 metric tons (30 tons) or more. The data used in Reference 16 were evaluated for use in this study. The database of very heavy loads in Reference 16 is considered relevant to the transfer cask.

Industry-wide experience on moving very heavy loads can be used to make inferences about the risk at a given nuclear power plant. The application of industry-wide data is not a matter of having identical plants, but of having relevant aspects of lifting a cask similar enough to analytically treat them the same. Reference 12 describes the results of a survey of crane operating experience at U.S. nuclear power plants during 1968 – 2002, and includes the industry's responses. Of 74 respondents to that bulletin, 18 reported that they have a single failure-proof crane, 7 reported that they do not have such a crane, 39 did not specify which type of crane they have, and another 10 indicated their cranes meet the heavy load requirements of NUREG-0612 (Reference 16). All crews are qualified according to accepted standards. Some plants use professional riggers, while other plants use trained plant staff, but all follow the guidance discussed in Reference 16.

In contrast to some plants in the industry database, the subject plant has a single failure-proof crane, and professional rigging personnel are contracted to move the cask. Therefore, the industry's estimated drop frequency is a conservative estimate of the drop frequency at the subject plant.

The drop height probability used in this study is determined from empirical data that reflect lifts of various heights. In some cases, the probability of dropping the transfer cask may depend on the height of the lift. Two drop scenario examples are a drop that results when the block of the lift yoke is forced against the block of the crane boom ("two-blocking") or a drop attributable to a failure of a flawed cable. In this study, the drop probability is over all possible lift heights.

As reported in Reference 12, nine sites were visited to collect operational data on very heavy load lifts. Each site was chosen to represent one type of plant [i.e., nuclear steam supply system (NSSS)]. The type of NSSS reflects the types of loads that have to be lifted. Although some sites were selected for convenience, the nine sites are broadly representative of all nuclear power plant sites in the United States.

The 9 selected sites have a total of 19 plants. At each of the 19 plants, the number of very heavy load lifts was determined from maintenance logs. Table 7 lists the number of lifts, from both refueling and power operation, at the representative sites in 1968 – 2002. Most, but not all of those lifts were done during refueling outages. Thus, the number of refueling outages is used to determine the total number of lifts throughout the population of plants in the United States.

Table 7. Very Heavy Load Lifts at Representative Sites in 1968 – 2002

Group	Type of Plant	Representative Site and Units	Number of Very Heavy Load Lifts
1	BWR, Mark I, G4	Browns Ferry 1, 2, 3	980
2	PWR, Westinghouse, 4-loop	Comanche Peak 1, 2	230
3	PWR, Westinghouse, 4-loop	Diablo Canyon 1, 2	344
4	BWR, Mark-I, G3	Dresden 2, 3	554
5	BWR, Mark-III, G6	Grand Gulf	118
6	BWR, Mark-II, G4	Limerick 1, 2	950
7	PWR, B&W	Oconee 1, 2, 3	1656
8	BWR, Mark-I, G2	Oyster Creek	504
9	PWR, CE80	Palo Verde 1, 2, 3	2277

The estimated total number of heavy lifts for all operating plants in United States (54,000) was obtained from Reference 12 and is used as a reasonable surrogate value in determining the load drop frequency.

The number of times that drops occurred was obtained from docketed information and licensee event reports of all plants in the United States (not just the representative plants). In the subject time period (1968 – 2002), there were three related drop events. Based on these events, a conservative estimate of the drop probability in 1968 – 2002 is obtained by taking the number of drops of very heavy loads as three. The probability of a drop given a lift is then estimated by Equation 1.

$$\Pr\{drop\} = \frac{N_{drops}}{L_{total}} \qquad (1)$$

where: N_{drops} = number of drops of a very heavy load
L_{total} = number of lifts of a very heavy load

Solving Equation 1 with $N_{drops} = 3$ and $L_{total} = 54{,}000$, the probability of dropping a cask given a lift is 5.6×10^{-5}.

The estimated drop probability is considered to be a conservative estimate for two reasons:

- The subject plant has a single failure-proof crane to move its transfer cask. Most plants use non-single failure proof cranes, which are not as reliable as single failure-proof cranes. The collective experience during the subject period (1968 – 2002) should, therefore, reflect more unreliability than would be expected from a single failure-proof crane.
- The initiating events of dropping a cask in Table 4 are drops of very heavy loads. During the study period of Reference 12, only one free-fall drop occurred. Two of the three events used in the numerator of Equation 1 were not drops, but were uncontrolled descents of loads. Because these events had the potential to damage the transfer cask if it were being lifted, they were included in the numerator of Equation 1.

3.3.3 Seismic Events

The storage cask will not see significant stresses attributable to a seismic event unless it tips over. For any given ground acceleration, the likelihood of a tip-over can only increase as the coefficient of friction between the storage cask and the storage pad increases. From Section 4.1.3.2, the maximum coefficient of friction is 0.53. With this maximum coefficient of friction and at an acceleration of 1.35 g [nine times the design-basis earthquake (DBE) of the subject plant], the storage cask will slide, but will not tip-over. Therefore, only seismic events with ground accelerations exceeding 1.35g have the potential to tip-over the storage cask.

Figure 8 shows the annual probability of exceedance as a function of ground acceleration attributable to a seismic event at the subject site in terms of the mean, 15^{th}, and 85^{th} percentiles of the uncertainty distribution. The curves in Figure 8 are based on information in Reference 17, which provides frequency estimates for ground accelerations up to 1.0g at nuclear power plant sites in the Eastern United States. These estimates are linearly extrapolated on a semi-log scale as the dotted portion of the curves in Figure 8. From the extrapolation of the curve for the mean of the uncertainty distribution, the annual probability of an earthquake with ground acceleration exceeding 1.35g is 7×10^{-7}/year. Since even this ground acceleration will not cause a tip-over, a conservative estimate of the frequency of an earthquake that will cause the storage cask to tip-over is 7×10^{-7}/year.

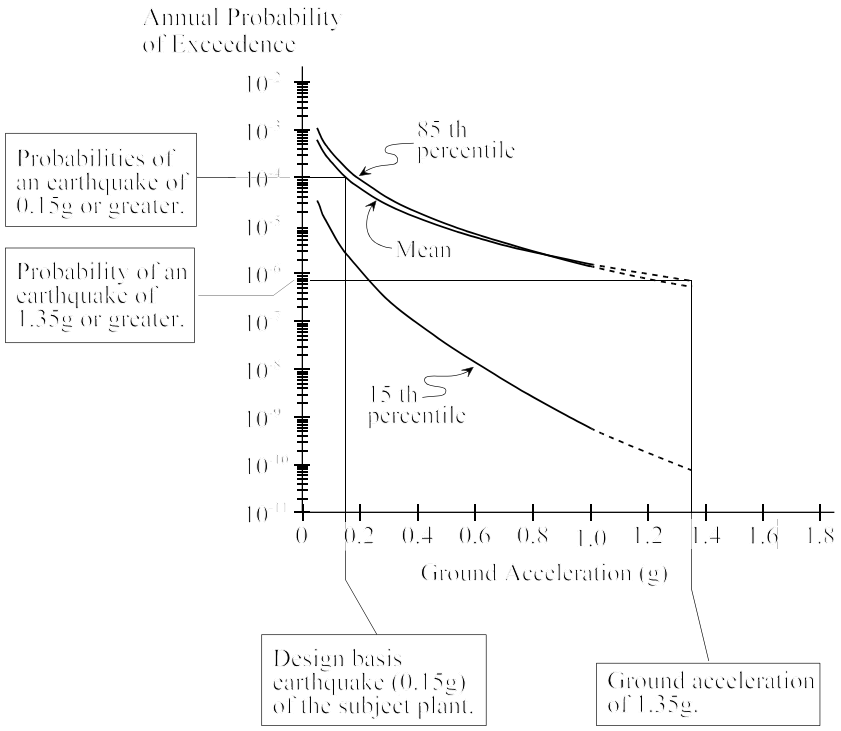

Figure 8. Annual Probability of Exceedance as a Function of Ground Acceleration Due to a Seismic Event at the Subject Plant

The potential for soil liquefaction at the site was evaluated. The portion of soil susceptible to liquefaction at the subject site is within the range of 13.7–27.4 meters (45–90 feet) below grade. Thus, the region of potential liquefaction at the site is too far below the surface to expect appreciable dispersal of soil into the cask vents.

3.3.4 High Winds

The effect of a tornado could be to slide the storage cask on the storage pad, tip it over, or propel a heavy object into it. The weight of the storage cask that is loaded with BWR fuel assemblies is about 163,293 kg (360,000 lb). Analysis (Section 4.1.3.2) indicates that a wind speed of approximately 644 km/hr (400 mph) would be required to cause sliding of a storage cask on the storage pad, while a wind speed of 966 km/hr (600 mph) would be required to cause the storage cask to tip-over, and winds in excess of 1448 km/hr (900 mph) would be required to propel a heavy object into a storage cask with enough force to cause significant damage.

Table 8. Probability of Exceeding Selected Tornado Wind Speeds (Reference 18)

Wind Speed (mph)	Exceedance Probability
73	0.746
113	0.336
158	0.0766
207	0.0138
261	0.00118

The probability of a tornado affecting a storage cask is determined as follows. Reference 18 gives the probabilities that any given tornado occurring in the United States will equal or exceed a specific wind speed (exceedance probability). The exceedance probabilities for selected wind speeds were deduced from the tornado data for 1954 – 1983 (Reference 18). The reported speeds were derived from inspection of damage caused by tornados and the assignment of intensity ratings using the Fujita system of classification (Reference 19). In Figure 9, the data in Table 8 is plotted on a lognormal scale. On the ordinate, the wind speeds needed to affect the storage cask are also indicated.

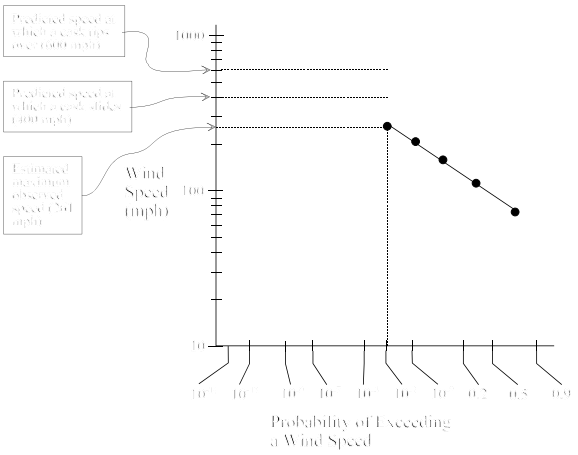

Figure 9. Probability of Tornado Winds Exceeding Speeds

There is no recorded evidence of tornado wind speeds beyond 482.8 km/hr (300 mph) from 1955 to the present, the period for which reliable records have been kept. The highest recorded wind speed reported in Reference 18 is 420 km/hr (261 mph). There is no experimental or empirical information supporting a physical limit of tornado wind speeds, however, some scientists believe there may be a limit. Accordingly, for this study, the maximum wind speed is taken to be 482.8 km/hr (300 mph). The wind speeds required to affect the cask are significantly larger than that maximum wind speed. Thus, high winds are treated as having no effect on the storage cask.

3.3.5 Meteorites

Meteorites continually enter the Earth's atmosphere with initial speeds of tens of thousands of miles per hour. However, most disintegrate to a large extent as they are slowed by friction with the Earth's atmosphere. Over 90% of the meteorites are of a stony composition and tend to break apart upon entering the atmosphere. A smaller number (approximately 6%) are of an iron-like composition and are more likely to reach the ground with less breakup than the stony meteorites (References 20–22).

A dynamic structural analysis was performed to determine the size, weight, and velocity of a meteorite that would have just enough energy to fail the storage cask. It was assumed that a meteorite striking the cask vertically with sufficient kinetic energy to cause the concrete to reach an ultimate strain of 0.003 would result in failure of the cask (Section 10.3 of Reference 23). Meteorites weighing less than 10 tons are slowed by the Earth's atmosphere such that they strike the earth with terminal velocities varying between 321.9 and 643.7 km/hr (200 and 400 mph), depending on the mass and cross-sectional area of the meteorite. By iteratively solving the equations used to predict terminal velocity and the kinetic energy (various combinations of mass and velocity) predicted to cause failure, it was determined that a stony meteorite with a mass less than 1,542 kg (3,400 lb) would not be expected to cause cask failure. It was similarly predicted that an iron-like meteorite with a mass less than 1,088.6 kg (2,400 lb) would not result in failure. Knowing the meteorite diameters associated with the failure masses, the frequency of meteorites striking the earth that could fail the cask can be estimated. For stony meteorites, for which there is the most data, meteorites having a diameter corresponding to a mass of about 1,542 kg (3,400 lb) would strike the earth intact approximately once per year. Considering the differences in density and frequency of occurrence for stony and iron-like meteorites, iron meteorites weighing 1,088.6 kg (2,400 lb) would strike the earth intact about once each 1½ year. Given the sparseness of data for iron-like meteorites, it is believed that this latter prediction is less robust than that for stony meteorites. Based on the above estimates, it is conservatively assumed that the total frequency of strikes from meteorites that could fail the storage cask is about twice per year. Thus, the following assumption was used in this assessment:

- A meteorite capable of breaching the storage cask strikes the earth about twice per year.

The surface area of the earth is 5.08×10^{8} km^2 (1.96×10^{8} mi^2). Thus, a meteorite with sufficient energy to fail the cask is predicted to strike the earth with a frequency per unit of surface area of 4.0×10^{-9} events/yr-km^2 (1.0×10^{-8} events/yr-mi^2).

The storage cask is 3.35 m (11 ft) in diameter, giving a surface area on the top of the storage cask of 8.8 m^2 (95 ft^2) or 8.8×10^{-6} km^2 (3.41×10^{-6} mi^2). Considering a meteorite approaching the storage cask from directly above, the additional surface area from the sides of the storage cask can be ignored. Using this as the target area, A_T, the impact frequency estimated above as f_M, and assuming that a meteorite that strikes the storage cask breaches it, the annual frequency of a breach of a single storage cask by a meteorite is estimated by Equation 2:

$$F_C = f_M A_T \qquad (2)$$

where: F_C = annual frequency of meteorites breaching a storage cask
f_M = annual frequency of meteorite strike which could breach the cask (events/km^2)
A_T = target area of a storage cask (km^2)

Substituting $f_M < 4.0\times10^{-9}$/yr-km^2 and $A_T = 8.8\times10^{-6}$ km^2 into Equation 2 results in a frequency of meteorites breaching the storage cask of $F_C < 3.5\times10^{-14}$events/yr.

3.3.6 Lightning Strikes

Lightning activity in the United States is monitored by the National Lightning Detection Network (NLDN). Data from the monitoring system is collected and disseminated by Global Atmospherics, Inc. The geographical region of the subject plant has a moderately high occurrence of lightning strikes (compared to other areas of the United States) (Reference 24). Data from the NLDN taken over the past 10 years indicate that there has been an average lightning strike density of about 4.3 strikes/yr-km^2 (11 strikes/yr-mi^2). This parameter is often referred to in the literature (Reference 25) as the ground flash density (GFD). Knowing the GFD and an effective target area for the lightning to strike, the annual number of strikes on the target may be estimated from Equation 3 (Reference 25):

$$F_L = \rho_{GF}\ A_{ET} \qquad (3)$$

where: F_L = frequency of lightning strikes in a target area per year
ρ_{GF} = ground flash density, frequency of strikes per year per km^2 in the target area
A_{ET} = equivalent target area (km^2)

There are no structures in the vicinity of the storage pad that are close enough to affect either the strike location or the frequency of strikes on the casks. The storage casks are the tallest objects in the area of the storage pad, and their height is accounted for in the calculation of the equivalent area.

The equivalent target area must include an adjustment to account for the height of the target structure because higher structures present a larger attractive target area than those of less height. A_{ET} is defined as an area of ground surface that has the same annual frequency of direct lightning strikes as the target structure. For an isolated single structure with a height less than 55 meters (180 feet), the equivalent area can be determined using the standard approach in Reference 25. This was estimated as a circular area surrounding the target, with a radius determined by extending a line with 1:3 slope (3 units of horizontal distance for each vertical unit) from the top of the structure to the ground. The storage cask height is 5.7 meters (18.7 feet); the extended radius of the equivalent target area is then 17.1 meters (56.1 feet) and, therefore, the equivalent target area is $A_{ET} = \pi\ (17.1)^2 = 918.6$ m^2 $= 9.2\times10^{-4}$ km^2.

As indicated by NLDN data, the average lightning strike density for the past 10 years in the vicinity of the subject plant is $\rho_{GF} = 4.3$ strikes/yr-km^2 (11 strikes/yr-mi^2). From Equation 3, the lightning strike frequency is 4.0×10^{-3} strikes/year.

3.3.7 Aircraft

Two categories of aircraft flights that pose a crash threat to the storage cask are (1) crashes of planes landing or taking off from airfields in the vicinity of the subject plant, and (2) crashes of planes flying en route in the vicinity of the subject plant (i.e., overflights).

There are four airfields in the vicinity of the subject plant. These airfields are listed in Table 9, along with other information needed to determine the frequency of crashes attributable to landing and taking off into the storage cask.

Table 9. Airfields near the Subject Plant Site

Airfield	Distance from Subject Plant (mi)	Annual Number of Flights
I	16	10,500
II	18	6,100
III	18	6,000
IV	29	6,000

Reference 26 describes a standard approach for estimating the frequency of an aircraft crashing into a target during takeoff or landing by the use of Equation 4.

$$F_{tl} = A_{tl} \sum_{j=1}^{n} C_j \, N_j \qquad (4)$$

where: F_{tl} = frequency of crashes during takeoffs or landings
A_{tl} = effective target area for a plane to strike the target on takeoff or landing
C_j = probability per square kilometer of a crash per aircraft movement at airfield j
N_j = number of movements per year at airfield j
n = number of airfields near the subject plant

The summation is over all airfields in the vicinity of the storage cask. The crash parameter, C_j, is a decreasing function of the distance from the end of the runway of each airfield to the storage cask. From Reference 26 (Section 3.5.1.6), values of C_j for different values of distance from the runway are given for distances of 16 km (10 mi) and less. Since the closest airfield to the subject plant is approximately 25.7 km (16 mi), the values in Reference 26 were extrapolated using a logarithmic plot and regression analysis to determine values of C_j for the subject plant. The extrapolated value of C_j for the nearest airfield is estimated to be 3.9×10^{-10} crashes/km^2-movement. This value of C_j is conservatively used for all four airfields.

The effective target area, A_{tl}, depends on the dimensions of the storage cask and the plane and the length of the skid path. The diameter of the storage cask is 3.35 m (11 ft). The largest aircraft which is able to land at any of the four local airfields is the Gulfstream IV. The Gulfstream IV has two engines on either side of the fuselage, spaced about 4.2 m (13.8 ft) from centerline to centerline, and each engine is about 1.6 m (5.2 ft) in diameter. In order for the crash to possibly cause cask failure, one of the plane's two engines must strike the cask. The engines are spaced such that both engines shafts cannot fully strike the cask together. Evaluating aircraft trajectories that would result in impact by either engine, the lateral dimension (width) of the target area (perpendicular to the plane's trajectory) is the sum of the centerline spacing between the engines, the diameter of an engine, and the diameter of the storage cask. This dimension is 9.2 meters (30.3 feet). A reasonable value for shadow and skid length is 60.8 meters (200 feet), which takes into account the terrain surrounding the storage cask and the angular window through which a plane must pass to strike the storage cask. The impact area is considered to be a rectangle with length equal to the shadow and skid length, 60.8 meters (200 feet), and width equal to 9.2 meters (30.3 feet). Using these values, $A_{tl} = 5.6\times10^{-4}$ km^2 for the Gulfstream IV.

The frequency, F_{tl}, is conservatively estimated using the values of parameters from Table 9 and the value of A_{tl} for the Gulfstream IV. Because C_j is the same for every airfield, F_{tl} depends only on the total number of flights, which is 28,600/yr. Substituting into Equation 4 values of $A_{tl} = 5.6\times10^{-4}$, $C_j = 3.9\times10^{-10}$, and $N_j = 28{,}600$ yields a conservative value for frequency of crashes during takeoffs or landings at airfields in the vicinity of the site of $F_{tl} = 6.2\times10^{-9}$ crashes/yr that could impact the cask.

A large aircraft could potentially crash into the storage cask during overflights. To analyze the crash frequency for overflights, F_{of}, the method given in Reference 27 is used. In this approach, the frequency of crashes during overflights is estimated using Equation 5:

$$F_{of} = C_{of}\ A_{of} \qquad (5)$$

where: F_{of} = frequency of overflight crashes
C_{of} = overflight crash rate per square kilometer per year
A_{of} = equivalent target area for overflight crashes (km^2)

The value of C_{of} to be used in Equation 5 for air carriers is 1.6×10^{-7} crashes/km^2-yr (4×10^{-7} crashes/mi^2-yr).

Similar to the analysis for takeoffs and landings, the impact area is taken to be a rectangle with length equal to the skid length, 60.8 meters (200 feet), and width equal to 9.2 meters (30.3 feet). The value of A_{of} is 5.6×10^{-4} km^2 (2.2×10^{-4} mi^2).

Substituting in Equation 5 values of $C_{of} = 1.6\times10^{-7}$ crashes/km^2-yr, $A_{of} = 5.6\times10^{-4}$ km^2, yields a conservative value for the frequency of overflight crashes from air carriers that could impact the storage cask of 9.0×10^{-11} crashes/year.

The total frequency of aircraft crashes that could impact the cask is the sum of the crash frequency for takeoffs and landings and the crash frequency for overflight related crashes, or 6.3×10^{-9} crashes/year. As noted in Section 4.1.3.3, "Strikes on the Storage Cask from Heavy Objects," and Section 7.0, "Risk Assessment," the probability of MPC failure is assumed to be directly related to the overflight crash rate for commercial aviation, since only commercial aircraft larger than a Gulfstream IV and traveling at high velocity, could possibly cause a breach of the MPC on impact. For convenience, it is assumed that all overflights consist of large commercial aircraft and impact the cask at high velocity. Therefore, the probability of MPC failure and release, if struck by an aircraft, is, for the purpose of the PRA, equal to the frequency of overflight crashes ($9.0\text{x}10^{-11}$) divided by the total frequency of aircraft crashes ($6.3\text{x}10^{-9}$) which is 0.014.

An alternative approach for estimating the overflight crash rate is given in Reference 26. The approach allows for a more location-specific analysis in that it utilizes flight information on traffic in flight corridors that are approved by the Federal Aviation Administration (FAA). Four such corridors are in the vicinity of the subject plant, but information on the cumulative number of flights in these corridors is unavailable because it is not collected by the FAA.

4. MULTIPURPOSE CANISTER AND FUEL

4.1 Mechanical Loads

4.1.1 Mechanical Load Models

To evaluate the structural behavior of the transfer cask and storage cask for the postulated initiating events, simplified and conservative analyses were used in many cases. Table 10 presents key parameters of the storage cask and ISFSI. The analysis methods used included hand calculations based on first principles, common analytical methods and industry recognized approaches, and solution of the differential equations of motion for which closed form solutions were obtained. When an analysis required sophisticated computer codes and large amounts of resources, existing calculations performed by Holtec and reviewed by the staff were used in addition to independent analyses described in this report. In some cases the LS-DYNA computer code was used to perform non-linear dynamic impact analyses (Reference 28). The loads and stresses calculated for all of the examined initiating events were used in subsequent analyses to determine the probability of failure of the MPC and fuel cladding.

The following assumptions were made in this assessment:

- The transfer cask falls in a nearly vertical orientation.
- In most simplified analyses, the transfer cask and the storage cask are considered rigid.
- A drop of the transfer cask in the fuel-handling building occurs on a reinforced concrete floor supported by a 76-cm (30-in) thick concrete shear wall beneath the floor. The worst case impact occurs if the cask falls on the area of the floor that is supported by the wall because the stiffness provided by the wall maximizes the impact acceleration and forces in the MPC.
- During the transfer phase, the storage cask is carried by the cask transporter at a height of 0.3 meter (1 foot) above the ground surface.
- If the storage cask were dropped from the cask transporter during the transfer phase, the cask transporter is traveling in the direction of the open end of the cask transporter.

An analysis was done to evaluate the response of the MPC in the cask to the DBE at the ISFSI of the subject plant; this was set equal to one-half of the subject plant's seismic margin earthquake (½ SME) ground response spectrum. Seismic events were evaluated for different levels of seismic forces with different coefficients of friction between the bottom steel plate of the cask and the concrete pad using three-dimensional (3-D) coupled finite element models of the cylindrical cask, a flexible concrete pad, and an underlying soil foundation. Two coefficients of friction are considered at the interface between the cask bottom steel plate and the concrete pad. A lower-bound friction coefficient of 0.25 is used in investigating the sliding of the storage cask, and an upper-bound friction coefficient of 0.53 is used in examining the possibility of storage cask tip-over.

Table 10. Storage Cask and ISFSI Parameters for Load and Stress Calculations

Storage Cask

Parameter	Value
Diameter of the storage cask	3.4 meters (11 feet)
Height of the storage cask	5.9 meters (19 feet)
Height of the center of gravity	3.0 meters (10 feet)
Weight of storage cask, MPC, BWR fuel assemblies	163,293 kg (360,000 lb)

ISFSI

Parameter	Value
Thickness of concrete	0.61 m (2.0 ft)
Concrete compression strength	20.7 MPa (3,000 psi)
Yield strength of reinforcement top and bottom	413,685 kPa (60,000 psi)
Soil effective modulus of elasticity	193,058 kPa (28,000 psi)

For missiles caused by tornado or flood, the Spectrum II missiles identified in the Standard Review Plan (SRP, Reference 29) are considered. Based on the SRP, the most severe missile that has the potential to cause sliding or tip-over of the storage cask is an automobile weighing 1,810 kg (3,990 lb) at a velocity of 59 m/s (132 mph). An automobile of this weight is comparable to one of today's common sport utility vehicles. Based on studies of the behavior of heavy objects in high winds such as tornadoes, it has been determined that the maximum velocity of an automobile propelled by a tornado may be approximated by taking 0.2 times the maximum velocity of the tornado wind speed (SRP Section 3.5.1.4). An automobile velocity of 59 m/s (132 mph) would then correspond to a maximum tornado wind speed of about 295 m/s (660 mph) indicating that the analysis based on the SRP model is quite conservative. The frequency of tornado winds in excess of 295 m/s (600 mph) at the storage site is estimated to be 4×10^{-11} events/yr.

4.1.2 Response of the Transfer Cask to Loads

Analyses were performed for the initiating events to determine the stresses in the MPC while being moved in the transfer cask. Although the transfer cask can be carried on its side or in the upright position when the MPC is sealed, at the subject plant it is always carried in the upright position. All transfer cask drop analyses are conducted assuming an upright cask position. Thus, the following assumption was used in this assessment:

- The transfer cask is always carried in the upright position.

4.1.2.1 Drop of the Transfer Cask into the Cask Pit

In Stage 3, the transfer cask, which is filled with spent nuclear fuel assemblies, is lifted from the cask pit. The depth of the cask pit is 11.4 meters (37.5 feet). When the transfer cask is out of the water, it is lifted an additional 1.5 m (5 ft) to a height of 13 meters (42.5 feet). It takes 0.5 m (1.5 ft) to get to the level of the refueling floor and an additional 1.1 m (3.5 ft) to get high enough above the refueling floor to clear a railing on its way to the preparation area (Stage 4).

If the transfer cask were accidentally dropped while being lifted in Stage 3, the cask would fall a total of 1.5 meter (5 feet) through the air, drop through 11.4 meters (37.5 feet) of water, and impact the concrete floor of the pit. The analysis included buoyancy and drag effects, which slightly reduce the velocity and the energy at impact. Because the subject plant has a single-failure-proof crane and professional rigging personnel are contracted to move the cask, the consequences of a drop of the transfer cask on the structural integrity of the cask pit do not have to be evaluated. However, should the cask be accidently dropped, based on information available for design of the reinforced concrete spent fuel cask pit, the results of the impact analysis show that the shear stresses developed in the concrete exceed the ultimate capacity of the concrete floor. Therefore, cracking and possibly more severe damage or failure of the spent fuel cask pit floor may occur if the cask is dropped from the maximum height of 13 meters (42.5 feet) above the floor of the cask pit. It is assumed that the consequences to the integrity of the MPC and fuel from such a drop are the same as for a free drop in air of 12.2 meters (40 feet) regardless of whether the cask pit floor fails or not. For a drop onto concrete from this height, Table 13 shows that 100% of the fuel cladding is breached. Since the MPC is not sealed during this stage, the probability of a release from the MPC is 1.0.

4.1.2.2 Tip-Over of the Transfer Cask

In Stages 4–17, the crane is moving the transfer cask over the refueling floor. Analyses were performed to determine the effects of this movement at the maximum speeds; the bridge moves at 15 meters/min (50 feet/min); the trolley moves at 3 meters/min (10 feet/min); the hoist moves at 1.3 meters/min (4.2 feet/min). These velocities are very small and will have negligible effect on the conditions required for the cask to tip-over.

If the crane were not moving, the transfer cask would tip-over only if it is dropped at an angle such that the center of gravity of the cask is over the point of first contact with the floor. This angle requires that the cask axis be oriented at less than 67° with the horizontal. This angle cannot be reached unless the drop height is more than 40 cm (16 in.) measured at the center of the transfer cask base. From Table 1, the transfer cask is lifted more than 40 cm (16 in.) in Stages 4, 11, 12, 13, 15, 16, and 17. Accordingly, the transfer cask may tip-over if it is dropped in any of those stages at an angle such that the center of gravity is over the point of first impact. It will not tip-over if it is dropped in Stages 5–10 or Stage 14. A discussion of the consequences associated with cask tip-over is found in Section 4.1.3.2.

4.1.2.3 Drop of the Transfer Cask onto the Storage Cask

The accidental vertical drop of the transfer cask is analyzed during Stage 18 if the cask were dropped while being lowered from the operating floor, striking the storage cask. The maximum vertical drop in this case is 24.4 meters (80 feet). For this analysis, a detailed finite element model is used that includes the transfer cask, MPC, fuel assemblies, fuel basket, fuel basket support, and storage cask. Drop heights of 1.5, 12.2, and 24.4 meters (5, 40, and 80 feet) were selected for analysis. Analysis of this model using the LS-DYNA computer code calculated the maximum effective plastic strain in the MPC which was used in the weld failure analysis to calculate the probability of MPC failure. In Section 4.3.2, Table 12 summarizes the MPC failure probabilities for all of the drop scenarios evaluated. For the drop of the transfer cask onto the storage overpack, the probability of MPC failure is very small and, as expected, varies with drop height. For a drop of 24.4 meters (80 feet), the probability of MPC failure is 0.0002. This low probability of failure is attributable to the fact that the drop of the rugged transfer cask onto the storage overpack results is a relatively soft impact, with most of the impact energy being absorbed by the storage overpack.

For the purpose of the PRA, fuel cladding failure is linked to a 1.0% failure strain, which is a typical lower bound value for high-burnup fuel with circumferential hydrides. Table 13 summarizes fuel cladding failure for various drop heights and scenarios. For the 24.4-meter (80-foot) drop of the transfer cask onto the storage overpack, 100% of the fuel cladding is assumed to fail. Therefore, the probability of release of radionuclides from the MPC is set equal to the probability of MPC failure.

4.1.2.4 Drop of the Transfer Cask onto a Concrete Floor

The accidental vertical drop of the transfer cask while it is being lowered from the operating floor to the ground floor were analyzed. If the transfer cask were to drop from the operating floor and strike the concrete floor at ground level, the maximum drop would be 30.5 meters (100 feet). To perform the analysis, a detailed finite element model was developed that included the transfer cask, MPC, fuel assemblies, fuel basket, fuel basket support, concrete floor, and the wall beneath the floor. Drop heights of 1.5, 12.2, 21.3, and 30.5 meters (5, 40, 70, and 100 feet) were selected for analysis. Analysis of this model using the LS-DYNA computer code calculated the maximum effective plastic strain in the MPC which were used in the weld failure analysis to calculate the probability of MPC failure. In Section 4.3.2, Table 12 summarizes the MPC failure probabilities for all of the drop scenarios evaluated. For the drop of the transfer cask onto the concrete floor, the probability of MPC failure is small and, as expected, varies with drop height. For a drop of 30.5 meters (100 feet), the probability of MPC failure is 0.02. The probability of failure is relatively low because the drop of the rugged transfer cask onto the concrete floor results in a soft impact, with most of the impact energy being absorbed by the concrete floor and wall beneath the floor.

For the purpose of the PRA, fuel cladding failure is linked to a 1.0% failure strain, which is a typical lower bound value for high-burnup fuel with circumferential hydrides. Table 13 summarizes fuel cladding failure for various drop heights and scenarios. For the 30.5-meter (100-foot) drop of the transfer cask onto the concrete floor, 100% of the fuel cladding is assumed to fail. Therefore, the probability of release of radionuclides from the MPC is set equal to the probability of MPC failure.

The relative deformation between the transfer cask top lid and the top of the MPC was reviewed to ensure that there is no contact/impact between the transfer cask and the MPC. A review of the relative displacement, throughout the time history for the maximum drop (worst case), demonstrated that a gap is maintained, and therefore, the transfer cask top lid does not impact the top of the MPC.

4.1.2.5 Drop of the Transfer Cask onto the Refueling Floor

When the transfer cask is moved from the fuel pool to the handling area, the transfer cask may fall from a height of 0.3 meter (1 foot). For this drop, the refueling floor is expected to hold the transfer cask since the floor has beams, girders, or concrete walls underneath that lie along the load path. For a drop of 0.3 meter (1 foot), Tables 12 and 13 show that the probability of MPC failure is $1x10^{-6}$, and there is no fuel cladding failure.

4.1.2.6 Drop of the MPC While Being Lowered into the Storage Cask

When the MPC is lowered from the transfer cask into the storage cask (Stages 20 and 21), it could possibly fall a maximum of 5.8 meters (19 feet). This fall is analyzed using a finite element model that includes the MPC, storage cask inner shell, storage cask vertical channel sections, and the storage cask bottom lid (which serves as the target plate). The MPC model, its material properties model, fuel assemblies, and fuel basket and fuel basket support model are the same as those utilized in the drop of the transfer cask onto the concrete floor. The top plate of the storage cask bottom lid is modeled as a rigid target plate for the vertical impact of the MPC and its internal components. The storage cask vertical wall is modeled using a rigid shell to represent the storage cask inner shell, which surrounds the MPC shell wall.

A dynamic analysis using LS-DYNA was performed to calculate the maximum effective plastic strain in the MPC for input into the weld failure analysis to calculate the probability of MPC failure. From Table 12 in Section 4.3.2, the probability of the MPC failing when it is dropped during Stages 20 and 21 is 0.28. For the purpose of the PRA, fuel cladding failure is linked to a 1.0% failure strain, which is a typical lower bound value for high-burnup fuel. Table 13 summarizes fuel cladding failure for various drop heights and scenarios. For the 5.8-meter (19-foot) drop of the MPC into the storage overpack, 100% of the fuel cladding is assumed to fail. In contrast, for the 6.1-meter (20-foot) drop of the transfer cask onto concrete, fuel cladding failure is not expected to occur. These different outcomes for essentially the same drop height are due to the fact that the 5.8-meter (19-foot) drop is a much harder impact and results in a very different mode of fuel rod buckling, as explained in Appendix C. Because fuel failure occurs for the 5.8-meter (19-foot) drop, the probability of release of radionuclides from the MPC is equal to the probability of MPC failure, which is 0.28.

4.1.3 Response of the Storage Cask to Mechanical Loads

4.1.3.1 Drop of the Storage Cask onto Concrete, Asphalt, or Gravel Surfaces

During Stages 29–33, the storage cask is moved by the cask transporter to the ISFSI at a height of 0.3 meter (1 foot). A drop of the storage cask from this height onto concrete, asphalt, and gravel, was also evaluated. The two bounding cases considered were a drop without any rotation (i.e., end drop) and a drop causing the maximum rotation.

- During an end drop, calculations show that the frictional resisting force of the storage cask sliding against the concrete was much less than the overturning force; thus, the storage cask would slide and not tip-over regardless of the velocity of the cask transporter.
- Calculations demonstrate that it is geometrically impossible for the rotation of a dropped storage cask to be large enough to cause a tip-over. The maximum amount of rotation possible is 5.14° (with respect to the ground), which occurs when one of the two vertical supports holding the storage cask at the top breaks and the storage cask makes contact with the ground at one edge. Since this angle is less than 29.5°, the storage cask will not tip-over. Furthermore, the force required to tip-over the storage cask from the rotated orientation was calculated to be greater than the frictional resisting force. Therefore, the storage cask would slide but not tip-over.

In both the end drop and the rotation drop, the cask transporter can cause the storage cask to slide, not tip-over. The maximum stress in the MPC shell for a drop of 0.3 meter (1 foot) onto a concrete pad is calculated to be 53.3 MPa (7,732 psi). This stress produces extremely small strains in the MPC and in Section 4.3.2, Table 12 shows that the probability of failure is less that $1x10^{-6}$.

If the cask transporter is traveling at the maximum operating speed of 0.64 km/hr (0.4 mph) and the storage cask that it is carrying strikes another storage cask on the storage pad, the storage cask on the storage pad will slide but not tip-over. If the cask transporter does not stop and continues pushing the struck storage cask, the storage cask on the storage pad could slide into another storage cask or be pushed off the storage pad onto the surrounding gravel area. In any case, for the struck storage cask, the maximum stresses in the base plate, lid, and the MPC shell will be much less than the stresses of a drop of 0.3 meter (1 foot).

The stresses resulting from a drop onto the asphalt or gravel surface are bounded by a drop onto the ISFSI concrete pad. This is because asphalt and gravel are more flexible and have a lower strength and modulus than concrete, and neither of these surfaces have steel reinforcing bars. When the storage cask is dropped from a height of 0.3 meter (1 foot) onto concrete, asphalt, or gravel, the failure probability of the MPC is less than 1.0×10^{-6}.

4.1.3.2 Tip-Over of the Storage Cask

Hypothetically, if the storage cask were to tip-over because the center of gravity of the cask passes over the point of rotation without an initial force or velocity, the maximum circumferential stress in the MPC shell is approximately 421 MPa (61,044 psi) at 4.53 meters (14.9 feet) above the bottom of the MPC. This is based on Reference 2 where the stress in the MPC shell was calculated using a finite element model of a slice of the MPC and fuel baskets subjected to an acceleration of 45g. Under this loading, the MPC and fuel baskets deform outward until portions of the MPC shell reach the rigid boundary of the storage cask inner steel shell. This analysis is consistent with the methodology of the American Society of Mechanical Engineers (ASME) Boiler and Pressure Vessel Code and is based on a linear elastic approach. The maximum calculated stress in the MPC shell is less than the allowable stress intensity of 450 MPa (65,200 psi) based on the Level D Service Condition of the ASME Code (Reference 30). ASME Code Division 1, Subsection NG, Paragraph NG-3225 and Appendix F, Paragraph F-1331, limit the primary membrane (general or local) plus primary bending stress intensity to 150% of the general primary membrane stress intensity. For the purpose of evaluating MPC weld failure, the allowable stress limit of 450 MPa (65,200 psi) was used.

Since the weld failure criterion is based on plastic strain, the elastically calculated maximum stress must be converted to a plastic strain that could have reasonable resulted from a non-linear analysis of the same event. Also, since the "damage" that can be inflicted on the MPC during a tip-over event is energy-limited, an energy balance approach can be used to estimate the maximum plastic strain. In this approach, the strain energy per unit volume absorbed at the point of the elastically calculated maximum stress is equated to the strain energy per unit volume absorbed through elastic-plastic deformation of the material using the idealized engineering stress-strain curve in the LS-DYNA program that was used for the drop analyses.

Using this approach, and the data in Appendix A, Table A.2, the calculated maximum plastic strain is 0.0031 in/in. Since the maximum membrane plus bending stress must have occurred on the boundary, the maximum value that the triaxiality factor can be is 2.0 (see Appendix B, Section B.1.4). The maximum adjusted plastic strain is, therefore, 0.0062 in/in. Assuming that the maximum plastic strain occurs at one of the axial or circumferential welds, the probability of weld crack initiation from Appendix B, Table B.2 is less that $1x10^{-6}$.

Two initiating events, namely seismic events and high winds, could potentially tip-over the storage cask:

- Seismic events. A seismic event is evaluated for various levels of seismic forces with different coefficients of friction between the bottom steel plate of the cask and the concrete pad using 3-D coupled finite element models of the cylindrical cask, a flexible concrete pad, and an underlying soil foundation. When higher levels of seismic excitations are used in the analyses, the coefficient of friction at the cask/pad interface plays an increasingly important role in the sliding and rotational behavior of the storage cask. For a minimum friction coefficient, the storage cask exhibits a translational motion without much rotation. If the friction coefficient is 0.25 and an earthquake occurs equal to 11 times the DBE of the ISFSI (i.e., 11 DBE), the seismic excitations will cause the storage cask to slide 0.93 meter (36.6 inches). Even though the sliding storage cask may hit a neighboring storage cask, neither storage cask will tip-over. Assuming a maximum friction coefficient, the storage cask experiences more rotational movement, but does not tip-over. When the friction coefficient is 0.53 and an earthquake occurs equal to nine times the DBE of the ISFSI (i.e., 9 DBE), the storage cask top will move 1.19 meter (47 inches), and the storage cask base will slide 0.84 meter (33 inches). Even though the sliding storage cask may hit a neighboring storage cask, neither storage cask will tip-over.

- High winds. The wind speed required to slide the storage cask is at least 644 km/hr (400 mph), and the wind speed required to tip-over the storage cask is at least 966 km/hr (600 mph). The design wind speed for the plant is 580 km/hr (360 mph). Detailed calculations are discussed in Section A.5.9.6.

4.1.3.3 Strikes on the Storage Cask from Heavy Objects

Vehicle impact. A car or a truck crashing into the cask while stored on the ISFSI pad is not analyzed directly. However, by extrapolating from the analyses for sliding and tip-over attributable to missile impact, we can conclude that a vehicle weighing 4,536 kg (10,000 lb) and traveling at a speed of 241 km/hr (150 mph) speed will slide the cask less than 66 cm (26 inches), and will not cause tip-over. This conservatively considers that the impact for a tip-over occurs at the top of the cask for tip-over and the lowest coefficient of sliding friction applies for sliding. The MPC remains intact.

Accidental crash by an aircraft. Based on the results of the aircraft impact analysis (Section A.4.9.3), the probability of breaching the MPC, if struck by Gulfstream IV aircraft during landing or takeoff, is extremely small and is assumed to be zero. However, many commercial aircraft overflying the site would be larger than a Gulfstream IV and could impact the cask at high velocity. Since the makeup and characteristics of commercial aircraft overflying the site are not known and have not been evaluated, it is conservatively assumed for the purpose of the PRA that all commercial aircraft overflying the site are larger than a Gulfstream IV and that the probability of MPC breach due to the impact of an overflying commercial aircraft is, for the purpose of the PRA, 1.0. Therefore, the probability of MPC failure and release, if struck by an aircraft, is, for the purpose of the PRA, equal to the frequency of overflight crashes (9.0×10^{-11}, see Section 3.3.7) divided by the total frequency of aircraft crashes (6.3×10^{-9}, see Section 3.3.7), which is 0.014.

Wind-driven missiles. Missiles generated by a tornado have been analyzed. Two different cases of wind-driven missiles are discussed in Section 4.1.1 of this report. The first case analyzed is based on the SRP section addressing missiles generated by natural phenomena (Reference 26). This involves an impact from an automobile weighing 1,810 kg (3,990 lb), traveling with a velocity of 59 m/s (132 mph). Such missiles will not penetrate the storage cask, and will not cause sliding or tip-over. The concrete barrier thickness required to prevent penetration is 72.4 cm (28.5 inches). The entire wall (concrete and steel liners) of the storage cask is 75 cm (29.5 inches) thick. However, an automobile as a missile [1,810 kg (3,990 lb) with a velocity of 212 km/hr (132 mph)] may slide the storage cask if the coefficient of friction between the concrete pad and the storage cask were less than or equal to 0.26. This is near the low end of the coefficient of friction range. If the coefficient of friction were greater than 0.26, the storage cask will not slide. It is estimated the stresses in the cask attributable to missile impact will be much smaller than the tip-over case discussed in Section 4.1.3.2.

In addition, a second study assumes a larger vehicle with a weight of 3,251 kg (7,160 lb), propelled by a very severe tornado having a wind speed of 134 m/s (300 mph). This wind speed is slightly higher than any tornado wind speed recorded to date. To assess the potential impact of such a missile striking a storage cask, the kinetic energy of this missile is compared to that of an aircraft crash. Since the kinetic energy of the large vehicle wind-driven impact would be less than 1% of the kinetic energy of a large aircraft impact, it is concluded that the impact of a very large vehicle traveling as a tornado missile at a relatively high velocity will not result in cask failure.

4.1.3.4 Shockwaves on the Storage Cask from Explosions

Tanker trailer. The nearest public highway is at least 914 meters (3000 feet) from the ISFSI. The shockwaves caused by a tanker trailer containing explosive materials (e.g., gasoline, liquid, natural gas) at this distance from the storage cask will not jeopardize the integrity of the MPC. Reference 31 was utilized to evaluate this event. The cask is designed for a 69 kPa (10 psi) peak transient external pressure. At 914 meters (3,000 feet), the peak pressure attributable to the explosion would be less than 10 percent of the pressure magnitude for which the cask is designed. Therefore, the MPC will remain intact.

Gas pipeline. The nearest gas pipeline (natural gas) is 7.2 km (4.5 miles) from the subject site. The shockwaves caused by the pipeline explosion will not jeopardize the integrity of the MPC. The methods described in References 31 and 32, which analyzed a tanker trailer explosion, were utilized to evaluate this event. To compare a pipeline explosion with the tanker trailer explosion, Equation 1 in Reference 31 was used for a distance of 7.2 km (4.5 miles). This resulted in a 6.9 kPa (1 psi) transient pressure on the storage cask, which is negligible. Based on these assessments, it is concluded that the storage cask will remain intact, and a pipeline explosion will not jeopardize the integrity of the MPC.

4.2 Thermal Loads

4.2.1 Heating During Normal Operation, Blocked Vents, and Fires

4.2.1.1 Heatup Model

The thermal analysis employed the use of Fluent (Reference 33), a computational fluid dynamics (CFD) program, to model the relevant physical phenomena resulting from both the fire and blocked vents scenarios of the dry cask. Fluent is a general-purpose CFD program with the ability to model a wide range of practical problems by solving the conservation equations for mass, momentum, energy and chemical species using a control volume based, finite difference method. Complex two-dimensional (2-D), axisymmetric and 3-D geometries can be modeled. Fluent has been validated for a wide range of flow conditions, including laminar and turbulent flow in various geometries, natural and forced convection problems, heat exchange flow, and combustion phenomena. Additionally, the NRC staff reviewed Holtec International's confirmation of Fluent code's capability to reliably predict temperature fields in the dry storage application using an independent full-scale test on a loaded cask (Reference 34).

CFD analyzes fluid flow, heat and species transport in two or three dimensions. In the present analysis, the computational domain includes the storage cask and the ambient conditions. The domain is divided into control volumes, and the governing conservation equations are solved for each control volume, providing detailed information of all the flow variables. The conservation equations are reduced to a set of algebraic equations by discretization, which are then solved by numerical techniques.

Figure 10 shows the geometrical configuration and computational grid generated for the storage cask. The MPC is inside the storage cask. The fuel basket containing fuel assemblies is inside the MPC. A combination of heat source and porous media was used to model the MPC. The chosen grid was refined until a grid independent solution was obtained. Figure 10 shows two exploded views to depict the airflow channel around the MPC. Arrows indicate the airflow direction. The sides and top boundaries of the computational domain were extended far away from the dry cask structure to safely apply pressure boundary conditions at the top and the sides. Axisymetry was used in this model. Thus, the vents in the computational model appear narrower than the physical model so that the total airflow cross-sectional area in both models are identical.

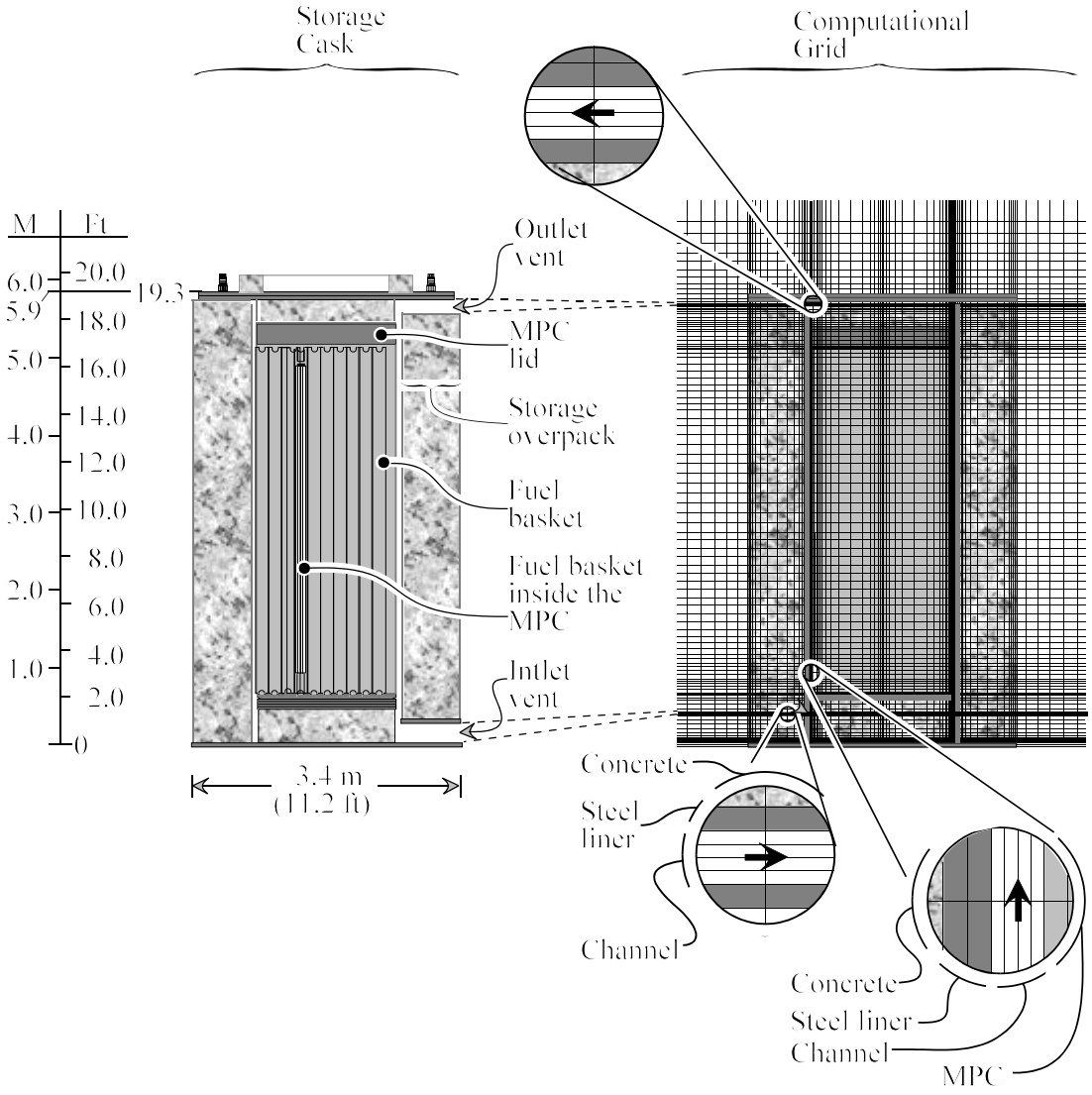

Figure 10. Geometrical Configuration and the Computational Grid Generated for the Storage Cask

Normal storage conditions were obtained first using steady state analysis to be used as initial conditions for the transient analysis. The MPC-68 design holds 68 BWR fuel assemblies. It consists of a fuel basket inside a cylindrical shell. Within the fuel basket, a grid work of stainless steel plates forms an array of square cross-section compartments, each holding a single fuel assembly. The fuel basket is positioned within the shell by basket supports. To allow thermal expansion of the fuel basket, small gaps exist between the fuel basket and the basket supports. Heat is continuously transported from the MPC interior to the periphery of the fuel basket by conduction through the stainless steel plates. Materials present in the MPC include stainless steels (Alloy X), Boral neutron absorber, aluminum Alloy 1100 heat conduction elements, and helium. Materials present in the HI-STORM storage cask include carbon steels and concrete.

Effective values of thermal conductivity, density and heat capacity were taken from References 34 and 35. These effective thermal properties were evaluated using ANSYS (a finite element code). The analysis looked at the combined effect of conduction and radiation inside the MPC. For accurate analysis, all the properties in Fluent were supplied as a function of the temperature and mass fraction. Kinetic theory was used to derive the thermo-physical properties of pure substances like air or helium. The normal storage condition as well as the blocked vent scenario were modeled in a steady mode. The fire scenario was modeled in a transient fashion using a second-order time marching scheme for 3 hours.

In all the cases, the convective terms in the transport equations used a second order forward differencing scheme. Semi-Implicit Method for Pressure-Linked Equations (SIMPLE) was used to bridge the momentum to the continuity equation. All modes of heat transfer (i.e., conduction, radiation, and convection) were taken into account. Porous medium was used to model the axisymmetric inner basket region and the peripheral gap between the basket and the MPC shell. Turbulence was modeled using low Reynolds k-epsilon model. In this model, the conservation equations for turbulence kinetic energy and its dissipation were solved. A full buoyancy effect was added in the turbulence production and its dissipation. Standard wall functions were not used to bridge the sub-laminar layer near the walls to the fully turbulent flow in the core region as in widely used standard k-epsilon model. Instead, full integration to the wall was carried out using fine mesh near the wall. The discrete ordinates method was used to model radiation. Only surface-to-surface radiation was considered. Absorption and scattering in the gas phase was neglected (no participating media was considered). All walls were modeled as thick walls. Conduction was modeled through each wall in all directions. The computational domain was extended away from the cask boundaries. No boundary conditions were assigned at the inlet and outlet vents for the airflow. The external walls of the cask were allowed to exchange heat with the surrounding atmosphere through convection and radiation.

The heat source representing the decay heat from the fuel rods was assumed to not be uniformly distributed. Instead, it was distributed as a function of the axial burnup peaking factor. The axial burnup peaking factor for BWR fuel is provided in Reference 34. The total heat decay used was 21.4 kW.

In the fire scenario, the combustion of the jet fuel was considered. An air-fuel ratio of 14.67 was used. Product gases (flue gas) arise from combustion. As a result, an additional conservation equation was solved to track the species generated in the combustion. The solution of the problem involved a total of eight conservation equations to be solved simultaneously.

4.2.1.2 Response of the Storage Cask to Heat Loads

Normal Steady-State Operation

The results of the steady state for normal storage operation were compared to the analysis performed in Reference 34, and shown in Table 11.

Table 11: Comparison of Results for Normal Storage Conditions

Parameter	Reference 34 Analysis	Recalculated CFD Analysis
Maximum cladding temperature (°C)	393	298
Average temperature inside the MPC (°C)	250	179
Maximum MPC shell (°C)	175	180
Normal operating pressure inside the MPC (kPa)	564	564

The maximum fuel temperature values in Reference 34 are more conservative. In Reference 34, to be conservative, atmospheric pressure was used inside the canister. This lower pressure results in low helium density and, thus, less mass to cool the inside of the canister. Additionally, at higher pressure, the hotter helium is at the top of the canister instead of the middle as seen in Reference 34. This upward temperature profile shift as seen in Figure 11 increases the temperature of the MPC wall at the top as seen in Table 11.

MPC centerline fuel temperatures as a function of axial direction are shown in Figure 11. A maximum temperature of 298 °C (568 °F) was reached in the fuel region with the highest burnup peaking factor.

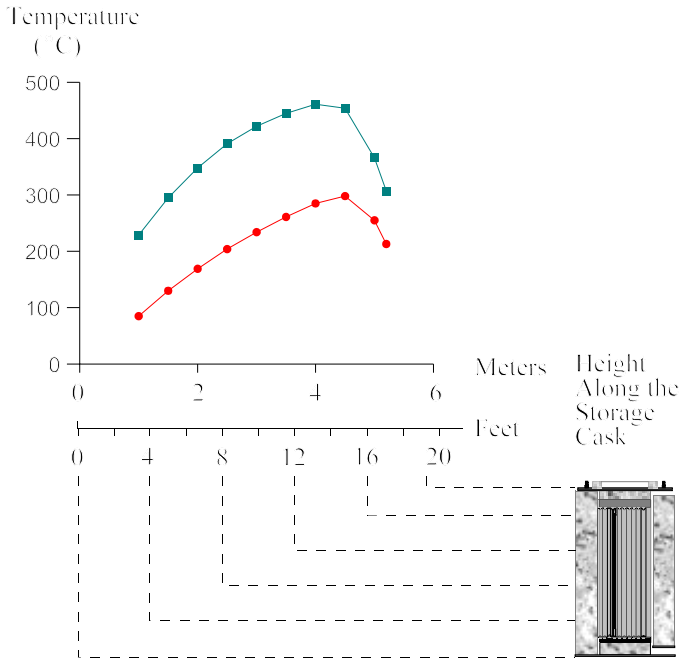

Figure 11. Centerline Fuel Temperature
- Normal Operating Temperature
- Temperature with Blocked Vents

Figure 12 illustrates the temperature variation as a function of the axial position at three radial positions across the cask concrete overpack. As expected the inner surface of the concrete will be at higher temperature for the normal storage operation. Figure 12 also reflects the increase of the air temperature as it flows upward in the cooling passage between the MPC and the cask. The maximum temperature of the MPC shell under normal conditions is 180 °C as shown by the time zero temperature in Figure 15.

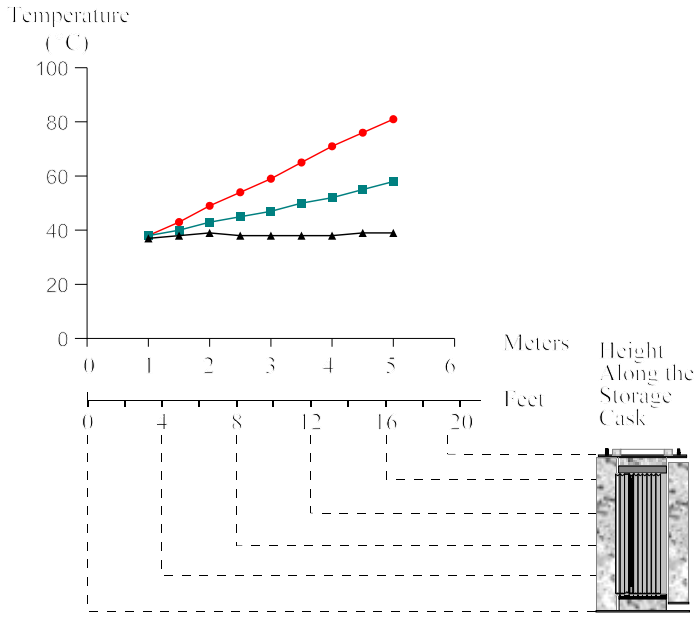

Figure 12. Storage Overpack Concrete Temperature During Normal Operation

- Inner Boundary Temperature
- Middle of Concrete

Blocked Vents

Steady-state and transient analyses were performed, assuming that all the vents were closed. The transient analysis showed that it will take approximately 25 days to reach steady-state values. The analysis was performed using the Fluent CFD program (Reference 33).

In Appendix C, Figure C.21 shows that a maximum temperature of 461 °C (862 °F) was reached in the fuel region with the highest burnup peaking factor.

In Appendix B, Figure B.12 shows that the maximum temperature in the MPC shell for the blocked vents scenario was 283 °C (542 °F).

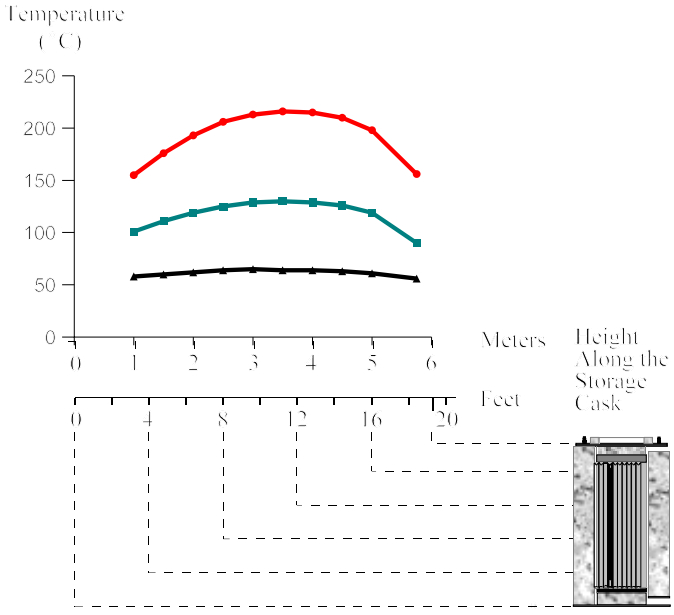

Figure 13. Storage Overpack Concrete Temperature with Bottom Vents Blocked

- Inner Boundary Temperature
- Middle of Concrete
- Outer Border Temperature

Figure 13 shows the storage cask concrete temperature variation as function of the axial direction. A maximum temperature of 216 °C (421 °F) is reached in the concrete overpack. None of the blocked vent or other thermal scenarios resulted in conditions that could fail the MPC.

Fires

An accident scenario was developed that takes into account a crash of a Gulfstream IV aircraft from a nearby airport, and used, as a key assumption, the volume of fuel this aircraft carries. An 82.5 MW (heat release rate) engulfing external fire was, therefore, modeled in a transient mode. The intensity of the fire is based on a conservative bounding estimate using the amount of fuel that could combust over a 3-hour period as a result of the crash of a Gulfstream IV, the largest private/commercial aircraft that takes off and lands at any of the four airfields located around the site; however, a credible fire scenario will be less than 30 minutes.

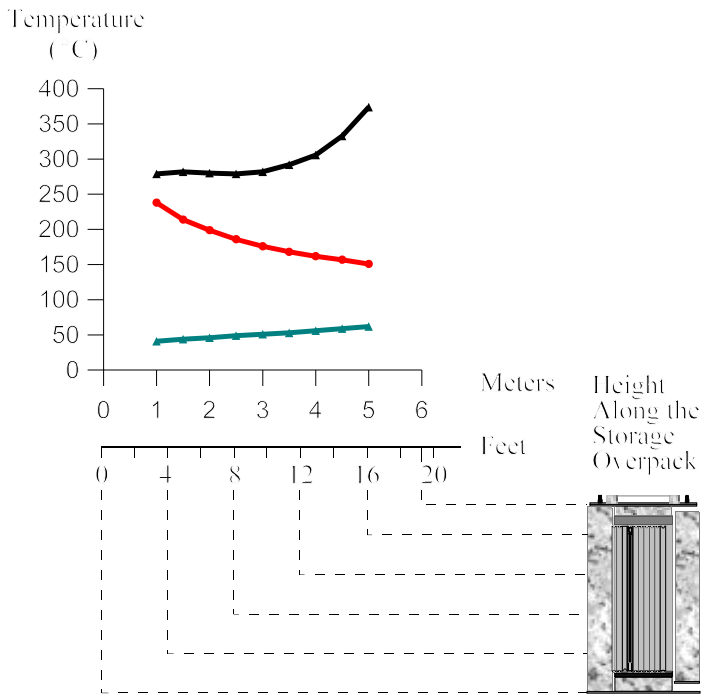

Figure 14. Temperature of Storage Cask after 3-hour Fire with an Energy of 82.5 MW
• Inner Boundary Temperature
▪ Middle of Concrete
▲ Outer Border Temperature

As the fire started, hot gases emanating from the fire surrounded the entire cask. The stream introduced to the cooling passage is now hot and consists of combustion product gases as well as air. The analysis was performed using the Fluent CFD program (Reference 33). A peak temperature of 1,200 °C (2,433 °F) was reached in the fire region. In the fire region immediately surrounding the cask, temperatures closer to the outer wall of the cask are significantly lower than the maximum temperature reached in the fire zone. As cooler air mixes with hot gasses, it flows upward along the surface of the cask.

Figure 14 shows the temperature variation as function of the axial direction in the cask concrete structure at three radial locations at the last time step of the analysis (180 min). The concrete wall inner border temperature (middle curve) reflects the temperature change of the hot mixture as it flows up the cooling channel. The mixture will lose heat to the MPC as it flows upward. The external border of the cask concrete layer (upper curve-triangles) and the middle of the concrete (lower curve-squares) are more affected by the hot gases bordering the dry cask from the outside (References 36–38).

Figure 15 depicts the rise in MPC shell temperature during a 3-hour (180-minute) fire scenario. The maximum temperature reached in 180 minutes was 352 °C (666 °F). Note that steady state (i.e., equilibrium temperature) had not been reached at the 3-hour point. In Appendix C, Figure C.19 shows that the maximum fuel temperature reached was 298 °C (568 °F).

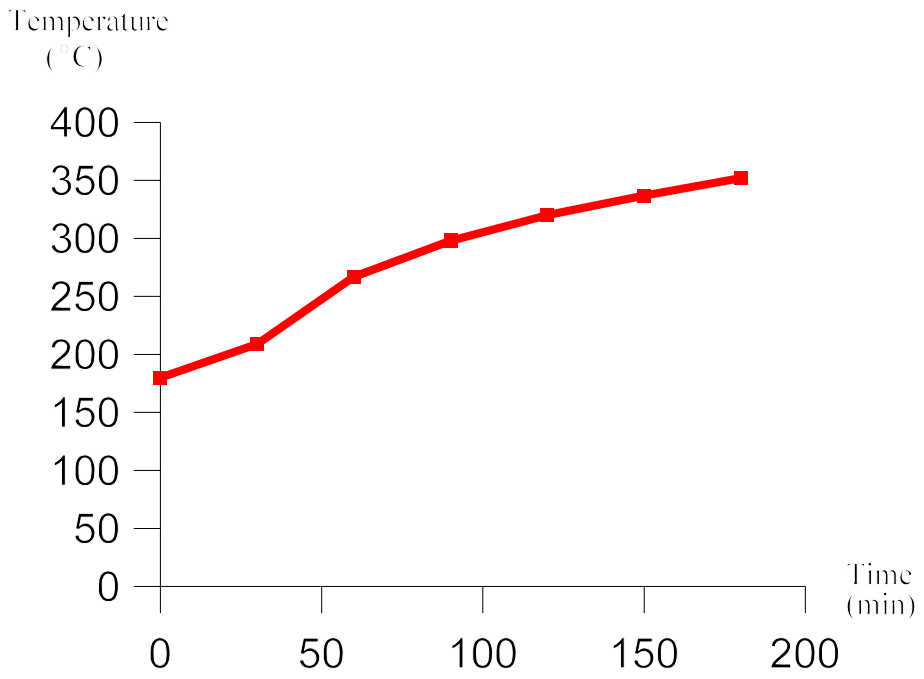

Figure 15. Maximum MPC Shell Temperature in a Fire Scenario

4.2.2 Heating During Lightning Strikes

4.2.2.1 Lightning Dissipation Model

Reference 2 states that lightning would cause no damage to the storage cask. The underlying assumption is that the lightning energy is discharged to ground. Reference 39 (on requirements of the lightning protection code addressed in Reference 40) states that a direct connection to a grounding system is a necessary element of lightning protection for metal towers and tanks, the category best matching the storage cask. However, the storage cask at the subject plant does not have direct grounding. Therefore, a detailed analysis of the potential event scenarios resulting from a lightning strike was conducted to more fully characterize the potential consequences of a lightning strike on the storage cask in both grounded and ungrounded configurations.

For the pilot PRA, the material representing the MPC contents was assumed for calculation purposes to be homogenized by using average properties for electrical and thermal analyses. A model with uniformly distributed, homogenized material will have continuous electrical paths throughout the structure. While the material has average properties to account for the spatial dilution of the material, the possible paths for currents to flow are continuous in all directions. In contrast, the MPC is made up of discrete components with voids and discontinuities between them, making their electrical contact imperfect. Because the homogeneous model allows current to flow uniformly throughout the MPC and contents, the predicted average power deposition would likely be higher than in the physical situation where the current is along much more restricted paths. The homogeneous model gives average predictions and cannot give information about local maxima and minima. A much more detailed and complex model would be required to obtain accurate local values for heat deposition or temperature. However, this also means that locally, the power deposition can be much higher than the average values calculated with the simple models. Analysis of both grounded and ungrounded models of the storage cask predict that power deposited within the MPC is insufficient to cause temperature increases that could cause internal damage or rupture of the MPC. The models predict a power deposition to cause only a small average temperature increase in the MPC of approximately 2 °C (4 °F).

4.2.2.2 Response of the Storage Cask to Lightning Strikes

Power Deposition in Concrete Radiological Shielding. Substantially more power is deposited in the concrete radiological shielding within the storage cask when the cask is ungrounded compared to when grounded. The ratio of power deposition in grounded and ungrounded casks varies during the excitation pulse from a factor of 2 to a factor of 13 more power deposited in the concrete in an ungrounded cask. As an overall average, about 3 times as much power is deposited in the concrete shielding in an ungrounded cask than in a grounded cask. In either case, the peak and average temperature rises in the concrete were small. In a 2-D calculation, with an initial temperature of 66 °C (151 °F) (Reference 2), the average temperature rise was found to be about 0.2 °C (0.4 °F). The peak temperature rise was found to be 5.9 °C (10.6 °F) in the grounded cask and 25.3 °C (45.5 °F) in the ungrounded cask. The 2-D results for an ungrounded cask indicate the possibility of a local temperature excursion sufficient for some damage to the concrete (e.g., fracture or cracking), but that is not considered to be sufficient to cause rupture of the steel liner encasing the concrete.

Power Deposition in the Storage Cask Lid. The largest power deposition density occurs at the lightning strike location, which was assumed to be on the storage cask lid in these simulations. Because of the wide variation of spatial resolution between various models, different simulation models predicted widely varying peak temperatures at the lightning strike location. A failure of the storage cask lid does not appear to be a credible outcome in any of the models.

Voltage on the Outer Shell of the Storage Cask. A major difference between grounded and ungrounded storage casks is the voltage profile on the outer shell of the storage cask. With the cask grounded, the cask voltage at the interface with the pad will be close to zero. With the cask ungrounded, the voltage at the concrete interface is several megavolts, causing concern for any personnel, if they were near the cask during a lightning strike. In a real lightning strike, voltages will also be higher in the concrete pad and soil for both grounded and ungrounded casks because the currents cannot be spread and dissipated as quickly as in an idealized case. However, these voltages should cause no structural damage to the storage cask itself (Reference 41).

4.2.2.3 Conclusions

The lack of a ground connection to the cask allows high electric potentials to develop on the cask near the concrete pad. These electrical potentials may result in arcing to nearby structures. Without a ground connection, voltages on the cask near the concrete pad can reach several megavolts and could pose a significant electrical hazard to workers if they were near the cask. Grounding the cask significantly modifies the voltage distribution on the outer shell of the cask, reducing it to near zero at the concrete pad.

Although lightning currents are predicted to penetrate both the storage cask and MPC for both the grounded and ungrounded configurations, calculations indicate that the MPC will remain intact. Grounding the cask appears to have little effect on power deposition in the interior of the MPC, but results in a threefold decrease in the average power deposited in the concrete shielding within the cask. Although the concrete immediately below the simulated lightning strike location on the cask lid is heated by current penetrating through the steel lid, the deposited energy is insufficient to cause structural damage. The temperature rise in all regions of the cask, except for the metal at the strike location itself, is well below the level where damage to the integrity of the storage cask would occur. Localized heating of the metal lid at the lightning strike location is predicted to be sufficient to melt and vaporize some material. However, this occurs only in a very localized region at the lightning strike location and a failure of the storage cask does not appear to be a credible outcome.

4.2.3 Response of the Fuel Rods to Thermal Loads

The thermal models described in Section 4.2.1.1 do not model the spent fuel assemblies in the MPC; therefore, the cladding temperatures are not explicitly known. However, the temperature of the helium fill gas within the MPC is modeled for these accident scenarios (blocked vents and 3-hour fire).

One of the key assumptions made in this assessment is as follows:

- The cladding temperature is equal to the temperature of the helium.

For thermal loads, spent fuel rod failure is determined by comparing the cladding temperature to the temperature limit imposed by Reference 2. The reference lists 394 °C (742 °F) as the Zircaloy temperature limit for BWR spent fuel assemblies that are 5 years old. This temperature limit is based on a methodology developed by Pacific Northwest National Laboratory for calculating permissible peak clad temperatures for generic commercial spent fuel rods. More recent Interim Staff Guidance Memorandum No. 11, “Cladding Considerations for the Transportation and Storage of Spent Fuel” (November 2003, ADAMS Accession No. ML022110372) identifies the temperature limit as 400 °C (752 °F) for normal conditions of storage and short-term loading operations. For off-normal and accident conditions like fire and blocked vent scenarios, the maximum cladding temperature should not exceed 570°C (1,058 °F). Fuel damage does not occur at this temperature. However, events that result in temperatures exceeding this limit are, for the purposes of this PRA, conservatively assumed to cause damage to portions of the fuel.

Analysis performed using the Fluent CFD program (Reference 33) shows that once steady-state is achieved, the maximum helium temperature in the MPC under normal conditions is 298 °C (568 °F). If vent blockage occurs, this temperature will increase until a new equilibrium condition is reached. Appendix C, Figure C.12 shows that the cladding temperature reaches a steady temperature of 462 °C (862 °F) after vent blockage has occurred. The cladding temperature for the blocked vents scenario did not exceeded the accident temperature limit.

The analysis was performed using the Fluent CFD program (Reference 33). During a 3-hour fire, the Zircaloy temperature only reaches 298 °C (568 °F), which is less than both the short-term temperature limit of 570 °C (1,058 °F) and the long-term temperature limit of 400 °C (752 °F). Even though the long-term temperature limit is approached, the fuel will not fail as a result of exceeding the long-term temperature limit during this short-term event because the long-term temperature limit was based on a change in material properties, rather than failure of the cladding. The time needed for the fuel temperature to equal temperature limits specified in Reference 2 is 3.7 hours.

4.3 MPC Integrity

4.3.1 Integrity Models

The MPC is the confinement boundary for the spent fuel. A drawing of the welds joining the shell and plate components of the MPC is shown in Figure 16. The MPC is made entirely of austenitic stainless steel. The 1.27-cm (0.5-inch) thick cylindrical shell is constructed with one circumferential and four axial seam welds. The two axial welds on each side of the MPC are slightly offset at the circumferential weld. The cylindrical shell is then welded to a 6.35-cm (2.5-inch) thick baseplate. These are full-penetration submerged arc welds which undergo dye penetrant (PT) and radiographic examinations. They are not post-weld heat treated to remove residual stresses. After the MPC is loaded with spent fuel assemblies, the MPC lid is welded to the shell. This 0.75-inch (1.9-cm) thick weld undergoes PT examinations after the root, intermediate, and final weld passes.

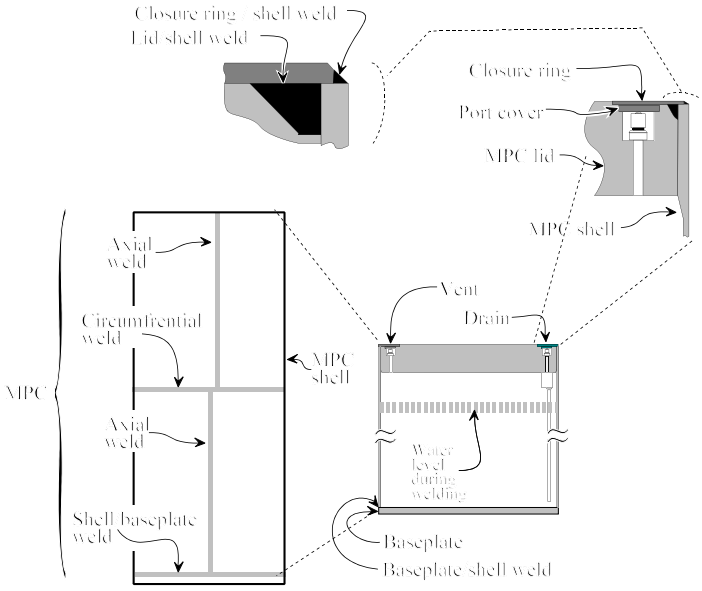

Figure 16. Welds of the MPC

The vent and drain ports used for hydrostatic testing, drying, and inerting are welded closed with cover plates. These welds undergo a final penetrant examination only. The MPC lid-to-shell weld and the vent and drain cover plate welds form the primary seal of the MPC lid. A closure ring is then placed on the MPC lid and welded to the shell and lid to form a redundant seal. The vent and drain cover plate welds and the ring welds are also performed using the tungsten-inert gas (TIG) process. This design ensures that the MPC environment is separated from the outside atmosphere by two independent lid welds. The MPC lid welds were not considered in the MPC failure assessments for the following reasons:

- The TIG process used on the lid produces is expected to produce a much tougher weld than the submerged arc (SA) weld used in the shell of the MPC.
- The redundancy of the lid design requires at least two welds to fail in order to compromise MPC confinement.
- The applied stresses at these locations are less than the stresses in the MPC shell for all events analyzed.

The following failure mechanisms were postulated for the MPC under mechanical and thermal loads:

- weld fracture
- exceeding the limit load
- creep rupture

All three failure mechanisms were considered for thermal events, while only weld fracture was postulated for mechanical impacts. For the purposes of this PRA, failure mechanisms are assumed to be independent. The probability of MPC failure is given as the sum of the failure probabilities from each failure mechanism.

The failure models used in this PRA do not attempt to predict the hole size in the MPC for a given failure probability. Any failure is assumed to create a hole in the MPC large enough to allow the particles and gases within the MPC to be released. This assumption was made because of the difficulty inherent in trying to predict the equivalent hole size produced from a particular MPC failure mode.

The thermal analyses described in Section 4.2 indicated steady state conditions of the MPC under normal conditions would be attained prior to the various handling and transfer events used to move fuel out to the storage pad. These conditions are an internal pressure of 0.56 MPa (81 psi) with an MPC temperature that varies from 73 °C (163 °F) to 180 °C (356 °F).

Several mechanical impact accident scenarios are considered:

- Drop of the transfer cask onto the refueling floor (Stages 4–8, 11–13, 15–17). The transfer cask is dropped on a concrete floor from heights less than 0.91 m (3 feet). All such drops are bounded by the 1.5-meter (5-foot) drop onto the concrete floor.
- Drop of the transfer cask onto the storage cask (Stage 18). This is a handling accident, in which the transfer cask is being lowered from a height of up to 24.4 m (80 feet) and falls on the storage cask.

- Drop of the MPC while moving the MPC into the storage cask (Stages 20–21). The MPC falls from a height of 5.8 m (19 ft) while being lowered from the transfer cask to the storage cask.
- Drop of the transfer cask onto the concrete floor (Stage 18). This is a handling accident, in which the transfer cask is being lowered from a height of up to 30.5 m (100 feet) and, rather than striking the storage cask, falls onto the concrete floor.
- Drop of the storage cask during the transfer phase (Stages 23, 24, and 26–33). The storage cask is dropped from a height of 0.30 m (1 feet) on concrete, gravel, or asphalt.

It was assumed that the MPC is under normal steady-state conditions during the mechanical load impact scenarios listed above. In addition, all of the fuel is assumed to be intact during these events. Fuel cladding failure would cause the internal pressure of the MPC to increase. If a mechanical impact event did cause fuel cladding failure, the resulting increase in pressure would not occur during the accident scenario. The increase in internal pressure due to fuel cladding failure would be a result of the mechanical loading, but because of the extremely short duration of the impact, it would not affect the MPC internal pressure until after the mechanical loading is complete.

There are six stages (Stages 11–13, and 15–17) in which the transfer cask could be dropped 0.6 meters (2 feet) onto the refueling floor. Stress levels at this drop height are not sufficient to cause failure of the MPC, and are bounded by the analysis of a 1.5-meter (5-foot) drop onto the concrete floor. Therefore, a drop from this height was not pursued in the mechanical impact scenarios.

4.3.1.1 Weld Fracture Model

The failure analysis model for weld fracture was based on test data of Type 308 weld deposited stainless steel specimens, and specimens taken from the stainless steel weldments of Process Water Piping of nuclear production reactors constructed in the 1950s at the Savannah River Site (Reference B.19). The mean and standard deviation of the reduction in cross sectional area of these specimens was calculated from the data and converted to true strain at failure. The true strain at failure data was then adjusted for the effects of strain rate, temperature and state of stress. These results provided a normal distribution of failure data, which was used directly to determine the probability of weld fracture given the maximum strain calculated for each impact event.

4.3.1.2 Limit Load Model

For the case of an MPC with no flaws, a flow stress model was used to predict MPC failure. Failure occurs if the primary membrane stress equals or exceeds the flow stress of the material.

The probability of failure was calculated by performing Monte Carlo simulations at various temperatures. The probability of MPC failure is the number of MPC failures divided by the total number of simulations. At a given temperature, the applied stresses were calculated. The yield and ultimate tensile strengths of the material were sampled so the critical flow stress values could be determined. If the circumferential or axial stresses of the MPC were greater than the membrane flow stress, failure was predicted. Similarly, if the bending and membrane stress of the MPC shell-to-baseplate weld exceeded the bending plus membrane flow stress, failure was also predicted. If either of these limits was exceeded, the MPC was considered failed.

4.3.1.3 Creep Rupture Model

The methodology used to predict creep rupture of the MPC is based on the model developed by Argonne National Laboratory for creep rupture of steam generator tubes (Reference 42). In this model, the structure accumulates a fraction of creep damage after exposure to any specific time/temperature/stress condition. If the sum of these creep damage fractions exceeds 1, failure is predicted.

The probability of creep rupture failure as a function of temperature was determined as follows. The MPC stresses at any time-temperature condition were determined. For this stress, the Larson-Miller parameter required to cause creep rupture was sampled from a distribution. Given this temperature and Larson-Miller parameter, the time required to cause creep rupture failure was determined. The incremental creep damage was calculated by dividing the actual time spent in these conditions by the time needed to cause creep rupture. This procedure was repeated for the next time-temperature-stress condition. Once the summation of creep damage fractions exceeds 1, MPC failure would be predicted at the corresponding temperature.

Over time, the heat load in the storage cask would decrease because of the reduced decay heat. This heat reduction would cause a corresponding reduction in MPC temperature and internal pressure even if the cooling vents were blocked. The following conservative assumption is made:

- The internal heat load of the MPC does not decrease over time.

Monte Carlo simulations were performed to determine the probability of creep rupture failure. A simulated MPC consists of both flawed and unflawed regions. The flawed region consists of the four axial welds, one circumferential weld, and one shell-to-baseplate weld. Since the occurrence of large crack-like flaws in these welds is small, relatively few failures are predicted. Only welds are analyzed using this model, since plates are not expected to contain any crack-like flaws. It is assumed that the only flaws of potential concern are produced during welding. If any of the regions were predicted to fail, the MPC was considered to fail. The probability of MPC failure is the number of failures divided by the number of simulations.

Under thermal loads the only significant MPC stresses are attributable to internal pressure. Stresses are calculated using the classical shell theory equations for pressurized cylinders. The highest stress associated with internal pressure loads occurs at the shell-to-baseplate connection. Section 3.4.4.3.1.2 of Reference 2 analyzed the MPC stresses attributable to an internal pressure of 689 kPa (100 psi) at various locations. The results indicated that the membrane plus bending stress at the MPC shell-to-baseplate connection was 303.3 MPa (43,986 psi). The axial membrane stress for this situation is 23.6 MPa (3,419 psi). The difference in these values gives the bending stress acting on the shell-to-baseplate weld as 280.0 MPa (40,567 psi). The total stress at other pressures was assumed to be directly proportional to those at 0.69 MPa (100 psi). Therefore, at a pressure of 0.565 MPa (82 psi), the total stress at this location is only 248.7 MPa (36,068 psi). Subtracting the axial membrane stress of 19.05 MPa (2762 psi) gives a bending stress of 229.6 MPa (33,306 psi).

Appendix B (Figure B.14) shows the temperature variation as a function of axial height for the steady-state conditions of the MPC under normal operating conditions with internal pressure of 0.56 MPa (81 psi). If all four cooling vents of the cask become blocked, the MPC temperature and internal pressure would increase until a new steady-state condition was reached. In this case, the potential of the MPC failing due to creep rupture is introduced. See Appendix B, Sections B.1.7 and B.1.8 for a more detailed discussion of MPC creep rupture response to blocked vents. In summary, none of the blocked vent or other thermal scenarios resulted in conditions that could fail the MPC.

4.3.2 Probability of MPC Failure

Mechanical Loads

Appendix A evaluated the structural response of the MPC for various drop scenarios. The objective was to determine the maximum effective plastic strain on the MPC confinement boundary for each of these scenarios. The analyses showed that the most highly stressed regions of the MPC are near the base of the cylindrical shell and in the weld joining the shell to the 6.4-cm (2.5-inch) thick baseplate.

To determine if the integrity of the confinement boundary is compromised, the maximum effective plastic strain in the MPC must be compared to an appropriate strain failure criterion. For a valid comparison, the conditions under which the maximum effective plastic strain is calculated, and the conditions under which the failure strain limit is measured, should be consistent. The comparison, therefore, must account for how the strain is measured, as well as the effects of strain rate, temperature and state of stress. Appendix B, Section B.1.4 establishes a valid basis for this comparison, and estimates the probability of exceeding the failure strain limit for a given drop event.

Table 12 provides a summary of MPC failure probabilities for various mechanical impact loads. Those stages where the MPC is sealed are briefly discussed below.

If the transfer cask were dropped during Stages 11–17, the probability of MPC failure is $<1x10^{-6}$. During these stages the transfer cask is sealed and carried 0.3–0.6 meter (1–2 feet) above the refueling floor. In Stage 18, the transfer cask is lowered 24.4 meters (80 feet) to the storage cask. If the transfer cask is dropped from this height onto the storage overpack, the probability of MPC failure is very small (0.0002). On-the-other-hand, should the transfer cask drop 30.5 meters (100 feet) and impact the concrete floor, the probability of failure is approximately 0.02.

During Stages 20 and 21, the MPC can potentially be dropped 5.8 m (19 ft) into the storage overpack. If this were to occur, the probability of MPC failure is 0.28.

During Stages 29–33 if the storage cask were to be dropped from a height of 0.3 m (1 ft) onto concrete, asphalt, or gravel, the failure probability of the MPC is $<1x10^{-6}$. For both the end drop and rotation drop, the cask transporter can cause the storage cask to slide, but not tip-over. The stresses generated during sliding events are much lower that for the drop events or tip-over and would not cause the MPC to fail.

The probability of MPC failure in the event of tip-over during storage is calculated to be $<1x10^{-6}$. The dry storage cask system SAR also analyzed a tip-over and concluded that it would not lead to MPC failure. The probability of cask tip-over attributable to various potential events, such as seismic events, high winds, collision by vehicles, tornado-driven missile impacts, and shock waves from tanker or pipeline explosions was evaluated, and for all such events it was concluded that there would be no tip-over and, therefore, zero probability of damage to the MPC.

Table 12. Summary of MPC Failure Probabilities for Various Mechanical Impact Loads

Event Scenario	Impact Surface (Target)	Drop Height (feet)	MPC Failure Probability(1)
Transfer Cask Vertical Drop	Concrete Floor	5	< 0.000001
		40	0.000360
		70	0.002600
		100	0.019600
	Storage Cask	5	0.000002(2)
		40	0.000014
		80	0.000203
Drop of MPC from Transfer Cask into Storage Overpack during Transfer Operations	Storage Overpack Pedestal	19	0.282000
Storage Cask Vertical Drops on Various Surfaces	Concrete	1	< 0.000001
	Asphalt	1	< 0.000001
	Gravel	1	< 0.000001
Storage Cask Tip-over	Concrete Pad	NA	< 0.000001

(1) See Note 1 of Table B.3 and Section B.1.4 of Appendix B.
(2) This result is not consistent with other results presented in the table (i.e., it should be <0.000001). This is because the response results for this case were based on the original (unmodified) LS-DYNA analysis, which, due to a number of factors, produced very conservative results at low drop heights.

Thermal Loads

Evaluations of the probability of MPC failure attributable to fracture, load limit, and creep rupture from thermal loads are detailed in Appendix B, Sections B.1.3 and B.1.5–B.1.7. Failure models were created in Microsoft Excel with an add-on module called @RISK (www.palisade.com), which allows Monte Carlo simulations to be run in Excel by allowing values in the spreadsheet cells to be sampled from statistical distributions. The spreadsheet cell specified as output identifies each iteration as either an MPC success or failure. This process is repeated many times in a Monte Carlo simulation. The probability of failure was calculated by dividing the total number of MPC failures by the total number of iterations performed. If normal steady-state conditions are maintained for the full 20-year license period of the cask, no MPC failures are expected. If the storage cask is exposed to an external fire for 3 hours or all four cooling vents become blocked, the MPC temperature and pressure will increase, but no MPC failures are expected.

Even with the yield and tensile strengths below the minimums, the limit load model was never the limiting failure mechanism in any of the heat-up scenarios. None of the blocked vent or other thermal scenarios resulted in conditions that could fail the MPC.

4.4 Fuel Failure

4.4.1 Fuel Integrity Model

The peak g loads imposed on a fuel rod from the vertical drop scenarios considered in the PRA far exceed the elastic buckling load of the fuel rods in the assemblies. Therefore, to determine the strain demand on the fuel cladding, the inelastic buckling capacity of the fuel rods must be considered. The approach taken in Appendix C was to analyze the fuel rod as an elastic-plastic beam-column with initial curvature under dynamic impact. Failure of the fuel rod is determined by comparing the maximum strain in the cladding to a strain limit based on experimental data.

Since the impact event entails the interaction of potentially hundreds of rods, their spacer grids, tie plates, fuel spacers, basket, cask, and target under dynamic loading, computational efficiency was achieved by modeling a single fuel rod. Thus, an explicit finite element analysis model of a single fuel rod with lateral displacement constraints was used to study the inelastic behavior of a fuel rod under dynamic impact loads. (See Appendix C for details.)

4.4.2 Fuel Rod Cladding Failure

For each drop height, Table 13 lists the maximum principal strain in the cladding, the failure strain limit and whether or not fuel cladding failure occurs based on the limit strain. For the drop of the transfer cask (TC) onto the concrete floor, additional drops of 6.1 and 16.8 meters (20 and 55 feet) were added to the standard drop heights of 0.3, 1.5, 12.2, 21.3, and 30.5 meters (1, 5, 40, 70, and 100 feet) in order to highlight transitions in buckling behavior or differences in response attributable to target stiffness.

Table 13. Probability of Fuel Cladding Failure for Various Drop Scenarios

Event Scenario	Impact Surface (Target)	Drop Height (feet)	Maximum Principal Strain in Cladding (in/in)	Strain Limit Selected for High-Burnup Fuel (in/in)	Probability of Fuel Cladding Failure
Transfer Cask Vertical Drop	Concrete Floor	1	0.0043	0.010	0.0
		5	0.0062	0.010	0.0
		20	0.0072	0.010	0.0
		40	0.011	0.010	1.0
		55	0.025	0.010	1.0
		70	0.037	0.010	1.0
		100	0.052	0.010	1.0
	Storage Overpack	5	(1)	na	0.0
		40	(1)	na	1.0
		80	(1)	na	1.0
MPC Drop into Storage Overpack	Storage Overpack Pedestal	19	0.090	0.010	1.0
Storage Cask Tip-Over	Concrete Pad	na	0.0055	0.010	0.0

(1) This drop was not evaluated for cladding response. Results for the transfer cask drop onto the concrete floor from the same height were used to determine cladding failure.

The results show that the cladding yield strain of 0.0084 in/in is not exceeded until drops of the transfer cask are in the range of 6.1–12.2 meters (20–40 feet). The results also show that target stiffness has a significant influence on cladding strain. For example, the 6.1-meter (20-foot) drop of the transfer cask on to the concrete floor results in a strain less than yield, whereas, the 5.8-meter (19-foot) drop of the MPC into the storage overpack, which is a much harder impact, produces cladding strains that are 10 times greater than yield. This is because the buckling modes for these two impacts are completely different, as discussed in Appendix C.

The cladding strain at failure (rupture or breach) of high-burnup fuel, with circumferential hydrides, which is fuel with a burnup greater than 45 GWd/MTU, is expected to range from 1.0% to 3.0%. For the purpose of the PRA, the lower value of 1.0% strain is selected as the strain limit at failure.

Appendix D of the PRA shows that the particulate release fraction from a spent fuel rod is a function of three variables: (1) the fraction of the fuel rim layer that fractures, (2) the percentage of particulate entrained by gasses during release, and (3) the number of tears (breaches) per rod. In addition, the fraction of the rim layer fractured and the number of breaches per rod are in turn functions of the g loads experienced by the fuel and the severity of the buckling that takes place during a given drop.

In a detailed PRA each of these variables would be associated with a probability distribution and sampled as part of an overall simulation. However, because of the level of effort inherent in such an approach, Appendix D simplifies the effort by recommending an upper bound value for release fractions to be used in the consequence analysis. This in turn simplified the effort in Appendix C by not requiring an estimate of the number of breaches per rod, but only whether or not the rod breaches at all. Also, since the analysis of fuel rod failure is based on a single pin model, it was assumed that when one rod fails, all rods fail, although this is very unlikely.

A tip-over of the storage cask will cause a peak lateral load of 45g on the fuel assemblies. Based on an evaluation of eight different laterally loaded BWR and PWR fuel assemblies ranging from 7x7 to 17x17 arrays, Reference 43 concludes that, for the particular cladding properties used, the cladding yield strain of 0.0077 in/in is reached for a lateral loading of 63g. Since this is a linear elastic analysis, the strain at 45g would be 0.0055 in/in, which is much less than the cladding failure strain limit of 0.01 in/in.

The failure probability of fuel rods if a single assembly were dropped, as in Stage 1, is estimated by using data on individual assemblies. To estimate a failure probability when no failures have been observed, the 50% confidence limit can be used. For a binomial distribution, the 50% confidence limit when no failures have been observed is calculated by dividing 0.7 by the number of cases. Thus, the probability of fuel assembly failure is estimated as 6.4×10^{-2} (0.7/11 = 0.064). (See Section 3.3.1.)

This page intentionally left blank

5. SECONDARY CONTAINMENT ISOLATION

5.1 Containment Isolation Reliability Model

Given a release of radioactive material inside the secondary containment following a drop of the transfer cask, the three distinct functions that occur are to detect radioactive material, isolate the containment, and operate the SGTS. Each of these functions is accomplished by redundant and independent trains of systems. The release of radioactive material will be detected by one or more of six detector systems that signal the secondary containment to isolate. Each of these detector systems consists of two trains, each train having two detectors. Both detectors in a train must detect radiation to isolate the secondary containment. Only 1 of the 12 trains is needed to isolate the secondary containment.

The secondary containment is modeled as one large volume as shown in Figure 17. The letters in circles next to the names of the HVAC systems relate these systems to the event tree that is illustrated in Figure 18. The success criteria for the secondary containment model are as follows:

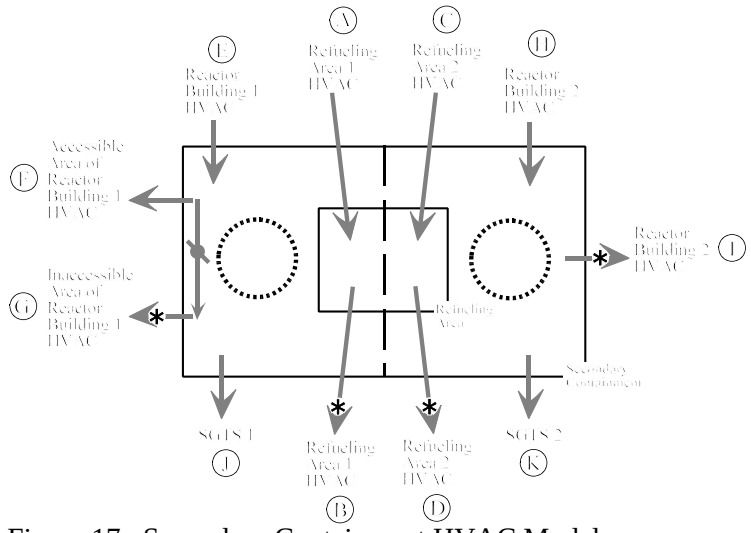

Figure 17. Secondary Containment HVAC Model

- During normal operation, all direct paths to the external environment are closed.
- A negative differential pressure is maintained between the inside of the secondary containment and the environment.
- When an isolation signal occurs, the SGTSs of Unit 1 and Unit 2 take suction from the inside of the secondary containment, filtering the intake and directing the exhaust to the plant stack (elevated release).

The event tree used to determine the probability of failing to isolate the secondary containment is shown in Figure 18. The top events of the event tree are the failure of valves along the ventilation paths to close and the failure of fans to stop moving air through the secondary containment. Each top event is a valve or fan of the ventilation system, except for the last two top events, which are the SGTSs. The valves and fans are paired in their respective system for brevity and clarity. The systems have letters (A) – (K) corresponding to the same systems illustrated in Figure 17. The top events are quantified with fault trees that model the fans, valves, and radiation sensors to initiate the isolation of the secondary containment if radioactive material were released from a transfer cask. Inputs to the fault trees are determined from published sources of reliability data, such as References 44 and 45.

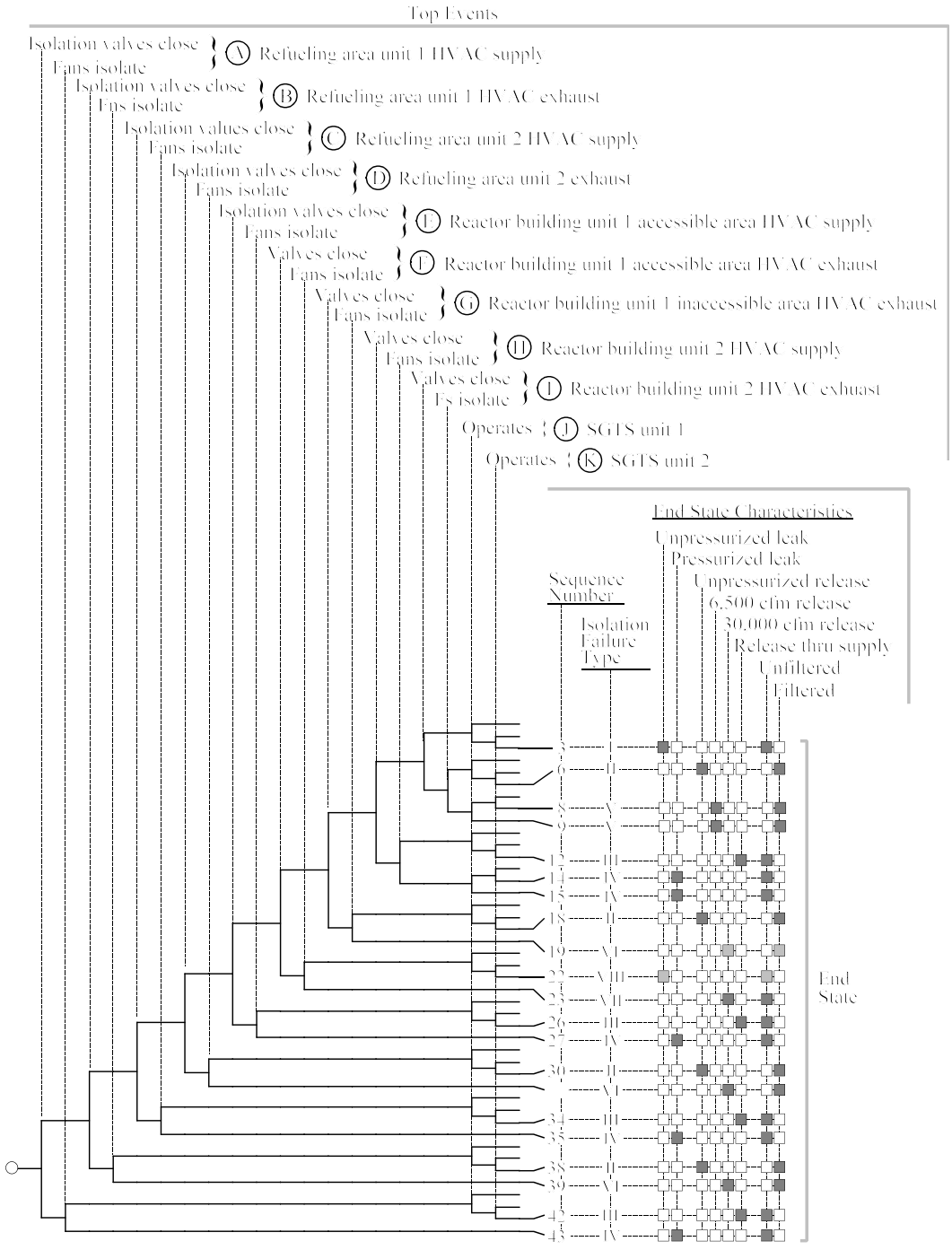

Figure 18. Secondary Containment Isolation Event Tree

The event tree delineates the ways in which the secondary containment isolation can fail by modeling the failure of valves to close, fans to isolate, and the SGTSs to operate. It does not model the progression of events that would occur if the secondary containment receives an isolation signal. If the secondary containment fails to isolate, thereby opening a release path for radioactive material, other release paths are not modeled. The analysis conservatively treats all the material that is released from the transfer cask as being released to the environment.

The 20 top events delineate 43 sequences in the event tree analysis. Of these 43 sequences, 22 result in successful isolation of the secondary containment. The secondary containment successfully isolates when one or both SGTS(s) functions, even if there is an open path between the secondary containment and the outside atmosphere. SGTSs filter the release through an elevated plant stack. The other 21 sequences result in a failure to isolate the secondary containment. Eight types of secondary containment isolation failures are delineated in Figure 18. The isolation failure types (IFTs) are defined in Table 14.

The following assumptions were made in developing and evaluating the event tree model:

- Doors, hatches, and personnel locks are secured according to procedures before the cask operation begins.
- The possibility of an open door or other access opening during the cask operation is negligible. The justifications for this assumption are as follows. First, the HVAC system automatically adjusts to provide a negative differential pressure across the secondary containment boundary. Second, if a door or other access opening were inadvertently left open, the HVAC would not be able to draw a vacuum. An open door in the secondary containment would alarm in the control room. Workers would be directed to close the open door. The handling phase of the operation would cease until the negative pressure in the secondary containment could be reestablished.
- Because the SGTS filters are passive components, they have a negligible probability of failing to reduce the radioactive material content of the gas passing through them.
- If the HVAC systems isolate and both SGTSs fail to operate, the elevated temperature inside the secondary containment, with respect to the outside air, provides a driving pressure for a release of radioactive material from the failed MPC. However, as compared to other releases from reactor accidents, the flow rate is small.

5.2 Probability of Secondary Containment Isolation Failure

Table 14 shows the results of probability calculations for sequences in Figure 18. To calculate the probability of the secondary containment failing to isolate, only the sequence probabilities are summed as shown in Table 15. The small total probability of 1.5×10^{-4} is attributable to the large amount of redundancy in the secondary containment isolation systems.

Table 14. Secondary Containment Isolation Failure Types

Isolation Failure Type (IFT)	Probability†	Sequences	Description
I	1.4×10^{-4}	3	Unpressurized leak. All systems have isolated (automated design response of the isolation system or over-current trip of HVAC fan due to closure of the isolation valves) and both SGTS fail. Leak occurs through cracks, around doors, etc.
II	3.1×10^{-8}	6, 18, 30, 38	Unpressurized filtered release through exhaust. Release through HVAC exhaust system due to exhaust isolation valves failing to close. Supply and exhaust fans isolate. Exhaust filtered release through reactor building vent plenum.
III	2.7×10^{-8}	12, 26, 34, 42	Unpressurized unfiltered release. Release through HVAC supply system due to supply isolation valves failing to close. Supply and exhaust fans isolate. Unfiltered release through supply louvers.
IV	8.0×10^{-6}	14, 15, 27, 35, 43	Pressurized-leak. All HVAC exhaust systems isolate but the secondary containment is pressurized by failure of HVAC supply system to isolate with fan continuing to run. Leak occurs through cracks, and around doors.
V	1.3×10^{-8}	8, 9	Filtered release at 6,000 cfm. Reactor building Unit 2 exhaust system fails to isolate with fan running and either SGTS fails. Exhaust filtered release through reactor building vent plenum.
VI	6.9×10^{-6}	19, 31, 39	Filtered release at 30,000 cfm. Refueling area Unit 1, refueling area Unit 2 or reactor building Unit 1 inaccessible area HVAC exhausts fail to isolate, associated fan continues to run at 30,000 cfm. Exhaust filtered release through reactor building vent plenum.
VII	2.3×10^{-6}	23	Unfiltered release at 30,000 cfm. Reactor building accessible area HVAC exhaust fails to isolate. Fan continues to run at 30,000 cfm. Unfiltered release occurs through reactor building vent plenum.
VIII	7.6×10^{-9}	22	Unpressurized unfiltered release. Reactor building accessible area HVAC exhaust fails to isolate. Fan isolates. Unfiltered release through reactor building vent plenum.

† Values in this table are shown as they are computed in the SAPHIRE software.

Table 15. Sequences Where the Secondary Containment Fails to Isolate

Sequence Number	Probability	Sequence Number	Probability
3	1.4×10^{-4}	23	2.3×10^{-6}
6	$7.6\text{x}10^{-9}$	26	$2.7\text{x}10^{-8}$
8	$2.8\text{x}10^{-9}$	27	8.0×10^{-6}
9	$1.0\text{x}10^{-8}$	30	$7.6\text{x}10^{-9}$
12	$4.9\text{x}10^{-12}$	31	2.3×10^{-6}
14	$1.5\text{x}10^{-12}$	34	$4.9\text{x}10^{-12}$
15	$6.2\text{x}10^{-12}$	35	$1.6\text{x}10^{-9}$
18	$7.6\text{x}10^{-9}$	38	$7.6\text{x}10^{-9}$
19	2.3×10^{-6}	39	2.3×10^{-6}
22	$7.6\text{x}10^{-9}$	42	$4.9\text{x}10^{-12}$
		43	$1.6\text{x}10^{-9}$
		Total	1.5×10^{-4}

This page intentionally left blank

6. CONSEQUENCES

6.1 Source Term

This consequence assessment addresses the severe accident scenario related to the inadvertent drop [30.5-meter (100-foot) drop] of the HI-STORM 100 cask system while in the Stage 18 of the transfer process. This consequence assessment was performed to support development of a PRA for dry cask storage for the specific BWR reactor facility analyzed in the report. In order to examine radiological consequences, release fractions for this accident were developed. Release fractions were estimated as the product of a rod-to-canister release fraction and a canister-to-environment release fraction. Input was obtained from Sandia National Laboratories (SNL) for the development of source term. Detailed re-analysis on source term analysis is documented in Appendix D.

This assessment was performed using the MELCOR Accident Consequence Code System (MACCS2) (Reference 8 and Appendix E, Reference E.2) for a BWR facility. Specific data needed to model a 30.5-meter (100-foot) HI-STORM 100 drop accident scenario for the MACCS2 consequence calculation were collected and used. The important parameters/variables required to model the BWR site are the radionuclide inventory, the source term (i.e., release fraction, release start time, and release duration), the initial plume dimensions (related to the system geometry), the plume heat content, the population density/distribution, and the subject site weather. Other input parameters and models necessary for a MACCS2 calculation were taken from the NUREG-1150 study MACCS2 input file prepared for the Surry nuclear power plant. The input file is documented in Appendix C of the MACCS2 code manual and is referred there as Sample Problem-A (SP-A)[1]. This SP-A MACCS2 input file was used because of the availability and pedigree of this input file. Additionally, the SP-A input parameters are suitable to model the subject site's dry cask storage consequence calculation. A summary of the results obtained by MACCS2 is presented in Table 18. A discussion of the parameters used for the subject site's variables, shown in Table 18, can be found in Appendix E, Sections E.3 – E.11.

The consequence measures chosen for this study were the mean values given by MACCS2 for individual risk of early fatality within 1.6 km (1 mi) and the individual risk of cancer fatality within 16 km (10 mi) of the site boundary.[2] The 1.6 km (1 mi) value is the distance from the exclusion area boundary (EAB), assumed to be 0.5 km (0.3 mi), out to a distance of 2.1 km (1.3 mi). These distances and consequence measures were chosen to allow comparison to the NRC's quantitative health objectives for reactor accident risk. Since cask accident consequences in terms of individual risk of early fatality and cancer fatality are small, the mean consequence values calculated for individual lifetime dose commitment (the mean values of the variable known in MACCS2 as "peak dose found on spatial grid") may also be of interest. Therefore, this section includes the estimated mean individual lifetime dose between 1.2 and 1.6 km (0.75 and 1.0 mi) as measured from the release point. Also, close-in consequences are generally more representative of the source term, while consequences further away tend to be controlled by assumptions on long-term relocation.

---

1 Evacuation was not considered in the MACCS2 consequences calculations for this study.

2 All consequence measures given in Appendix E are mean values as calculated by the MACCS2 code unless stated otherwise. The mean values in MACCS2 are defined as the average (expected) consequences over all weather conditions (Reference E.2).

An impact on the cask will fail a fraction of the fuel rods (F_{rods}) and make their contents available for release. A portion of this available material will be released from the rod to the cask environment (F_{RC}). Part of the inventory that has been released to the cask will be transported through the breach in the cask to the environment (F_{CE}). The fractional release from the cask (F_{rel}) can be approximated by the equation:

$$F_{rel} = F_{rods} \times F_{RC} \times F_{CE}$$

The fuel rods can have radionuclides on the cladding surface in the form of solid Chalk River unidentified deposits (CRUD), inside the fuel rod as gases and volatile fission products, and within UO_2 fuel grains as both solids and gases. Due to the different physical forms of the radionuclides, the above equation is analyzed separately for each group of similar radionuclides.

This release fraction model (Appendix D) accounts for the different properties of the rim region formed in high-burnup fuel and the reduction in ductility of the cladding due to higher burnup and hydrogen absorption. The methodology, as presented, is only applicable to impact type events and not those that result in an elevated temperature attributable to a long-duration fire.

The fraction of the rods fractured (F_{rods}), calculated in Appendix C, is dependent on the energy imparted to the rods, which in most cases is a function of drop height. The release from the rods to the cask makes use of the properties of high-burnup fuel and analyzes the particulate release from the rim and body regions of the fuel separately. Fracture of the fuel into fines is based on a modification of the equations in the DOE Handbook (see Appendix D), which relate the fraction of fuel that fragments into a respirable size to the impact energy that the fuel experiences. F_{RC} depends on the number of fracture sites in a rod, the entrainment of the fines in the gas stream during the depressurization of the rod, and the extent to which the rim region actually fractures. Uncertainty in these parameters is analyzed. The release of radionuclides from the cask to the environment is based on the fraction of gas that is ejected when the cask depressurizes to atmospheric pressure. An ideal gas law relationship is assumed. An analysis of the propensity for settling and plating out of particulate, by a number of mechanisms, so they are not in the gas stream during depressurization is also conducted. Details can be found in Appendix D.

6.1.1 Source Term Estimates

In addressing source term estimates, the discussion necessarily includes consideration of release fraction, release start time and release duration.

6.1.1.1 Release Fraction

The release fractions calculated in Appendix D are based on the number of fuel fractures calculated in Appendix C.

6.1.1.2 Release Start Time

In the MACCS2 calculation for the cask drop event, it was conservatively assumed that as soon as the accident occurs, the release to the environment occurs immediately.

6.1.1.3 Release Duration

The probability of failure of the MPC, in the event of a drop of 30.5 meters (100 feet), is discussed elsewhere in this report. While the likelihood of failure of the MPC in this type of event is in reality quite low, in order to examine radiological consequences, release fractions for this accident were developed. Release fractions were estimated as the product of a rod-to-canister release fraction and a canister-to-environment release fraction. The release fractions presented in Table 16 for a transfer cask dropped 30.5 meters (100 feet) are the fraction of inventory that can be released by depressurization from the cask at the time of the accident. Details are provided in Appendix D.

Table 16. Release Fraction Values for a Transfer Cask Drop of 30.5 Meters (100 Feet)

Radionuclide	Release Fraction	Release Fraction with Filtration
Nobel Gases	0.12	0.12
Particles	7×10^{-6} to 1.2×10^{-3}	7×10^{-7} to 1.2×10^{-4}
CRUD	1.5×10^{-3}	1.5×10^{-4}

6.2 Consequences

6.2.1 Consequence Model

Table 17 shows the major inputs for the calculation, including a brief description. Details are given in Appendix E.

Offsite consequences from radioactive material released from a transfer cask or storage cask during a severe accident are modeled with the MACCS2 code (Reference 46). A plume of radioactive gases and aerosols are released from a point and dispersed in the atmosphere, exposing the surrounding population. The characteristics of the release, such as the amount of material, the type of material, and the heat content, are determined from other studies (see Appendix E). The consequence measure that is used in risk estimates is an expected value of the consequences from the dose calculations given a release of radioactive material (i.e., source term). The calculated consequence measures are early fatalities and latent cancer fatalities as seen in Table 18. Sheltering and evacuation were not considered in the MACCS2 consequence analysis.

Table 17. Major Inputs for Consequence Calculations

Input	Description
Radionuclides Inventory:	Specifies the radionuclides that are to be modeled.
Source Term:	Specifies the characteristics of the radioactive plume such as the number of releases (i.e., plume segments), the heat content, the time of the release, and the duration of the release.
Meteorological Data:	Hourly information of 1 year of meteorological data at the subject site. Each hourly data set includes the stability of the atmosphere, the wind speed, the wind direction, and the precipitation.
Population Data:	Population distribution surrounding the release point developed from census data for the subject site location.
Emergency Response:	Emergency response actions modeled in the region surrounding the release point. Emergency response actions modeled was relocation. Relocation defines the actions taken at the appropriate time to move individuals residing in zones where dose criteria are expected to exceed critical values, and the duration they will be kept in a relocated status.

Table 18. MACCS2 Consequence Calculation Results

Release Fraction			Release Height meters (feet)	Individual Risk of Prompt Fatality within 16 km (10 miles)	Individual Risk of Cancer Fatality within 16 km (10 miles)	Individual Peak Dose (1.2–1.6 km Sv (rem)
Noble Gases	Particles	CRUD				
.12	1.2×10^{-3}	1.5×10^{-3}	50 (164)	0	3.6×10^{-4}	1.85 (185)
.12	1.2×10^{-3}	1.5×10^{-3}	120 (393)	0	2.1×10^{-4}	0.14 (14)
.12	1.2×10^{-4}	1.5×10^{-4}	50[1] (164)	0	5.2×10^{-5}	0.22 (22)
.12	7×10^{-6}	1.5×10^{-3}	50 (164)	0	4.3×10^{-6}	0.026 (2.6)
.12	7×10^{-6}	1.5×10^{-3}	120 (393)	0	2.6×10^{-6}	0.0036 (0.36)
.12	7×10^{-7}	1.5×10^{-4}	50[1] (164)	0	4.3×10^{-7}	0.0028 (0.28)

[1] Results corresponding to a release fraction with filters operable.

6.2.2 Consequence Measures

The dose conversion factors (DCFs) used in this study are the same as those used in the NUREG-1150 study (DOSDATA.INP), as provided by K. Eckerman from Oak Ridge National Laboratory (ORNL) (Reference E.4). These DCFs for 60 radionuclides important in reactor accidents include definitions for 19 organs. The DOSDATA.INP DCF file is appropriate to generate long-term health effects calculations, but is not suitable to generate acute health effect calculations (e.g., early fatalities) for the dry storage cask PRA study because the MACCS2 calculation with the DOSDATA.INP DCF generate overestimated values for acute health effects. Even with this limitation for the DCF file with acute health effects, the MACCS2 calculations predicted zero early fatalities.

It should be noted the estimated consequences (individual probability of a latent cancer fatality) from a release of the inventory of the MPC, for example, for high fuel burnup and a release height of 50 meters (164 feet), include the essentially negligible contribution from noble gases ($\sim 10^{-10}$), and the contribution from radionuclides other than noble gases is 3.6×10^{-4}. These estimated values are based on the output of the MACCS2 code calculations.

This page intentionally left blank

7. RISK ASSESSMENT

7.1 Risk Models

Reference 1 defines risk for NRC use as the risk triplet, in which the elements of risk are the scenarios, the frequencies of the scenarios, and the consequences of the scenarios. Reference 1 also states that a measure of risk is the consequences multiplied by the frequency of the consequences. The measure of risk is given by Equation 6 for one initiating event:

$$R = f\sum_{n=1}^{m} P_n K_n \qquad (6)$$

where: R = aggregate risk
f = frequency of the initiating event (1/time)
P_n = conditional probability of the n^{th} accident scenario given the initiating event
K_n = consequence of the nth accident scenario

The aggregate risk is the risk measure used in this study.

To determine the risk of all plausible accident scenarios in the stages of the dry cask storage operation, Equation 6 can be rewritten as Equation 7:

$$R = \sum_{j}\sum_{m} f_{j,m}\sum_{n} P_{j,m,n} K_{j,m,n} \qquad (7)$$

where: R = aggregate risk
$f_{j,m}$ = frequency of the m^{th} initiating event while in the j^{th} stage
$P_{j,m,n}$ = conditional probability of the n^{th} accident scenario given the m^{th} initiating event while in the j^{th} stage
$K_{j,m,n}$ = consequence of the n^{th} accident scenario from the m^{th} initiating event while in the j^{th} stage

The aggregate risk of storing spent fuel in a dry cask is the risk incurred during the service life of a cask. As shown in Table 1, the service life is divided into three phases:

(1) handling within the refueling building
(2) transfer to the storage pad
(3) storage on the storage pad

An important consideration is that the risk of handling and transfer is demand-related while the risk of storage is time-related. Thus, the risks of the three phases must be expressed in a manner that permits them to be added to obtain the total risk. For each phase, the units of risk are consequences per year, expressed as either prompt or individual probability of a latent cancer fatality.

Consider a cask in the first year of its service life at the subject plant. During this year, the cask passes through the handling and transfer phases and begins the storage phase. In this study, the handling phase is treated as a demand-related activity because of its short duration. Because the handling phase lasts no longer than a few days, time-related external initiating events that could disturb the lifts of the transfer cask or otherwise challenge the integrity of the transfer cask are unlikely to occur. For example, an earthquake is unlikely to occur during the short period of lifting. The transfer cask is not subject to other external events, such as high winds or floods, because all the handling is done inside the containment. For these reasons, the time-related risk during the handling phase is negligible relative to the demand-related risk. In the handling phase, the only demand-related initiating event is a drop while the cask is lifted, moved, or lowered by the crane.

The only initiating event that can occur in the handling phase is a drop of the transfer cask or a drop of the MPC (Stages 20 and 21). The risk associated with drops in the handling phase is given by Equation 7. Therefore, there is no need to sum over the initiating events. Equation 7 is rewritten as Equation 8, where the first summation is over all stages during the handling phase:

$$R^H = \sum_j f_j^H \sum_n P_{j,n}^H K_{j,n}^H \qquad (8)$$

where: R^H = risk of the handling phase

f_j^H = frequency of dropping the transfer cask or MPC during the j^{th} stage in the handling phase

$P_{j,n}^H$ = probability of a release of radioactive material to the environment during the nth sequence given that the cask is dropped in the j^{th} stage of the handling phase

$K_{j,n}^H$ = consequence of a release of radioactive material during the n^{th} sequence the transfer cask is dropped during the j^{th} stage of the handling phase

The frequency of each lift is expressed as one per year during the first year of service life. The handling risk is expressed as the individual probability of a prompt or latent cancer fatality per year, but it applies only to the first year of service life.

The risk of the transfer phase is determined analogously to the risk of the handling phase. Although the transfer phase occurs outside of the secondary containment where time-related events such as high winds and floods can occur, the transfer phase activities are performed only under favorable weather conditions. An earthquake is very unlikely to occur during the brief transfer period. A fire from the diesel fuel in the overpack transporter will not lead to a radionuclide release. For these reasons, the time-related risk during transfer is negligible relative to the demand-related risk. In the transfer phase, the only demand-related initiating events are drops.

The risk in the transfer phase is given by Equation 9. The first summation is over the stages during the transfer phase. The second summation is over all of the demand-related initiating events that can occur during the transfer phase:

$$R^T = \sum_j \sum_m f^T_{j,m} \sum_n P^T_{j,m,n} K^T_{j,m,n} \qquad (9)$$

where: R^T = risk of the transfer phase
$f^T_{j,m}$ = frequency of the mth initiating event during the j^{th} stage of the transfer phase
$P^T_{j,m,n}$ = probability of a release of radioactive material during the n^{th} sequence given the m^{th} initiating event in the j^{th} stage of the transfer phase.
$K^T_{j,m,n}$ = consequence given a release of radioactive material during the nth sequence given the m^{th} initiating event in the j^{th} stage of the transfer phase

During the storage phase, the overpack cask is subject to time-related initiating events (e.g., earthquakes, high winds) that can challenge the integrity of the overpack and the MPC. Because the storage phase has only one stage, the risk in the storage phase is given by Equation 9 without the first summation. This equation is rewritten as Equation 10, where the first summation is over all initiating events that can occur in the storage phase:

$$R^S = \sum_m f^S_m \sum_n P^S_{m,n} K^S_{m,n} \qquad (10)$$

where: R^S = risk of the storage phase
f^S_m = frequency of the m^{th} initiating event while in the storage phase
$P^S_{m,n}$ = probability of a release of radioactive material during the nth sequence given the m^{th} initiating event while in the storage phase
$K^H_{m,n}$ = consequence of a release of radioactive material during the n^{th} sequence given the m^{th} initiating event while in the storage phase

The storage risk is expressed as the individual probability to the public of a prompt or latent cancer fatality per year.

The aggregate risk during the first year of operation is the sum of the risks of the three operational phases. During the first year of operation, the MPC passes through the handling and transfer phases and moves into the storage phase. The handling and transfer phases last a small fraction of a year, so that the MPC is in storage for almost a full year. Accordingly, the aggregate risk of the transfer cask and overpack cask for the first year of its service life is given by Equation 11:

$$R(1) = R^H + R^T + R^S \qquad (11)$$

After the first year of operation, the overpack cask is no longer handled or transferred. Only the storage risk is incurred for each of the remaining 19 years of the MPC's service life.

The total risk of the cask during 20 years of its service life is equal to the first year risk plus 19 times the storage risk. The contribution of handling and transfer to risk is much larger than the risk incurred during storage.

7.2 Risk Results

For this pilot PRA, the risk calculations are summarized in Table 19. Each row of the table represents an initiating event in a stage. The initiating events in Table 19 are those listed in Tables 4, 5, and 6 that have the potential to affect the subject plant or breach the MPC. Each initiating event has only one accident scenario — the failure of the MPC and fuel rods. Aggregate risk is the sum of the risks of the accident scenarios. Table 19 shows the risk for the first year of service and the annual risk for subsequent years. The risk during the first year consists of the risk from the handling and transfer phases and part of the storage phase. The risk of subsequent years consists only of the annual risk of storage on the ISFSI.

The risk measure in Table 19 is the annual individual risk of a latent cancer fatality. Because all offsite releases result in doses to individuals that are below the threshold for prompt fatalities, no prompt fatalities are expected.

The components of risk (frequencies of initiating events, probabilities of subsequent events following the initiating events, and the consequences of the scenarios) are shown in the columns of Table 19. These components are consistent with the definition of risk in Reference 1 where the frequency of the scenario is the product of the initiating event frequency and the event probabilities. The accident scenarios consist of MPC failures and, in the handling phase, releases from the secondary containment. The numbers in the last column of Table 19 are the products of the entries in the previous columns and are the risks of the scenarios.

The notes for each scenario in Table 19 state the sections in this study that discuss the corresponding initiating event frequency, the probability of MPC failure, the probability of a radioactive release from the containment (where applicable), and the consequences as measured by the individual probability of a latent cancer fatality given the occurrence of the scenario. The notes also identify which radionuclides are released from the containment noble gases only (NG), radionuclide inventory other than noble gases (OT), or all radionuclides in the inventory of the MPC (All). The distinction is necessary because the noble gases are not filtered by the containment isolation system while the remainder of the radionuclide inventory is filtered.

For example, consider the initiating event of a drop of the transfer cask in Stage 3 while it is being lifted out of the cask pit. The drop frequency is 5.6×10^{-5}/yr because the transfer cask is lifted once in Stage 3 and the drop probability is 5.6×10^{-5}/yr (Section 3.3.2). Because the drop height is as much as 13.0 meters (42.5 feet), all of the fuel rods are assumed to breach the cladding (Section 4.4.2) and the probability of MPC failure is 1.0 because the lid has not yet been welded to the MPC shell (Section 4.1.2.1); thus, the probability of a release from the fuel rods and the MPC is 1.0. The release consists of both noble gases and the radionuclide inventory in the MPC. However, only the noble gases that are released pass through the water of the spent fuel pool. Because the noble gases are not filtered by the containment isolation system, the probability of noble gases release is 1.0. The consequences of a release of noble gases is 1×10^{-10} probability of a latent cancer fatality (Section 6.2.2). The total risk for this scenario is 5.6×10^{-15} annual individual probability of a latent cancer fatality.

Table 19. Summary Table of Dry Cask Storage Risk Calculations

Stage: Initiating Event	Initiating Event Frequency	Probability of release from fuel rod and MPC	Radionuclides released	Probability of Release from Containment	Consequences	Risk
1: Fuel assembly dropped	2.2×10^{-3}	6.4×10^{-2}	NG	1	1.5×10^{-12}	1.9×10^{-16}
2	Not Applicable					0
3: Transfer cask dropped	5.6×10^{-5}	1	NG	1	1.0×10^{-10}	5.6×10^{-15}
4: Transfer cask dropped	5.6×10^{-5}	1.0×10^{-6}	All	1.5×10^{-4}	3.6×10^{-4}	3.0×10^{-18}
5: Transfer cask dropped	5.6×10^{-5}	1.0×10^{-6}	All	1.5×10^{-4}	3.6×10^{-4}	3.0×10^{-18}
6: Transfer cask dropped	5.6×10^{-5}	1.0×10^{-6}	All	1.5×10^{-4}	3.6×10^{-4}	3.0×10^{-18}
7: Transfer cask dropped	5.6×10^{-5}	1.0×10^{-6}	All	1.5×10^{-4}	3.6×10^{-4}	3.0×10^{-18}
8: Transfer cask dropped	5.6×10^{-5}	1.0×10^{-6}	All	1.5×10^{-4}	3.6×10^{-4}	3.0×10^{-18}
9–10	Not Applicable					0
11–17: Transfer cask dropped	5.6×10^{-5}	1.0×10^{-6}	All	1.5×10^{-4}	3.6×10^{-4}	3.0×10^{-18}
18: Lowering transfer cask thru equipment hatch 100 ft drop	5.6×10^{-5}	0.020	NG	1	1.0×10^{-10}	1.1×10^{-16}
			OT	1.5×10^{-4}	3.6×10^{-4}	6.0×10^{-14}
19	Not Applicable					0
20: MPC drop (19-ft drop)	5.6×10^{-5}	0.28	NG	1	1.0×10^{-10}	1.6×10^{-15}
			OT	1.5×10^{-4}	3.6×10^{-4}	8.5×10^{-13}
21: MPC drop (19-ft drop)	5.6×10^{-5}	0.28	NG	1	1.0×10^{-10}	1.6×10^{-15}
			OT	1.5×10^{-4}	3.6×10^{-4}	8.5×10^{-13}
22–24	Not Applicable					0
25	Not Applicable					0
26–33: Storage cask dropped	-	0		X		0
34 tipped by seismic event	7.0×10^{-7}	1.0×10^{-6}	All	X	3.6×10^{-4}	2.5×10^{-16}
34 struck by aircraft	6.3×10^{-9}	0.014	All	X	3.6×10^{-4}	3.2×10^{-14}
34 struck by meteorite	3.5×10^{-14}	1	All	X	3.6×10^{-4}	1.3×10^{-17}
34 heated by aircraft fuel	3.7×10^{-9}	0		X	N/A	0
TOTAL 1ST YR RISK						1.8×10^{-12}
Subsequent Years of Storage						
34 tipped by seismic event	7.0×10^{-7}	1.0×10^{-6}	All	X	3.6×10^{-4}	2.5×10^{-16}
34 struck by aircraft	6.3×10^{-9}	0.014	All	X	3.6×10^{-4}	3.2×10^{-14}
34 struck by meteorite	3.5×10^{-14}	1	All	X	3.6×10^{-4}	1.3×10^{-17}
34 heated by aircraft fuel	3.7×10^{-9}	0		X	N/A	0

Notes: "NG" = noble gases
"OT" = radionuclides other than noble gases
"All" = noble gases and all other types of radionuclides released
"X" = probability of release from containment in the storage phase is not applicable

Notes For Table 19

1. Stage 1: Loading fuel assemblies into the MPC. The probability of dropping a fuel assembly, 2.2×10^{-3}, is the product of the probability of dropping a single assembly, 3.2×10^{-5} (Section 3.3.1), and the number of spent fuel assemblies loaded into a cask, 68. The drop probability is discussed in Section 3.3.1. The probability of the fuel failing given that it is dropped is 6.4×10^{-2} (Section 4.4.2).

   The noble gases that are released pass through the water of the spent fuel pool and the secondary containment filters. The probability of release from the containment is 1. Other radionuclides are retained by the water. This is discussed in Section 3.1. Because this release is from a cask holding 68 assemblies, the consequence for one assembly is 1/68 of this release, or 1.5×10^{-12}. The risk of Stage 1 is the product of the fuel assembly drop frequency, the probability of the fuel failing, the probability of a release of nobles gases from the containment, and the consequences of the noble gas release, or 1.9×10^{-16}.

2. Stage 2: Placing the MPC lid on the MPC and engaging the lift yoke on the transfer cask. The transfer cask is on the floor of the cask pit where it cannot fall any farther. There are no initiating events that can occur in this stage. Therefore, the risk of Stage 2 is zero.

3. Stage 3: Lifting the transfer cask out of the cask pit. The probability of dropping the transfer cask is 5.6×10^{-5} (Section 3.3.2). All of the fuel rods fail (Section 4.4.2). The MPC is unsealed, thereby rendering it ineffective in confining radionuclides. Section 4.1.2.1 discusses cracking and possibly more severe damage or failure of the spent fuel cask pit floor that may occur if the cask is dropped from the maximum height of 13 meters (42.5 feet) above the floor of the cask pit. Because the subject plant has a`single-failure-proof crane and professional rigging personnel are contracted to move the cask, the consequences of a drop of the transfer cask on the structural integrity of the cask pit do not have to be evaluated. It is assumed that the consequences to the integrity of the MPC and fuel from such a drop are the same as for a free drop in air of 12.2 meters (40 feet). For a drop onto concrete from this height, Table 13 shows that 100% of the fuel cladding is breached. Since the MPC is not sealed during this stage, the probability of a release from the MPC is conservatively assumed to be 1.0. This assumption is conservative because it is expected that the preponderance of the radioactive inventory will remain in the cask under a drop. The water is too cold and the time is too short to have breaching other than the inventory in the pellet-cladding gap. The water may wash the particulate that would have settled to the cask interior. The noble gases that are released pass through the water of the spent fuel pool. Other radionuclides are retained by the water. Because the noble gases are not removed by the filters, the probability of noble gasses release from containment is 1. The consequences of a release of noble gases is $1.0\text{x}10^{-10}$ (Section 6.2.2). The total risk for this scenario is $5.6\text{x}10^{-15}$ annual individual probability of a latent cancer fatality.

4. Stage 4: Moving the transfer cask over a railing of the spent fuel pool. The probability of dropping the transfer cask is 5.6×10^{-5} (Section 3.3.2). The MPC is unsealed and remains in the upright position when dropped (Section 4.1.2.2). No fuel rods are expected to fail if the cask drops 0.9 meter (3 feet) during this stage. Even if the rods don't fail, the drop will dislodge CRUD from the rod surface. This CRUD is available for release. For the calculation of risk, it was assumed that all radionuclides are available for release. The risk of Stage 4 is 3.0×10^{-18}.

5. Stage 5: Moving the transfer cask to the preparation area (1st segment). The difference between Stages 4 and 5 is that the transfer cask is lowered from about 0.9 meter (3 feet) above the refueling floor to about 0.3 meter (1 foot). The possibility of dropping the transfer cask stems from the lowering. The other constituents of risk are as discussed in the note for Stage 4.

6. Stage 6: Moving the transfer cask to the preparation area (2^{nd} segment). The possibility of dropping the transfer cask stems from the changed direction of travel along the load path of the refueling floor. The other constituents of risk are as discussed in the note for Stage 4.

7. Stage 7: Moving the transfer cask to the preparation area (3rd segment). The possibility of dropping the transfer cask stems from the changed direction of travel along the load path of the refueling floor. The other constituents of risk are as discussed in the note for Stage 4.

8. Stage 8: Lowering the transfer cask onto the preparation area. The difference between Stage 8 and Stage 5 is that the transfer cask is lowered from about 0.3 meter (1 foot) above the refueling floor to the refueling floor. The possibility of dropping the transfer cask stems from the lowering. The other constituents of risk are as discussed in the note for Stage 4.

9. Stages 9 and 10: Stage 9: Preparing (drain, dry, inert, seal) the MPC for storage. Stage 10: Installing the short stays and attaching the lift yoke. The transfer cask is on the refueling floor and cannot fall. There are no other initiating events in Stages 9 and 10. The risk of Stages 9 and 10 is zero.

10. (Stages 11–17) Stage 11: Lifting the transfer cask. Stage 12: Moving the transfer cask to exchange the bottom lids of the transfer overpack (1st segment). Stage 13: Moving the transfer cask to exchange the bottom lids of the transfer overpack (2nd segment). Stage 14: Replacing the pool lid with the transfer lid. Stage 15: Moving the transfer cask near the equipment hatch. Stage 16: Holding the transfer cask. Stage 17: Moving the transfer cask to the equipment hatch. The frequency of dropping the transfer cask in any one of the stages is 5.6×10^{-5} (Section 3.3.2). No fuel rods are expected to fail. These stages are represented by one row in Table 19 because the risk of each stage is 3.0×10^{-18}.

11. Stage 18: Lowering the transfer cask to the storage overpack through the equipment hatch. The probability of dropping the transfer cask is 5.6×10^{-5} (Section 3.3.2). The probability of MPC failure is 0.0002 for a drop of 24.4 meters (80 feet) onto the storage overpack, and 0.02 (0.0196) for a drop of 30.5 meters (100 feet) onto the concrete floor. The more conservative 30.5-meter (100-foot) drop results are used (Sections 4.1.2.3 and 4.1.2.4). The entire inventory of radionuclides is considered to be released. Noble gases are not removed by the filters and their probability of release from the containment is 1.0. The consequences of a release of noble gases is 1.0×10^{-10} (Section 6.2.2). The total risk for this scenario is 1.1×10^{-16} annual individual probability of a latent cancer fatality. The inventory of other radionuclides will be released only if the containment isolation system fails, which has a probability of 1.5×10^{-4}. The probability of latent cancer fatality if the filters are off is 3.6×10^{-4}. For the release of other nuclides, the product of the risk components is 6.0×10^{-14}.

12. Stage 19: Preparing (remove short stays, disengage lift yoke, attach long stays) to lower the MPC. The transfer cask is on the storage overpack where it cannot drop. The doors of the transfer lid of the transfer cask are closed, hence, the MPC itself cannot drop. There are no initiating events in this stage. The risk of Stage 19 is zero.

13. Stage 20: Lifting the MPC and opening the doors of the transfer lid.
Stage 21: Lowering the MPC through the transfer cask into the storage overpack.
The frequency of dropping the MPC in any one of the stages is 5.6×10^{-5} (Section 3.3.2). This frequency is the same as that in the preceding stages because the crane used to lift the transfer cask and the MPC itself is the same and the rigging is similar. For this drop, 100% of the fuel is assumed to fail (Section 4.4.2). The probability of the MPC failing is 0.28 (Sections 4.1.2.6 and 4.3.2). For this site, the risk associated with these two stages is 8.5×10^{-13}. For sites where the transfer of the MPC from the transfer cask to the storage cask is done at the ISFSI pad instead of inside the 10 CFR Part 50 facility, the risk is approximately 5.6×10^{-9}, since the secondary containment is not available. In addition, since for these sites the transfers are done using a hydraulic lift gantry instead of the plant's single failure proof crane, the drop frequency could be higher which would then increase the final risk above 5.6×10^{-9}.

14. Stage 22: Moving the storage cask into the airlock on Helman rollers. Stage 23: Moving the storage cask out of the airlock on Helman rollers. Stage 24: Moving the storage cask away from the secondary containment on Helman rollers. The storage cask is on rollers and cannot be dropped because it is not lifted. The base of the storage cask on the platform of the rollers is sufficiently wide so that it cannot tip. There are no other initiating events that occur in these stages. These stages are represented by one row in Table 19 because the risk of each stage is zero.

15. Stage 25: Preparing (install lid, vent shield cross-plates, vent screens) the storage cask for storage. The storage cask is stationary while it is being prepared and cannot be dropped. The base of the storage cask is sufficiently wide that it cannot tip. There are no other initiating events that can occur. Hence, the risk is zero.

16. Stage 26: Lifting the storage cask above the Helman rollers with the overpack transporter. Stage 27: Moving the storage cask above a cushion on the preparation area. Stage 28: Holding the storage cask above the cushion while attaching a Kevlar belt. Stage 29: Moving the storage cask above the concrete surface of the preparation area. Stage 30: Moving the storage cask above the asphalt road. Stage 31: Moving the storage cask above the gravel surface around the storage pads. Stage 32: Moving the storage cask above the concrete storage pad. Stage 33: Lowering the storage cask onto the storage pad. The MPC failure probability and the fuel failure probability are both approximately zero if the storage cask is dropped from an elevation of 0.3 meter (1 foot) onto concrete, asphalt, or gravel (Section 4.1.3.1). Because the risk is so small, the initiating event frequencies and the consequences are not determined. These stages are represented by one row in Table 19 because the risk of each stage is approximately zero.

17–24. Stage 34: Storing the storage cask on the storage pad for 20 years. To calculate the risk, this stage is divided into substages depending on the initiating event. The risk is also calculated separately for the first year of service and for the subsequent 19 years on the storage pad. However, because the duration of the handling and transfer phases is much less than 1 year, the frequencies of all initiating events in the first year of service are essentially the same as the corresponding frequencies for subsequent years on the storage pad.

17. Storage cask tipped by a seismic event during the first year of service. The initiating event frequency is 7×10^{-7} (Section 3.3.3). If the storage cask tips over no fuel rods are expected to fail (Sections 4.1.3.2 and 4.4.2). Even if the rods don't fail, a tip-over will dislodge CRUD from the rod surface. This CRUD is available for release. For the calculation of risk, it was assumed that all radionuclides are available for release. The risk at this stage is 2.5×10^{-16}, because the MPC has such a low probability of failure.

18. Storage cask struck by an aircraft during the first year of service. The frequency of the strikes that could impact the storage cask is 6.3×10^{-9} (Section 3.3.7). Based on the results in Section A.4.9.3, the probability of breaching the MPC, if struck by an aircraft during landing or takeoff is extremely small and is assumed to be zero. However, many commercial aircraft overflying the site would be larger than a Gulfstream IV and could impact the cask at high velocity. Since the makeup and characteristics of commercial aircraft overflying the site are not known and have not been evaluated, it is conservatively assumed that all commercial aircraft overflying the site are larger than a Gulfstream IV and that the probability of MPC breach due to the impact of an overflying commercial aircraft is, for the purpose of the PRA, 1.0. Therefore, the probability of MPC failure and release, if struck by an aircraft, is, for the purpose of the PRA, equal to the frequency of overflight crashes ($9.0\text{x}10^{-11}$, see Section 3.3.7) divided by the total frequency of aircraft crashes ($6.3\text{x}10^{-9}$, see Section 3.3.7), which is 0.014. Because the ISFSI is outside the containment, the radionuclides are released to the environment. Because all of the fuel rods are assumed to fail, the consequences are 3.6×10^{-4} (Section 6.3.1, Table 18). The risk is the product of the aircraft strike frequency, the MPC failure probability and the consequences, or 3.2×10^{-14}.

19. Storage cask struck by a meteorite during the first year of service. The frequency of meteorites that could breach the storage cask is 3.5×10^{-14} (Section 3.3.5). The probability of a release from the MPC is conservatively set to 1, for the purposes of this PRA. Because the ISFSI is outside the secondary containment, the radionuclides are released to the environment. Because all of the fuel rods are assumed to fail, the consequences are 3.6×10^{-4} (Section 6.3.1, Table 18). The risk is the product of the meteorite strike frequency, the MPC failure probability and the consequences, or 1.3×10^{-17}.

20. Storage cask heated by burning fuel when an aircraft crashes during the first year of service. It is assumed that a fire will result whenever an aircraft hits the storage cask. The frequency of this is the sum of the frequencies of takeoff or landing crashes plus overflight crashes. From Section 3.3.7, the frequency of the storage cask being struck by an aircraft and heated by burning jet fuel is 6.3×10^{-9}. From Appendix B, Section B.1.8, any fire caused by a takeoff, landing or overflight crash will not fail the cask. Hence, the probability of a release and the risk are both zero.

21–24. These notes are the same as Notes 17–20, respectively, for each of the subsequent 19 years of storage.

8. OTHER ASPECTS OF DRY CASK STORAGE RISK

Table 19 identifies conditions that could potentially affect the MPC's response to loads. Other possible conditions are described in the paragraphs of this section and summarized in Table 20. None of these conditions is expected to affect the integrity of the MPC.

Table 20. Conditions Potentially Affecting MPC Response to Initiating Events

Conditions Affecting the MPC Storage	Section
Excessive hot fuel assemblies mistakenly loaded	8.1
Criticality	8.2
Corrosion from coastal atmosphere	8.3
Corrosion from long-term industrial releases	8.3
Pressurization from corroding fuel	8.4
Pressurization from failed fuel	8.4
Hydrogen gas accumulation when the MPC lid and shell are welded	8.5

8.1 Mis-Loading of Spent Fuel into the MPC

For the purposes of the PRA, sensitivity analyses were performed to determine MPC failure probabilities for a gross mis-loading of wrong fuel assemblies into the MPC. The scenario of a gross series of errors, resulting in every fuel assembly loaded into the MPC being incorrect/insufficiently cooled is not considered credible, but useful for the purposes of exploring the impact of such an event. In these scenarios the heat load in the MPC was increased from 21 kW to 33 kW, 66 kW, and 126 kW. These heat loads correspond to fuel that has cooled in the spent fuel pool for 5 years, 2.5 years, 1 year, and 0.5 year, respectively. Even if every single fuel assembly loaded into the MPC were incorrect, no MPC failures are predicted for heat loads of 21 kW, 33 kW, and 66 kW. But if the heat load were 126 kW, the MPC could be expected to fail from creep rupture. The probability of failure in such an unlikely case would be 0.02 after 20 years of storage. No fuel failures are expected for heat loads of 21 kW and 33 kW. In these extremely unlikely scenarios, fuel failure could be expected to occur when the heat load is 66 kW and 126 kW. The fuel temperature would reach 543 °C (1,010 °F) and 809 °C (1,488 °F), respectively when the cask reaches thermal equilibrium. The long-term temperature limit for dry fuel storage is 400 °C (752 °F). [It is highly unlikely that rods at 543 °C (1,010 °F) would fail. Also, 400 °C (752 °F) is not a rod failure criterion. It was chosen to limit the hydride reorientation problem. It also limits creep.] Based on the extremely low likelihood of a gross mis-loading scenario, made all the more unlikely by the significant procedural requirements, fuel assembly verifications and instrumentation used in the process, it is concluded MPC integrity will not be affected by any occurrences of fuel mis-loading.

8.2 Potential for Criticality

A criticality study was performed on the transfer cask in Stage 3, during which the MPC is loaded with spent nuclear fuel while it is in the cask pit. This study was intended to provide insights as to degree of sub-criticality expected during limiting (not conservative) MPC loading operations. The reader is encouraged to keep in mind that these assumptions, while possible, are highly unlikely because we are effectively assuming that reactor operators will be discharging fuel well before its operational lifetime. Further depletion in the core will reduce the eigenvalues shown in this section and, therefore, the results of this study can be considered limiting. This study is not a rigorous nuclear criticality analysis of MPC operation. Since the results demonstrated roughly a 20% sub-critical margin, a more detailed analyses was deemed unnecessary. The analysis is only of events and conditions that are within the scope of the PRA as discussed in Section 1.2. The possibility of criticality was also studied in other stages, such as Stage 34, during which the storage cask is in the ISFSI. Given the assumptions of this analysis, the results are applicable to only BWR fuel in the subject cask. A BWR fuel assembly designed by General Electric was studied because it is highly enriched and contains large amounts of burnable poisons that will tend to maximize the reactivity increase effect. The BWR assembly was the most reactive assembly found in available fuel design references. Burnable poisons were modeled as four concentric annuli, and the assembly was burned pin-by-pin in steps of 1000 megawatt-days per metric ton (MWd/MTU). The enrichment was used as designed; the fuel depletion was modeled using the as designed assembly, rather than by assuming an initial homogeneous enrichment.

The SCALE suite of codes (Reference 47) was used to perform this analysis. The fuel was depleted with the TRITON module and criticality analysis were performed with KENO-VI using the 238 group ENDF/B-V library.

The fuel in the canister was modeled to the same level of detail as in the burnup calculation. The model was essentially 2-D. A 15.2-cm (6-inch) “slice” of the fuel using its most reactive axial zone and applied reflective top and bottom boundary conditions was modeled. One-quarter of the MPC basket was modeled with two lines of symmetry. The basket can be modeled as being surrounded by an effectively infinite annulus of water because an infinite reflector should yield the most reactive configuration.

To allow for fuel compression/expansion studies, it was confirmed that an isolated cell of the basket model yields effectively equivalent answers as the entire model. By this we mean that an isolated cell gave approximately the same eigenvalue as the complete MPC model. The fuel compression/expansion study assumed a reduction (or increase) of the pin pitch to ensure that there is not a compression (or expansion) accident condition that could lead to a significant increase in reactivity which would cause the eigenvalue to approach a 5% sub-critical margin. The MPC poisons were assumed to stay in the cask. This model is sufficient for trending studies, given the expectation that the results will be highly sub-critical.

Four concerns of criticality are the following:

(1) excessive heat generation can overpressurize the MPC
(2) excessive gamma radiation may be insufficiently shielded
(3) excessive neutron radiation may be insufficiently shielded
(4) radionuclides could be released if the fuel cladding were to fail

Several calculations were performed to evaluate MPC performance. The first observation is that the compression/expansion study demonstrates that there are no credible compression/expansion scenarios which lead to an increase in the eigenvalue to anywhere near the 5% sub-critical margin. Similar analyses are shown in Reference 48. The second observation is that there are no low density, optimal moderation configurations which means that pool draining events will not lead to a reduction in the sub-critical margin. Figure 19 and the work in Reference 49 confirm this by showing the predicted eigenvalue at the upper bound 95th percentile confidence interval with reduced water density. As is evident from the figure, even when changes in water density are considered, the fuel in the MPC is highly sub-critical. In summary, the criticality analyses performed for this study, while limited in scope, show similar trends as other studies by confirming that the configuration is under-moderated and highly sub-critical.

When the MPC is dry, criticality is not physically possible under any conditions in the absence of other neutron sources. This is true because the original fuel enrichment was limited to 5 weight percent, which is a limit based in part on the requirement that unmoderated criticality is not possible, even for BWR fuel at its most reactive point in life. This position is based on experimental data and calculations in Reference 50.

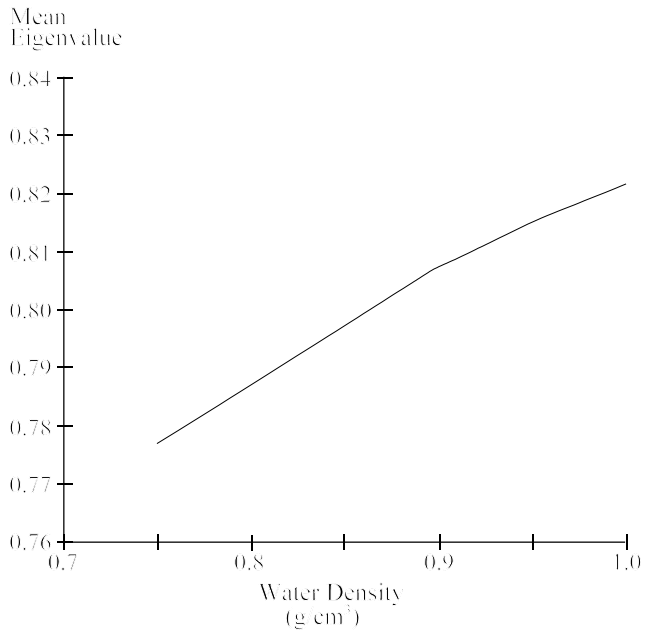

Figure 19. Upper 95th Percentile Confidence Interval Eigenvalue for MPC-68 in Pure Water at 27 °C (81 °F)

The boral plating in the MPC-68 basket is an effective means of criticality control; criticality is not allowed whether moderated or unmoderated. No credible scenario which would eliminate the boral and leave the geometry of the fuel intact has been identified. Even if the boral plates were to separate from the basket structure, they would have limited room to move and, once the basket is sealed, there is no credible means by which they could fall out of the basket. If the contents of the MPC-68 were to somehow relocate, the boral would relocate with the debris. In all likelihood, this postulated configuration would be highly subcritical because of the boral and because a bed of debris is not an optimal geometry. At the enrichments used in BWR fuel, a square pitch lattice is the optimal geometry for criticality. In the absence of moderation, experiments and calculations have demonstrated that criticality is not possible at the enrichments currently used in light-water reactor (LWR) fuel.

8.3 Corrosion

The MPC, which acts as the confinement boundary for the HI-STORM dry cask storage system, is constructed entirely from austenitic stainless steel Types 304, 316, 304L, or 316L. All of these stainless steel grades are corrosion resistant in high-humidity and industrial environments. Therefore, coastal and industrial atmospheres should have no effect on the confinement ability of the MPC (Reference 51).

The MPC is drained, dried, and filled with helium. Helium is an inert gas; it does not react with the fuel cladding or the internal structures of the MPC.

8.4 Pressurization

BWR fuel rods are normally pressurized with helium to 0.69 MPa (100 psi) (Reference 14). The fuel failure analysis of Appendix C uses a conservative assumption of 15.5 MPa (2250 psi) for internal fuel rod pressure. If the fuel rods were to breach, such as by creep rupture, the pressure in the rods would pressurize the MPC. An incremental increase in pressure from all of the fuel rods in the MPC rupturing is addressed in the Appendix B assessment of the response of the MPC to mechanical and thermal loads, Section B.1.8, "Results." Fuel failure would cause the internal pressure of the MPC to increase. If a mechanical impact event did cause fuel failure, the resulting increase in pressure would not occur during the drop accident scenarios. The increase in internal pressure due to fuel failure would be a result of the mechanical loading, but because of the extremely short duration of the impact, it would not affect the MPC conditions until after the mechanical loading is complete.

The failure analysis of the vent blockage scenario assumed bulk internal pressure takes into account the increased pressure from fuel failure. These results are shown in Appendix B, Table B4. The failure analyses show that even after 20 years of vent blockage and 20% fuel failure, the added pressure from failed fuel does not result in any expected MPC failures.

Calculations discussed in more detail in Appendix C determined that for the vent blockage scenario, all fuel rods located within a radius of 0.38 meter (1.25 foot) from the cask center will have a maximum clad temperature exceeding the long-term temperature limits. Using a ratio of affected areas, the fraction of fuel expected to exceed long-term temperature limits is 0.20.

8.5 Hydrogen Generation in the MPC

In Stage 9, the transfer cask is in the preparation area where the MPC lid is welded to the MPC shell. The water in the MPC is lowered to about 0.3 meter (1 foot) below the lid. While welding the lid to the shell, the root pass, several intermediate passes, and the final pass are tested with dye penetrant. The water level is then raised to the lid elevation, and the MPC is pressurized to hydrostatically test the weld. Should no leakage occur, the MPC is drained, dried, and filled with helium. The cover plates and closure ring are then installed and welded.

When the MPC contains water, reactions can occur that generate hydrogen gas. When the water level is below the MPC lid prior to hydrostatic testing, hydrogen gas can accumulate in the space between the lid and the surface of the water while the lid is welded to the shell. To prevent accumulation, the subject plant vents the space by pumping argon into the MPC through the drain line. The argon percolates through the water to the top of the MPC and exits through the port, purging hydrogen from the space.

Another reason for purging the space between the water surface and the lid is to eliminate any possible adverse effect that hydrogen could have on the lid-to-shell weld. Hydrogen in weld metal can cause cracks if the concentration is high enough and the material being welded is carbon steel or alloy steel. The type of stainless steel presently used for spent fuel canisters is highly resistant to hydrogen induced cracking. Despite this resistance to hydrogen induced cracking, this step to preclude hydrogen from the weld area is always implemented to further ensure high-quality welds.

The lid/shell and the closure ring/shell welds are not evaluated in the PRA because the lid/shell weld is more robust than the other welds of the MPC. Less-ductile welds, such as the baseplate weld, are evaluated in the PRA. For the following reasons the lid/shell weld is not evaluated:

- Because of the welding process, the lid/shell weld and the closure ring/shell weld is expected to be tougher than other welds of the cask.
- The MPC lid has redundant welding, consisting of the lid/shell weld and the closure ring/shell weld.
- Stress in the lid/ shell weld are low for all drop events.

The baseplate weld is modeled in the failure models of the MPC.

This page intentionally left blank

9. CONCLUSIONS

Starting with a comprehensive list of initiating events (Tables 3–5), the annual risk to the public from the onsite handling, transfer, and storage of a single transfer cask and storage cask at a specific BWR site is estimated. First, the frequencies of all initiating events which could affect the subject cask at the subject site are estimated. Second, the responses of the MPC and fuel to the mechanical and thermal loads induced by the initiating events are determined. Third, the consequences of a release of radioactive material to the environment is calculated in terms of the individual probability of a latent cancer fatality. (No prompt fatalities are predicted.) Finally, these results are combined to estimate the risk to the public in terms of the annual probability of a latent cancer fatality.

Because no uncertainty analysis was performed, the identification of the dominant contributors was based on the point estimates developed by this study. The dominant contributors might possibly change if uncertainty were considered.

The risk estimates are extremely low. Some of the scenarios have zero risk because either their initiating events cannot occur at the subject plant or no radioactive release will result. As Table 19 shows, the risks of the scenarios with nonzero risk are extremely low because they are the products of two or three very small numbers.

For example, when lowering the transfer cask through the equipment hatch, the initiating event of dropping the transfer cask has a frequency of 5.6×10^{-5} per year and a probability of 0.02 failure of the MPC. If only noble gases are released, the consequence probability is 1.0×10^{-10}, if other radioactive materials are released, the consequence probability is 3.6×10^{-4}, and the probability of the secondary containment failing to isolate is 1.5×10^{-4}. Thus, the risk of the noble gas release is:

$$(5.6\times10^{-5})(0.02)(1.0\times10^{-10}) = 1.1\times10^{-16}$$

and the risk of the release of other radionuclides is:

$$(5.6\times10^{-5})(0.02)(1.5\times10^{-4})(3.6\times10^{-4}) = 6.0\times10^{-14}$$

The handling phase Stages 4–8 have negligible risk due to drops of small heights. The probability of release of radioactive material from the MPC is $1x10^{-6}$. This produces extremely low risk and is shown in the risk columns of Table 19 as 3.0×10^{-18}.

There are two other stages (Stages 1 and 3) in the handling phase that have negligible risk. These stages involve release of noble gases if the containment fails to isolate. The releases occur because the lid of the MPC is not welded shut until Stage 9. The risk of a noble gas release is 1.9×10^{-16} in Stage 1 and 5.6×10^{-15} in Stage 3.

The estimated aggregate risk is an individual probability of a latent cancer fatality of 1.8×10^{-12} during the period encompassing the initial cask loading and first year of service, and 3.2×10^{-14} per year during subsequent years of storage. The only significant contributions to the risk during the handling phase are from drops of the transfer cask. There is zero risk associated with the transfer phase. During the transfer phase (movement of the storage cask out to the storage pad), drops of the storage cask are not high enough to induce sufficient stresses to fail the MPC or fuel cladding. During the storage phase, the dominant contribution to the risk is from aircraft striking the storage cask, although the risk is still extremely small.

10. REFERENCES

1. Memorandum to William D. Travers, Executive Director for Operations, from Annette L. Vietti-Cook, Secretary, "Staff Requirements — SECY-98-144 — White Paper on Risk-Informed and Performance-Based Regulation," Washington, DC, March 1, 1999.

2. HOLTEC International, "HI-STORM Topical Safety Analysis Report," HI-951312, Revision 8, Marlton, New Jersey, June 25, 1999.

3. U.S. Nuclear Regulatory Commission, "Severe Accident Risks: An Assessment for Five U.S. Nuclear Power Plants," NUREG-1150, Washington, DC, December 1990.

4. U.S. Nuclear Regulatory Commission, "Safety Goals for the Operation of Nuclear Power Plants" (Corrections and Republication of Policy Statement), *Federal Register*, Volume 51, No. 162, pp. 30028–30033, Washington, DC, August 21, 1986.

5. Chapman, O.J.V., and F.A. Simonen, "RR-PRODIGAL Model for Estimating the Probabilities of Defects in Reactor Pressure Vessel Welds," NUREG/CR-5505, U.S. Nuclear Regulatory Commission, Washington, DC, 1998.

6. R Kenneally, J. Price, and D. Koelsch, "Dry Cask Storage Characterization Project: Final Report," Electric Power Research Institute, Palo Alto, California; U.S. Nuclear Regulatory Commission, Washington, DC; U.S. Department of Energy, OCRWM, North Las Vegas, Nevada; and U.S. Department of Energy, Idaho Operations, Idaho Falls, Idaho, EPRI Doc. No. 1002882, September 2002.

7. U.S. Nuclear Regulatory Commission, "PRA Procedures Guide," NUREG-2300, Washington, DC, January 1983.

8. U.S. Nuclear Regulatory Commission, "Code Manual for MACCS2," NUREG/CR-6613, Vol. 1, Washington, DC, May 1998.

9. Hall, Eric J., *Radiobiology for the Radiologist*, 4th Edition, J.B. Lippencott Co., Philadelphia, Pennsylvania, 1994.

10. Generic Letter 89-22, "Resolution of Generic Safety Issue No. 103, 'Design for Probable Maximum Precipitation'," U.S. Nuclear Regulatory Commission, Washington, DC, October 19, 1989.

11. National Oceanic and Atmospheric Administration, National Weather Service, Hydrometeorological Report (HMR) No. 51, "Probable Maximum Precipitation Estimates, United States East of the 105th Meridian," Washington, DC, June 1978.

12. U.S. Nuclear Regulatory Commission, "A Survey of Crane Operating Experience at U.S. Nuclear Power Plants from 1968 through 2002," NUREG-1774, Washington, DC, July 2003.

13. U.S. Department of Energy, "Integrated Database Report — 1994: U.S. Spent Nuclear Fuel and Radioactive Waste Inventories, Projections, and Characteristics," DOE/RW-006, Rev. 11, Washington, DC, September 1995.

14. U.S. Nuclear Regulatory Commission, "A New Comparative Analysis of LWR Fuel Designs," NUREG-1754, Washington, DC, December 2001.

15. U.S. Nuclear Regulatory Commission, "Information Digest," NUREG-1350, Vol. 11, Washington, DC, 1999.

16. U.S. Nuclear Regulatory Commission, "Control of Heavy Loads at Nuclear Power Plants: Resolution of Generic Technical Activity A-36," NUREG-0612, Washington, DC, July 1980.

17. U.S. Nuclear Regulatory Commission, "Revised Livermore Seismic Hazard Estimated for Sixty-Nine Nuclear Power Plant Sites East of the Rocky Mountains," NUREG-1488, Washington, DC, April 1994.

18. U.S. Nuclear Regulatory Commission, "Tornado Climatology of the Contiguous United States," NUREG/CR-4461 (PNL-5697), Washington, DC, 1986.

19. Fujita, Theodore, *U.S. Tornadoes, Part One, 70-Year Statistics, Satellite and Mesometeorology Research Project (SMRP)*, Department of the Geophysical Sciences, The University of Chicago, SMRP Research Paper Number 218, Library of Congress Catalog Card Number 86-51637, National Technical Information Service PB 87-127742, Chicago, Illinois, Copyright 1987.

20. Kring, D.A., *Meteorites and Their Properties*, Lunar and Planetary Laboratory, University of Arizona, Tucson, Arizona, 2nd Edition, 1998.

21. French, Bevan M., *Traces of Catastrophe: A Handbook of Shock-Metamorphic Effects in Terrestrial Meteorite Impact Structures*, Lunar and Planetary Institute, 1998.

22. Cassidy, William A., *Estimated Frequency of a Meteorite Striking An Aircraft*, University of Pittsburgh, Department of Geology and Planetary Science, Pittsburgh, Pennsylvania, December 17, 1997.

23. HOLTEC International, HI-STORM 100 LAR 1014-1, Revision 1, Supplement 1, Marlton, NJ, October 2000.

24. Watson, A.I., and R.L. Holle, "An Eight-Year Lightning Climatology of the Southeast United States Prepared for the 1996 Summer Olympics," *Bulletin of the American Meteorological Society*, Vol. 77, No. 5, Boston, Massachusetts, May 1996.

25. International Electrotechnical Commission, "Protection of Structures Against Lightning — Part 1: General Principles, Section 10: Guide A: Selection of Protection Levels for Lightning Protection Systems," IEC 61024-1-1, Ed. 1.0 b:1993.

26. U.S. Nuclear Regulatory Commission, "Standard Review Plan for the Review of Safety Analysis Reports for Nuclear Power Plants," NUREG-0800, Rev. 2, Section 3.5.1.6, "Aircraft Hazards," Washington, DC, July 1981.

27. U.S. Department of Energy, "Guidance and Data for Impact Frequency Calculation," Appendix B to DOE Standard 3014-96, Washington, DC, October 1996.

28. Lawrence Livermore Software Technology, LS-DYNA Computer Code, Version 960, Livermore, California, March 2001.

29. U.S. Nuclear Regulatory Commission, "Standard Review Plan for the Review of Safety Analysis Reports for Nuclear Power Plants," NUREG-0800, Rev. 2, Section 3.5.1.4, "Missiles Generated by Natural Phenomena," Washington, DC, July 1981.

30. American Society of Mechanical Engineers, ASME Boiler and Pressure Vessel Code, Section III, New York, New York, 1989.

31. U.S. Nuclear Regulatory Commission, "Evaluation of Explosions Postulated to Occur on Transportation Routes Near Nuclear Power Plants," Regulatory Guide 1.91, Revision 1, Washington, DC, February 1978.

32. Mechanics Research, Inc., for the Tennessee Valley Authority, "Nuclear Power Plant Risks from a Natural Gas Pipeline," Knoxville, Tennessee, 1974.

33. Fluent Incorporated, Fluent (Computational Fluid Dynamics Software), Release 6, Lebanon, New Hampshire, 2000.

34. HOLTEC International, HI-STORM 100 Thermal Calculations, HOLTEC Report No: HI-981892, Marlton, NJ, November 2000.

35. American Concrete Institute, ACI 349-01, "Code Requirement for Nuclear Safety Related Concrete Structures," Farmington Hills, Michigan, 2001.

36. Society of Fire Protection Engineers (SFPE), *The SFPE Handbook of Fire Protection Engineering*, 2nd Edition, Chapter 3-11, Section 3, pp. 3-202, and 3-199, Bethesda, Maryland, 1995.

37. Kramer, M.A., et al., "Measurements of Heat Transfer to a Massive Cylindrical Object Engulfed in a Regulatory Pool Fire," *Proceedings of NHTC'01: 35th National Heat Transfer Conference, Anaheim, California, June 10–12, 2001*.

38. Drysdale, D., *An Introduction to Fire Dynamics*, John Wiley and Sons, Hoboken, New Jersey, 1996.

39. National Fire Protection Association, "Standard for the Installation of Lightning Protection Systems," NFPA-780, Quincy, Massachusetts, 1995.

40. U.S. Nuclear Regulatory Commission, "Standard Review Plan for Dry Cask Storage Systems," NUREG-1536, Chapter 2 "Guidance: Principal Design Criteria," Washington, DC, February 1, 1996.

41. Brauer, J.R., and B.S. Brown, *EMAS User's Manual*, Version 4, Ansoft Corporation, Pittsburgh, Pennsylvania, July 1997.

42. U.S. Nuclear Regulatory Commission, "Failure Behavior of Internally Pressurized Flawed and Unflawed Steam Generator Tubing at High Temperatures: Experiments and Comparison with Model Predictions," NUREG/CR-6575, ANL-97/17, Washington, DC, March 1998.

43. Chun, R., Witte, M., Schwartz, M., "Dynamic Impact Effects on Spent Fuel Assemblies," UCID-21246, Lawrence Livermore National Laboratory, Livermore, California, 1987.

44. General Electric Corporation, "ABWR Standard Safety Analysis Report," Chapter 19D, "Probabilistic Evaluations," Amendment 31, July 1993.

45. Combustion Engineering, Inc., "CESSAR Design Certification, System 80+ Standard Design FSAR, Appendix 19.5A – Data Calculations for Generic Component Data," Amendment M (March 15, 1993) and Amendment W (June 17, 1994).

46. Jow, J.N., et al., "MELCOR Accident Consequence Code System (MACCS), Model Description," NUREG/CR-4691, SAND-1562, Vol. 2, U.S. Nuclear Regulatory Commission, Washington, DC, February 1990.

47. U.S. Nuclear Regulatory Commission, "SCALE: A Modular Code System for Performing Standardized Computer Analyses for Licensing Evaluation," Vols. I–III, NUREG/CR-0200, Rev. 6 (ORNL/NUREG/CSD-2/R6), Washington, DC, May 2000.

48. U.S. Nuclear Regulatory Commission, "Technical Study of Spent Fuel Pool Accident Risk at Decommissioning Nuclear Power Plants," NUREG-1738, Washington, DC, February 28, 2001.

49. U.S. Nuclear Regulatory Commission, "Reexamination of Spent Fuel Shipment Risk Estimates," NUREG/CR-6672, Washington, DC, March 2000.

50. Paxton, H.C., and N.L. Pruvost, "Critical Dimensions of Systems Containing U235, Pu239, and U233," Report LA-10860-MS, Los Alamos National Laboratory, Los Alamos, New Mexico, July 1967 (1986 Revision).

51. American Society for Metals, "Corrosion Resistant Materials," *Metals Handbook Desk Edition*, Materials Park, Ohio, 1985.

APPENDIX A
MECHANICAL LOADS

APPENDIX A
MECHANICAL LOADS

A.1 Purpose

While conducting the dry cask storage PRA, specific questions were identified that related to the handling, transfer, and storage of the cask system and the effects of natural phenomena such as wind, flood, and earthquake. This appendix contains summaries of the results and corresponding calculations to address each of those questions.

The purpose of this appendix is to examine several initiating events during the handling, transfer, and storage of the cask system and to determine the effects of natural phenomena (wind, flood, and earthquake). The results of this evaluation will provide the stresses in the multi-purpose canister (MPC), which contains the spent fuel that will be used in subsequent evaluations to determine the probability of breaching the MPC.

A.2 Scope

The scope of this evaluation is limited to performing calculations in response to specific questions. These questions all relate to the transfer cask and the storage cask used at the subject plant. The questions are as follows:

Handling Phase Questions

(1) If the fuel handling building crane is traveling at maximum speeds [bridge 15 m/min (50 ft/min), trolley 3 m/min (10 ft/min), and hoist 1.3 m/min (4.2 ft/min)] with an MPC and its lid secured by gravity in the transfer overpack, what drop height causes the transfer cask to tip-over onto the concrete floor?

(2) Same question as Question 1, but the MPC lid is "sealed."

(3) Analyze the vertical drop of the transfer cask containing a sealed MPC falling on the concrete floor at ground elevation from heights of 1.5, 12.2, 21.3, and 30.5 meters (5, 40, 70, and 100 feet). Determine the magnitude and location of maximum stresses/strains in the MPC.

(4) Analyze the vertical drop of the transfer cask containing a sealed MPC falling onto the storage overpack at ground elevation from heights of 1.5, 12.2, and 24.4 meters (5, 40, and 80 feet). Determine the magnitude and location of maximum stresses/strains in the MPC.

(5) Determine the magnitude and location of maximum stresses/strains in the MPC when a sealed MPC falls vertically 5.8 meters (19 feet) into the storage overpack.

Transfer Phase Question Topics

(6) If the storage cask drops onto the independent spent fuel storage installation (ISFSI) concrete pad, asphalt area, or gravel area, while it is hung from the top trunnion and being transported by the crawler, will it slide and/or tip-over? If tip-over can occur, what velocity of the crawler would be required to tip it over? How much time does the operator have to stop the crawler before tip-over occurs? What are the stresses in the MPC?

(7) If the crawler vehicle weighing 71,440 kg (157,500 lb) is traveling at 0.64 km/h (0.4 mi/h) while carrying the storage cask weighing 163,293 kg (360,000 lb) and hits another storage cask on a concrete pad, will the impact cause the struck cask to slide or tip-over?

1. If it slides, will a sliding storage cask hit another storage cask? If it hits another storage cask, what are the maximum stresses in the MPC?
2. If it tips over, what are the maximum stresses in the MPC?
3. If it does not slide or tip-over, what travel velocity of the crawler would be necessary to strike the storage cask and cause it to slide and/or tip-over?

Storage Phase Question Topics

(8) What seismic forces will cause the storage cask to slide and/or tip-over?

(9) What impact forces attributable to a given small aircraft, tornado missiles (beyond design basis) and heavy objects in flood waters will cause the storage cask to slide and/or tip-over? If the impacting object penetrates the storage overpack, what will be the stresses in the MPC?

(10) If the storage cask tips over on the concrete pad, what will be the stresses in the MPC?

(11) If the storage cask tips over, will the impact of the cask tipping over on another storage cask or on the concrete pad cause the overpack lid to be dislodged such that the MPC could slide out?

(12) Will the structural integrity of the cask system be jeopardized by shock waves caused by postulated explosions? If not, provide the supporting arguments.

A.3 Method

To evaluate the structural response of the cask system to the event scenarios posed by the twelve questions, several methods of analysis were used, which included hand calculations based on first principles, common analytical methods and industry recognized approaches, and solution of the differential equations of motion for which closed form solutions were obtained. Wherever possible existing analyses, such as the Holtec finite element analysis of the MPC, fuel basket and fuel basket supports (Reference A.1), that had been performed for a number of impact events were utilized by scaling the stress results in Reference A.1 by the ratio of the maximum acceleration calculated in response to the question divided by the acceleration in Reference A.1. For the cask drop impact scenarios, the Holtec finite element models were modified and expanded, as discussed in the appropriate sections below.

A.4 Calculation Summary Descriptions

A.4.1 Question 1

If the fuel handling building crane is traveling at maximum speeds [bridge 15 m/min (50 ft/min), trolley 3 m/min (10 ft/min), and hoist 1.3 m/min (4.2 ft/min)] with an MPC and its lid secured by gravity in the transfer overpack, what drop height causes the transfer cask to tip-over onto the concrete floor?

A.4.2 Question 2

Same as Question 1 but the MPC lid is "sealed."

The response to Questions 1 and 2 are combined into one evaluation. Solutions are obtained for various cask orientations when it is dropped. When the transfer cask impacts the concrete floor it is assumed to have the same orientation and horizontal velocity as when it was dropped. The vertical velocity is increased (positive measured down) by the velocity added during free fall. At impact the horizontal and vertical velocity components are transferred to an equivalent rotational velocity. The transfer cask then rotates about the point of impact until it either tips over (when the center of gravity intersects a vertical line immediately above the point of impact) or rotates back to a vertical orientation. The question is resolved by determining the rotational velocity needed to tip-over the transfer cask. It should be noted that the transfer cask drops at an acceleration of 1 g so that the lid secured by gravity would not separate from the MPC during the fall. Therefore, the answers to Questions 1 and 2 are the same. Detailed analyses are first summarized and then followed by a discussion of the answer.

With No Initial Velocity

The specific geometry of the transfer cask is shown in Figure A.1. The weight of the loaded transfer cask is assumed to be 86,636 kg (191,000 lb) but as will be seen the weight does not enter into the solution. Note that the transfer cask is dropped at an angle (α) with the vertical and the drop height to the center on the base of the cask is H. When the angle (α) equals $90 - \Phi = 67^\circ$, the transfer cask is oriented so that the center of gravity of the cask is located above the point on the cask that first impacts the slab. It is obvious that the transfer cask will tip-over if it is dropped at angles less than 67°.

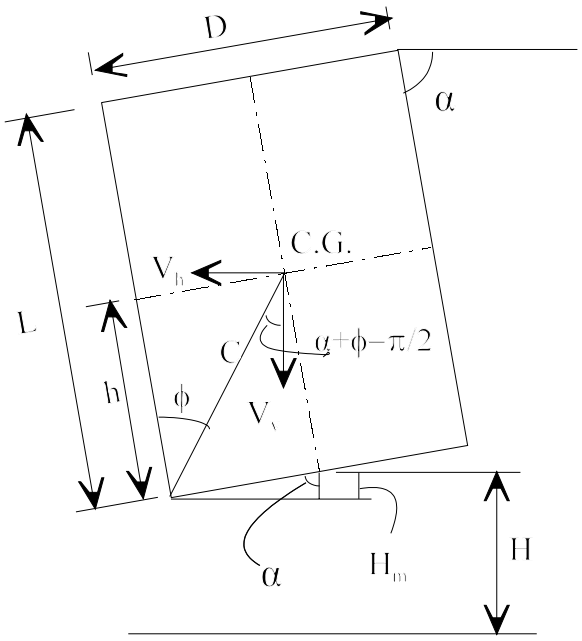

Figure A.1. Geometry of Transfer Cask

Note that it is not possible to drop the transfer cask at angles smaller than $\alpha = 67°$ unless the drop height (H_m) is greater than that calculated from the following expression:

$$\text{Cos } \alpha = \frac{H_m}{D/2} \qquad \text{(A.12)}$$

where: D = 2.06 m (81.25 inches)
L = 4.84 m (190.5 inches)
h = 2.39 m (93.95 inches)
C = 2.64 m (104 inches)
Φ = 23°
H_m = ½ * D * Cos α

Therefore, with no initial velocity a tip-over will occur only if the drop height is greater than 40 cm (15.9 inches) and the angle α is less than 67°.

With Initial Velocity

At impact the horizontal (V_h) and vertical (V_v) velocities of the cask are transformed to a rotational velocity of the transfer cask (θ_o').

The subsequent response of the transfer cask is developed next. A sketch of the transfer cask defining the response parameters used is shown in Figure A.2.

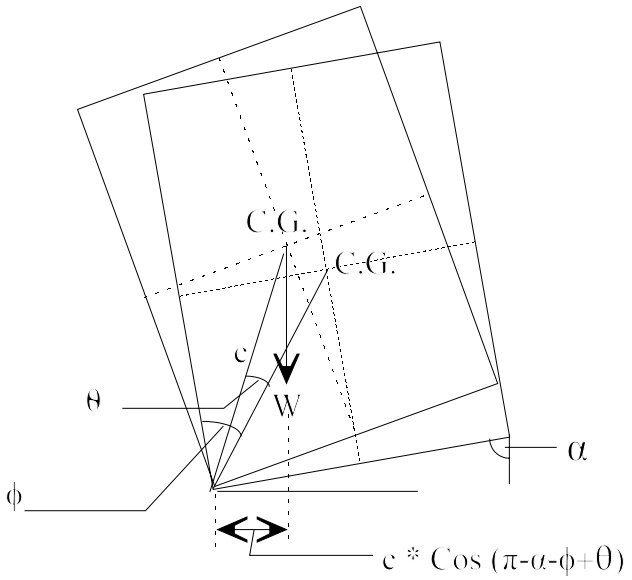

Figure A.2. Rotation of Transfer Cask after Impact

The response of the cask is then governed by:

$$\theta_0' = \frac{V_h \mathrm{Sin}\left(\pi - \phi - \alpha\right) - V_v \mathrm{Sin}\left(\phi + \alpha - \pi/2\right)}{C} \qquad (A.13)$$

$$J\theta'' + W\ C\ \ \mathrm{Cos}\left(\pi - \phi - \alpha + \theta\right) = 0 \qquad (A.14)$$

with the initial conditions, $\theta(0) = 0$; and $\theta'(0) = \theta_o'$ and where J is the rotational inertia of the transfer cask.

It is interesting to examine this family of equations before discussing their solution. Equation A.2 demonstrates that the vertical velocity reduces the rotational velocity imparted to the transfer cask at impact. It can, therefore, be concluded that any positive vertical velocity decreases the possibility that the transfer cask will tip-over.

Because of free fall, the upward initial velocity 1.3 m/min (4.2 ft/min) caused by the hoist is reduced to zero at some drop height. Therefore, a solution is sought where the vertical velocity is zero at impact. This solution can be found simply by equating the kinetic energy (KE) of the transfer cask at impact to the potential energy (PE) developed as the center of gravity is raised to a point where it is directly over the point of impact. The kinetic energy is as follows:

$$KE = \frac{WV_h^2}{2g} \qquad (A.15)$$

The potential energy when the center of gravity is over the point of rotation is as follows:

$$PE = W\,C\left[1 - \mathrm{Cos}\left(\phi - \frac{\pi}{2} + \alpha\right)\right] \qquad (A.16)$$

Equating the two, we obtain the following:

$$V_h = \left\{2\,g\,C\left[1 - \mathrm{Cos}\left(\phi - \frac{\pi}{2} + \alpha\right)\right]\right\}^{1/2} \qquad (A.17)$$

The maximum horizontal velocity is $(50^2 + 10^2)^{1/2} = 51$ ft/min and Equation A.6 shows that at this velocity the transfer cask will tip-over only when the angle $\alpha < 70°$. If the horizontal velocity is zero the solution to Equation A.6 shows that the transfer cask will tip-over when the angle $\alpha < \pi/2 - \Phi = 67°$. The fact that these two solutions are so close indicates that the horizontal velocities imparted to the transfer cask by the crane are very small and have little effect on the problem. It is also interesting to note that the height of the drop is not involved in the solution. In effect, it has been assumed that the vertical velocity is zero which can only occur for very low drop heights. Any higher drops would reduce the solution $\alpha=70°$, but it cannot be reduced further than 67°.

In summary the velocities imparted by the crane are very small and have little effect on the conditions required for the transfer cask to tip-over. The solutions indicate that, for the given crane velocities, the transfer cask will tip-over only if it is dropped at an angle such that the center of gravity of the cask is over the point of first contact with the floor. This angle requires that the transfer cask axis be oriented less than 67° with the horizontal. This can only occur when the drop height of the transfer cask is greater than 40 cm (15.9 inches).

A.4.3 Question 3

Analyze the vertical drop of the transfer cask containing a sealed MPC falling on the concrete floor at ground elevation from heights of 1.5, 12.2, 21.3, and 30.5 meters (5, 40, 70, and 100 feet). Determine the magnitude and location of maximum stresses/strains in the MPC.

Model Development

To respond to this question, a finite element model was developed that includes the MPC, fuel assemblies, fuel basket, fuel basket supports, transfer overpack, and concrete floor and wall (Reference A.24). These components are shown in Figures A.3 through A.5. The finite element model (FEM) shown in Figure A.3 contains all of the structural components mentioned above. The model is a quarter-model representation of the cask system and concrete floor/wall, which takes advantage of symmetry about two orthogonal vertical planes through the centerline of the MPC. Figure A.4 shows a close-up view of the transfer overpack (TO) and MPC resting on the concrete floor, and Figure A.5 shows another close-up view at the MPC connection to the MPC baseplate along one plane of symmetry. The fuel basket plate on the plane of symmetry has been removed so that the fuel assemblies within the basket compartments can be seen.

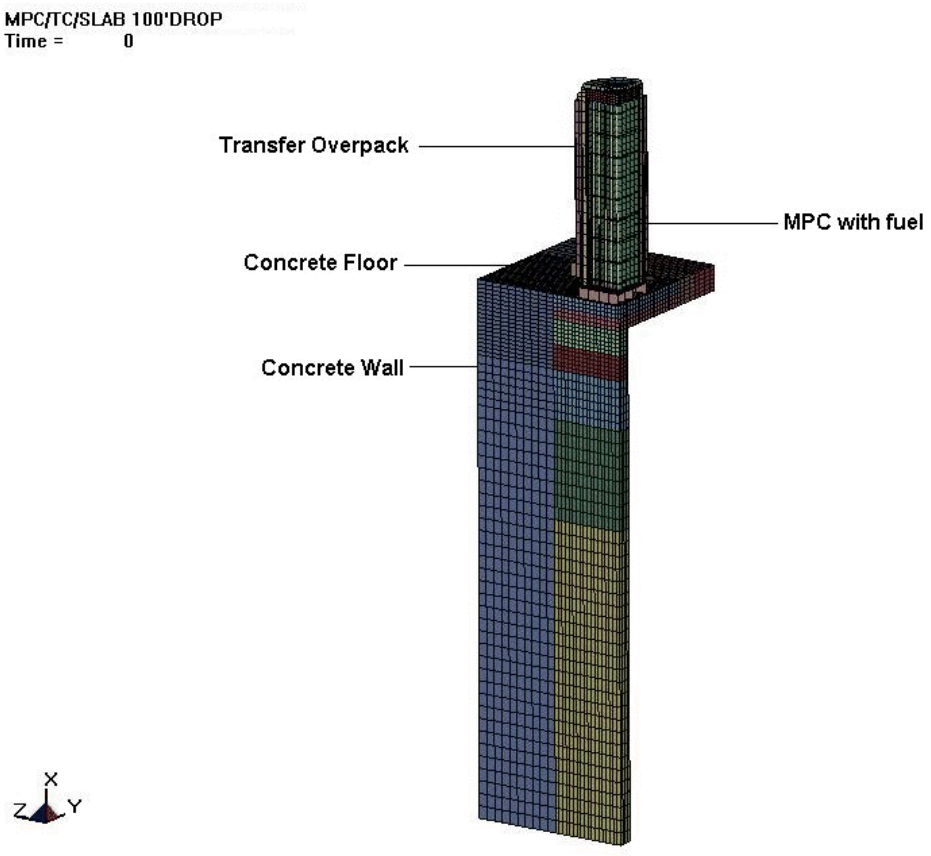

Figure A.3. Transfer Cask Vertical Drop onto Concrete Floor/Wall Finite Element Model

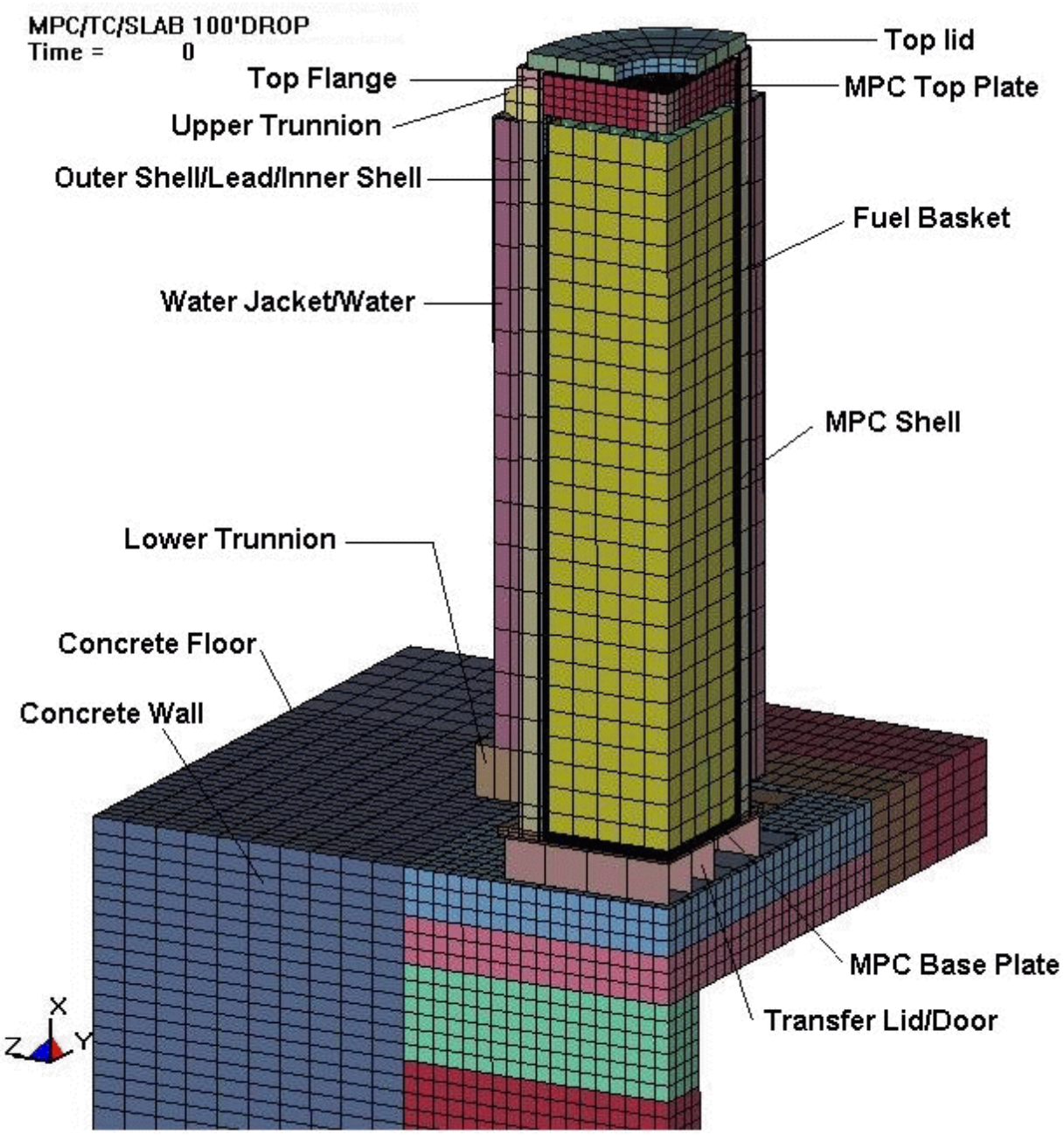

Figure A.4. Transfer Cask Vertical Drop onto Concrete Floor/Wall. Close-Up View of the Cask Resting on the Concrete Floor.

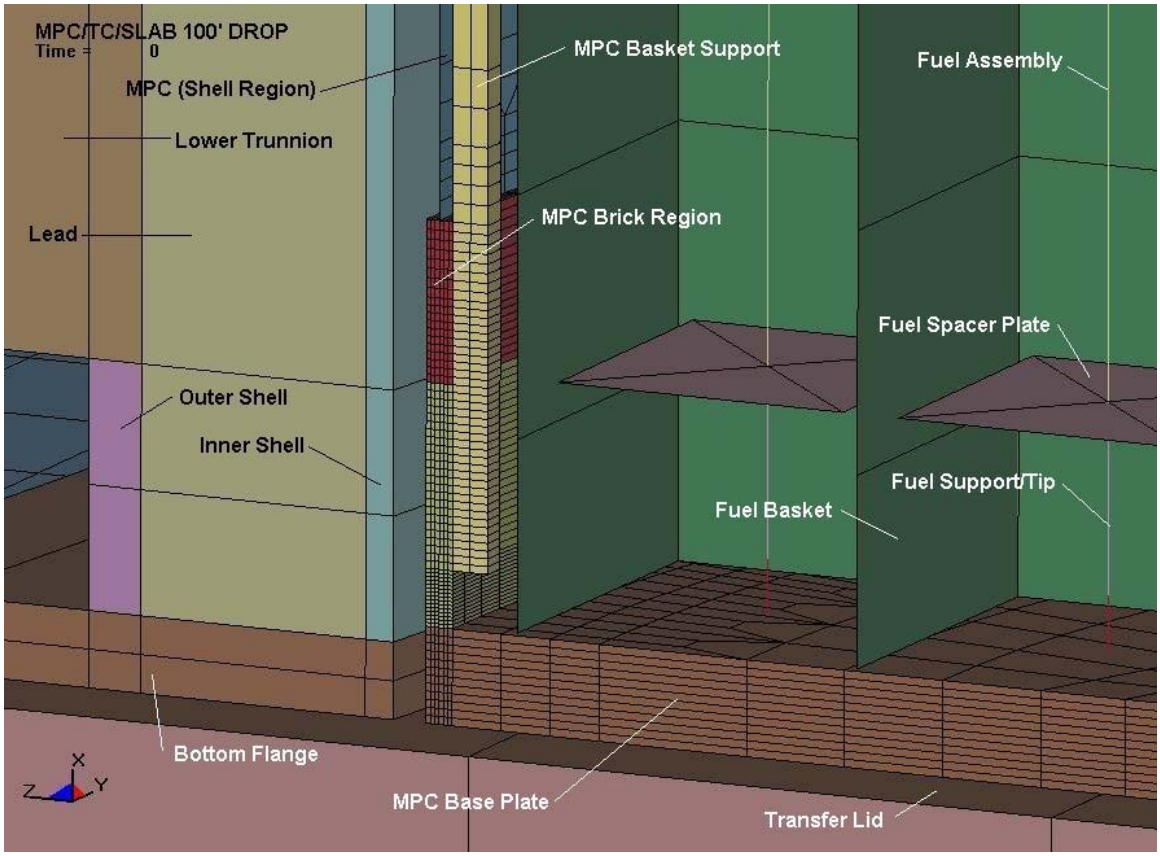

Figure A.5. Transfer Cask Vertical Drop onto Concrete Floor/Wall Showing MPC Connection to the MPC Baseplate at Plane of Symmetry (Time = 0)

The TO model used in this analytical study is the 125 ton HI-TRAC Model with the MPC-68 canister (full of fuel) and bottom transfer lid, as received from HOLTEC International. The major revisions made are as follows (A complete listing of changes can be found in Reference A.24.):

(1) To minimize the significant computational effort, a quarter model representation of the TO, MPC, and concrete floor/wall beneath the floor was developed. This quarter model was created considering the two vertical planes of symmetry that exist for the TO and the MPC. The TO quarter model was developed from the HOLTEC half model by deleting half of the nodes and element definitions and creating a node set to define the two planes of symmetry.

(2) Contact surfaces within various components of the TO and between the TO and the concrete floor were defined to properly transfer impact forces.

(3) The HOLTEC TO model represents the combined MPC/fuel region modeled as brick type finite elements. This single brick representation of the MPC/fuel was deleted and replaced by a detailed finite element model of the MPC and internal components, as described later. (Removal of the single brick representation of the fuel and basket and replacing it with an explicit representation of the fuel and basket is not necessary for the analysis of the MPC. This was only done in the event that the model would be used to predict fuel cladding strains.)

The dynamic impact analyses were performed using the LS-DYNA computer code, Version 970, Rev. 3858 (Reference A.4). LS-DYNA is a general-purpose finite element code for analyzing the large deformation dynamic response of structures. The computer code utilizes an explicit solution method to solve for the dynamic impact response. Strains in all elements are calculated at each time step, and if the effective plastic strain (EPS) reaches the user specified failure strain for a particular element, that element is automatically eliminated from the model and the analysis continues.

The material model for the Type 304 stainless steel components in the TO and MPC are based on a bilinear elastic plastic stress strain curve, which requires the elastic modulus, yield strength, tangent modulus, and failure strain as input. The modulus of elasticity was taken from the ASME Code, Division 1 - Appendices (Reference A.5). The material properties for the yield strength and ultimate strength were based on the data contained in Appendix B, and then adjusted for strain rate effects using the information in Reference A.6. The engineering strain at failure was based on the data contained in Reference A.6 at a high strain rate. The tangent modulus was calculated from the yield strength, ultimate strength and engineering failure strain. All of these material properties were developed at the appropriate temperature for each component of the TO and MPC.

The design temperatures for the various TO and MPC components are presented in Table A.1, and are consistent with HOLTEC's design (Reference A.1). The material properties (modulus of elasticity, yield strength, tangent modulus, and rupture strain) at the temperatures of the TO and MPC components are presented in Table A.2.

Table A.1. Transfer Overpack, MPC, and Fuel Cladding Temperatures

Components	**Temperature °C (°F)**
Fuel and fuel basket	393 (740)
MPC Shell	237 (459)
Transfer overpack inner shell and water jacket inner surface	162 (323)
Water jacket outer surface	106 (223)
Top lid, transfer lid, trunnion, water jacket ribs, water, and transfer lid vertical plates	162 (323)

Table A.2. Material Properties

Material	Temp °C (°F)	Modulus of Elasticity (psi)	Yield Strength (psi)	Tangent Modulus (psi)	Engineering Strain at Failure (in/in)	Minimum True Strain at Failure (1) (in/in)
Stainless Steel (Type 304)	393 (740)	2.35×10^{7}	23386	1.03×10^{5}	0.377	0.92
	237 (459)	2.61×10^{7}	38344	5.85×10^{4}	0.456	0.92
	162 (323)	2.69×10^{7}	44719	4.60×10^{4}	0.48	0.92
	106 (223)	2.75×10^{7}	51012	4.03×10^{4}	0.498	0.92
Zircaloy-2	393 (740)	9.80×10^{6}	43807	1.41×10^{5}	NA	NA
Lead	162 (323)	1.90×10^{6}	380	0	NA	NA

1 psi = 6.895 kPa
(1) Includes the effects of strain rate and temperature up to 100/sec and 1000F respectively.

Although stainless steel material Types 304LN, 316, and 316LN might also be used to construct the TO, MPC and other stainless steel components, the material properties (yield and ultimate strength) for stainless steel Type 304 are equal to or less (i.e., more conservative) than the values for Type 304LN, 316, and 316LN for the temperature range of interest and, therefore, were used in the analysis.

The material model used in the analysis assumes that the stress-strain curve and failure criterion (rupture strain), which are derived from tensile test data, are also applicable to elements in compression. Using the same stress-strain curve in tension and compression is realistic for steel materials.

Since the LS-DYNA computer program considers the reduction in the area of the finite elements in the computation of stress during the execution of the analysis, a true stress strain curve is expected to be input for the material properties. In the analyses, however, the more conservative engineering stress strain curve was used. It is well known that engineering stress strain values are very close to the true stress strain values during the initial stages of yielding, and that in the plastic region the engineering stress values are always lower than the true stress values. Thus, at any given deformation level the total energy absorbed by the MPC will be underestimated. This results in a conservative response because it overestimates the total deformation (strain). For comparison, the minimum true strain at failure of Type 304 stainless steel is also shown in Table A.2.

The MPC consists of the 1.27-cm (½-inch) thick vertical cylindrical shell, a 25.4-cm (10-inch) thick top shield plate, and a 6.35-cm (2.5-inch) thick baseplate. The top plate and baseplate are modeled using brick elements. The MPC cylindrical shell is modeled using six brick elements through the thickness from the top of the baseplate to 30 cm (11.75 inches) above the baseplate. Beyond this elevation, the vertical shell wall is modeled using shell elements. Shell elements are sufficiently accurate for the region above 30 cm (11.75 inches), and this transition to shell type elements reduces the execution time for solution. Even with this transition to shell type elements, the entire model is quite large with 79,973 nodes and 66,704 elements.

The fuel basket is modeled as a grid of 0.635-cm (¼-inch) thick vertical plates spaced 16.5 cm (6.5 inches) apart to form the square cells that hold the fuel assemblies. The fuel basket is freestanding on top of the MPC baseplate. The LS-DYNA model of the fuel basket is shown in Figures A.4 and A.5. In Figure A.5, the basket plates at the plane of symmetry have been removed to show the fuel assemblies within the basket cell walls. The mass density of the basket plates was increased to account for the additional boral material attached to the sides of the basket plates. The material model used for the TO and MPC was also utilized for the stainless steel fuel basket plates. The specific material properties used for the fuel basket are shown in Tables A.1 and A.2.

To maintain a reasonable execution time, a single equivalent beam model of a typical fuel assembly was developed and placed inside each of the basket cell compartments. Each fuel assembly model consisted of a fuel support region (at the bottom of the fuel assembly), fuel region, and a handle (at the top of the fuel assembly). To capture the interaction between the fuel assemblies and the MPC baseplate, it was necessary for the fuel beam to have plastic capability. To incorporate plasticity in a beam element, LS-DYNA requires that the beam be defined with explicit dimensions. To obtain the correct assembly stiffness and nonlinear behavior, the fuel region was modeled as a single circular tube with cross-sectional dimensions equal to an individual fuel rod, and the yield stress, modulus of elasticity, tangent modulus, and mass density were multiplied by the total number of fuel rods in the assembly.

In this analysis, the primary purpose of the fuel assembly model is to capture the overall effects of the fuel assembly on the structural response of the MPC in a vertical drop. Therefore, the most important parameters are the mass, vertical stiffness, and energy absorption capability of the fuel assemblies. An assumption made in the fuel assembly model is that the mass of the fuel is added to the mass of the fuel cladding, but only the fuel cladding provides stiffness. This assumption is consistent with the methodology utilized by HOLTEC in its design (Reference A.7), and complies with References A.25 and A.26.

The same material model and material properties (elastic modulus, yield strength, tangent modulus, and rupture strain) used for the fuel basket described above, were also utilized for the stainless steel fuel support (beneath the fuel region) and the handle (above the fuel region). The material properties used for the fuel region were based on the properties of Zircaloy-2 cladding material at a temperature of 483 °C (902 °F) (References A.8 and A.9). Table A.2 presents the various material properties used for the fuel assembly members.

Based on calculations performed by HOLTEC (Reference A.7), the fuel region was expected to buckle elastically. However, LS-DYNA does not check for classical bifurcation buckling directly; but it can achieve an accurate prediction of static buckling by introducing a tiny bias (initial deflection) in the middle of the fuel rod. Therefore, a small bias was introduced in the middle of each equivalent fuel beam (between spacer grids) to allow large lateral deformation to take place.

Also included in the fuel assembly model are nine spacer plates (grids), at the elevations specified in the fuel assembly design drawings. The spacers, modeled with shell elements, are constrained to move vertically and horizontally with the equivalent fuel beams. A small gap is modeled between these spacer plates and the basket cell walls. Once the gap is closed, the basket cell walls provide lateral restraint for the spacer plates, which provide lateral restraint to the fuel rods. The fuel assemblies, like the fuel basket, are also freestanding on top of the MPC baseplate.

A finite element model of the concrete floor and wall beneath the floor was developed. The model of the concrete wall is 12.5 meters (41 feet) high from the bottom of the floor, 3.96 meters (13 feet) long and 38

cm (15 inches) thick. The concrete floor is 3.96 meters (13 feet) wide, 3.96 meters (13 feet) long and 61 cm (24 inches) thick. This concrete floor/wall model is a quarter model representation of the actual structure and is consistent with the quarter models of the TO and MPC. Although the actual floor and wall do not have two well-defined planes of symmetry, this representation is considered reasonable.

The concrete floor/wall model was developed with 10 separate "parts" using the same concrete material model, each of which can be adjusted independently when needed for hourglass control or to change element formulation types. A finer mesh was developed near the impact region, while a coarser mesh was created away from this critical region. The concrete floor/wall has fixed boundary conditions at the ends of the wall and at the edges of the floor, excluding the two planes of symmetry.

The concrete material model and the material properties utilized in the analyses are those used by the cask manufacturer in their analyses for design certification and are presented in Appendix C to Reference A.11. A comparison analysis using an alternate concrete material model was also performed to determine whether LS-DYNA Material Model Type 16, which was used in the analysis, is reasonable and comparable to other more recently developed material models. The results indicate that the alternative material model gives comparable results to Material Model Type 16.

The transfer cask rests on top of the concrete floor at the start of the analysis, and the drop height was simulated by introducing an initial velocity corresponding to the desired drop height. The initial velocity was calculated using the following expression:

$Velocity = \sqrt{2gh}$, where g is the acceleration of gravity and h is the drop height.

Four different drop heights at 1.5, 12.2, 21.3, and 30.5 meters (5, 40, 70, and 100 feet) were considered in the vertical drop analyses.

The design of the TO specified a small gap between the MPC shell wall and the inner shell of the TO. If after the fall the MPC lands at the center of the bottom lid of the TO, there would be a uniform gap equal to 0.5 cm (0.203 inches) based on average construction tolerances. Under this configuration, when the MPC shell deforms radially by an amount greater than the uniform radial gap, the TO provides resistance to further radial deformation. For the analysis reported herein, a worst-case assumption was made that during the accidental drop of the MPC/TO, the MPC may land completely to one side of the TO. This creates a maximum gap on the opposite side equal to approximately 1.03 cm (0.406 inches) which is twice the average. This off-center drop location is simulated in the analysis by circumferentially enlarging the gap between MPC shell and TO inner shell to 1.03 cm (0.406 inches). In this manner, the analysis can provide an estimate of the effect of an off-center drop, while keeping the quarter model representation of the actual casks.

Analysis Strategy and Modifications to the Finite Element Model

The strategy behind the development of a finite element model and subsequent analysis must reflect the intended use of the results. In this case the results will ultimately be used to predict the probability of failure of the MPC confinement boundary. As such, the results from the finite element analysis must support the methodology used to predict material failure in the MPC shell and weldments.

Following receipt of the report and models (Reference A.24), the engineering failure strain limit was eliminated which had been set for the deletion of "failed" elements. This was done as a result of the a revision of the weld failure methodology in Appendix B so that the actual true strain, which is the result that is directly linked to the probability of weld failure in Appendix B, could be continuously computed until the end of the event. By running the models this also allowed to calculate the Triaxiality Factor at the location of maximum strain. As explained in Appendix B, the Triaxiality Factor is an important parameter for predicting failure, because it accounts for loss of material ductility in regions where a triaxial state of stress may constrain plastic flow.

As part of accepting the drop analysis report and input files, shakedown evaluations of the model were performed. Based on those results the following modifications were made:

(1) All analyses were run using double-precision.

(2) The basket supports' attachment to the MPC shell was modified to more accurately reflect the Holtec drawings.

(3) The MPC baseplate mesh was slightly modified at the junction with the shell to remove a local hard spot in the mesh.

These modifications were included in all analyses of the drops of the transfer cask onto the concrete floor and the 5.8 meters (19 foot) drop of the MPC into the storage overpack. They were not included in the analysis of the drops of the transfer cask onto the storage overpack because the strains were relatively low for these drops.

Analysis Results

The drop heights selected for analysis were 1.5, 12.2, 21.3 and 30.5 meters (5, 40, 70, and 100 feet), which provide results at the maximum drop height and at intermediate levels. The structural response of the MPC for the vertical end drop of the transfer cask onto the concrete floor are summarized in Table A.3. For each drop height, the maximum EPS in the MPC shell, the element producing the maximum EPS and the true strain at failure are tabulated. Only the 30.5-meter (100-foot) drop is discussed in detail.

Table A.3. Structural Response of the MPC for Various Drop Heights

Drop Height m (ft)	Maximum EPS cm/cm (in/in)	Element Number with Maximum EPS	Minimum True Strain at Failure cm/cm (in/in)
1.52 (5)	0.024	16539	0.92
12.2 (40)	0.195	15973	0.92
21.3 (70)	0.24	15997	0.92
30.5 (100)	0.256	15997	0.92

Figures A.6 and A.7 show the deformation of the MPC shell and basket supports for the 30.5-meter (100-foot) drop case at the end of the event (0.022 seconds) when the kinetic energy has reached a minimum and the transfer overpack and MPC begin rebounding from the impact. These figures show the response of the structural components at the connection of the MPC cylindrical shell to the baseplate adjacent to the plane of symmetry through the center of the concrete wall. They clearly show that the deformation is dominated by buckling in the lower region of the shell. The figures also show that the MPC shell wall deforms primarily in a vertical downward direction, and radially outward near the baseplate. In addition, Figure A.7 shows that there is some rotation of the MPC baseplate at the junction with the shell wall. This helps relieve some of the strain in the shell at this intersection location. Figure A.7 also shows the separation between the basket support and MPC shell in the region between the stitch welds. (Note that the actual location of the one inch stitch weld is on the far side of the support since the centerline of the support is on the plane of symmetry.) The figure shows that the shell meridional curvature changes several times in this region. This is primarily attributable to the constraint of radial displacement caused by the radial contact of the MPC shell with the inner shell of the transfer cask.

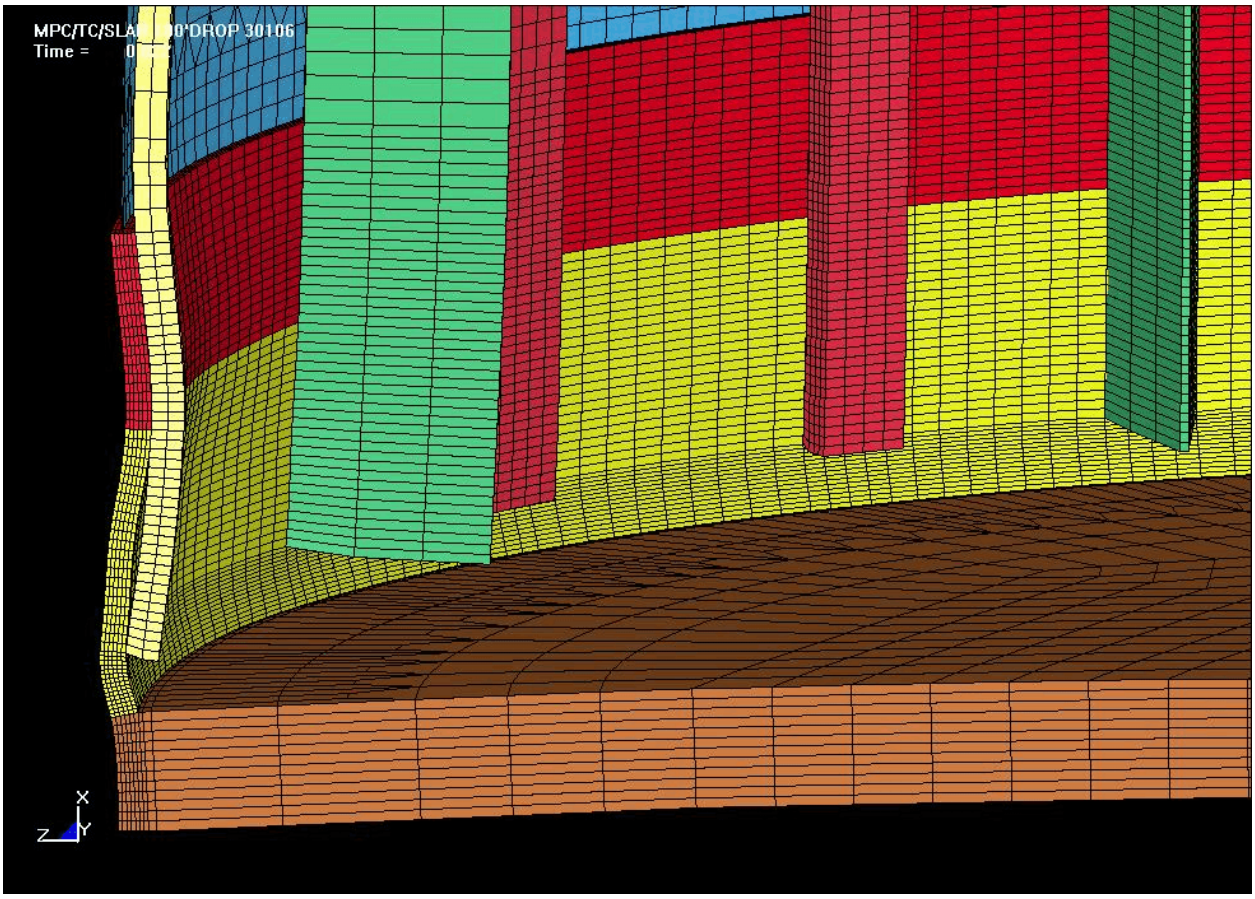

Figure A.6. Deformation of the MPC Shell and Basket Supports at 0.022 seconds for the 100-foot Drop of the Transfer Cask onto the Concrete Floor

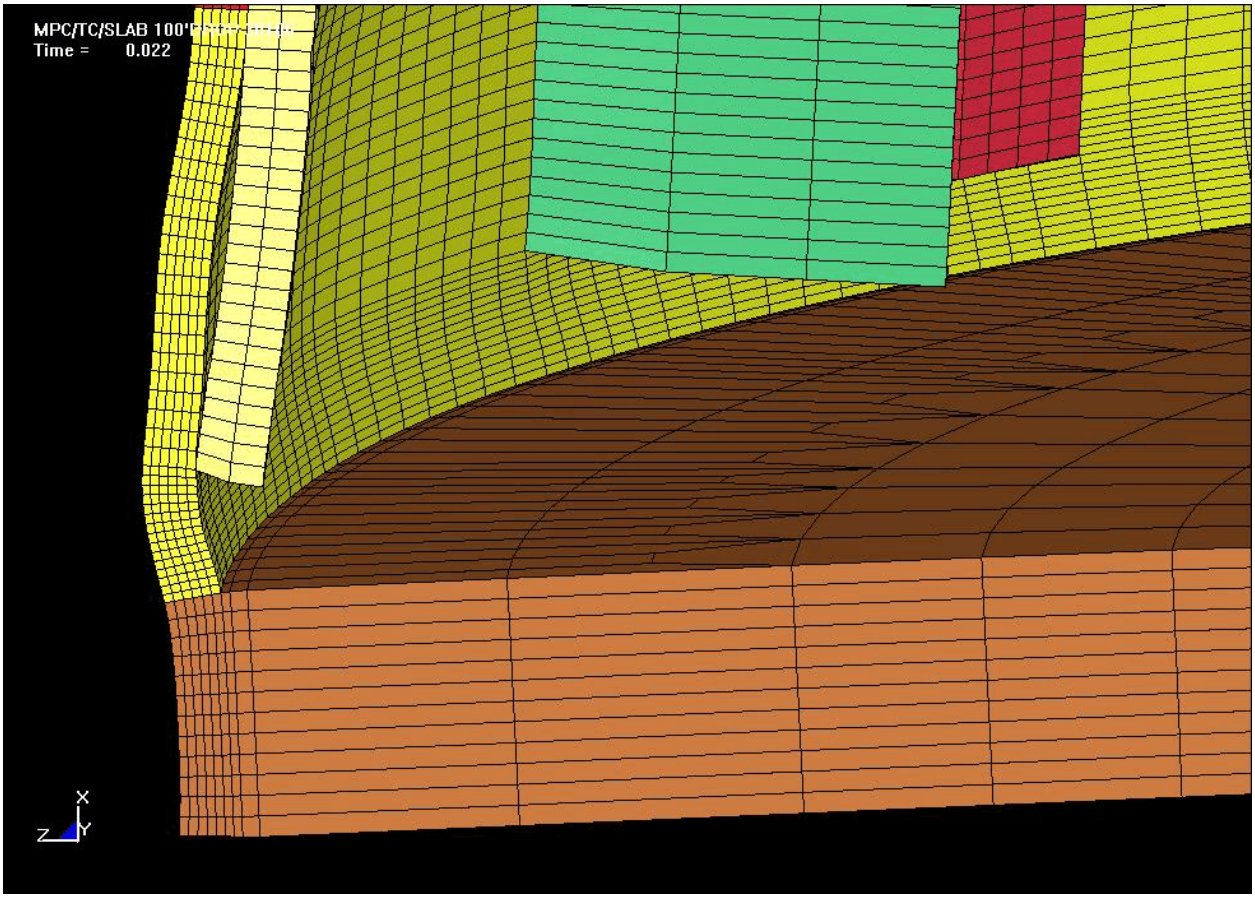

Figure A.7. Deformation of the MPC Shell and Basket Supports at 0.022 seconds for the 100-foot Drop of the Transfer Cask onto the Concrete Floor

Figure A.8 is a plan view of a horizontal section through the MPC shell showing the location of the basket supports. Figure A.9 is an elevation view of the MPC shell, baseplate and basket supports in their undeformed position, and Figure A.10 is the same view at the time of maximum response (0.022 seconds). Figure A.11 shows contours of EPS at the time of maximum response, and when viewed together with Figure A.10 shows that the maximum EPS occurs in the shell at the bottom of the supports. Figure A.12 shows the EPS contours along the back of the shell. Both Figures A.11 and A.12 show that the maximum strains occur in the MPC shell region between the bottom of the basket supports and the baseplate. Away from the bottom region of the MPC shell, strains diminish rapidly to very small values.

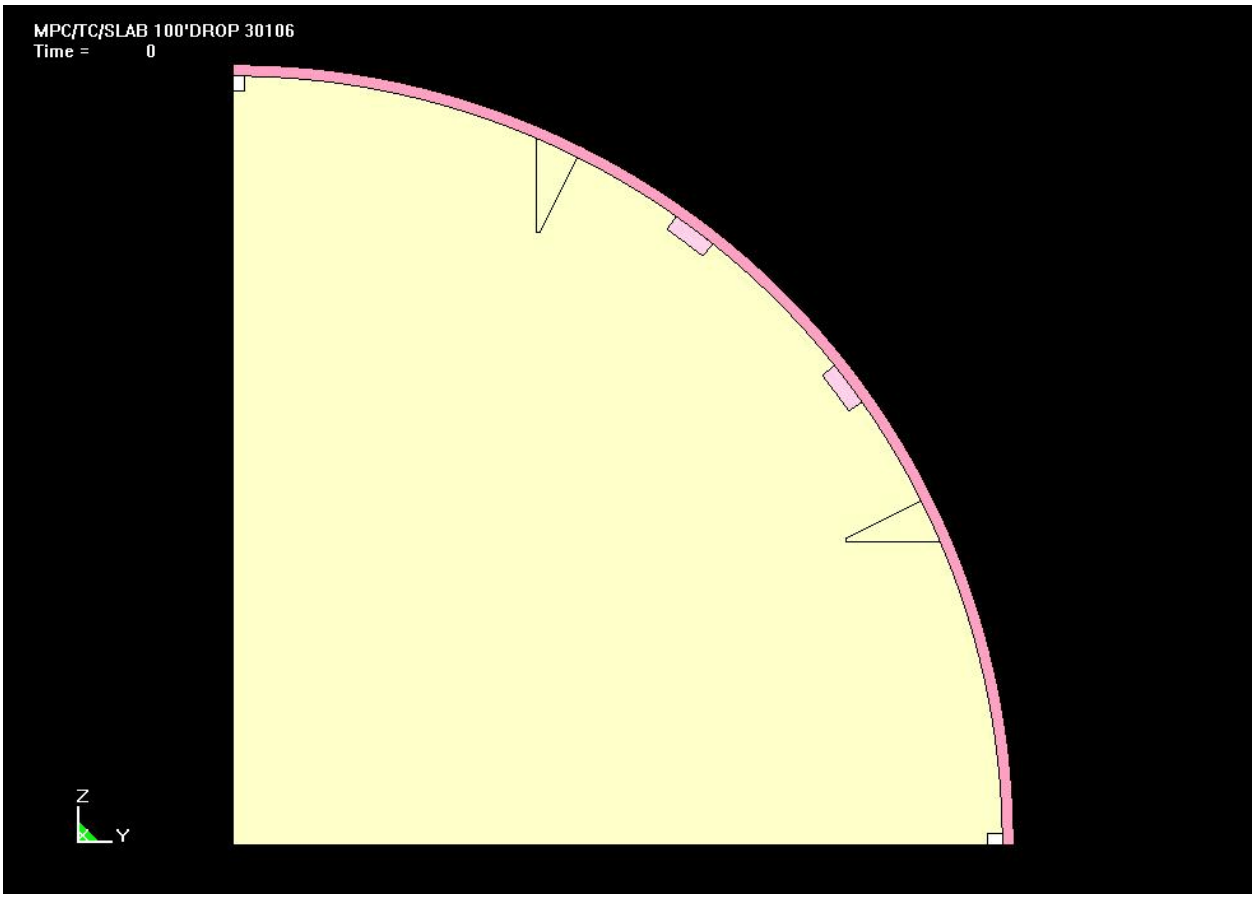

Figure A.8. Plan view of a horizontal section through the MPC shell showing the location of the basket supports

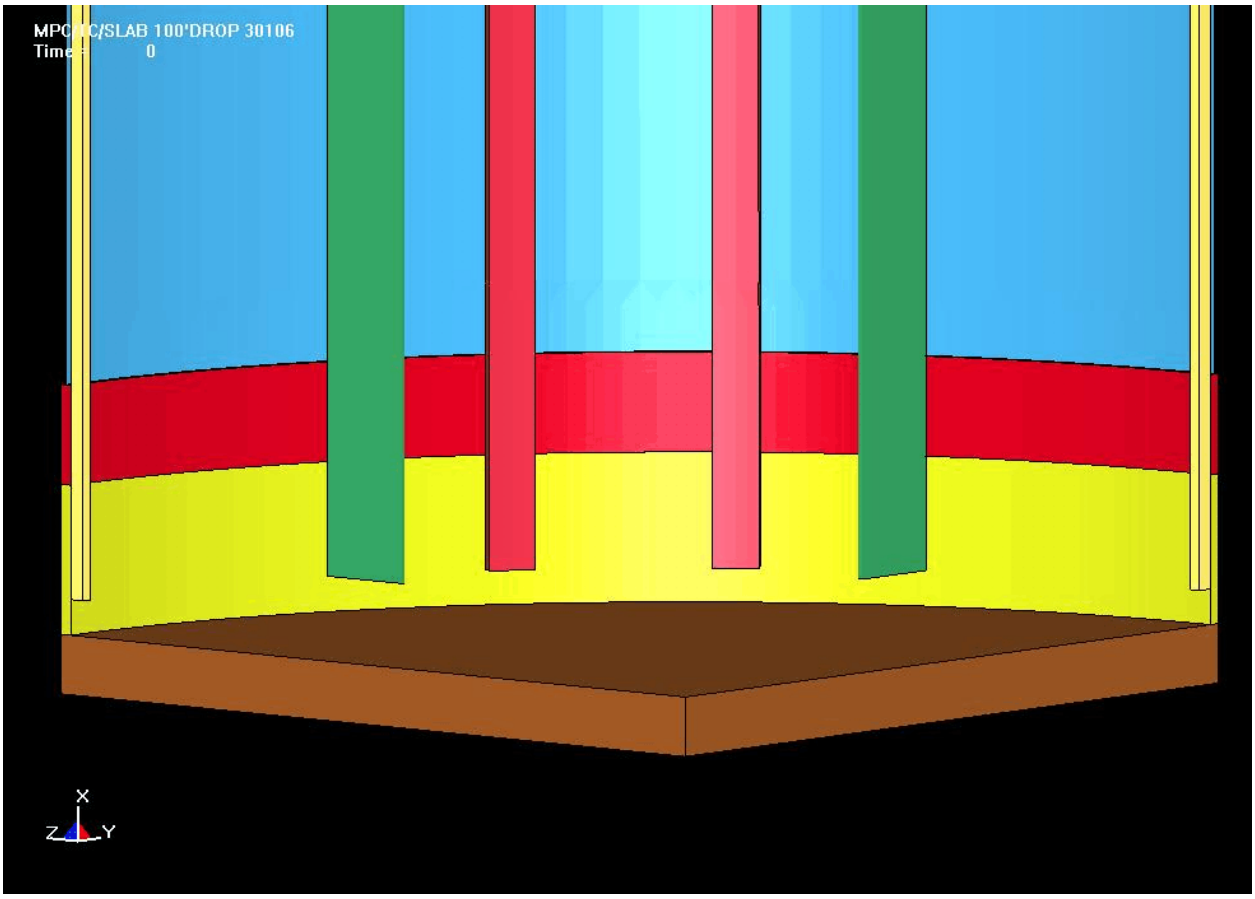

Figure A.9. Elevation View of the MPC Shell, Baseplate, and Basket Supports In Their Undeformed Positions

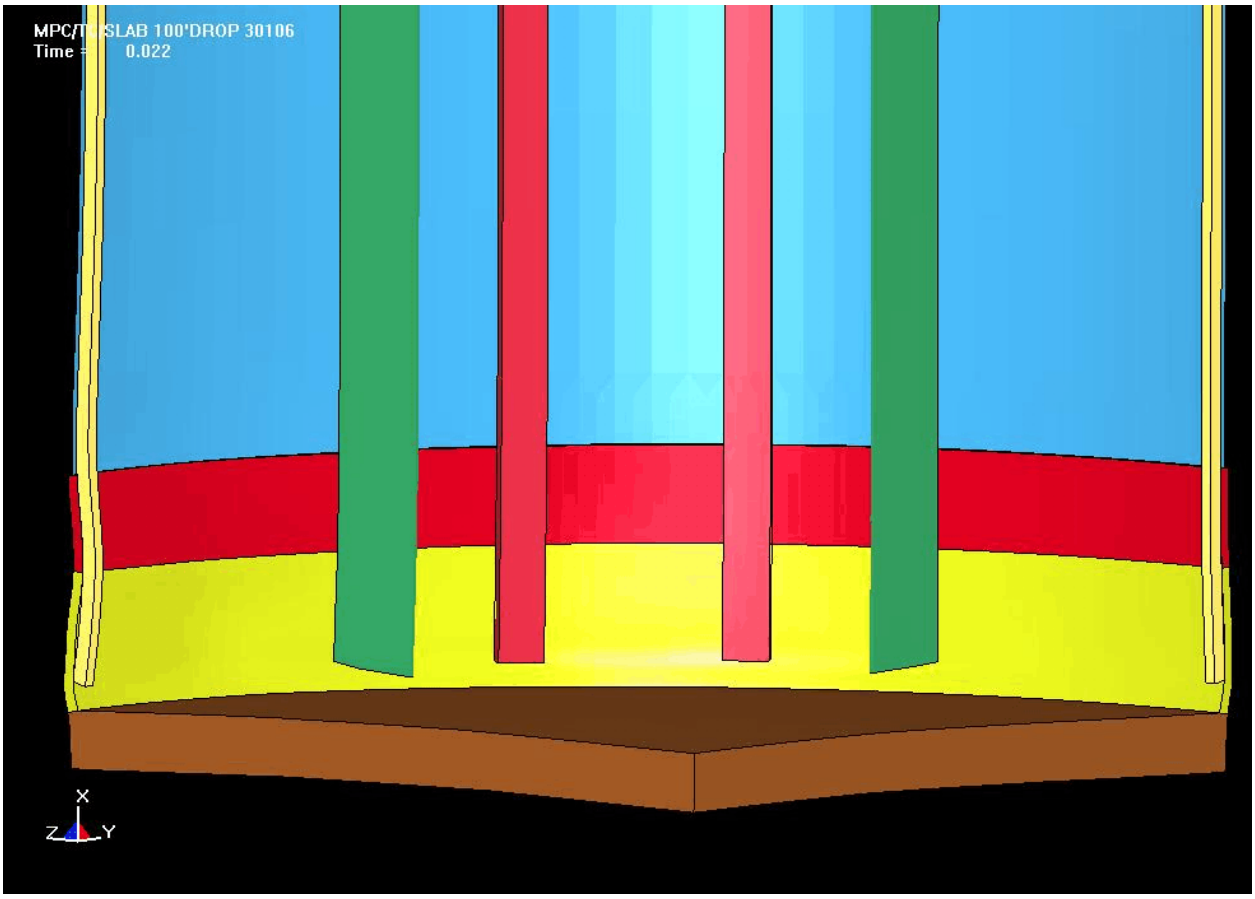

Figure A.10. Elevation View of the MPC Shell, Baseplate, and Basket Supports at 0.022 seconds (100-Foot Drop)

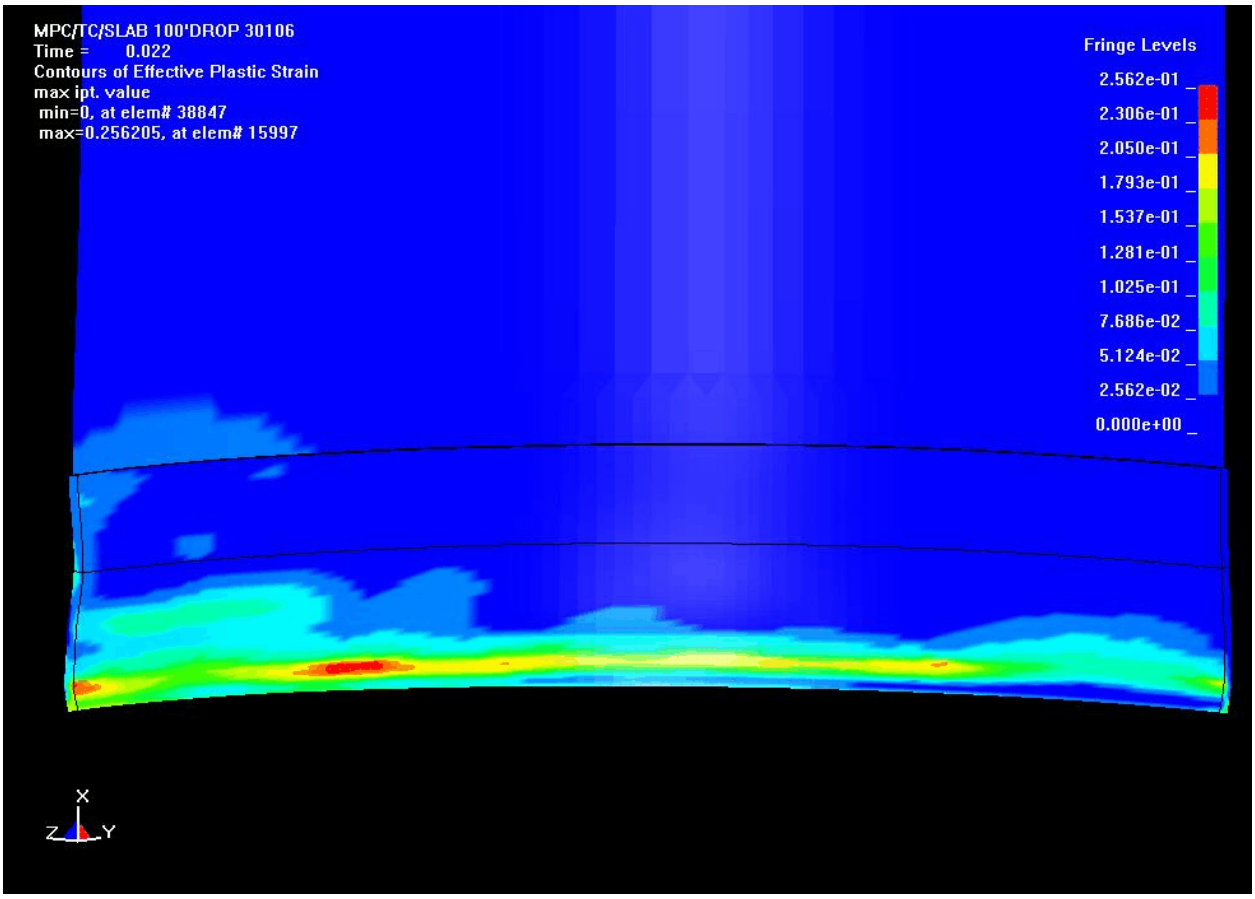

Figure A.11. Contours of EPS on the Interior of the MPC Shell at the Time of Maximum Response (0.022 seconds) (100-Foot Drop)

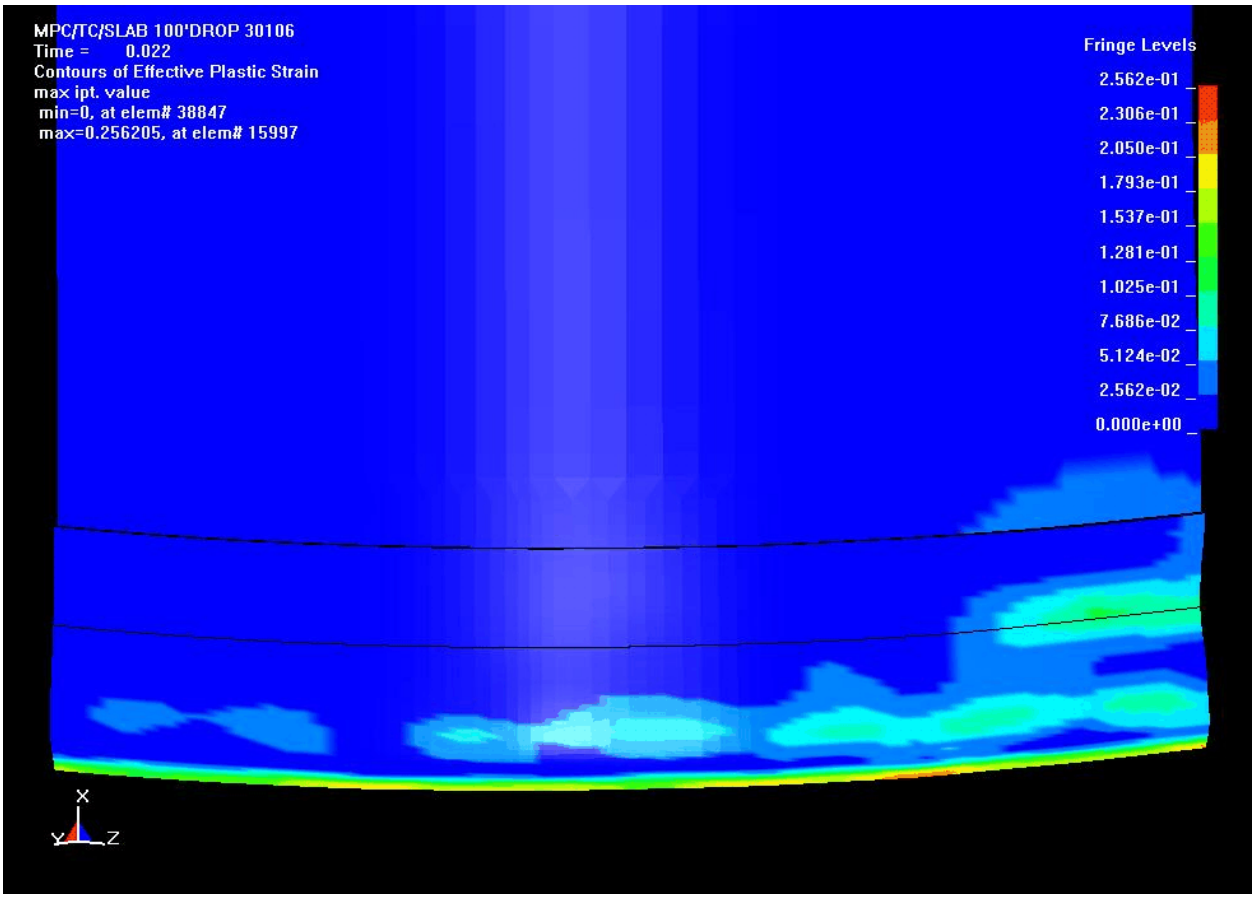

Figure A.12. Contours of EPS on the Exterior of the MPC Shell at the Time of Maximum Response (0.022 seconds) (100-Foot Drop)

Figure A.13 is a close up view of Figure A.11 showing the location of the element with the maximum EPS (Element 15997) and Element 9421 at the junction of the shell and baseplate on the plane of symmetry. Figure A.14 is a vertical section through the MPC shell at the location of Element 15997 and the maximum EPS. Element 15997 is on the inside surface of the shell and Element 15577, also shown in the figure, is on the outside surface at the same elevation. Figure A.15 shows the time history of EPS in each element through the thickness at this location. The figure shows how rapidly the plastic strains diminish from a maximum of 0.256 in/in on the inner surface to a minimum of 0.040 in/in at the outer surface. Figure A.16 shows the time history of EPS in each element through the thickness between Elements 9445 and 9025 at the bottom of the shell where it joins the baseplate on the same vertical section as shown in Figure A.14. Figure A.16 shows that the EPS in Element 9025, which is at the location of the MPC shell to baseplate weld, is 0.220 in/in, which is close to the maximum EPS.

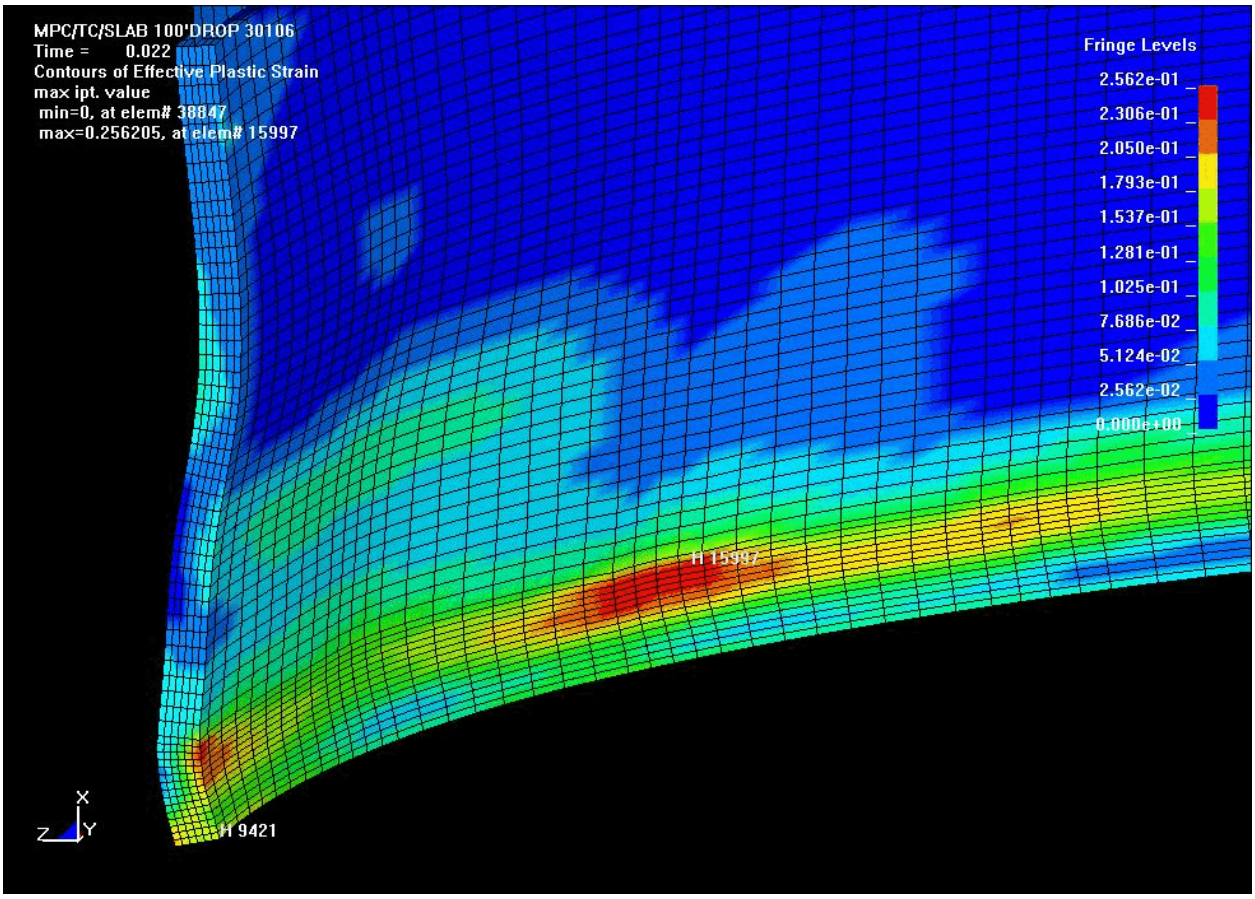

Figure A.13. Close-up View of Figure A.11 Showing the Location of the Element With the Maximum EPS (Element 15997) and Element 9421 at the Junction of the Shell And Baseplate on the Plane of Symmetry (100-Foot Drop)

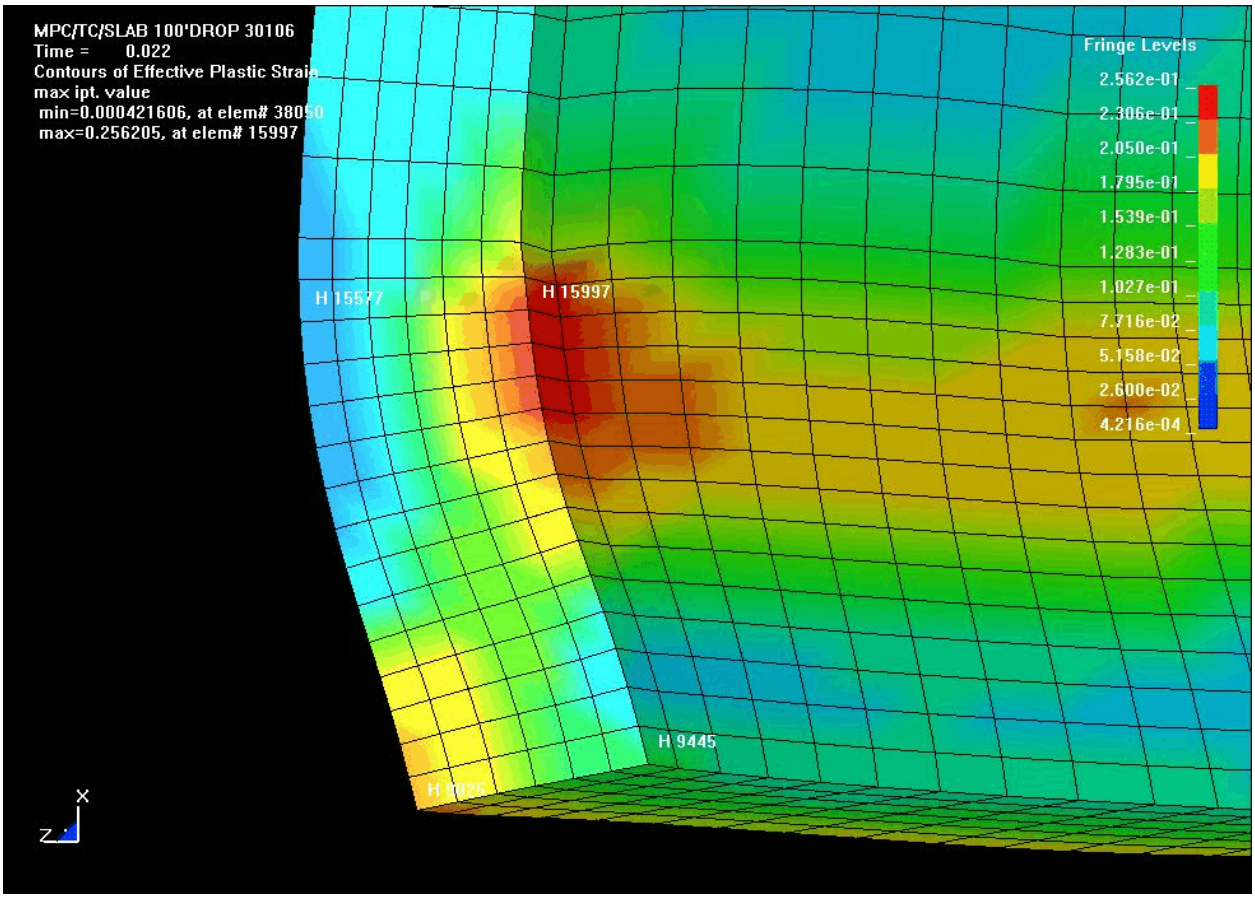

Figure A.14. Vertical Section through the MPC Shell at the Location of Element 15997 and the Maximum EPS (100-Foot Drop)

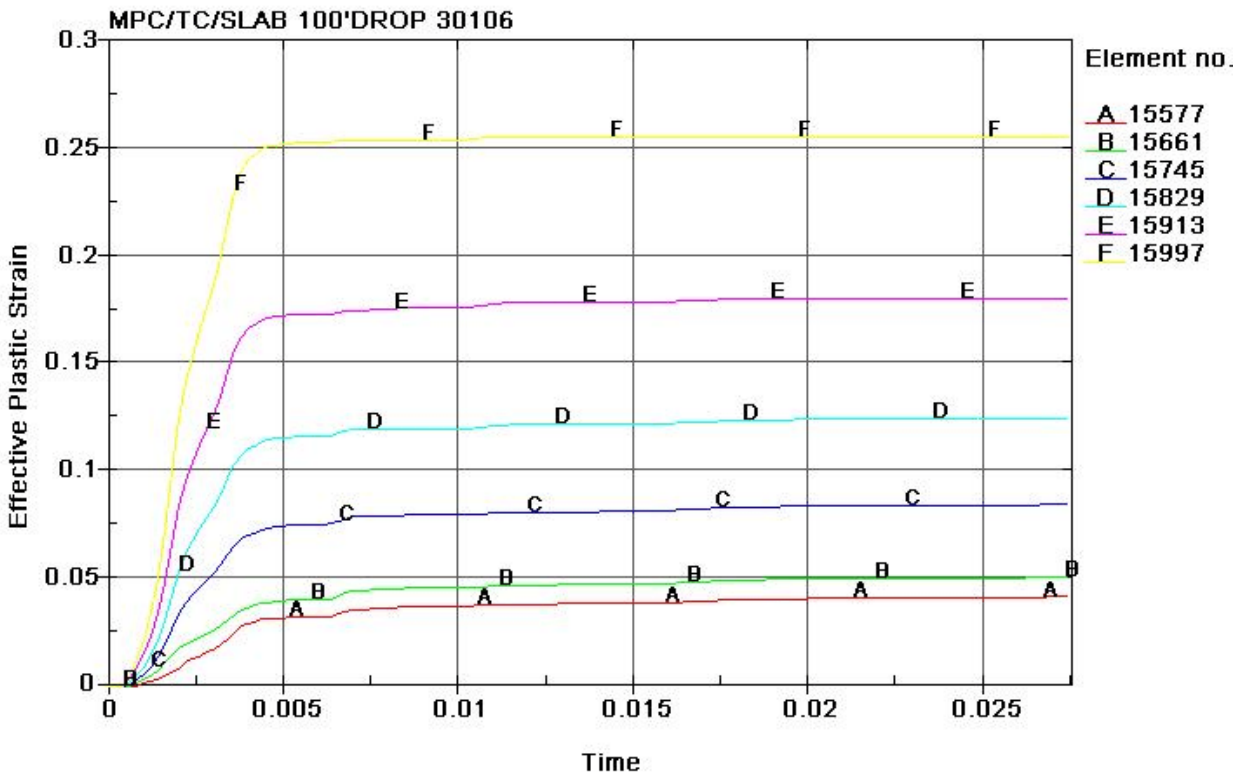

Figure A.15. Time History of EPS in Each Element Through the Thickness At the Location of the Maximum EPS (100-Foot Drop)

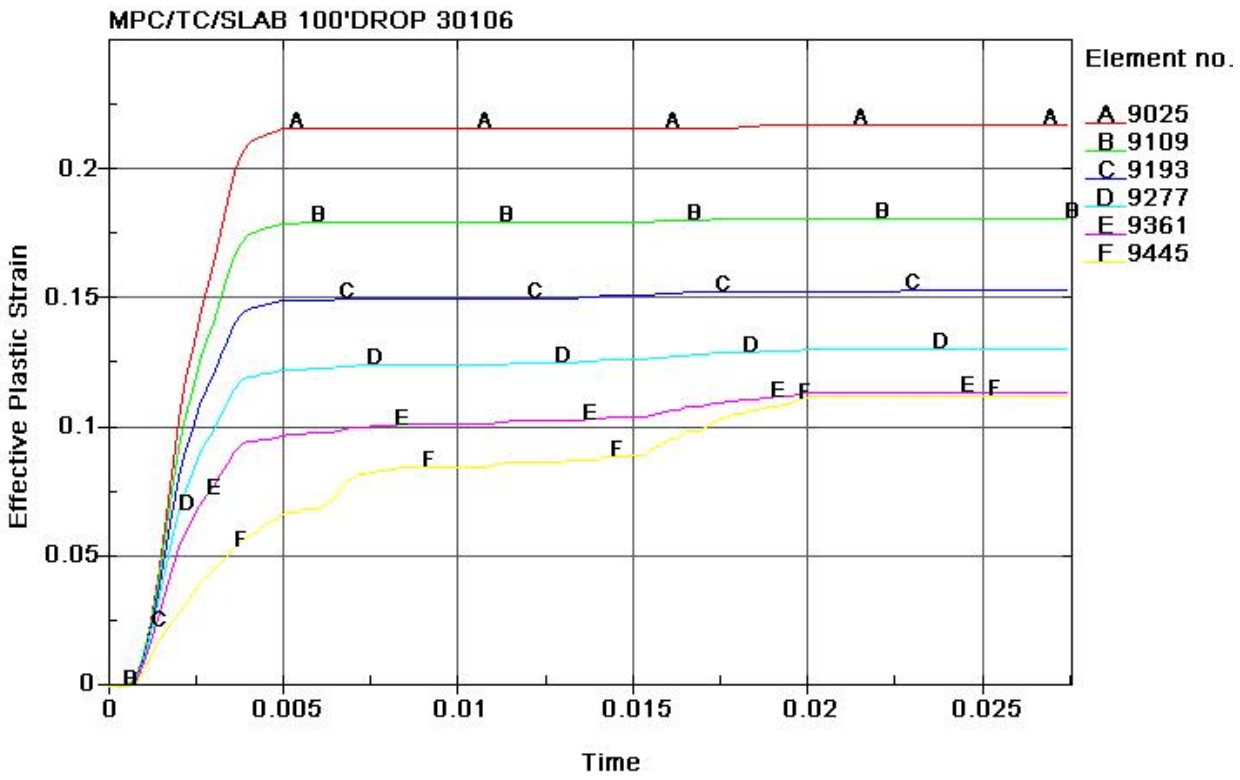

Figure A.16. Time History of EPS in Each Element Through the Shell Thickness At the Location of the MPC Baseplate on the Vertical Section Shown in Figure A.14 (100-Foot Drop)

In Table A.3, it is tempting to compare the maximum EPS in the element to the true strain at failure. Such a comparison, however, is not an accurate predictor of margin against element failure because these two strain measures, (i.e., calculated maximum EPS and true strain at failure), are each derived from different states of stress and must be adjusted by a Triaxiality Factor before a meaningful comparison can be made. The derivation of the Triaxiality Factor and its application to predicting material failure in the MPC is discussed in Appendix B.

A.4.4 Question 4

Analyze the vertical drop of the transfer cask containing a sealed MPC falling onto the storage overpack at ground elevation from heights of 1.5, 12.2, and 24.4 meters (5, 40, and 80 feet). Determine the magnitude and location of maximum stresses/strains in the MPC.

To respond to this question, dynamic analyses using LS-DYNA were performed for the accidental vertical drop of the transfer cask onto the storage overpack, while the transfer cask is being lowered from the operating floor to the ground floor. The maximum drop height corresponds to the distance between the operating floor and the top of the storage overpack, which could be up to 24.4 meters (80 feet). Several drop heights up to the maximum height were analyzed.

The finite element model of the transfer cask (transfer overpack, MPC, and internals), utilized for this drop case, is the same model used in the response to Question 3 except for the MPC, which did not include the modifications stated above. A finite element model of the storage overpack was also developed and placed beneath the transfer cask model. A quarter model representation of the storage overpack was created to be consistent with the quarter model transfer cask. The storage overpack model consists of a 68 cm (26.8 inches) thick concrete cylinder with steel plates on the top, inside, and outside surfaces of the concrete wall. The concrete and steel plates are modeled using brick type finite elements. The material model and properties for the concrete cylinder are the same as those described in the response to Question 3. The material model and properties for the steel plates are taken at room temperature. The bottom of the storage overpack is restrained in the model. This is slightly conservative, since it is actually resting on the concrete floor that is supported by a concrete wall beneath the floor.

The drop heights selected for analysis were 1.52, 12.2, and 24.4 meters (5, 40, and 80 feet). The MPC stainless steel material properties correspond to a temperature of 237 °C (459 °F), which is the temperature used by the manufacturer for the design of the MPC. The structural response of the MPC is presented in Table A.4.

Table A.4. Structural Response of MPC

Drop Height m (ft)	[1]Max. EPS at Element 9421 (Azimuth = 0) cm/cm (in/in)
1.52 (5)	0.0363 [2]
12.2 (40)	0.0601 [2]
24.4 (80)	0.0976 [2]

[1] EPS is the effective plastic strain; Element 9421 is the first MPC vertical brick element at the plane of symmetry.

[2] The drop of the transfer cask onto the storage overpack is a softer impact than the drop of the transfer cask onto the concrete floor. Therefore, the resulting strain in the MPC for this drop is less at the higher (12.2 and 24.4 meters) drop heights than for the drop onto the concrete floor. The result for the 1.52 meters drop is larger than the result for the 1.52 meters drop onto the concrete floor because (a) the difference in target stiffness has less effect at lower drop heights, and (b) the modifications to the model discussed in response to Question 3 were not made to this model because it produced very conservative results that were bounded by the 12.2, 21.3, and 30.5 meters drops onto the concrete floor.

A.4.5 Question 5

Determine the magnitude and location of maximum stresses/strains in the MPC when a sealed MPC vertically falls 5.8 meters (19 feet) into the storage overpack.

Such an event could occur during the transfer of the MPC from the transfer overpack to the storage overpack.

When the MPC is moved from the transfer overpack to the storage overpack (Stage 21), it could possibly fall a maximum of 5.8 meters (19 feet). This load drop is analyzed using a finite element model.

Model Development

The finite element model includes the MPC, storage overpack inner shell, storage overpack vertical channel sections, and the storage overpack bottom lid (which serves as the target plate). The analysis strategy and the finite element models of the MPC, fuel assemblies, fuel basket and fuel basket support are the same as those used in response to Question 3. These components are shown in Figures A.17 and A.18. The FEM shown in Figure A.17 is a quarter-model representation of the cask system (due to symmetry about two vertical planes). Figure A.18 shows a close-up view at the MPC connection to the MPC bottom baseplate at the plane of symmetry. The fuel basket plate on the plane of symmetry has been removed, so that the fuel assemblies within the basket compartments can be seen.

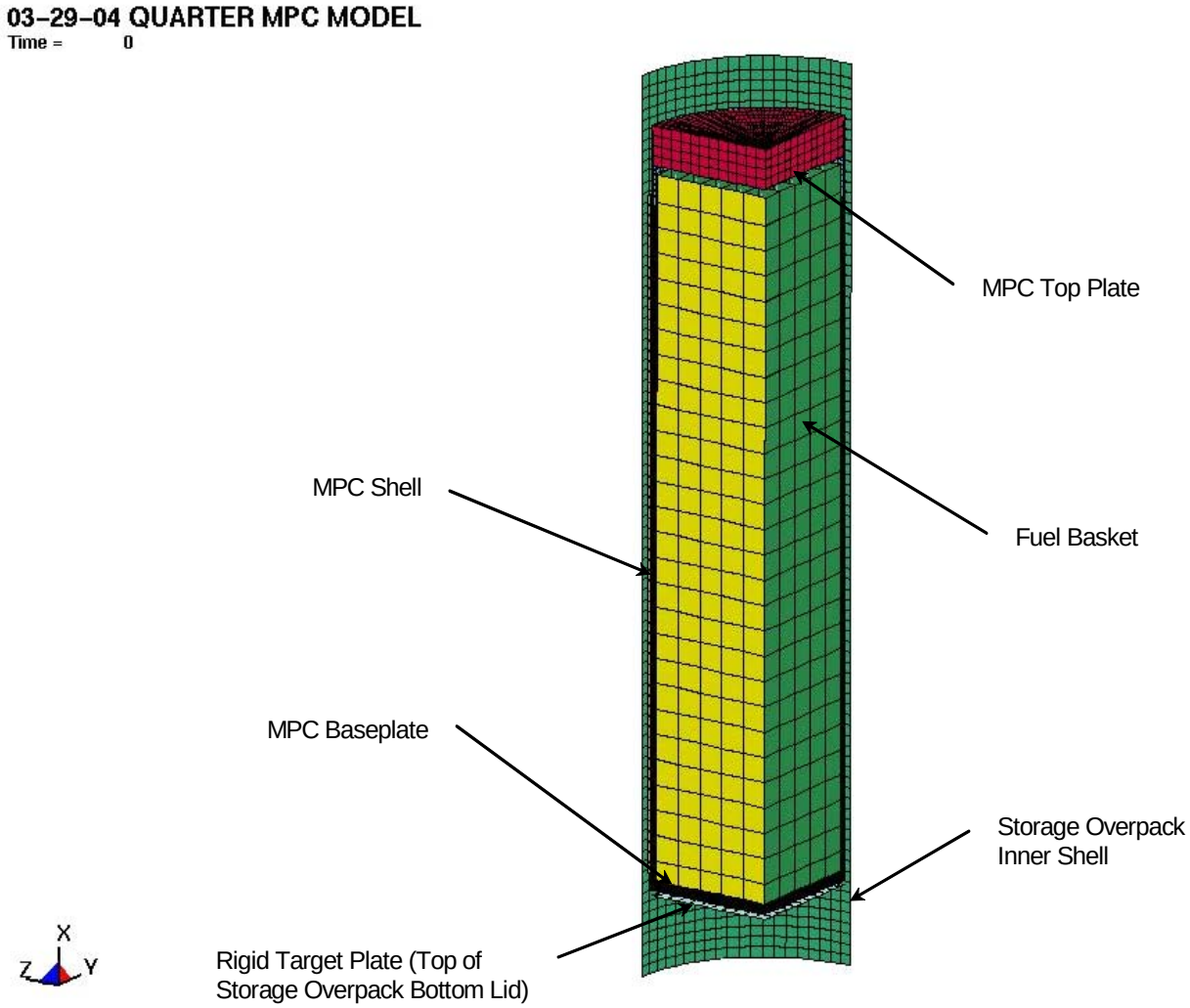

Figure A.17. Finite Element Model of the MPC for 19-Foot Drop into Storage Overpack

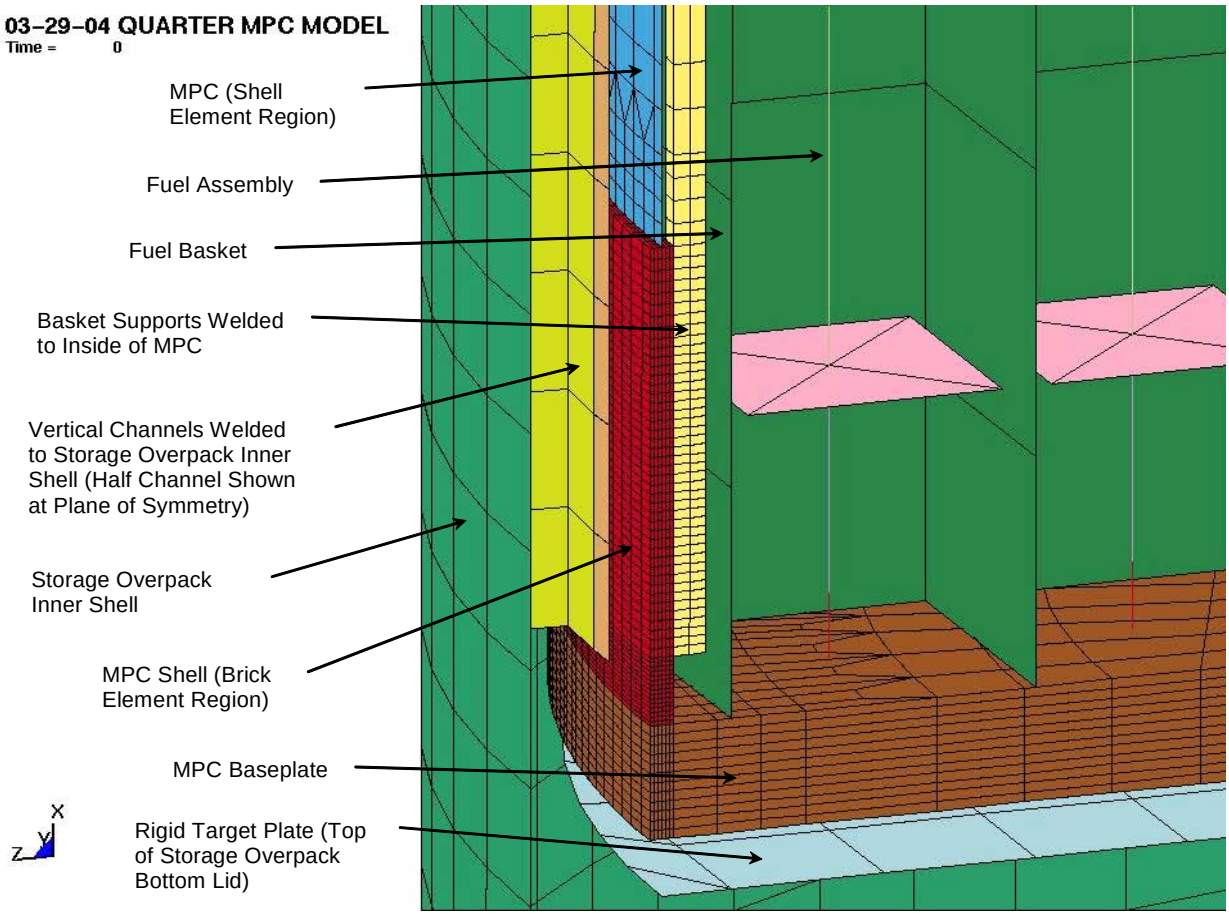

Figure A.18. MPC 19-Foot Drop into Storage Overpack.
View of Model at MPC Shell Wall Connection to Baseplate at Plane of Symmetry

The top plate of the storage overpack bottom lid is modeled as a rigid target plate for the vertical impact of the MPC and its internal components. The target plate is fully restrained in the model for the following reasons:

- The storage overpack bottom lid is considered to be rigid since it is constructed from a 12.7-cm (5-inch) top plate, a 5.1-cm (2-inch) bottom plate, and 43.2 cm (17 inches) of confined concrete between the plates.
- The storage overpack rests on a reinforced concrete floor supported by a reinforced concrete wall beneath the floor. The assumption of a rigid target plate for this drop scenario is conservative.

The storage overpack vertical wall is modeled using a rigid shell to represent the storage overpack inner steel shell, which surrounds the MPC shell wall. The vertical channels, which are welded to the storage overpack inner shell, are included in the model using shell elements. The gap between the channel webs and the MPC shell wall is included in developing the model.

For this drop scenario, a dynamic analysis was performed using LS-DYNA. The MPC and internal components rest on the target plate at the start of the analysis, and the drop height was simulated by introducing an initial velocity that was calculated using the following expression:

$$V = \sqrt{2gh} \qquad (A.18)$$

where: V = velocity
g = gravitational acceleration
h = drop height.

To permit the insertion of the MPC into the storage overpack, the cask design specified a gap between the MPC shell wall and the inner radius of the vertical channel sections welded to the storage overpack inner shell. If the MPC impacts the bottom lid of the storage overpack in the center, there would be a uniform gap equal to 1.67 cm (0.657 inches) based on average construction tolerances or a uniform gap of 2.18 cm (0.859 inches) based on maximum construction tolerances. Under this configuration, when the MPC shell deforms radially by an amount greater than the uniform radial gap, the channel sections attached to the storage overpack provide resistance to further radial deformation. For the analysis reported herein, a worst case assumption was made that during the accidental drop of the MPC, it may land completely to one side of the storage overpack bottom lid. This creates a maximum gap on the opposite side equal to approximately 3.34 cm (1.313 inches) based on average construction tolerances. This off-center drop location is simulated in the analysis by removing from the computer model the contact definition between the MPC shell and the storage overpack channel sections. This permits the MPC shell to deform radially outward without the resistance provided by the channel sections. In this way, the analysis can provide an estimate of the effect of an off-center drop.

Analysis Results

Figure A.19 shows the displacement of the MPC shell and basket support on the xz plane of symmetry at the time of maximum displacement (0.005 seconds). Figures A.20 and A.21 are plots of radial (z) and vertical (x) displacements at the three nodes located on the MPC shell in Figure A.19. The maximum radial displacement is less than the maximum gap of 3.34 cm (1.313 inches) and, therefore, no contact occurs between the MPC shell and the channel sections attached to the inside of the storage overpack. The curvature of the shell and basket support, as well as the contact and separation between the shell and support can be clearly seen. In contrast to Figure A.7, where the radial displacement was limited by contact with the transfer overpack, Figure A.19 shows a smoother variation in curvature because radial displacement is allowed to occur freely.

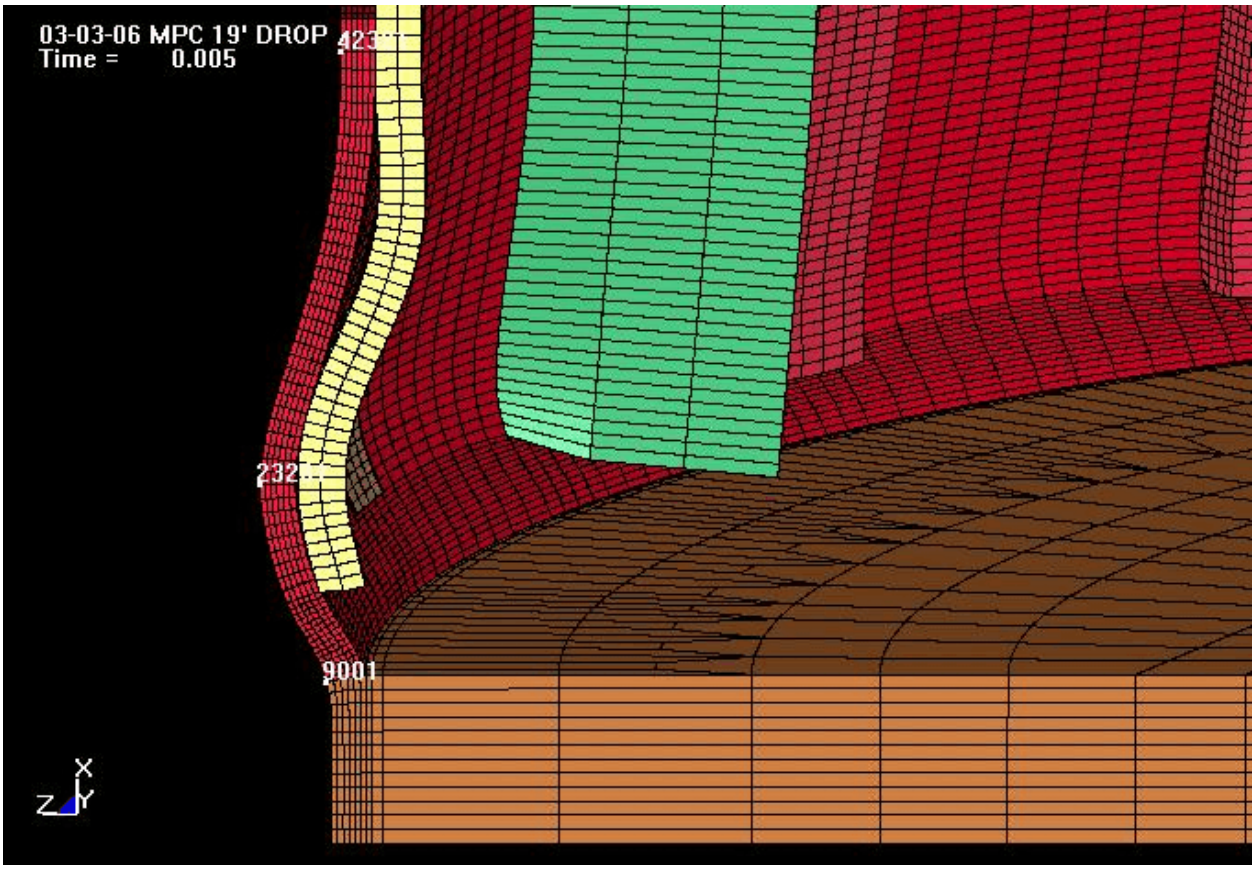

Figure A.19. Displacement of the MPC Shell and Basket Support Along the xz Plane of Symmetry at the Time of Maximum Displacement (0.005 seconds)

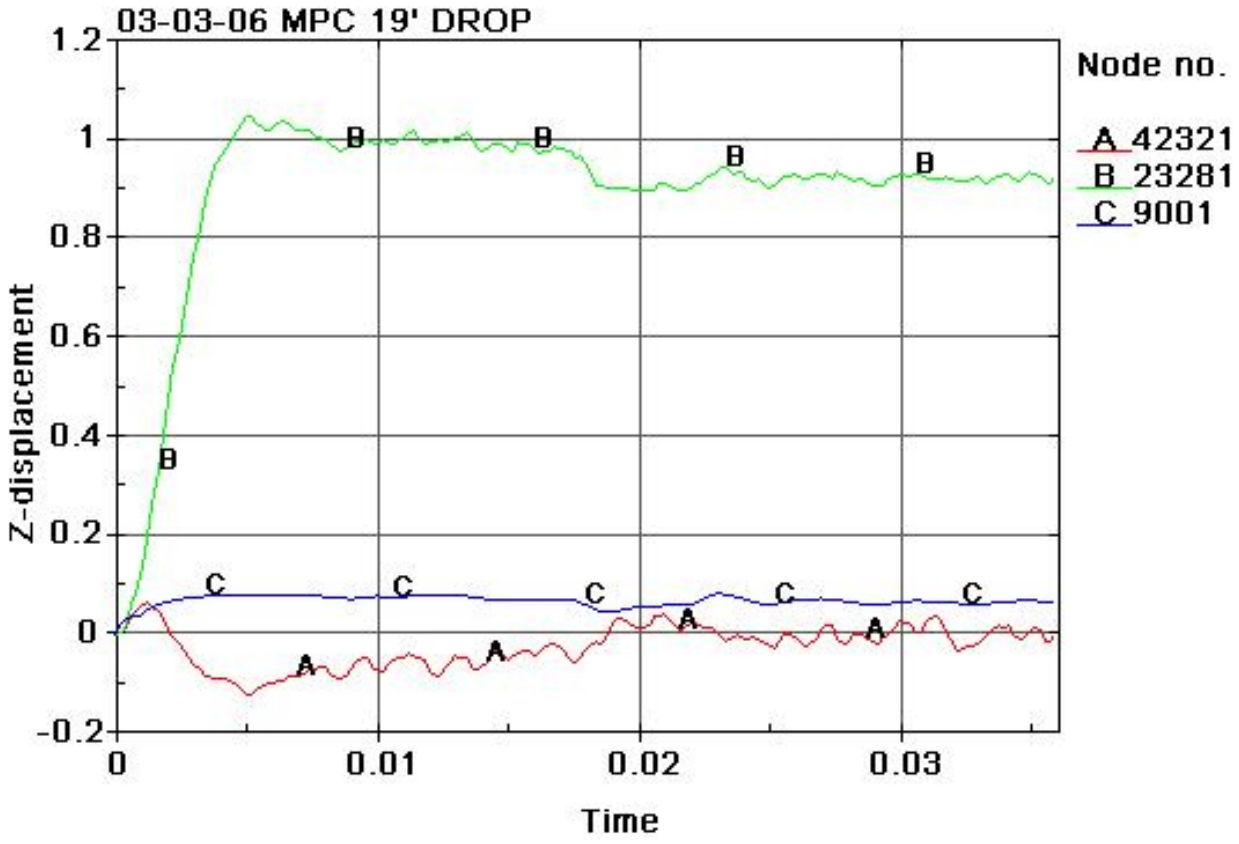

Figures A.20. Plots of Radial (z) Displacement at the Three Nodes Located on the MPC Shell in Figure A.19

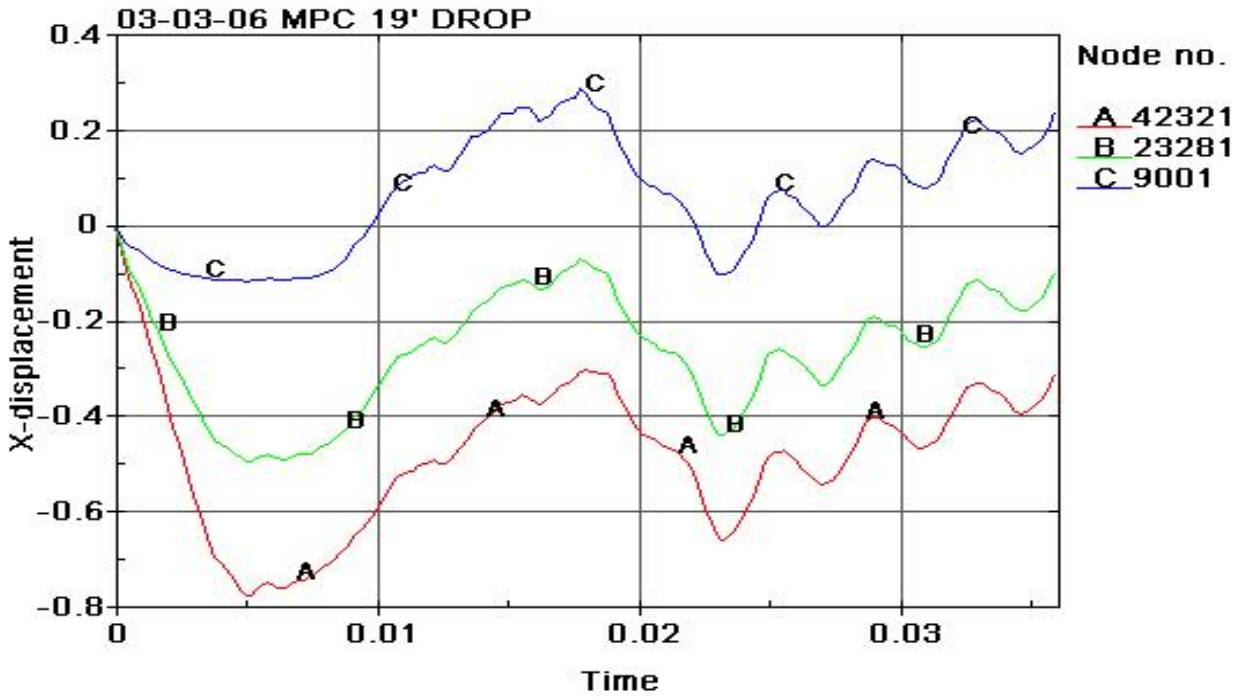

Figures A.21. Plots of Vertical (x) Displacement at the Three Nodes Located on the MPC Shell in Figure A.19

Figure A.22 shows the contours of EPS in the MPC shell, basket supports and baseplate at the time of maximum response, which is the time in Figure A.23 when the kinetic energy of the system is a minimum. Figure A.22 shows that the EPS is 0.459 in/in and occurs in Element 9035. With the basket supports removed, Figures A.24 and A.25 show the location of Element 9035 where the maximum EPS occurs. This element is located at the bottom of the shell on the outside surface within the weld joining the shell to the baseplate. Figure A.26 is the same view as Figure A.25 except the basket support is included and the element mesh is defined.

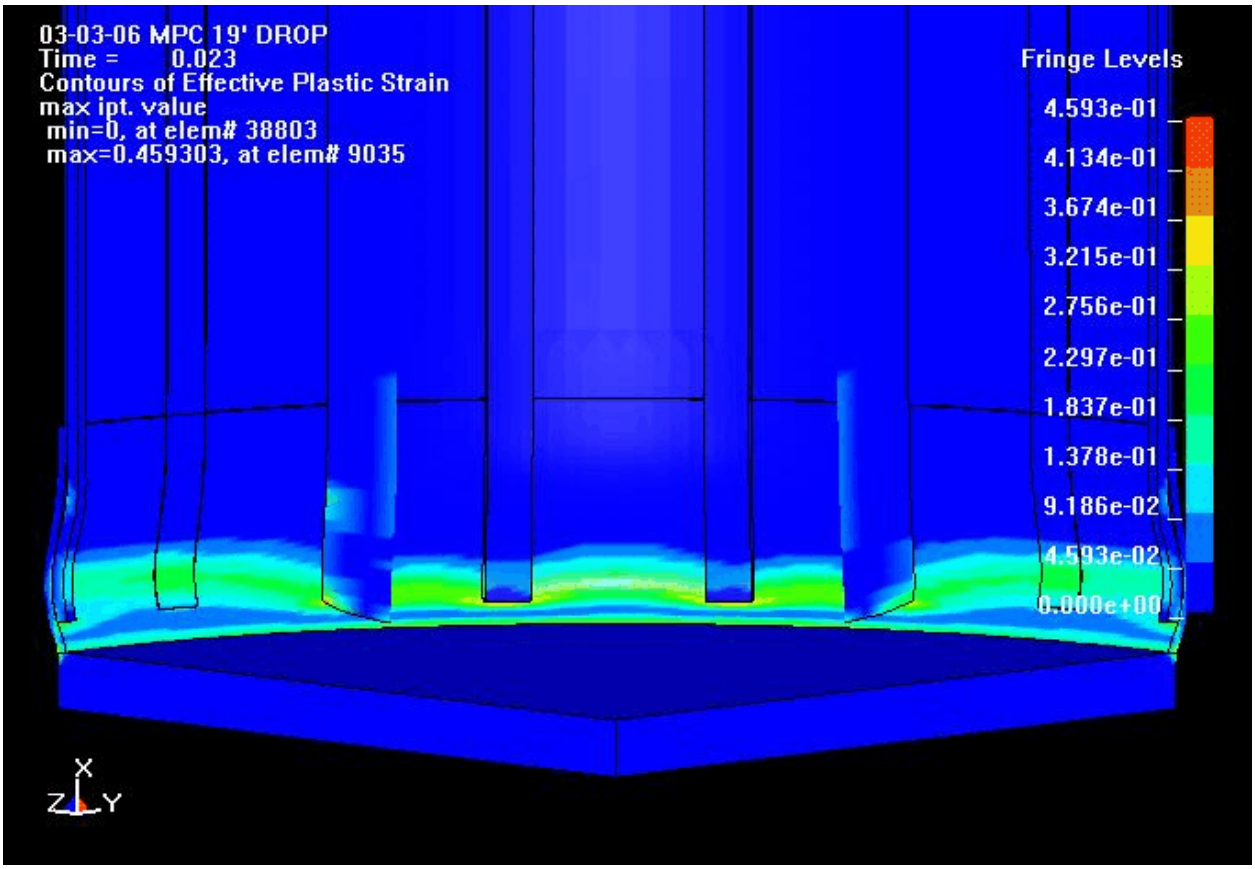

Figure A.22. Contours of EPS in the MPC Shell, Basket Supports, and Baseplate at the Time of Maximum Response, Which Is the Time in Figure A.23 When the Kinetic Energy Is a Minimum

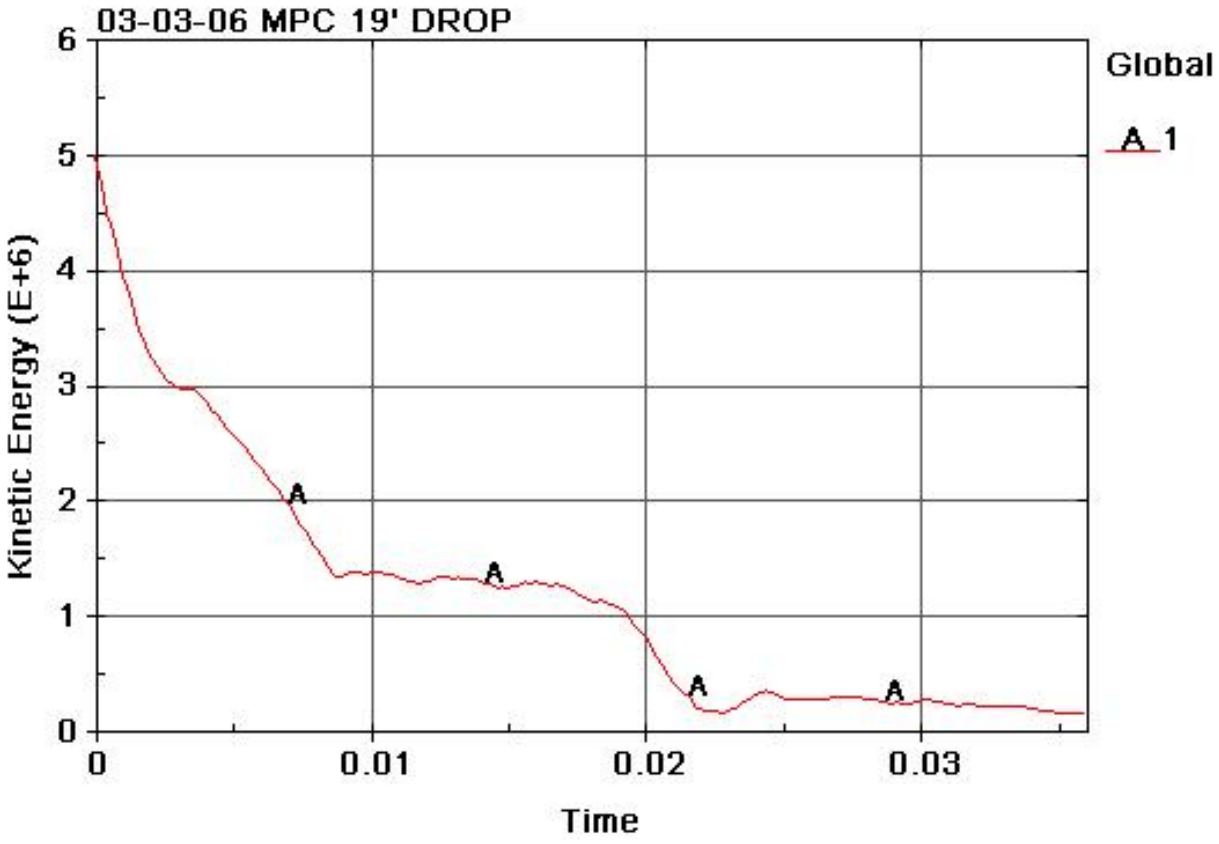

Figure A.23. Global System Kinetic Energy

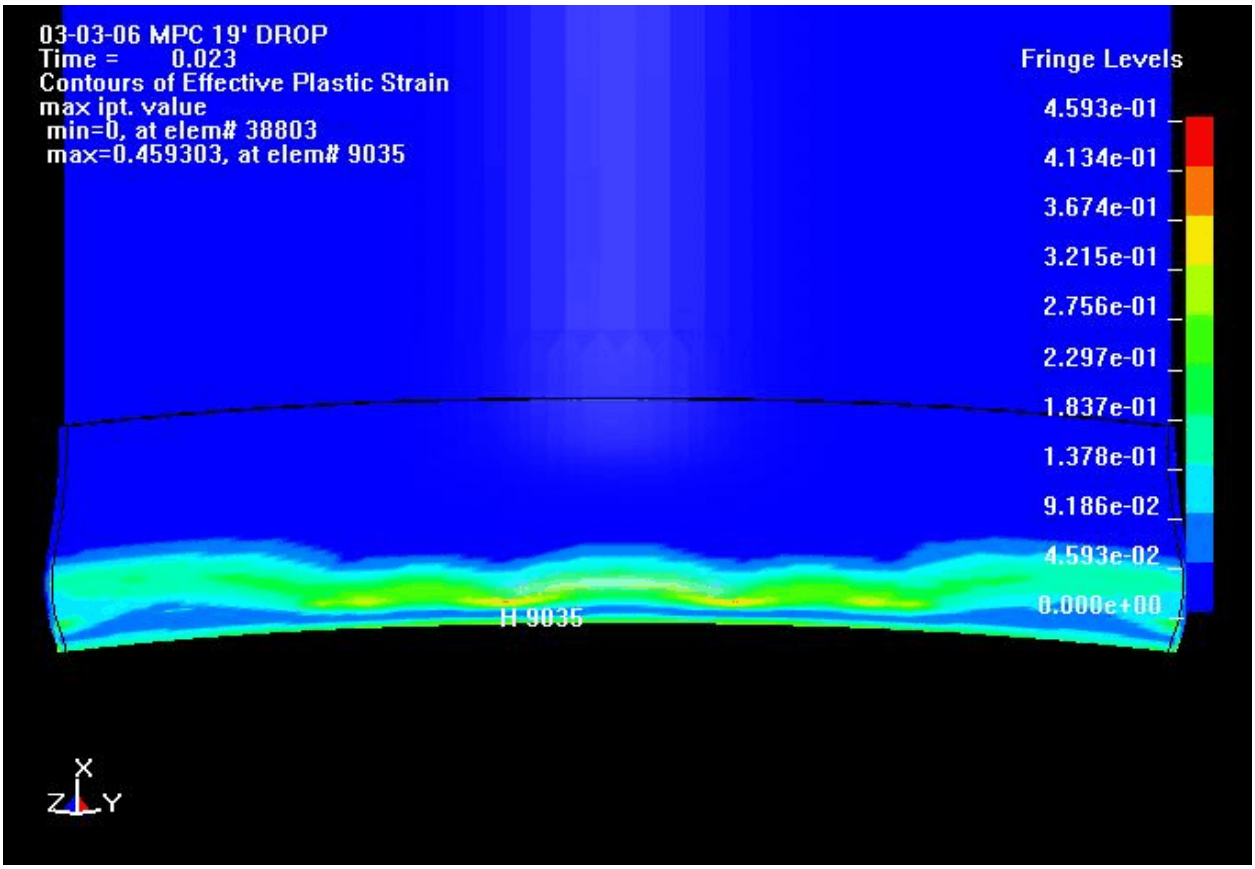

Figure A.24. With the Basket Supports Removed from Figure A22, Figure A.24 Shows the Location of Element 9035 Where the Maximum EPS of 0.459 Occurs

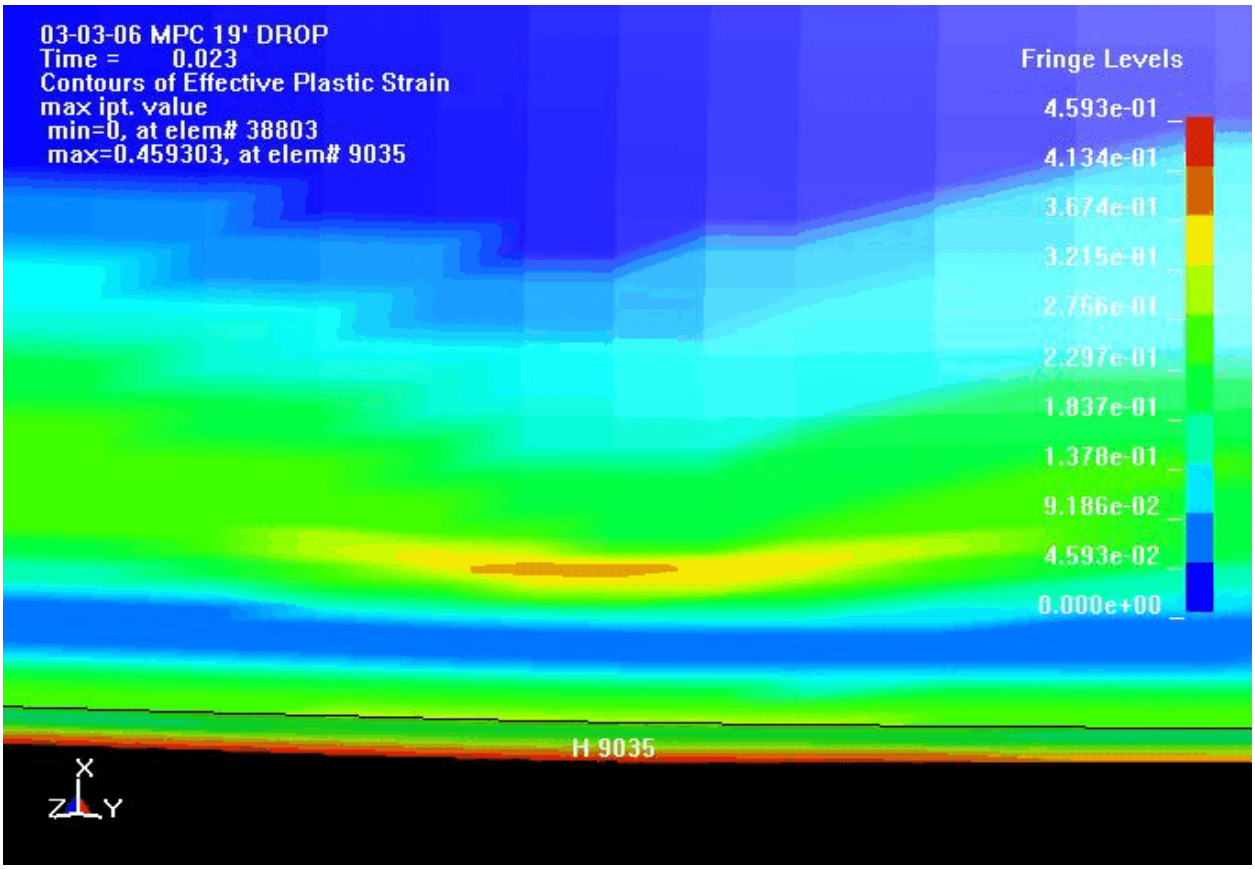

Figure A.25. Closeup View of the Location of Element 9035 On the Bottom Outside Edge of the MPC Shell

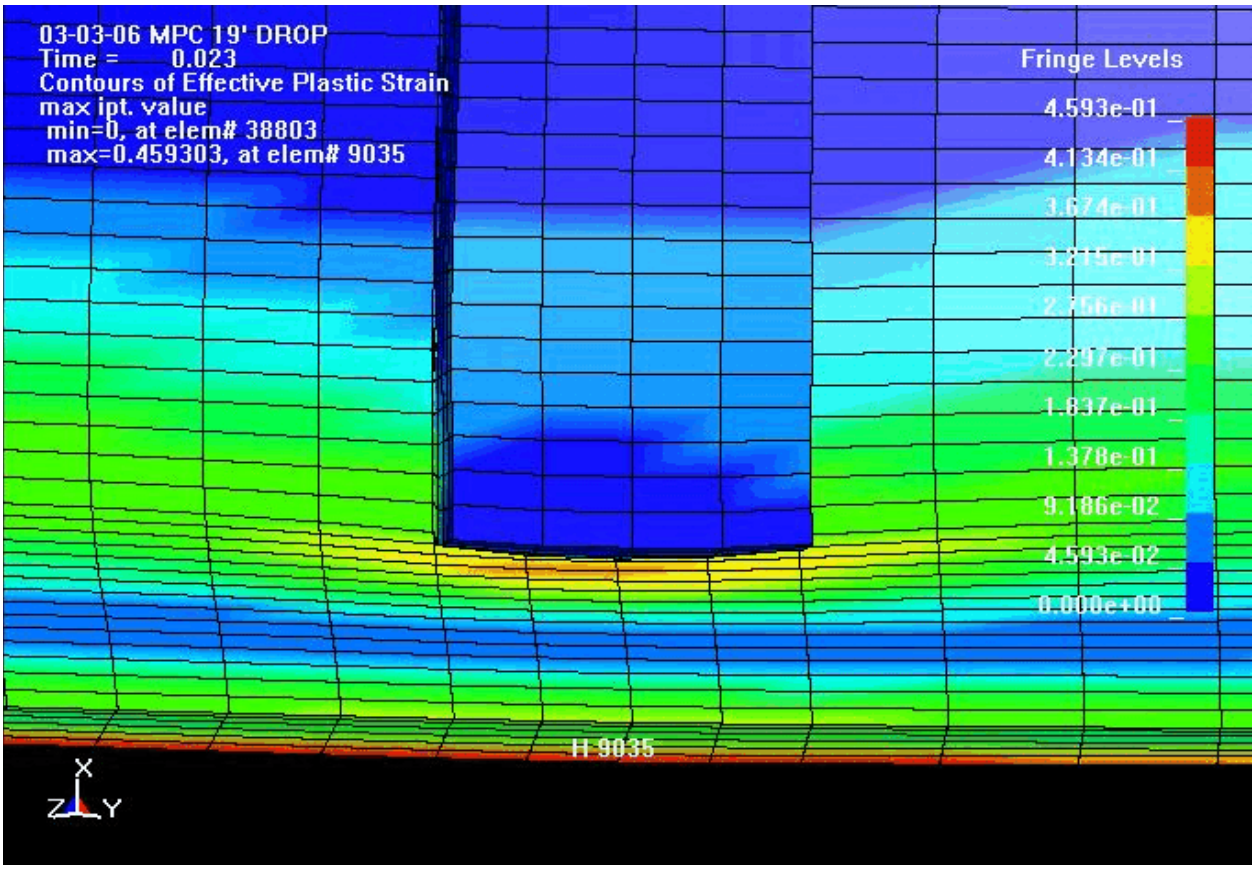

Figure A.26. Same View as Figure A.25
Except the Basket Support Is Included and the Element Mesh Is Defined

Figure A.27 is a vertical section through the shell and baseplate at the location of Element 9035. The figure shows the relative displacement between the shell and basket support. Because the stiffness of the basket support at this location is so much greater than the basket support on the plane of symmetry (Figure A.19) the shell does not separate as much from the basket support between the stitch welds. Figure A.28 is the displacement history of node 20340 shown in Figure A.27, and shows that the maximum radial displacement is about the same as it is on the plane of symmetry.

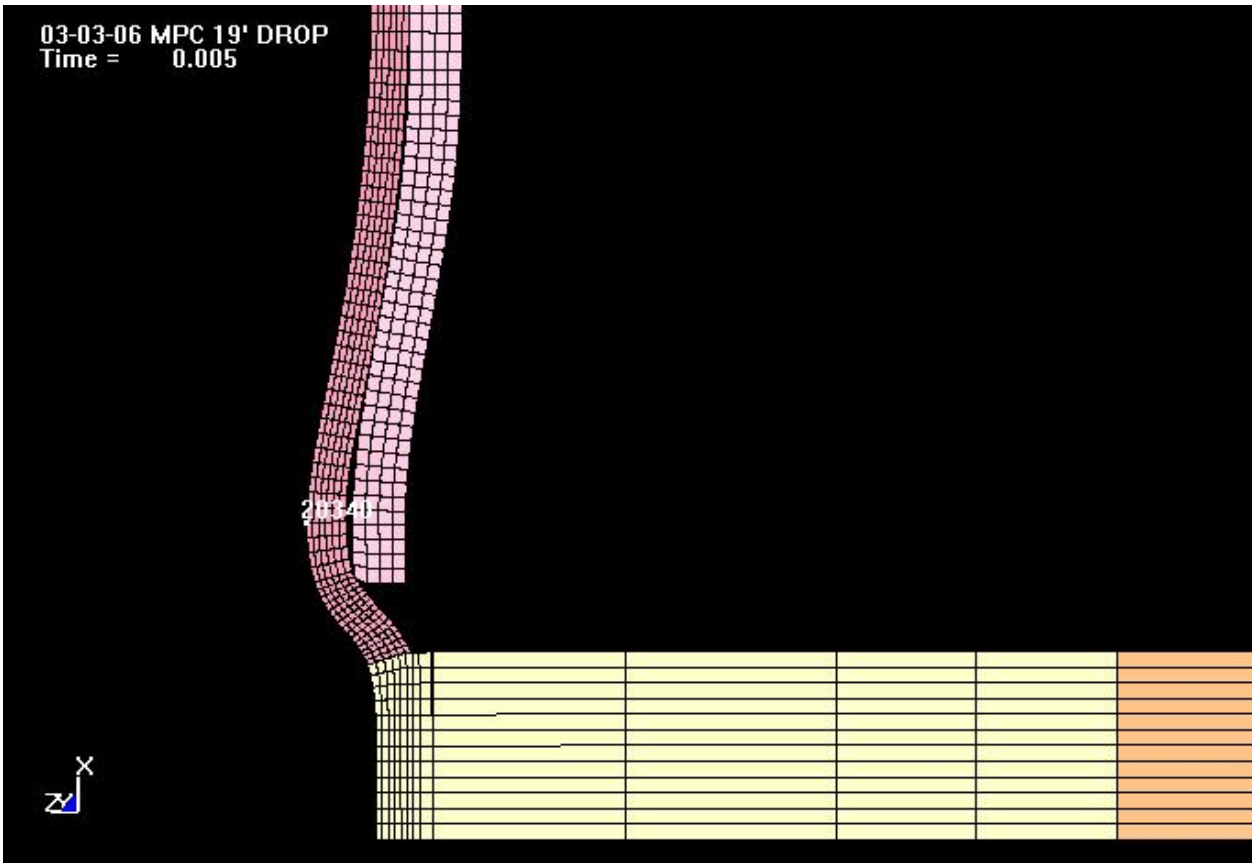

Figure A.27. Vertical Section Through the Shell and Baseplate at the Location of Element 9035 Showing the Relative Displacement Between the Shell and Basket Support

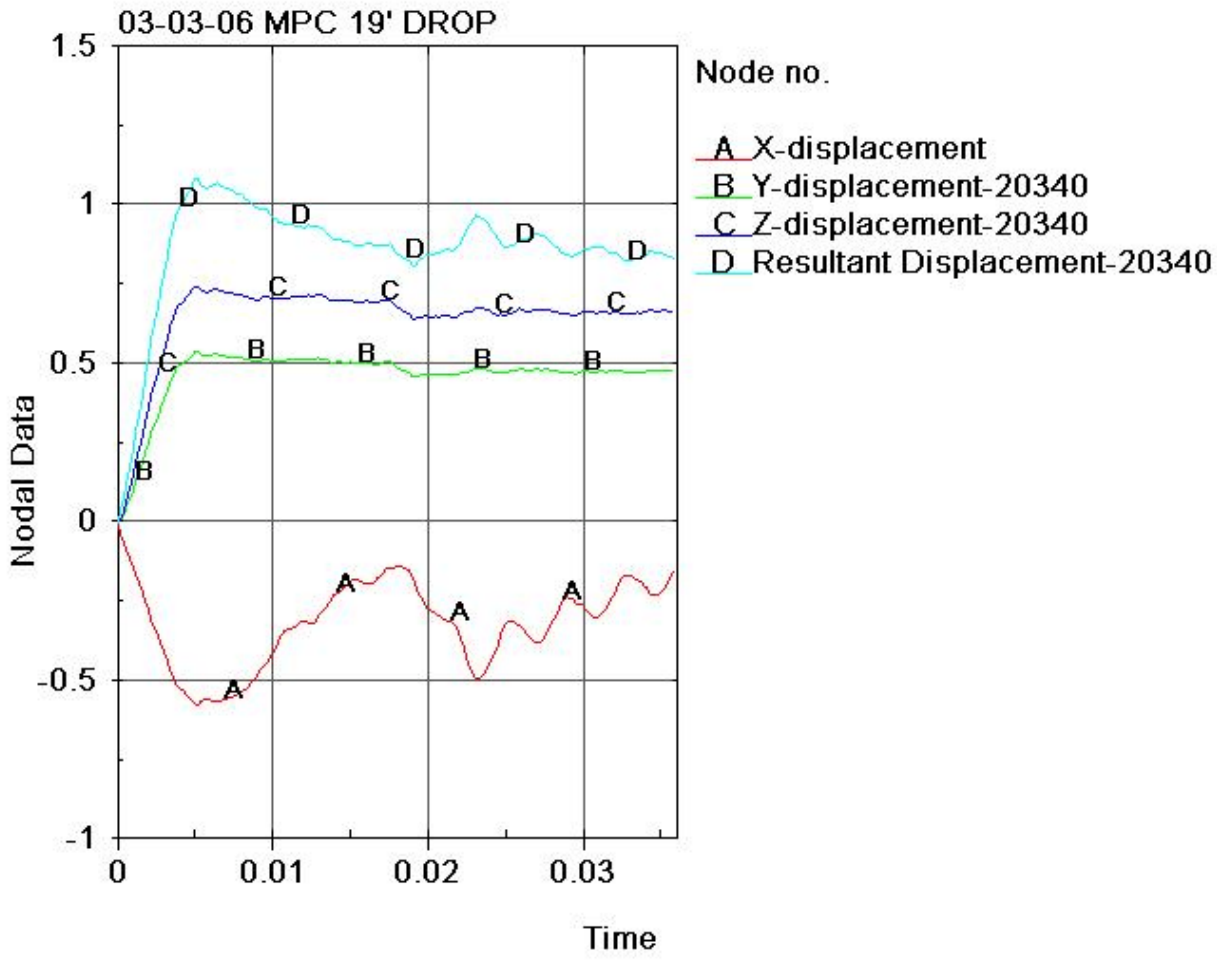

Figure A.28. Displacement History of Node 20340 Shown in Figure A.27

Figure A.29 is a vertical slice through the MPC shell and baseplate showing the location of Element 9035 and the local distribution of EPS within the shell. Figure A.30 labels the elements through the shell thickness at the junction of the shell and baseplate, and Figure A.31 plots the time history of EPS within each element. These plots show the significant decrease in the maximum EPS away from the outside surface of the shell. The 5.8 meters (19 feet) drop of the MPC into the storage overpack produces the highest EPS (0.459 in/in) of any of the cask and MPC drop events. This event, and the probability of breaching the MPC confinement boundary are discussed in greater detail in Appendix B.

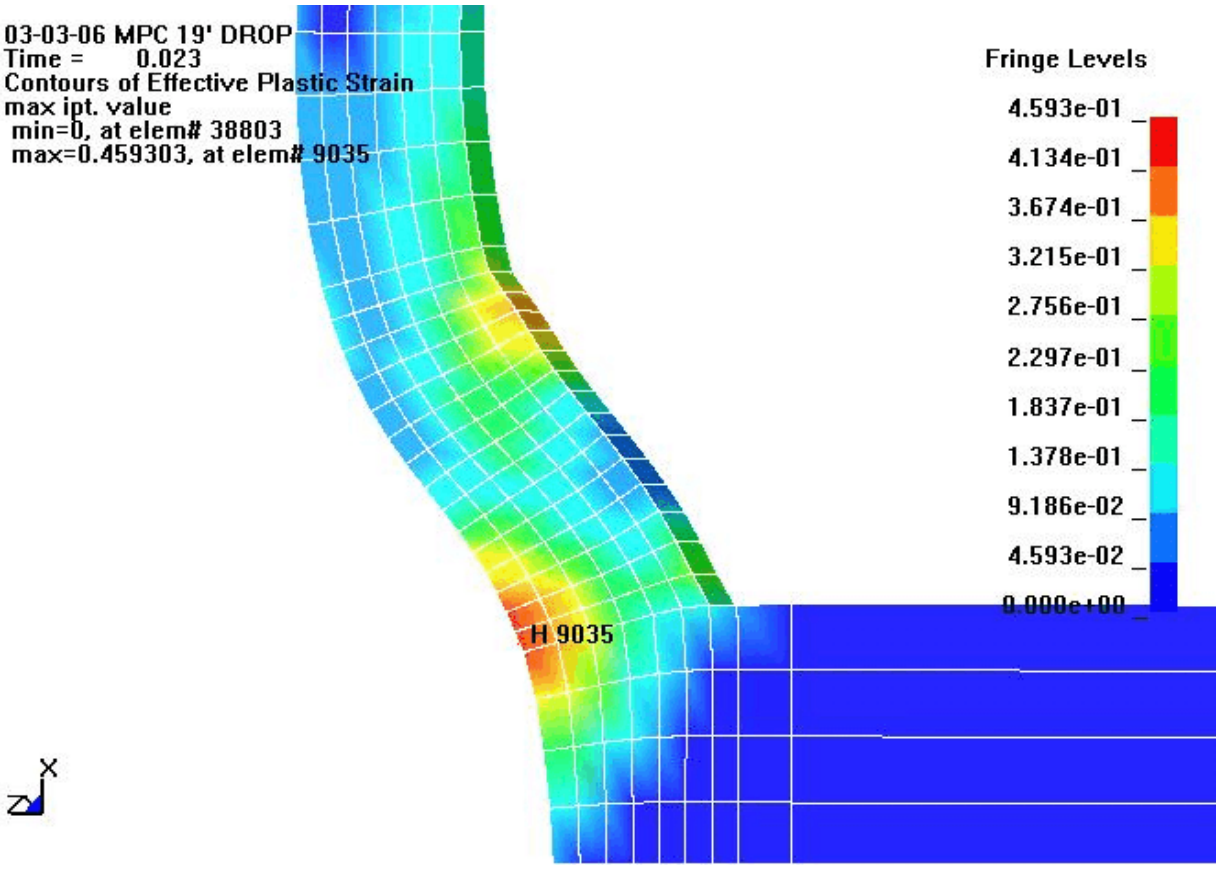

Figure A.29. Slice Through the MPC Shell and Baseplate Showing the Location of Element 9035 and the Local Distribution of EPS Within the Shell

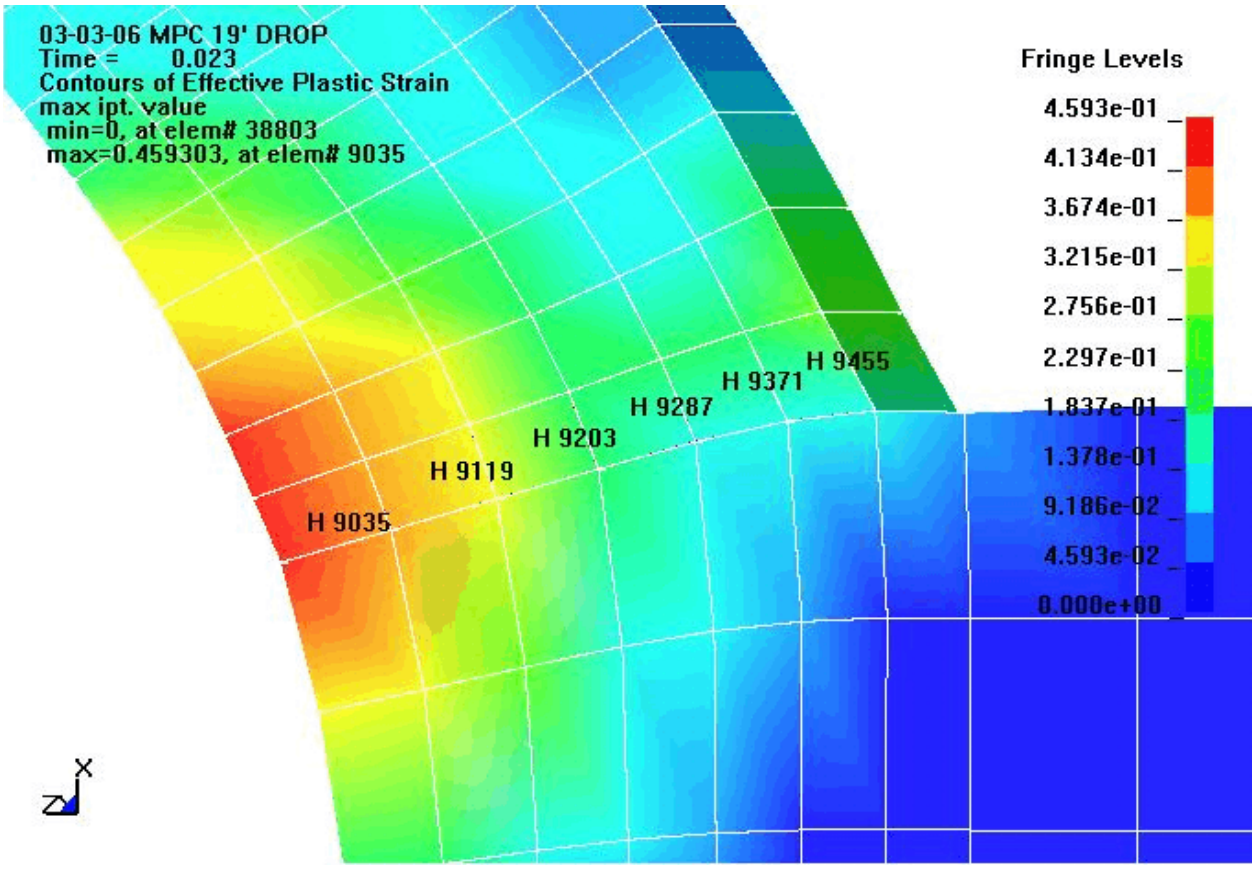

Figure A.30. Labels the Elements Through the Shell Thickness at the Junction of the Shell And Baseplate at the Location of Maximum EPS

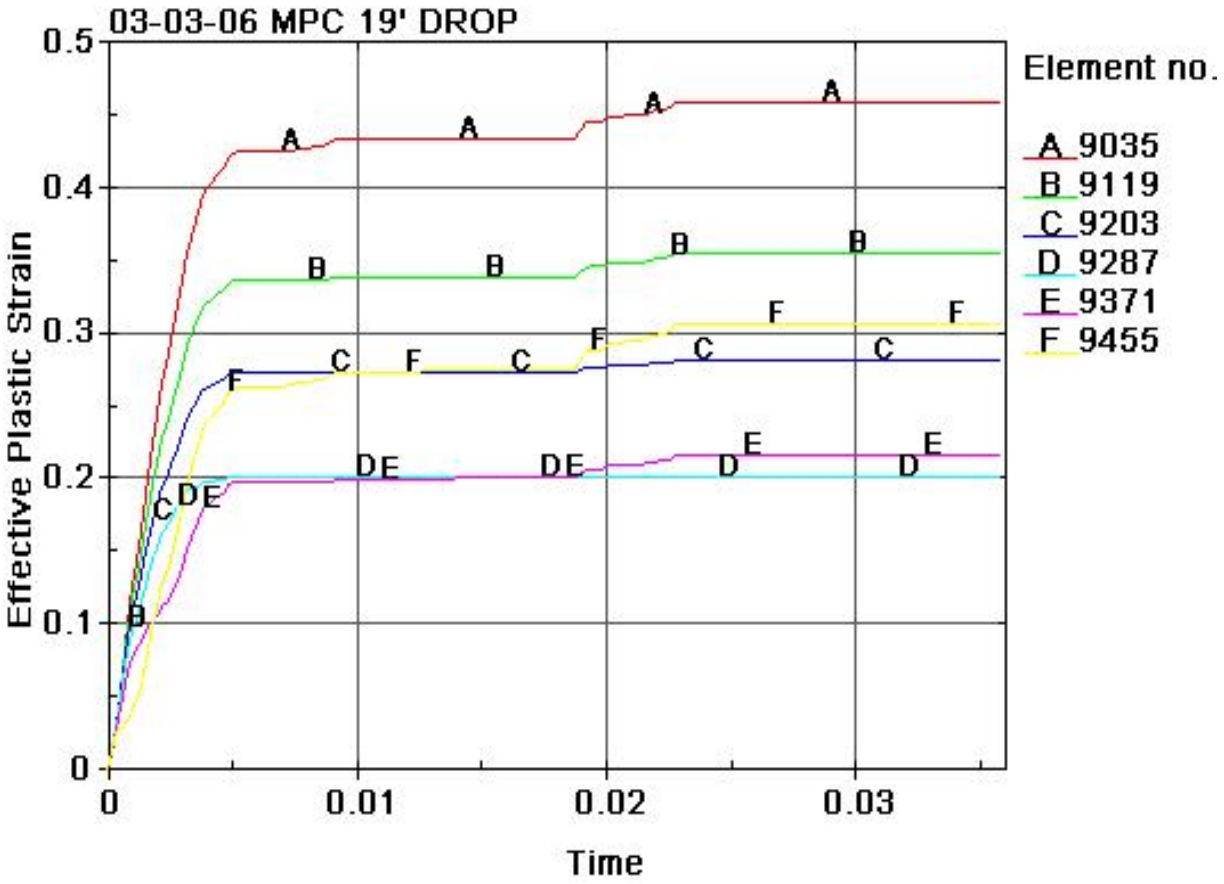

Figure A.31. Time History of EPS Within Each Element Through the Thickness as Shown in Figure A.30

A.4.6 Question 6

If the storage cask drops onto the ISFSI concrete pad, asphalt area, or gravel area, will it slide and/or tip-over? If tip-over can occur, what velocity of the crawler would be required to tip it over? How much time does the operator have to stop the crawler before tip-over occurs? What are the stresses in the MPC?

The storage cask is hung from the top while being transported by the crawler. To perform this calculation a few assumptions were made based on photos and a drawing of the crawler. The height of the storage cask above the ground surface before the drop occurs is assumed to be 30.5 cm (12 inches). The crawler is traveling in the direction of the open end of the crawler. The crawler horizontal square tube bumper support members that make contact with the storage cask are 1.85 m (73 inches) off the ground based on a telephone conversation with Lift Systems (crawler manufacturer).

Two bounding cases were evaluated for a drop of the storage cask onto the ISFSI concrete pad:

Case 1. vertical drop without any rotation ("end drop")
Case 2. drop causing maximum possible rotation

For Case 1, the calculation showed that the frictional resisting force of the storage cask sliding against the concrete was much less than the tip-over force and, thus, the storage cask would slide and not tip-over regardless of the velocity of the crawler. The maximum acceleration of the storage cask for an "end drop" case was calculated to be 44.13 g by Holtec (Reference A.1) assuming a drop of 27.9 cm (11 inches). This acceleration was increased by a factor of 1.045 to account for the drop height of 30.5 cm (12 inches) being considered. This load factor was calculated using the Law of Conservation of Energy which equated the kinetic energy at impact to the work done in compressing the concrete pad and soil. Applying this load factor, the acceleration for the drop of 30.5 cm (12 inches) was calculated to be 46.1 g. To obtain stresses for this end drop case use the stress results presented in the calculations for Question 10 (end drop case) and scale the results by the ratio 46.1 g / 60 g (= 0.768 factor).

For Case 2, the calculation demonstrated that it is geometrically impossible for the rotation of the dropping storage cask to be large enough to cause a tip-over. The maximum amount of rotation possible is 5.14° (with respect to the ground) which occurs when one of the two vertical supports holding the storage cask at the top breaks and the cask makes contact with the ground at one edge. Since this angle is less than the "tip-over" angle of 29.5° (angle which would cause the storage cask to tip-over), the storage cask will not tip-over. Furthermore, the force required to tip-over the storage cask from the rotated orientation was calculated to be greater than the frictional resisting force. Therefore, the storage cask would slide but not tip-over. The acceleration and stresses under case 1 would also apply to this case.

In both cases, it is demonstrated that if the crawler has sufficient force, it would cause the storage cask to slide (not tip-over). However, if one object is pushing against another object (with both objects having the same coefficient of friction), the lighter object will slip or slide regardless of the magnitude of the coefficient of friction. Since the crawler weight is 71,440 kg (157,500 lb) and the storage overpack with MPC and fuel is 163,290 kg (360,000 lb), the crawler "tank treads" will slip and the storage cask will not slide or tip-over.

The drop of the storage cask onto an asphalt or gravel surface was also considered. The g values corresponding to this drop and the resulting stresses would be bounded by the drop onto the ISFSI concrete pad. This occurs because the asphalt and gravel have a lower strength and Young's modulus than concrete and both of these surfaces do not have steel reinforcing bars. Regarding sliding or tip-over, the same conclusion for the drop onto a concrete pad applies here that the crawler will slip and will not be able to slide or tip-over the storage cask. This assumes that both the crawler and storage cask are on the same surface (i.e., gravel or asphalt).

A.4.6.1 Refined Evaluations and Results for Question 6

Subsequently, refined calculations were performed for the 30.5-cm (12-inch) drop of the storage cask onto the three surfaces (the asphalt, gravel, and ISFSI concrete pad). These refined nonlinear impact analyses were performed on the computer code LS-DYNA (Reference A.2) using existing computer models of the storage overpack obtained from Holtec International.

A.4.6.2 Storage Cask Drop onto Reinforced Concrete Storage Pad

A 30.5-cm (12-inch) vertical end drop of the storage cask impacting a 61-cm (24-inch) thick reinforced concrete pad, resting on soil was analyzed. Three analyses were performed corresponding to the lower bound, best estimate, and upper bound elastic soil modulii, which are equal to 324 MPa, 641 MPa, and 1,579 MPa (47,000 psi, 93,000 psi, and 229,000 psi), respectively. Poison's ratio is equal to 0.4 and the soil density is 2,003 kg/m^3 (125 lb/ft^3).

The maximum acceleration values for the 30.5-cm (12-inch) drop of the storage cask onto the 61-cm (24-inches) concrete pad resting on soil are shown in Table A.5.

Table A.5. Storage Cask Drop Analyses

Impact Surface	Thickness of Target Layer (in)	Elastic Soil Modulus* (psi)	Maximum Acceleration (g)	Comment
Concrete	24	47000	40.4	Lower bound soil property
	24	93000	41.2	Best estimate soil property
	24	229000	44.5	Upper bound soil property
Asphalt	12	93000	25.4	Best estimate asphalt property at 4.4 °C (40 °F) and best estimate soil property
	12	93000	23.2	Best estimate asphalt property at 23.9 °C (75 °F) and best estimate soil property
	12	93000	Bounded by 23.9 °C (75 °F Case)	Best estimate asphalt property at 43.3 °C (110 °F) and best estimate soil property
Gravel	24	93000	21.9	Best estimate gravel and soil properties
	12	93000	15.8	Best estimate gravel and soil properties
	12	93000	19.0	Upper bound gravel property and best estimate soil property

* Elastic soil modulus was based on the shear modulus calculated from the shear wave velocity of the free field

The maximum acceleration at the bottom center of the storage cask is 41.2 g for the best estimate soil property. The acceleration time history at this location is shown in Figure A.32. The acceleration time history plot is initially flat at 1.0 g for a period of time because the storage cask was dropped from a height of 30.5 cm (12 inches) above the concrete pad and then impacted the pad at about 0.248 seconds. As shown in Table A.5, the variation in soil property does not have a significant effect on the maximum acceleration of the storage cask for the configuration and parameters defined for this load case.

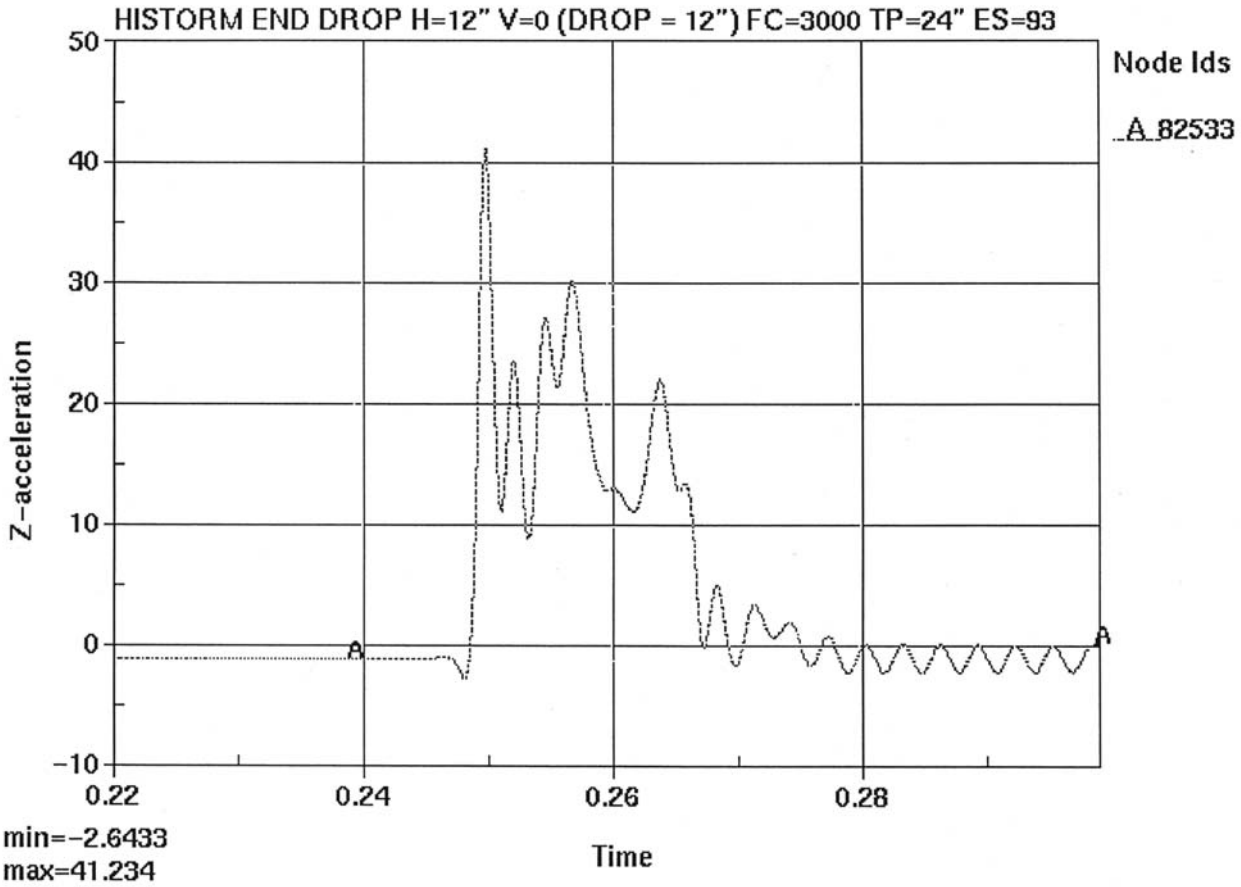

Figure A.32. Acceleration Time History: 30.5-cm (1-Foot) Drop on Concrete Pad

Since the MPC shell was not discretely modeled, the stresses in the MPC were calculated using the stresses from Table A.6 [Reference 9] for the end drop case and scaling the results in proportion to the new calculated g values.

Using this approach and the appropriate dynamic load factor, the stresses in the MPC shell were calculated to be 53.3 MPa (7,732 psi). This stress value is well below the elastic buckling stress and yield for the MPC stainless steel material.

A.4.6.3 Storage Cask Drop onto Asphalt Surface

A 30.5-cm (12-inch) vertical end drop of the storage cask impacting a 30.5-cm (12-inch) thick layer of asphalt resting on soil was analyzed. Because asphalt material properties are sensitive to temperature, three loading cases were considered. The three cases correspond to material properties of asphalt at 4.4 °C, 23.9 °C, and 43.3 °C (40 °F, 75 °F, and 110 °F). This approximates the expected average temperature at the subject facility corresponding to winter, spring/fall, and summer. The properties for the asphalt layer were determined from a literature review of available information for a "good" asphalt mix. The best estimate values for the elastic modulus of asphalt are 10,342 MPa (1,500,000 psi) at 4.4 °C (40 °F), 4,482 MPa (650,000 psi) at 23.9 °C (75 °F), and 1,379 MPa (200,000 psi) at 43.3 °C (110 °F). At 4.4 °C (40 °F) the modulus of asphalt is approximately one-half the modulus of concrete.

Table A.6. MPC Stress Summary

Case	MPC Component	Drop Orien-tation	Safety Factor (SF)		Max. Stress (psi)	Direction/ Type of Stress	Acceleration (g)	Notes
			Value	Ref. A.1 Table #				
End Drop	Fuel Basket	Vertical	3.591	3.4.3	-3739	longitudinal	60	(A)
	Fuel Basket Support	Vertical			N.A.			(B)
	MPC Shell	Vertical	1.21	3.4.4	-11260	longitudinal	60	(C)
	MPC Lid	Vertical	2.8	3.4.4	± 2,723	bending	60	(D)
	MPC Baseplate	Vertical	1.282	3.4.4	N.A.		60	(E)
Tip-over	Fuel Basket	45 Deg.	1.283	3.4.3 & 3.4.6	± 38,335[4]	PL + Pb	45	(F)
	Fuel Basket Support	0 Deg.	1.185	3.4.4 & 3.4.6	± 15,130[4]	direct + bending	45	(G)
	MPC Shell	0 Deg.	1.1	3.4.4	+ 58,959[4] - 45,283[4]	circum-ferential	45	(H)
	MPC Lid				N.A.			(I)
	MPC Baseplate				N.A.			(I)

Negative stress = compression
Positive stress = tension
PL = Local membrane stress intensity
Pb = Primary bending stress intensity

1. SF of 3.59 is for lateral loading (not longitudinal)
2. Corresponds to ± 84.8 MPa (12,299 psi)
3. Corresponds to MPC-24
4. For tip-over case, stresses must be multiplied by a dynamic load factor of 1.04 (Ref. A.1)
5. Based on ANSYS Finite Element Model analysis

Notes column:
(A) Reference A.1, Sec. 3.4.4.3.1.3
(B) Basket support provides lateral not vertical restraint
(C) Reference A.21, App. 3.H Case 5 - Buckling
(D) Reference A.21, App. 3.E.8.2.1.1
(E) MPC baseplate supported by storage overpack baseplate.
(F) Reference A.1, App. 3.T.32
(G) Reference A.1, App. 3.Y.3 for MPC-68
(H) Reference A.1, App. 3.T.34; includes stress due to D.W. & internal pressure [σ of +47.1 MPa (+6,838 psi)]
(I) Bounded by End Drop Case

The maximum acceleration values for a 30.5-cm (12-inch) drop of the storage cask for the 4.4 °C and 23.9 °C (40 °F and 75 °F) are shown in Table A.5. The 43.3 °C (110 °F) drop case was not analyzed because at this high temperature, the acceleration would be lower than the 23.9 °C (75 °F) case. The maximum accelerations at the bottom center of the storage cask, for the best estimate asphalt property are 25.4 g and 23.2 g for the 4.4 °C and 23.9 °C (40 °F and 75 °F) cases, respectively.

The stresses in the MPC were calculated using the stresses from Table A.6 for end drop case and scaling the results in proportion to the new calculated g values. Using this approach and the appropriate dynamic load factor, the vertical stresses in the MPC shell were calculated to be 50.0 MPa (7,245 psi) and 45.6 MPa (6,618 psi) for the 4.4 °C and 23.9 °C (40 °F and 75 °F) cases, respectively. Both of these stress values are well below the elastic buckling stress and yield for the MPC stainless steel material.

A.4.6.4 Storage Cask Drop onto Gravel Surface

Two cases were considered for the storage cask drop on a gravel surface. A-30.5 cm (12-inch) vertical end drop of the cask impacting 30.5-cm (12-inch) and 61-cm (24-inch) thick gravel layers resting on soil were evaluated. The 61-cm (24-inch) layer corresponds to the gravel region surrounding the concrete pad where the storage casks are stored, while the 30.5-cm (12-inch) layer corresponds to the gravel region away from the concrete pad where the gravel layer tapers to smaller thicknesses. The properties for the gravel layer were determined from a literature review of available information on “well graded” crushed stone aggregate. The best estimate value of 345 MPa (50,000 psi) for the elastic modulus would tend to be somewhat higher than what might be expected at the subject facility. This would be conservative because a higher modulus would result in higher impact forces and accelerations. To gauge the effect of varying the modulus of the gravel material, an analysis was performed for the best estimate value 345 MPa (50,000 psi) and for the upper bound estimate 689 MPa (100,000 psi) for the 30.5-cm (12-inch) thick gravel layer case.

The maximum acceleration values for a 30.5-cm (12-inch) drop of the storage cask onto the 61-cm and 30.5-cm (24-inch and 12-inch) gravel layers are shown in Table A.5. The maximum accelerations at the bottom center of the storage cask, for the best estimate gravel property are 21.9 g and 15.8 g for the 61-cm and 30.5-cm (24-inch and 12-inch) gravel layer cases, respectively. As a measure of the sensitivity of the gravel material property, an upper bound case for the gravel property was performed for the 30.5-cm (12-inches) gravel layer. The maximum acceleration for this upper bound gravel property was 19.0 g.

The stresses in the MPC were calculated using the stresses from Table A.6 for end drop case and scaling the results in proportion to the new calculated g values. Using this approach and the appropriate dynamic load factor the vertical stresses in the MPC shell, for the 30.5-cm (12-inch) drop case, were calculated to be 39.7 MPa (5,754 psi) and 28.6 MPa (4,151 psi) for the 61-cm (24-inch) and 30.5-cm (12-inch) gravel layers, respectively. Both of these stress values are well below the elastic buckling stress and yield for the MPC stainless steel material.

A.4.7 Question 7

If the crawler vehicle weighing 71,440 kg (157,500 lb) is traveling at 0.64 km/h (0.4 mi/h) while carrying the storage cask weighing 163,293 kg (360,000 lb), hits another storage cask on a concrete pad, will this impact slide or tip-over the "struck" cask?

(1) If it slides, will a sliding storage cask hit another storage cask? If it hits another storage cask, what would be the maximum stresses (e.g., axial, circumferential, tensile, and compressive) in the MPC?

(2) If it tips over, what would be the maximum stresses in the MPC?

(3) If it does not slide or tip-over, what travel velocity of the crawler would be necessary to strike the storage cask and cause it to slide and/or tip-over?

The evaluation first determined whether a horizontal force would cause the storage cask to tip-over or slide. For tip-over, a horizontal force of 149,732 kg (330,103 lb) applied at 1.85 meters (73 inches) off the ground would be needed. This dimension off the ground corresponds to the height of the horizontal square tube bumper supports on the crawler. These supports show up on the photos and Lift System drawings and this dimension was confirmed by Lift Systems (crawler manufacturer). The force needed to overcome friction ranges from 40,823 kg (90,000 lb) for minimum coefficient of friction of 0.25 to 86,545 kg (190,800 lb) for maximum coefficient of friction of 0.53. For the range of coefficient of friction used see Question 8. Since the force necessary to overcome friction is much lower than the force needed to cause tip-over, the struck cask will slide and not tip-over.

Since the struck cask will slide, only Part (A) of Question 7 is applicable. The initial velocity of the struck cask was calculated using the principle of Conservation of Momentum. This led to the initial velocity of the struck cask:

$$x_0' = \frac{mV}{\left(m + \frac{W}{g}\right)} \qquad (A.19)$$

where: m = mass of crawler + mass of storage cask being transported
V = velocity of crawler
W = weight of storage cask

When the crawler carrying the storage cask strikes another storage cask, the resulting velocity will be reduced. The calculated resulting velocity x'_o of the combined crawler, storage cask being transported, and struck storage cask is 0.38 km/h (0.24 mi/h).

The equation of motion of the storage cask after impact is as follows:

$$M_3 x'' + \mu W - F_c = 0 \qquad (A.20)$$

where: M_3 = mass of crawler + 2 storage casks
F_c = horizontal force that the crawler can generate, 139,603 kg (307,772 lb)[3]

3 Source: Lift Systems Spec. Sheet and confirmed by telephone discussion with C. Perkins of Lift Systems

The solutions for velocity and displacement are found by integrating Equation A.10 and evaluating the two constants of integration from the initial velocity of Equation A.9 and zero initial displacement. Equations A.11 and A.12 for velocity and displacement are as follows:

$$x' = \left(\frac{F_c - \mu W}{M_3} \right) t + \frac{m\ V}{\left(m + \frac{W}{g} \right)} \qquad (A.21)$$

$$x = \left(\frac{F_c - \mu W}{M_3} \right) \frac{t^2}{2} + \frac{m\ V}{\left(m + \frac{W}{g} \right)} t \qquad (A.22)$$

The maximum displacement occurs when the velocity equals zero and is found to be as follows:

$$x = \left[\frac{1}{2\left(\frac{\mu\ W - F_c}{M_3} \right)} \right] \left[\frac{m\ V}{m + \frac{W}{g}} \right]^2 \qquad (A.23)$$

This equation tells us that as the value F_c approaches μ W, the displacement goes to infinity. By inserting the appropriate numbers, F_c is calculated to be greater than μ W. Therefore, it is concluded that the crawler will continually push the storage cask. The sliding storage cask will eventually hit another storage cask or slide off the pad onto the surrounding area. This assumes that the crawler does not stop but continues pushing the struck cask.

Part (A) of Question 7 also asks, what would be the maximum stresses in the MPC? Equation A.10 can be used to determine the acceleration of the storage cask. Solving for x" provides the acceleration as follows:

$$x'' = (F_c - \mu W) / M_3 = 0.25\ g$$

Therefore, the maximum acceleration of the storage cask would be 0.25 g. The positive value of acceleration indicates that the storage cask would accelerate under the constant force (not decelerate). The maximum stresses in the MPC could be approximated by multiplying the stresses presented in the calculations for Question 10 for the tip-over case by the ratio of accelerations 0.25g / 45g for the fuel basket, basket supports, and the MPC shell. For the MPC lid and baseplate, the end drop case bounds and the stresses would be multiplied by 0.25g / 60g. Note that there is also the dynamic load factor of 1.04 to be applied to the tip-over case (see calculations for Question 10).

A.4.8 Question 8

What seismic forces will cause the storage cask to slide and/or tip-over?

A.4.8.1 Simplified Seismic Evaluation

Simplified analyses without soil structure interaction were performed for a storage cask (containing a fully loaded MPC-68) subjected to earthquake forces. The storage cask was assumed to be resting on the ISFSI concrete pad. The seismic analyses used the equivalent static load method which simply multiplies the mass times the seismic equivalent static acceleration to arrive at the seismic forces. To determine whether any amplification occurs as a result of the flexibility of the storage cask, the natural frequency of the storage cask was calculated. The fundamental frequency of the storage cask was calculated to be well above 20.6 Hz which is above the amplified region of the ground spectra or the spectra that would exist on the ISFSI concrete pad. The storage cask frequency was calculated by treating the inner and outer steel cylindrical shells of the storage overpack as cantilever beams fixed at the base. Conservatively, the stiffness contribution of the concrete inside the overpack and the MPC shell was not included. The calculation considered flexural and shear effects in calculating the beam frequency. The seismic analysis also assumed no amplification attributable to soil-structure interaction. Based on the above discussion, the use of the equivalent static method without any amplification would be appropriate and the resulting acceleration calculated for sliding and tip-over would correspond to the maximum ground acceleration.

Two cases are considered in this evaluation, a 3-D earthquake (2 horizontal and 1 vertical) and a 2-D earthquake (1 horizontal and 1 vertical). Both are being considered because the subject plant FSAR indicates that the three directional responses are combined by the square-root-of-sum-of-squares method or by the absolute sum of the worst horizontal with the vertical. The vertical acceleration is assumed for this calculation to be equal to 2/3 of the horizontal acceleration. This is consistent with most nuclear power plants in the United States and is consistent with the FSAR for the subject plant.

To determine whether seismic forces cause sliding or tip-over, the seismic force that would initiate sliding was calculated and compared to the force needed to cause tip-over of the storage cask. Sliding would occur when the seismic force exceeds the frictional resistance of the storage cask attributable to dead weight. The frictional resistance (F_f) is defined in Equation A.13.

$$F_f = \mu N \qquad (A.24)$$

where: μ = coefficient of friction between steel and concrete
N = dead weight of the fully loaded storage cask

Since the coefficient of friction varies, a range of values for μ was utilized as follows:

- μ (minimum) is 0.25, based on a conservative value (for lower bound) in Reference A.1, Section 3.4.6 & 3.4.7.
- μ (maximum) is 0.53, based on Reference A.12, Section 3.4.
- μ (mean) is 0.43, based on Reference A.13. This paper presents results of tests conducted with anchored baseplates which confirm that the range of μ shown above is reasonable and also indicates that the standard deviation of μ is 0.09.

Using these coefficients of friction for a 3 D and 2 D earthquake, the seismic forces, in terms of individual horizontal acceleration, that would cause sliding are calculated. To obtain the corresponding vertical accelerations, the horizontal accelerations are multiplied by 2/3. The resulting governing case (sliding) is presented in Table A.7 for the 2-D and 3-D earthquake cases.

Horizontal acceleration required for tip-over was calculated to be 0.529 g for 3-D case, and 0.410 g for 2-D case. Since the accelerations shown in Table A.7 are less than the accelerations that would cause tip-over, it was concluded that the storage cask would slide and not tip-over.

Table A.7. Seismic Maximum Accelerations for Sliding

Coefficient of Friction (μ)	2 - D Earthquake Plant		3 - D Earthquake Plant	
	Horizontal Acceleration For Sliding (g)	Vertical Acceleration (g)	Horizontal Acceleration For Sliding* (g)	Vertical Acceleration (g)
0.25 (min)	0.214	0.143	0.243	0.162
0.43 (mean)	.334	0.223	0.413	0.275
0.53 (max)	0.392	0.261	0.5	0.333

* For the 3 D earthquake, the horizontal accelerations correspond to each of the two orthogonal directions. It should be noted that these two peak accelerations would not occur at the same time which is accounted for in the square-root-of-sum-of-squares method used in this calculation.

A.4.8.2 Refined Seismic Evaluation

Calculations for the seismic question were independently done with the consideration of soil-structure interaction. A three-dimensional coupled finite element model of a cylindrical storage cask, a flexible concrete pad, and an underlying soil foundation was analyzed using the ABAQUS/Explicit code, (Reference A.14). The cylindrical storage cask is partitioned into four horizontal sections with six rows of solid elements in each section and 64 elements around the outside perimeter. The density of solid elements in each horizontal section is calculated and distributed in such a manner that the center of gravity of the storage cask is located at the correct design position. The storage cask and its internals are modeled as elastic bodies.

In the coupled model, the base of the concrete pad was assumed rigidly bonded to the top surface of the soil foundation. At the storage cask/pad interface, a sliding contact condition was assumed with an assigned friction coefficient of 0.25, or 0.53. The top of the pad was designated to be the “master” surface and the underside of the module to be the “slave” surface to prevent any portion of the module from entering the pad. The four vertical sides of the soil foundation were represented by edge columns that allow horizontal shear deformation only in order to simulate infinite boundary conditions.

The earthquake excitation information was treated with a deconvolution procedure to produce a modified time history of deconvoluted accelerations with properly adjusted frequencies and magnitudes to be applied at the base of soil foundation. The concept of deconvolution is a mathematically rigorous solution process that applies the wave propagation equation of the free-field surface along with the boundary conditions. It has been proven that the solution would be unique and rigorously correct for a linear representation of the soil mass (that is, linear shear modulus and viscous damping model). The deconvolution procedure has been discussed in References A,15 and A.16. The input motions of deconvoluted seismic accelerations were applied to all nodes at the base of the soil foundation. The following data were used for the storage overpack with MPC-68 fully loaded with fuel:

- Weight = 163,293 kg (360,000 lb)
- Outside Diameter = 3.37 m (11.04 ft)
- Height = 5.87 m (19.27 ft)
- Height of center of gravity above pad = 3.00 m (9.86 ft)

A section of the concrete pad that holds 4 (2x2) storage casks was selected as the optimal dimension for the pad in the coupled model, even though only one storage cask was simulated. The selected pad was 9.45 meters (31 feet) square. The pad thickness was 0.61 meter (2 feet).

The size of soil foundation model plays an important role in assessing the soil-structure-interaction effect. Sensitivity studies on the size were performed to demonstrate that its chosen model size could simulate the behavior of a semi-infinite soil foundation underneath the concrete pad. Three different lateral dimensions were selected having 1.0, 1.22, and 1.33 times a baseline lateral geometry of a square of 85 meters (279 feet), which is nine times the pad dimension. It should be noted that the outside layer of elements on the four vertical sides of soil foundation model, with width equal to the pad dimension of 9.45 meters (31 feet), are represented by edge columns. This model setup indicates that the true model size is defined by the nodes at the inner row of the layer with degrees of freedom constrained to those at the outside row. Therefore, the baseline geometry of soil foundation model is only seven times the pad dimension. This selection of the lateral dimension of soil foundation model follows the soil-structure-interaction modeling guidelines in Reference A.17.

The sensitivity studies on the model sizes for the horizontal displacements of the storage cask base with respect to the pad showed closer displacement solutions for the cases of 1.22 and 1.33 times the baseline geometry, indicating that a convergence trend of soil foundation model sizes was observed. Therefore, the final soil foundation model, which was selected to be 1.22 times the baseline geometry, was a square with length of 103.94 meters (341 feet). In addition, a depth of 56.39 meters (185 feet) ,which was partitioned into eight horizontal layers was selected for soil foundation model.

The storage cask and the concrete pad are assumed to behave elastically when subjected to seismic excitations. Therefore, their elastic material properties were chosen as shown in Table A.8.

Table A.8 Elastic Material Properties of Storage Cask and Pad

Structural Element	Young's Modulus, E (MPa) (x 10^3)	Poisson's Ratio, μ	Density, ρ (kg/m^3)
Storage cask	27.789	0.2	6408 (Section 1)*
			2600 (Section 2)*
			2600 (Section 3)*
			3407 (Section 4)*
Pad	24.856	0.2	2403

The geometric definitions of the horizontal sections are as follows:

- Section 1: from storage cask base to 0.2 m (8 inches) above base
- Section 2: from 0.2 m (8 inches) above base to 0.6 m (2 ft) above base
- Section 3: from 0.6 m (2 ft) above base to 3 m (9.86 ft) above base
- Section 4: from 3 m (9.86 ft) above base to storage cask top

The 56.39-meter (185-foot) depth of soil foundation model is partitioned into eight horizontal layers. The depth variation of soil properties such as shear wave velocity and damping profiles was developed to incorporate the site specific soil profiles. The best-estimated strain-compatible soil properties were selected to be used in the seismic analyses. The weight density of the top 56.39 meters (185 feet) of soil foundation was estimated to be 2,162 kg/m^3 (135 lb/ft^3).

The final seismic analyses used the mass proportional soil damping, x_n for each layer such that

$$\xi_n = \frac{a_0}{2\omega_n} \text{ where } a_0 = 2\xi * \frac{2\pi}{T} \qquad (A.25)$$

For shear wave propagation model of horizontal motion site response, site period T is assumed as 0.53 second. For compression wave propagation model of vertical motion site response, site period T is assumed as 0.33 second.

The time history utilized was the one used by the applicant for the design basis. The selected PGA level is 0.15 g for the two horizontal directions and 0.1 g for the vertical direction. Two horizontal components and one vertical component of the seismic accelerations, which are "surface" motions, were applied simultaneously to the coupled model. A frequency domain deconvolution procedure was applied to the time histories of seismic surface accelerations. This procedure uses the Fourier transforms to adjust simultaneously their magnitudes and frequency contents. The net outcome is that when deconvoluted seismic motions are applied at the base of soil foundation model, the dynamic characteristics of the original seismic motions is preserved and the desired surface shaking intensity can be achieved.

For seismic excitation analyzed with horizontal PGA of 0.15g, and vertical PGA of 0.1g using 3-D coupled nonlinear finite element model of the storage cask, pad and soil underneath, the analyses show that the storage cask may slide less than 2.5 mm (0.1 inch) assuming lower bound coefficient of friction 0.25, and will not tip-over with any coefficient of friction from 0.25 to 0.53.

Sensitivity analyses were then performed for different level of seismic excitations with different coefficients of friction between the bottom steel plate of the storage overpack and the concrete pad using three-dimensional coupled finite element models of the cylindrical storage cask, a flexible concrete pad, and an underlying soil foundation. When higher levels of seismic excitations are used in the analyses, the coefficient of friction at the storage cask/pad interface plays an increasingly important role in the sliding and rotational behavior of the storage cask.

For a minimum friction coefficient, the storage cask exhibits a translational motion without much rotation. When the friction coefficient is 0.25, eleven times the design-basis earthquake of the ISFSI pad (i.e., 11 DBE) is needed to cause the storage cask to slide 0.93 m (36.6 inches); this is more than half the separation distance of 1.36 m (53.5 inches) between neighboring casks.

For a maximum friction coefficient, the storage cask experiences more rotational movement, but not tip-over. When the friction coefficient is 0.53 and the seismic excitations are increased to nine times the design-basis earthquake (i.e., 9 DBE), the neighboring storage casks may collide as the cask top moves 1.19 m (46.7 inches) and the cask base slides 0.84 m (33.1 inches). In these cases, the storage cask will slide but not tip-over. Collision may occur at the seismic excitation level of 9 DBE or higher. This level of earthquake is so intense that the plant may have serious consequences, and the consequences attributable to cask collision will be of no significance compared to the plant.

A.4.9 Question 9

What impact forces attributable to given small aircraft, tornado missiles (beyond design basis) and heavy objects in flood waters will cause the storage cask to slide and/or tip-over? If an object of such an impact penetrates the storage overpack, what would be the stresses in the MPC?

The aircraft impact to be evaluated is from a small, non-commercial aircraft, Gulfstream IV, accidentally hitting the storage cask either by a free fall or with its engine running.

The tornado missiles to be considered are the Spectrum II missiles identified in Reference A.18. The calculations below use the tornado missile which most likely will cause the storage cask to slide/tip and/or penetrate the storage overpack and strike the MPC. If this initial analysis shows no penetration or negligible stresses in the MPC, less severe missiles need not be evaluated; otherwise, analyze them in the order of severity (i.e., the most severe one first).

A.4.9.1 Missile Impact Analysis

This calculation addresses the effects of the missiles impact such as automobile and aircraft crashing into the storage overpack. The missile and storage cask are assumed to be rigid. Missile impact on the storage cask can result in either tip-over or sliding the storage cask. The tip-over and sliding modes are considered independently and it is assumed that the storage cask either slides or tips over with no interaction between the two response modes. An approach is first developed to evaluate the effects of any type of rigid missile impact. Then, this approach is used to analyze the impact attributable to an automobile and small aircraft crash.

A.4.9.1.1 Tip-Over Due to Missile Impact

The tip-over mode is considered first. Consider the storage cask with the configuration shown in Figure A.33. A missile of mass (m) and velocity (V) impacts the storage cask at a distance (h) above the base. The horizontal velocity of the missile is first converted to an angular velocity (ω_m) about point (O) using the following equation:

$$\omega_m = \frac{V \cos\xi}{C} \qquad (A.26)$$

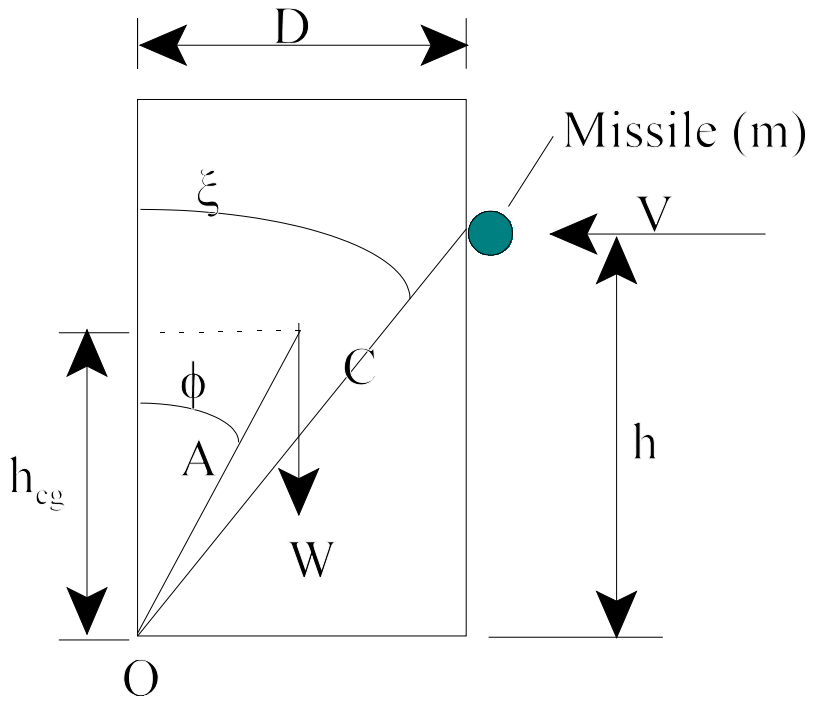

Figure A.33. Tip-Over of Storage Cask

Conservation of momentum results in a combined angular velocity of the storage cask and missile equal to the following:

$$\omega = \frac{m\,C\,V\,\mathrm{Cos}\xi}{\left(\frac{WA^2}{g} + m\,C^2\right)} \qquad (A.27)$$

Conservation of energy principles are then used to determine the initial angular velocity (ω_c) required to tip-over when the center of gravity is directly above point O:

$$\omega_c^2 = \frac{2\left[W\,A\left(1-\mathrm{Cos}\phi\right) + m\,g\;C\left(1-\mathrm{Cos}\;\xi\right)\right]}{\left(\frac{WA^2}{g} + mC^2\right)} \qquad (A.28)$$

Combining Equations A.16 and A.17 and solving for (V) results in the following equation:

$$V^2 = \frac{2\left[WA\left(1-\mathrm{Cos}\;\phi\right) + m\,g\,C\left(1-\mathrm{Cos}\,\xi\right)\right]\left[\frac{W\,A^2}{g} + m\,C^2\right]}{\left(m\,C\;\mathrm{Cos}\,\xi\right)^2} \qquad (A.29)$$

A spreadsheet is then used to evaluate, V, given a missile mass, m, where:

W	=	163,290 kg (360,000 lb)
D	=	3.4 m (133.875 inches)
h_{cg}	=	3 m (118.4 inches)
φ	=	29.5°
A	=	3.45 m (136 inches); $C = (h^2 + D^2)0.5$
ξ	=	$\tan^{-1}$ (D/h); the value of (h) is taken as 1, 0.75, 0.5, and 0.25 times the height of the storage cask= 5.87 m (231.25 inches)

The resulting velocities required to tip-over the storage cask are shown in Figure A.34.

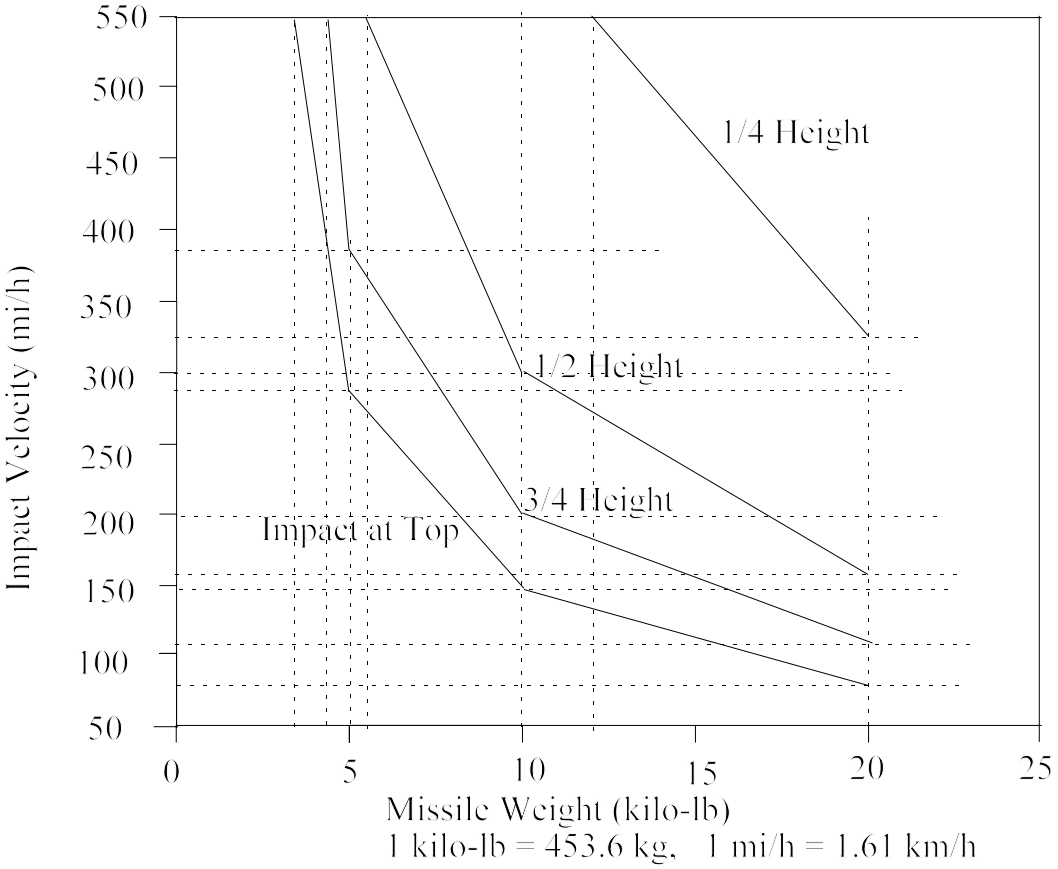

Figure A.34. Missile Velocity for Tip-Over of Storage Cask

A.4.9.1.2 Sliding Due to Missile Impact

Sliding of the storage cask is considered next. A sketch of the problem is shown in Figure A.35.

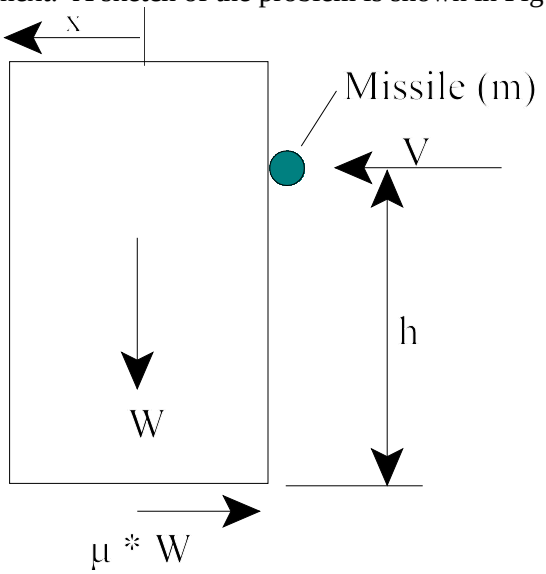

Figure A.35. Sliding of Storage Cask

The height of the missile impact is not important for this problem, because here we are concerned with the sliding mode only. Conservation of momentum results in the following initial velocity (x'_o) of the storage cask after impact:

$$x'_0 = \frac{m\,V}{\left(m + \frac{W}{g}\right)} \qquad (A.30)$$

The equation of motion for the storage cask after impact is as follows:

$$x'' + \mu\, g = 0 \qquad (A.31)$$

Integrating Equation A.20 and evaluating the two constants of integration from the initial velocity of Equation A.19 and zero initial displacement results in the following solutions for velocity and displacement:

$$x = \frac{m\,V\,t}{\left(m + \frac{W}{g}\right)} - \frac{\mu\, g\, t^2}{2} \qquad (A.32)$$

where t = time after impact

The maximum displacement occurs when the velocity equals zero and is found to be as follows:

$$x' = \frac{mV}{\left(m + \frac{W}{g}\right)} - \mu g t \qquad (A.33)$$

$$x_{max} = \frac{\left(\frac{mV}{\left(m + \frac{W}{g}\right)}\right)^2}{2\mu g} \qquad (A.34)$$

The clear spacing between the storage casks on the ISFSI pad is at least 1.3 meters (52.1 inches) and the closest clear distance from the edge of the storage cask to the edge of the pad is 66 cm (26 inches). Solutions are therefore obtained for x_{max} = 66 cm (26 inches). Three values of the coefficient of friction are used (see calculations for Question 8); a lower bound of 0.25, a mean value of 0.43, and an upper bound of 0.53. Equation A.23 is solved for the velocity required to slide the storage cask 66 cm (26 inches) given the missile mass. These solutions are shown in Figure A.36.

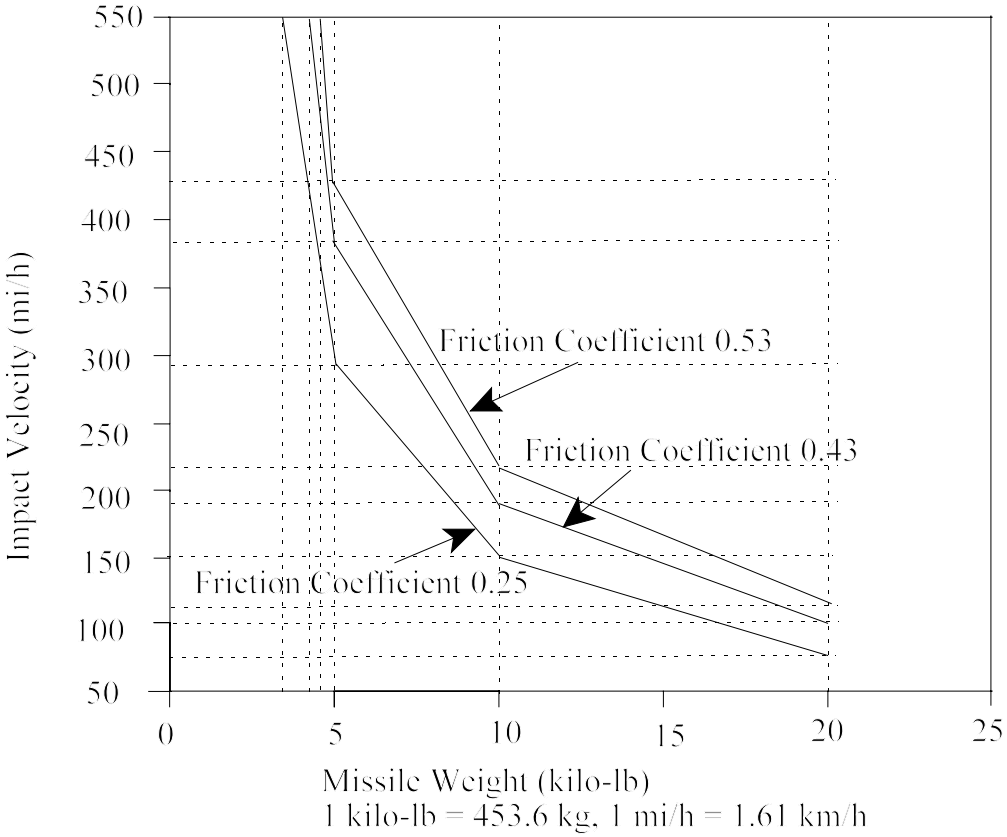

Figure A.36. Missile Velocity Required to Slide the Storage Cask by 66 cm (26 inches)

The following conclusions can be drawn by comparing Figures A.34 and A.36:

(1) Impact velocities required to cause the storage cask to slide are about the same as those required to cause it to tip-over if the coefficient of friction = 0.25 and the impact is at the top of the storage cask. The storage cask will slide rather than tip-over if the impact is below the top of the cask and the friction coefficient = 0.25.

(2) The storage cask will tip-over rather than slide if the friction coefficient = 0.43 and the impact height is larger than about 80 % of the height. It will slide if the impact is below this height.

(3) The storage cask will tip-over rather than slide if the friction coefficient = 0.53 and the impact height is larger than about 62.5 % of the height. It will slide if the impact is below this height.

A.4.9.2 Vehicle Impact Analysis

A car or a truck crashing into the storage casks while stored on the ISFSI pad is not analyzed directly for a driver's accidental maneuver, physical ailment or mistake. However, by extrapolation from the analyses done for tip-over and sliding attributable to missile impact (from Figures A.34, 35, and 36 respectively), it can be concluded that a 4,536 kg (10,000 lb) vehicle traveling at 241 km/h (150 mi/h) speed will slide the storage cask less 66 cm (26 inches), and will not cause tip-over. This conservatively assumes that the impact occurs at the top of the storage cask (for tip-over) and the lowest coefficient of friction applies (for sliding).

A.4.9.3 Aircraft Impact Analysis

The analyses described below are included in this appendix to provide a methodology for determining the response of a dry storage cask to aircraft impact. The results of the aircraft impact analyses are used in the PRA to evaluate aircraft impact events on overall risk.

As discussed in Section 3.3.7 of the main report, the largest aircraft that is able to land at any of the four local airfields near the ISFSI site is a Gulfstream IV. This aircraft's geometric characteristics were used to estimate the frequency of an aircraft crash into a storage cask during takeoff or landing. The data and equations presented in Sections A.4.9.3.1 and 2 are used to evaluate the global and local structural response of a storage cask to impact by a Gulfstream IV. Section A.4.9.3.3 summarizes the results and discusses the probability of breaching the MPC confinement boundary.

A.4.9.3.1 Global Response

The Gulfstream IV aircraft weighs 74,600 lbs on takeoff and is powered by two Roll-Royce Tay 611-8 turbofan jet engines each weighing 3,135 lbs. The DOE Standard on aircraft impact (Reference A.19) recommends that the gross response of a target can be evaluated by considering the impact of a rigid missile having a mass equal to twice the engine weight. Thus, the appropriate missile weight for the analysis is 2 x 3,135 = 6,270 lbs. Figures A.34 and A.36 are used to obtain the impact velocity required for tip-over and sliding. The results are shown in Table A.9a.

Table A.9a. Global Response of Storage Cask to Aircraft Impact

Tip-Over		Sliding	
h/L	Impact Velocity Required (mph)	m	Impact Velocity Required (mph)
1	250	0.25	260
0.75	340	0.43	330
0.5	500	0.53	370

A.4.9.3.2 Local Response

Another mode of response to missile impact is local penetration or perforation of the shell and lid of the storage overpack. The DOE Standard (Reference A.19) recommends that the local damage evaluation be performed using relatively nondeformable components of the aircraft. Such a component is the engine shaft. The Rolls-Royce Tay 611-8 engine is 94.8 inches long and 45.0 inches in diameter. Exact dimensions of the engine shaft were not available from the manufacturer, so dimensions were estimated from available photographs and cross sections of jet engines of this class.

A typical turbofan engine has multiple concentric shafts, but for the purpose of this analysis a single solid shaft is assumed. The shaft is assumed to have an average diameter of 4.0 inches over 80% of the engine length. The resulting weight of the shaft is ($p \times 2^2 \times 94.8 \times 0.80 \times 490/1728 = 270$) 270 lbs.

The shell of the storage overpack consists of an outer steel shell 0.75 inches thick, a poured concrete shell 26.75 inches thick and an inner steel shell 1.25 inches thick. The lid consists of a top steel plate 2.0 inches thick, a bottom steel plate 2.0 inches thick, a concrete shield plug 10.5 inches thick and a bottom shield plate 1.25 inches thick.

The DOE Standard on aircraft impact analysis (Reference A.19) recommends the Chang formula (Equation 24a) to compute the perforation thickness of concrete targets and the Ballistic Research Laboratory (BRL) formula (Equation A.24b) to compute the penetration thickness of steel targets:

$$t_p = \left(\frac{U}{V}\right)^{0.25} \left(\frac{MV^2}{D f_c'}\right)^{0.5} \qquad \text{(A.24a)}$$

where:

U = reference velocity = 200 ft/sec
V = missile impact velocity (ft/sec)
M = mass of the missile = W/g
W = missile weight (lb), g=32.2 ft/sec^2
D = effective missile diameter (ft)
f'c = ultimate compressive strength of concrete (lb/ft^2)
t_p = mean perforation thickness (ft)

$$T^{1.5} = \frac{0.5MV^2}{17{,}400 K_s D^{1.5}} \qquad \text{(A.24b)}$$

where

T = predicted thickness to just perforate a steel plate (in.)
M = W/g missile mass (lb-sec^2/ft)
V = missile impact velocity (ft/sec)
K_s = constant depending on the grade of steel (usually ≈ 1)
D = missile diameter (in.)

Both formulae in their standard form assume the missile is rigid. To prevent perforation of the target, Reference A.19 recommends that the thickness computed using the Chang and BRL formulae be reduced by a factor of 1.2 and 1.25 respectively.

The storage overpack shell and lid consist of multiple layers of steel and concrete. The approach used to determine the impact velocity that will just perforate all the layers of the storage overpack shell and lid is to separately calculate the kinetic energy associated with the impact velocity required to just perforate each of the steel and concrete layers, and then add the kinetic energies from each layer to determine the total kinetic energy and resulting impact velocity. This methodology is based on the conservative assumption that each layer behaves independently and that there is no interaction between layers. Since multiple layers resist perforation, it would be overly conservative to reduce the thickness of each layer by the reduction factors cited above, because these factors are intended to prevent perforation. To establish a realistically conservative best estimate of the impact velocity that will just perforate all the layers, only the layer contributing most to perforation resistance is reduced in thickness.

For each storage overpack shell and lid layer, Table A.9b shows the material and thickness of the layer, the reduced thickness, the kinetic energy required to just perforate the layer, the total kinetic energy from all layers and the resulting impact velocity of the aircraft. This methodology produces conservative results. More accurate results can be obtained using explicit dynamics found in several commercially available computer codes. Before using such codes, however, material models, elements and meshes should be benchmarked against the results of actual test data.

Table A.9b. Aircraft Maximum Impact Velocity that Does Not Perforate the Storage Overpack Shell or Lid.

Event	Target Layer	Thickness (in)	Reduced Thickness (in)	Kinetic Energy to Perforate (ft-lbs)	Total Kinetic Energy (ft-lbs)	Maximum Impact Velocity(1) (mph)
Horizontal Impact into Overpack Shell	Outer Steel Shell	0.75	0.75	(3)	(3)	(3)
	Concrete Shell	26.75	22.3	(3)		
	Inner Steel Shell	1.25	1.25	(3)		
Vertical Impact into Overpack Lid	Top Lid Plate	2	2	(3)	(3)	(2)(3)
	Bottom Lid Plate	2	1.6	(3)		
	Shield Concrete	10.5	10.5	(3)		
	Bottom Shield Plate	1.25	1.25	(3)		

(1) The methodology used here produces conservative results. More accurate results can be obtained using explicit dynamics found in several commercially available finite element computer codes. Before using such codes, material models, elements and meshes should be benchmarked against the results of impact test data.
(2) Assumes an impact angle of 50 degrees above the horizontal.
(3) Text withheld under 10 CFR 2.390.

A.4.9.3.3 Results of Aircraft Impact Analysis

Aircraft speeds during landing and takeoff generally range from 140 to 200 mph (Reference A.19). Table A.9a shows that cask tip-over or sliding attributable to aircraft impact would not be expected to occur until impact speeds exceed 250 mph, and then, only if the aircraft struck near the top of the cask. The response of the MPC to cask tip-over is far more significant than to cask sliding and, therefore, only cask tip-over need be considered. As reported in Table B.6, the probability of MPC failure attributable to cask tip-over is less than $1x10^{-6}$. Table A.9b shows that perforation of the storage overpack would not occur until impact speeds exceed (text withheld under 10 CFR 2.390). For the largest aircraft that can land or takeoff from any of the four airports near the site, these results show that the storage overpack provides a rugged barrier that makes the likelihood of an MPC breach from aircraft impact exceedingly small.

Based on these results, the probability of breaching the MPC, if struck by an aircraft during landing or takeoff is extremely small and is assumed to be zero. However, many commercial aircraft overflying the site would be larger than a Gulfstream IV and could impact the cask at velocities much higher than those associated with landing and takeoff. Since the makeup and characteristics of commercial aircraft overflying the site are not known, and have not been evaluated, it is conservatively assumed that all commercial aircraft overflying the site are larger than a Gulfstream IV and that the probability of MPC breach attributable to the impact of an overflying commercial aircraft is, for the purpose of the PRA, 1.0. Therefore, the probability of MPC failure and release, if struck by an aircraft, is, for the purpose of the PRA, equal to the frequency of overflight crashes (9.0×10^{-11}, see Section 3.3.7) divided by the total frequency of aircraft crashes (6.3×10^{-9}, see Section 3.3.7), which is 0.014.

A.4.9.4 Tornado Missile Impact Analysis

This calculation considers the local effects of tornado missiles hitting the storage cask and addresses the question of whether the missiles penetrate the storage overpack.

Reference A.1 states that the storage overpack (HI-STORM 100) system was checked for a constant wind speed of 579 km/h (360 mi/h), a pressure drop of 20.7 kPa (3.0 psi) and three tornado-generated missiles. The three missiles are the same as the Spectrum I missiles identified in Reference A.18 and are characterized as follows:

(1) automobile with a mass of 1,800 kg (3,970 lb) and a velocity of 203 km/h (126 mi/h)

(2) rigid solid steel cylinder having a diameter of 20.3 cm (8 inches) with a mass of 125 kg (276 lb) and a velocity of 203 km/h (126 mi/h)

(3) solid sphere having a diameter of 2.5 cm (1 inches) with a mass of 0.22 kg (0.49 lb) and a velocity of 203 km/h (126 mi/h)

The analysis in Reference A.1 demonstrates that the combination of the large tornado missile (automobile) plus either steady tornado wind or instantaneous pressure drop causes a maximum horizontal excursion of the storage cask midpoint (approximately equal to the cask center of gravity) of less than 14 cm (5.5 inches) or 2.7 degrees rotation. In order for the storage cask to tip-over, Reference A.1 reports the centroid must undergo a horizontal displacement of 168 cm (5.5 feet). Therefore, the storage cask will not tip-over as a result of the automobile impact. Furthermore, it is shown in Reference A.1 that the other two postulated missiles will not penetrate the storage overpack. The Spectrum II missiles in Reference A.18 are characterized in Table A.10.

Table A.10. Characteristics of Spectrum II Missiles

Missile	Mass (kg)	Dimensions (m)	Velocity m/s (mi/h)
(A) Wood Plank	52	0.092 x 0.289 x 3.66	83 (186)
(B) 6” Sch 40 pipe	130	0.168D x 4.58	52 (116)
(C) 1” Steel rod	4	0.0254D x 0.915	51 (114)
(D) Utility pole	510	0.343D x 10.68	55 (123)
(E) 12” Sch 40 pipe	340	0.32D x 4.58	47 (105)
(F) Automobile	1810	5 x 2 x 1.3	59 (132)

A.4.9.4.1 Automobile as Tornado Missile

The Spectrum II automobile has about the same mass as the Spectrum I automobile and the velocity is only slightly higher, i.e., 212 km/h versus 203 km/h (132 mi/h versus 126 mi/h). Therefore, the Spectrum II automobile missile when combined with the tornado wind or pressure drop will not cause the storage cask to tip-over.

The Reference A.1 report does not provide an evaluation of the potential for the storage cask to as a result of the combined effects of an automobile impact and tornado wind. The potential for this effect was evaluated in this appendix. The Principle of Conservation of Momentum was used to calculate the initial velocity of the storage cask attributable to the impact of the automobile. The initial velocity of the storage cask was determined to be 2.33 km/h (1.45 mi/h). The force attributable to tornado wind effects was taken from Reference A.1 which showed that the force attributable to pressure drop governed over the tornado wind pressure.

The equation of motion for the struck storage cask is as follows:

$$\frac{W}{g} x'' + \mu W - F_{Tornado} = 0 \qquad (A.35)$$

where: W = weight of storage cask
$F_{Tornado}$ = force attributable to tornado wind effect

Solving for x" results in the accelerations shown in Table A.11 for the range of coefficient of friction.

Table A.11. Acceleration for Range of μ

Coefficient of Friction (**μ**)	Acceleration(g)
minimum	0.005
mean	-0.18
maximum	-0.28

For a coefficient of friction of $\mu_{min} = 0.25$, the storage cask will have a positive acceleration of 0.005 g. This means that the storage cask will accelerate and continue to displace without stopping until it slides off the pad or hits another storage cask. For a coefficient of friction greater than 0.255, the storage cask acceleration is negative which means it will decelerate until it stops.

A.4.9.4.2 Other Spectrum II Tornado Missiles

The potential for the other Spectrum II missiles to penetrate the storage overpack was evaluated using the procedures given in Reference A.19 on pages C-6 through C-9. The penetration depth (x) is given as follows:

$$x = \left[4KNWD\left(\frac{V}{1000D}\right)^{1.8} \right]^{0.5} \quad \text{if } \frac{x}{D} < 2 \qquad (A.36)$$

$$x = KNWD\left(\frac{V}{1000D}\right)^{1.8} + D \quad \text{if } \frac{x}{D} > 2 \qquad (A.37)$$

where: x = penetration depth (in)
K = concrete penetrability factor = $180/ (f'_c)^{0.5} = 2.846$
N = shape factor = 0.72 for blunt missile
W = weight of missile
V = velocity of missile in ft/sec
D = diameter of missile (in.)

When the missile first strikes the target, there is a tendency for the front face of the concrete to scab. The barrier thickness (t_{ds}) required to prevent this is given as follows:

$$t_{ds} = 1.1\left(2.12D + 1.36x\right) \quad \text{for } 0.65 < x/D < 11.75 \qquad (A.38)$$

$$t_{ds} = 1.1\left(7.91x - 5.06\frac{x^2}{D}\right) \quad \text{for } x/D < 0.65 \qquad (A.39)$$

If this scabbing thickness is not satisfied the penetration depths are likely to be larger than computed with Equations A.25 and A.26. Note that the 1.1 factors in Equations A.27 and A.28 are safety factors added to curve fits of empirical data. Of course, the outer steel plate on the storage overpack prevents this scabbing and, therefore, is not considered in this analysis.

The barrier thickness required to prevent the missile from perforating the shield (t_{dp}) is then as follows:

$$t_{dp} = 1.2\left(1.32D + 1.24x\right) \quad \text{for } 1.35 < x/D < 13.5 \qquad (A.40)$$

$$t_{dp} = 1.2\left(3.19x - \frac{0.718x^2}{D}\right) \quad \text{for } x/D < 1.35 \qquad (A.41)$$

These calculations are conservative for the storage overpack for several reasons:

- The wall of the storage overpack includes inner and outer steel plates with the concrete contained within the plates. The above analysis includes only the effects of the concrete barrier so that lower penetration depths would be expected in the actual storage overpack.
- The above analysis was developed from data collected for plane barriers. The circular shape of the storage overpack would increase its strength as compared with a plane structure.
- The circular shape of the outer boundary of the storage overpack will tend to deflect missiles and, thereby, reduce the probability that a missile can penetrate the barrier.

The above calculations are carried out for the Spectrum II missiles. All of the missiles are included except for the automobile which was treated separately as discussed above because it is a large flexible missile and is more likely to cause gross response (sliding or tip-over) of the storage cask rather than to penetrate the storage overpack. The results of the calculations are shown in Table A.12.

The barrier thickness required to prevent penetration is less than the 68 cm (26.75 inches) of concrete provided except for the 12 inch Schedule 40 pipe where 72 cm (28.5 inches) is predicted as the thickness required to prevent penetration. Because of the conservatism cited above it is not likely that any of the missiles will penetrate the storage overpack.

Table A.12. Penetration of Missiles Through Reinforced Concrete Wall of Storage Overpack

Missile	f'c (psi)	K	N	Missile Weight (kg)	Missile Weight (lb)	Missile Velocity (m/s)	Missile Velocity (ft/s)	Missile Diameter (cm)	Missile Diameter (in)	V/1000D **1.8	x (in)	x/D	Req'd t (in)
Wood Plank	4000	2.846	0.72	52	114.64	83	272.3	18.4	7.244	0.00272	4.31	0.59	14.3
6" Sch 40 pipe	4000	2.846	0.72	130	286.6	52	170.6	16.8	6.614	0.00138	4.64	0.7	14.9
1" Steel Rod	4000	2.846	0.72	4	8.82	51	167.3	2.54	1	0.04003	1.7	1.7	4.1
Utility Pole	4000	2.846	0.72	510	1124.3	55	180.4	34.3	13.504	0.0004	7.26	0.54	26.6
12"Sch 40 pipe	4000	2.846	0.72	340	749.56	47	154.2	32	12.598	0.0004	5.29	0.42	28.5

Note: 1 inch = 2.54 cm; 1 psi = 6.895 kPa

A.4.9.5 Flood Water/Debris Impact Analysis

This calculation considers whether the effects of heavy objects in flood waters will cause the storage cask to slide and/or tip-over.

The subject plant FSAR states that none of the safety-related facilities would be exposed to river flooding by the most severe flood at the site. It is further reported that the probable maximum discharge concurrent with a severe wind of 72 km /h (45 mi/h) would develop a wave height of 2.5 meters (6.5 feet). The elevation of the wave crest attributable to a sustained wind of this magnitude occurring during the Probable Maximum Flood would be well below the elevation of the top of the dry cask storage pad. Thus, it would be an incredible event for flood waters to even reach the bottom of the storage cask and even more incredible for the storage cask to be impacted by heavy objects in flood waters.

The Reference A.1 report demonstrates that the accident condition design external pressure of 414 kPa (60 psi) for the MPC bounds the maximum hydrostatic pressure on the storage cask in a flood where the water level is conservatively set at 38 meters (125 feet). The Reference A.1 report also evaluated the factor of safety against tip-over and sliding for a design basis flood velocity of 4.6 m/s (15 ft/s). They calculated a sliding factor of safety of 2.09 and a tip-over factor of safety of 4.68.

A calculation is performed to evaluate what forces/conditions attributable to floating debris would cause the storage cask to slide and/or tip-over. For this calculation, a floating tree moving at varying velocities is considered. The mass of the tree was approximated as three times the weight of the Spectrum II utility pole which results in a total weight of 1,530 kg (3,370 lb) that is close to the weight of the automobile. Conservatively, the location of impact was assumed to occur at the top of the storage cask.

The drag force attributable to the flowing flood water was also included for the same varying velocities as used for the debris impact. The velocities considered are 1.5 m/s (5 ft/s), 3.0 m/s (10 ft/s), 6.1 m/s (20 ft/s), and 9.1 m/s (30 ft/s).

A.4.9.5.1 Tip-Over Evaluation

The same methodology developed for the aircraft impact tip-over analysis was utilized (with an additional term for the constant water drag force). In this calculation, the kinetic energy attributable to impact and drag force was compared to the potential energy required to cause tip-over. This comparison led to the conclusion that for velocities less than approximately 10.7 m/s (35 ft/s), the storage cask will not tip-over. The calculation also concluded that the contribution of the debris impact is negligible and can be dropped from the flood analysis of the storage cask. This occurred because the mass of the debris is a very small fraction of the storage cask mass and it is traveling at a very slow velocity.

A.4.9.5.2 Sliding Evaluation

Sliding would occur if the horizontal drag force is greater than the frictional resistance (the effect of debris impact can be neglected - see above). The calculation demonstrates that for velocities less than approximately 7.6 m (25 ft/s), the storage cask will not slide for the entire range of coefficients of friction. For velocities greater than that, the storage cask will slide depending on the velocity and the specific coefficient of friction. As an example, for a velocity of flowing water at 9.1 m (30 ft/s), the storage cask will slide for $\mu_{min} = 0.25$ but will not slide for $\mu_{mean} = 0.43$ and $\mu_{max} = 0.53$.

A.4.9.5.3 Analysis for Floods

An analysis for floods was performed with the following assumptions:

- Surface area of the storage cask subject to floods is 231.25 x 132.5 / 144 = 212.78 ft^2 or 19.8 m^2.
- Storage cask is rigid.
- Storage overpack has ventilation openings so it is assumed that the hydrostatic pressure from flood submergence acts only on the MPC.
- Water flow velocity is assumed to be uniform over the height of the storage overpack.
- C_d, the drag coefficient is 0.5.
- ρ, the water weight density is assumed to be 1,000 kg/m^3 (62.4 lbs/ft^3).
- μ, the coefficient of friction between steel plate and concrete pad is assumed to be 0.25.
- K_{min}, the buoyancy factor = 0.64 (Reference A.1)

Sliding Evaluation

Applied Force (lbs) $= C_d \cdot$ Velocity head $\cdot$ Area
$= 0.5 \times (\rho(lb/ft^3) \cdot V(ft/s)^2 / 2\ g(ft/s^2) \times 212.78 ft^2 = 106.39\ (62.4\ V^2 / (2 \times 32.2))$
$= 103.09\ V^2$ (where V is in ft/sec; g is in ft/sec^2)

Resisting Force $= \mu \cdot K \cdot W$ (lbs)

where: μ = coefficient of friction
K = buoyancy
W = weight (lbs)
= 0.25 x 0.64 x W
= 0.16 W

For equilibrium, $103.09\ V^2 = 0.16\ W$
$V^2 = 0.001552\ W$
$V = (0.001552\ W)^{½}$ (ft/sec)

For overpack with minimum MPC Weight (lbs) $V = (0.001552 \times 303000)^{½} = 21.7$ ft/s (6.6 m/s)

For overpack with full MPC Weight $V = (0.001552 \times 360000)^{½} = 23.6$ ft/s (7.2 m/s)

Tip-Over Evaluation

Applied Force (lbs) = $103.09\ V^2$ (where V is in ft/sec)

Applied Moment = Force $\cdot$ Height of A.G.
$= 103.09\ V^2 \times (118.46$ inches$)/12$ inches/foot
$= 1018\ V^2$ lb-ft

Resisting Moment $= K \cdot W \cdot$ Diameter / 2 where W is weight
$= 0.64 \times (132.5/24)\ W$
$= 3.533\ W$

For equilibrium, $1018\ V^2 = 3.533\ W$
$V^2 = 0.00347$ W (lbs)
V (ft/sec) $= (0.00347$ W (lbs)$)^{½}$

For overpack with minimum MPC Weight (lbs) $V = (0.00347 \times 303000)^{½} = 32.4$ ft/s (9.9 m/s)
For overpack with full MPC Weight (lbs) $V = (0.00347 \times 360000)^{½} = 35.3$ ft/s (10.8 m/s)

To summarize, the flood required to slide the storage cask is at least 23.6 ft/s (7.2m/s), and the flood required to tip-over the storage cask is at least 35.3 ft/s (10.8 m/s).

A.4.9.6 Analysis for High Winds

An analysis for high winds (tornado) was performed with the following assumptions:

- Storage cask is assumed to be subjected to a constant wind force for full height.
- Storage cask is assumed to be rigid.
- μ, the coefficient of friction between steel plate and concrete pad is assumed to be 0.25.
- Storage cask is assumed to pivot about a fixed point at the outer edge of the contact surface.
- Surface area of the storage cask subject to wind = 231.25 x 132.5 / 144 = 212.78 ft^2 or 19.8 m^2
- C_d, the drag coefficient = 1.0

Sliding Evaluation

Applied Force (lbs) = C_d · Velocity head · Area
= 1.0 x (ρ · V^2 / 2 g) x Area Where ρ = air density = 0.07651 lb/ft^3 @ 15 °C; V is in ft/sec; g is in ft/sec^2
= 0.07651 / (2 x 32.2) x V^2 x Area
= 0.00119 x (5280/3600)^2 x V^2 x Area Where V is converted to mi/h
= 0.00256 x V^2 x Area
= 0.00256 x 212.78 x V^2
= 0.5447 V^2

Resisting Force = μ · W where μ is coefficient of friction; W is weight (lbs)
= 0.25 W (lbs)

For equilibrium, 0.5447 V^2 = 0.25 W
V^2 = 0.459 W
V (mi/hr) = $(0.459\ W)^{½}$

For overpack with minimum MPC Weight (lbs) V = $(0.459 \times 303000)^{½}$ = 373 mi/h or 600 km/h

For overpack with full MPC Weight (lbs) V = $(0.459 \times 360000)^{½}$ = 406 mi/h or 653 km/h

Tip-Over Evaluation

Applied Force = 0.5447 V^2 Where V = wind in mi/h

Applied Moment = Force · Height of A.G.
= 0.5447 V^2 x 118.46/12
= 5.377 V^2 lb-ft

Resisting Moment = W · Diameter / 2 where W is weight
= (132.5/24) W = 5.52 W lb-ft

For equilibrium, 5.377 V^2 = 5.52 W
V^2 = 1.02675 W
V = $(1.02678\ W)^{½}$

For overpack with minimum MPC Weight V = $(1.02675 \times 303000)^{½}$ = 558 mi/h (898 km/h)

For overpack with full MPC Weight V = $(1.02675 \times 360000)^{½}$ = 608 mi/h (978 km/h)

To summarize, the wind speed required to slide the storage cask is at least 653 km/hr (406 mi/hr), and the wind speed required to tip-over the storage cask is at least 978 km/hr (608 mi/hr). The design wind speed for the plant is 580 km/hr (360 mph).

A.4.10 Question 10

If the storage cask tips over on the concrete pad, what would be the stresses in the MPC?

To calculate accurate stresses in the MPC would require more than simplified analytical methods. Since the Reference A.1 report has already performed refined analyses, often using detailed finite element models, it would be best to utilize their results and scale the stresses to suit the scenario/case being evaluated. Therefore, the stress results from the Reference A.1 report will be used to tabulate the stresses in the MPC attributable to the tip-over case, as well as the vertical "end drop" case. The end drop case is also included in this calculation because other calculations refer to this calculation to respond to some of the other questions. For example, stresses in the MPC attributable to transfer cask drop (Questions 3 & 4) refer to this calculation for a more complete listing of stresses.

For each type of loading, the acceleration and stresses are provided. If another calculation refer to this calculation for stresses, then the stresses presented herein should be scaled by the ratio of accelerations ($A_{New\ Ques.}/A_{Ques.\ 10}$). Scaling these stresses to higher acceleration values determined in other calculations is conservative.

Stresses in the MPC are provided for the fuel basket, basket supports, MPC shell, lid, and baseplate based on Reference A.1, Tables 3.4.3, 3.4.4, and 3.4.6. Maximum stresses are presented for the end drop case and the tip-over case for the MPC components listed above. The acceleration values corresponding to these stresses are also provided to permit scaling if needed in other calculations. For the tip-over case, two orientations of the basket walls with respect to the ground were considered, 0 degree and 45 degrees. The stresses and corresponding accelerations are summarized in the Table A.6.

A.4.10.1 Non-Mechanistic Tip-Over

Non-mechanistic tip-over refers to the case where the storage cask tips over attributable to the center of gravity of the cask passing over the point of rotation without any initial force or velocity. This case is non-mechanistic because there is no design basis type loading that would cause the cask to tip-over. It is presented to have a sense of what could be expected from a scenario that causes storage cask to be tilted to the point where it tips over. The maximum stress in the MPC, from Table A.6 for the tip-over case, is 406.5 MPa (58,959 psi). This is based on the Reference A.1 report which calculated the stress in the MPC shell using a finite element model of a slice of the MPC and fuel baskets subjected to an acceleration of 45 g. Under this loading, the MPC and fuel baskets deform outward until portions of the MPC shell reach the rigid boundary of the storage overpack inner steel shell. This analysis is considered conservative because it is based on a linear elastic approach. This stress of 406.5 MPa (58,959 psi) needs to be multiplied by a dynamic load factor of 1.04. Before applying the dynamic load factor, stresses attributable to internal pressure of 0.69 MPa (100 psi) must be removed, and then added after applying the dynamic load factor.

Stress attributable to 689 kPa (100 psi) internal pressure for the MPC shell thickness of 1.27 cm (0.5 inch) and an average diameter of 1.74 meter (68.375 inches or 5.7 feet) is calculated by $p \cdot r / t = (100 \cdot 68.375/0.5)/0.5 = 6{,}838$ psi or 47.1 MPa.

Stress in the MPC for tip-over = (58959-6838) · 1.04 + 6838 = 61,044 psi or 421 MPa

So, the maximum circumferential stress in the MPC shell is approximately 421 MPa (61,044 psi) at 4.53 m (178.5 inches or 14.9 feet) above the bottom of the MPC. The maximum calculated stress is less than the allowable stress intensity of 450 MPa (65,200 psi) under Level D Service Condition of the ASME Code. Therefore, it does not cause the failure of the MPC.

The stress intensity of the MPC shell at the junction with the baseplate is the combination of stress attributable to internal pressure and the stress attributable to g value caused by tip-over. The stress intensity attributable to internal pressure of 0.69 MPa (100 psi), is 303 MPa (43,986 psi), based on the finite element analysis from Reference A.13. The stress intensity attributable to the tip-over is negligible at the MPC shell junction with the baseplate.

The total stress intensity at that junction is nearly the same as the stress caused by the internal pressure alone, which is less than the allowable stress intensity for Level D Service Condition of the ASME Code. Therefore, it does not cause the failure of the MPC.

If the storage cask tips over on another storage cask or on the ISFSI pad, calculations demonstrate that the studs retaining the lid on the overpack will resist the impact loads. In addition, the struck cask(s) will not tip-over.

A.4.11 Question 11

If the storage cask tips over, will the impact of the cask tipping over on another storage cask or on the concrete pad cause the overpack lid to be dislodged such that the MPC could slide out?

The bounding case is when the storage cask falls onto the concrete pad because this causes a larger acceleration. An analysis of the overpack lid integrity has already been performed by Reference A.1, Section 3.4.4.3.2.2, Appendix 3.K, and Appendix 3.L. Section 3.4.4.3.2.2 of Reference A.1 provides a summary of the overpack lid evaluation. Reference A.1, Appendix 3.K provides the stress analysis of the overpack lid. The Reference A.1, Appendix 3.L provides the calculation that demonstrates that the 4 studs hold the lid in place. For the reader's benefit the relevant portions of Appendix 3.K and Appendix 3.L are reproduced below.

A.4.11.1 Appendix 3.K, Lid Stress Analysis

Appendix 3.K describes the analysis of the lid attributable to the tip-over of the storage cask. It states that the maximum acceleration at the top of the overpack lid is 49 g as determined in Reference A.1, Appendix 3.A. Using the 49 g loading, the following lid components were checked in Reference A.1:

(1) Lid Top Plate Stress Analysis (Plate Bearing Stress at Bolt Holes)
(2) Lid Shell-To-Lid Top Plate Weld
(3) Shield Block Shells-To-Lid Top Plate Weld
(4) Lid Shell Stress Evaluation

Reference A.1, Section 3.4.4.3.2.2 summarizes the limiting stress of the lid to be as follows:

τ = 61.6 MPa (8,940 psi)
τ (allowable) = 202.7 MPa (29,400 psi)
F actor of Safety = 3.29

A.4.11.2 Appendix 3.L, HI-STORM Lid Top Plate Bolting

The Appendix 3.L calculation shows that the four studs of 8.9 cm (3.5 inches) diameter holding the lid in place have sufficient strength. The calculation uses 48.5 g as the acceleration attributable to the tip-over based on Reference A.1, Table 3.A.4. Using a weight of 10,433 kg (23,000 lb) for the lid times 48.5 g divided by the four studs result in a shear load on each stud equal to 126,099 (278,000 lb). This results in a shear stress as follows:

τ (bolt) = 231.8 MPa (33,620 psi) per bolt
τ (allowable) = (min. of $0.42S_u$ or $0.6\ S_y$) = 420 MPa (60,900 psi)
Factor of Safety = 1.81

Appendix 3.L also calculated the tensile stress attributable to (1) bending of the stud as a result of the lateral load acting on the stud over the thickness of the lid plate and (2) the pre-load of 407 N·m (300 lb-ft). The total tensile stress was calculated to be as follows:

σ = 98,260 (bending) + 1,124 (pre-load) = 99,384 psi (685 MPa)
σ (allowable) = S_u = 1000 MPa (145,000 psi)
Factor of Safety = 1.46

Appendix 3.L then calculated the combined effect of tension and shear using an interaction equation which resulted in a factor of safety of 1.29.

It appears that the Reference A.1 report did not consider the effect of centrifugal force attributable to rotation of the storage cask. The centrifugal force would cause the MPC to push against the overpack lid imposing loads on the lid and studs. To determine the significance of this, the tensile stress on the studs attributable to centrifugal force was evaluated. The stress was calculated to be as follows:

σ (centrifugal force) =19.7 MPa (2,857 psi)

This stress would not be in addition to the pre-load but in-place of the pre-load because this load would relieve the pre-load. Considering tension only and re-calculating the factor of safety, it reduces from 1.46 to 1.43 (a very small reduction). Considering shear and tension interaction, the factor of safety also shows a slight reduction from 1.29 to 1.26.

Based on the above discussion, it can be concluded that the overpack lid and studs are structurally adequate to resist the loads attributable to a tip-over of the storage cask and, thereby, will prevent the MPC from sliding out of the storage cask.

A.4.12 Question 12

The explosion-related shock waves that should be evaluated are those generated from (1) an explosion from a typical tanker trailer containing explosive materials (gasoline, liquid/natural gas) at a distance of 914 meters (3,000 feet) from the storage cask, and (2) an explosion of a natural gas pipeline at 7.2 km (4.5 mi) from the storage cask. Would the structural integrity of the cask system be in jeopardy if the shock waves caused by the postulated explosions are applied? If not, provide the supporting arguments.

Event A - Tanker Trailer at 914 meters (3,000 feet)

Evaluation of Event A was conducted utilizing Reference A.22. Using the recommended Trinitrotoluene (TNT) equivalence factor of 240% and 22,680 kg (50,000 lb) cargo weight, the effective TNT weight is 54,431 kg (120,000 lb). From Equation (1) of Reference A.22, the peak transient pressure would be 1 psi at 677 meters (2,220 feet). At 914 meters (3,000 feet), the peak pressure would be less than 6.9 kPa (1 psi). The HI-STORM 100 cask (storage cask) is designed for a 69 kPa (10 psi) peak transient external pressure. Therefore, at 914 meters (3,000 feet), the peak pressure attributable to the explosion would be less than 1/10 the pressure magnitude that the storage overpack is designed for.

Event B - Pipeline at 7.2 km (4.5 mi)

Evaluation of Event B was conducted utilizing References A.22 and A.23, which developed the probability of exceeding 3 psi external overpressure on the containment building of a proposed plant from a 21-inch ID pipeline containing methane at 4.9 MPa (720 psi) at a distance of 808 meters (2,650 feet). The best estimate annual probability of exceedance was 6.0×10^{-7}/yr. Considering uncertainties, the range was 3.8×10^{-8}/yr to 2.3×10^{-6}/yr. Considering the higher allowable external pressure 69 kPa (10 psi) versus 21 kPa (3 psi), the much greater distance of 7.2 km (4.5 mi) versus 0.8 km (0.5 mi), and the smaller pipe ID (12-inch versus 21-inch) for the present case, the annual probability of accedence should be significantly lower, perhaps by two to three orders of magnitude.

Reference A.22 does not address pipelines because of uncertainty associated with the formation of combustible gas clouds. However, for comparison to Event A, the equivalent of 6 river vessels [(27,215,542 kg (60,000,000 lb cargo)] simultaneously exploding at 7.2 km (4.5 mi) would produce a transient pressure of 6.9 kPa (1 psi) on the storage cask, based on Equation 1 of Reference A.22.

A.5 Conclusions

The events analyzed for the transfer cask are presented in response to Question 1 through 4. The conclusion reached from the analyses is that the strains in the MPC shell are well below the failure strain of the material. The MPC may yield and undergo some plastic deformation depending on the drop height, however, the MPC shell is not expected to rupture.

The event of MPC transfer from the transfer overpack to the storage overpack is addressed in response to Question 5. The results of the analysis demonstrate that the strains in the MPC are well below the failure strain of the shell material. The probability of the MPC shell rupture is discussed in Appendix B.

The events analyzed for the storage cask are presented in response to Questions 6 through 12. The analyses demonstrate that the storage cask will not slide significantly nor tip-over. For the Gulfstream IV impact analysis (Question 9) this conclusion is valid for an aircraft velocity less that 250 mph assuming worst case impact parameters. Furthermore, there will be no penetration of the storage overpack attributable to the Gulfstream IV impact or tornado missiles.

A.6 References

A.1. NRC Docket No. 72-1014, "Topical Safety Analysis Report for the Holtec International Storage and Transfer Operation Reinforced Concrete Module Cask System (HI-STORM 100 Cask System)," Holtec Report HI-951312, Volumes I and II, Revision 8, June 25, 1999.

A.2. LS-DYNA Computer Code and associated manuals, Version 960, March 2001, Livermore Software Technology Corporation.

A.3. American Concrete Institute, "Code Requirements for Nuclear Safety Related Concrete Structures (ACI 349)."

A.4. LS-DYNA Manual, Version 970, Rev. 3858, LSTC, April 2003.

A.5. ASME Code, Section III, 1989, American Society of Mechanical Engineers.

A.6. Holt, J., H. Mindlin, O. C, *Structural Alloys Handbook*, CINDAS/Purdue University Press, 1996.

A7. NRC Docket No. 72-1014, "HI-STORM Final Safety Analysis Report," Holtec International Report HI-2002444, Revision 0.

A.8. DOE Fundamentals Handbook, Material Science, Volume 2 of 2, DOE-HDBK-1017/2-93, January 1993, U.S. Department of Energy, Washington, DC.

A.9. LLNL report, Dynamic Impact Effects on Spent Fuel Assemblies, by Ramsey Chun et al., Lawrence Livermore National Laboratory, Livermore, California, October 1987.

A.10. *TrueGrid Manual*, Version 2.1.0, XYZ Scientific Applications, Inc., September 7, 2001.

A.11. NUREG/CR-6608, Summary and Evaluation of Low-Velocity Impact Tests of Solid Steel Billet Onto Concrete Pads, by LLNL, February 1998.

A.12. U.S. Nuclear Regulatory Commission, Certificate of Compliance No. 1014, Appendix B, "Approved Contents and Designed features for the HI-STORM 100 Cask System."

A.13. Cook, R., and R. Klingner, "Behavior of Ductile Multiple-Anchor Steel to Concrete Connections with Surface-Mounted Baseplates," ACI Publication SP-130, 1999.

A.14. *ABAQUS/Explicit: User's Manual*, Version 5.8-19, Hibbitt, Karlsson, and Sorensen, Inc., Pawtucket, Rhode Island, 1998.

A.15. Idriss, I.M., and H.B. Seed, "Seismic Response of Horizontal Layers," *Journal of the Soil Mechanics and Foundation Division*, ASCE, Vol. 94, No. SM 4, July 1968.

A.16. Schnabel, P.B., J. Lysmer, and H.B. Seed, "SHAKE: A Computer Program for Earthquake Response Analysis of Horizontally Layered Sites," Report No. UCB/EERC-72/12, Earthquake Engineering Research Center, University of California, Berkeley, California, December 1972.

A.17. U.S. Army Corps of Engineers, Engineer Technical Letter No. 1110-2-339, March 1993.

A.18. U.S. Nuclear Regulatory Commission, NUREG-0800, "Standard Review Plan," Section 3.5.1.4, "Missiles Generated by Natural Phenomena," Rev. 2, July 1981.

A.19. DOE Standard 3014-96, "Accident Analysis for Aircraft Crash into Hazardous Facilities," October 1996.

A.20. U.S. Nuclear Regulatory Commission, NUREG/CR-5042, "Evaluation of External Hazards to Nuclear Power Plants in the United States," December, 1987.

A.21. NRC Docket No. 72-1008, "HI-STAR 100 Final Safety Analysis Report," Holtec Report HI-2012610, Rev. 0.

A.22. U.S. Nuclear Regulatory Commission, Regulatory Guide 1.91, "Evaluation of Explosions Postulated to Occur on Transportation Routes Near Nuclear Power Plants," Revision 1, February 1978 (For Comment).

A.23. Mechanics Research Inc., Report No. MRI-2687-75, "Nuclear Power Plant Risks from a Natural Gas Pipeline," prepared for Tennessee Valley Authority, Knoxville, Tennessee, August 2, 1974.

A.24. Braverman, J.I., J. Nie, R.J. Morante, N. Simos, and C.H. Hofmayer, "Accidental Drop Analyses of a Spent Fuel Dry Cask System," Brookhaven National Laboratory, BNL-Y6423-032905, March 2005.

A.25. Bjorkman, G.S., "The Buckling of Fuel Rods in Transportation Casks under Hypothetical Accident Conditions," *Proceedings of PATAM 2004,* Berlin, Germany, 2004.

A.26. U.S. Nuclear Regulatory Commission, "Buckling of Irradiated Fuel under Bottom End Drop Conditions," ISG-12, Revision 1, 1999.

APPENDIX B
CASK RESPONSE TO MECHANICAL AND THERMAL LOADS

APPENDIX B
CASK RESPONSE TO MECHANICAL AND THERMAL LOADS

B.1 Purpose and Scope

This appendix provides a more detailed analysis and discussion of the response of the multi-purpose canister (MPC) to the mechanical and thermal load events that could occur as a result of the sequence of actions that occur during the handling and transfer process, and conditions that could be experienced during storage. Toward that end, this appendix provides information in addition to that presented in the main body of the probabilistic risk assessment (PRA) report.

The scope of this appendix encompasses the range of possible responses to mechanical and thermal load scenarios and events that could pose challenges to the MPC. It is assumed that the MPC is built as designed (so fabrication errors are not included in the scope), and that materials are procured and components constructed to the quality standards set forth in the safety analysis report (SAR, Reference B.1) and the American Society of Mechanical Engineers (ASME) Boiler and Pressure Vessel (B&PV) Code.

Although weld metal typically has a higher strength than base metal, it is generally known that weld-deposited austenitic stainless steels, while very ductile, have a tendency to be less ductile than the wrought product. At the strain levels that may be encountered in beyond-design-basis events, such as severe drop impacts, this potential reduction in ductility of the deposited weld metal is important and, therefore, is considered in evaluating the structural integrity of the MPC.

B.1.1 MPC Description

In the HI-STORM dry storage cask system, the MPC acts as the confinement boundary. A drawing of the major welds of the MPC and its components is shown in Figure B.1. The MPC is made entirely of austenitic stainless steel. The cylindrical shell is constructed from one circumferential and four axial seam welds that join the 1.27-cm (0.5-inch) thick plates. The two axial welds on each side of the MPC are slightly offset at the circumferential weld. This cylindrical shell is then welded to a 6.35-cm (2.5-inch) thick baseplate. The MPC seam welds and shell-to-baseplate weld are then subjected to a hydrostatic test of 0.86 MPa (125 psi). The welds are fabricated in accordance with the specifications of ASME Code, Section III, Subsection NB. These are full-penetration submerged arc welds, which undergo dye-penetrant (PT), radiographic (RT), or ultrasonic (UT) examinations in accordance with Section V of the ASME Code, (Articles 2, 6, and 5 respectively). The acceptance criteria for the welds are those in Articles NB-5320, NB-5350, and NB-5360 for PT, RT, and UT examinations, respectively. They are not post-weld heat-treated to remove residual stresses.

After the cask is loaded with fuel, the MPC lid is welded to the shell. This 1.9-cm (0.75-inch) thick weld undergoes PT examinations after the root, intermediate and final weld passes. These lid welds are performed using the tungsten-inert-gas (TIG) process.

The vent and drain ports used for drying and inerting are welded closed with cover plates. These welds undergo a final PT examination and leak test. The MPC lid-to-shell weld and the vent and drain cover plate welds form the primary seal to the MPC lid. A closure ring is then placed on the MPC lid and welded to the shell and lid to form a redundant cask seal. These vent and drain cover plate welds and the ring welds are also made using the TIG process. This design ensures the cask environment is separated from the outside atmosphere by two independent lid welds.

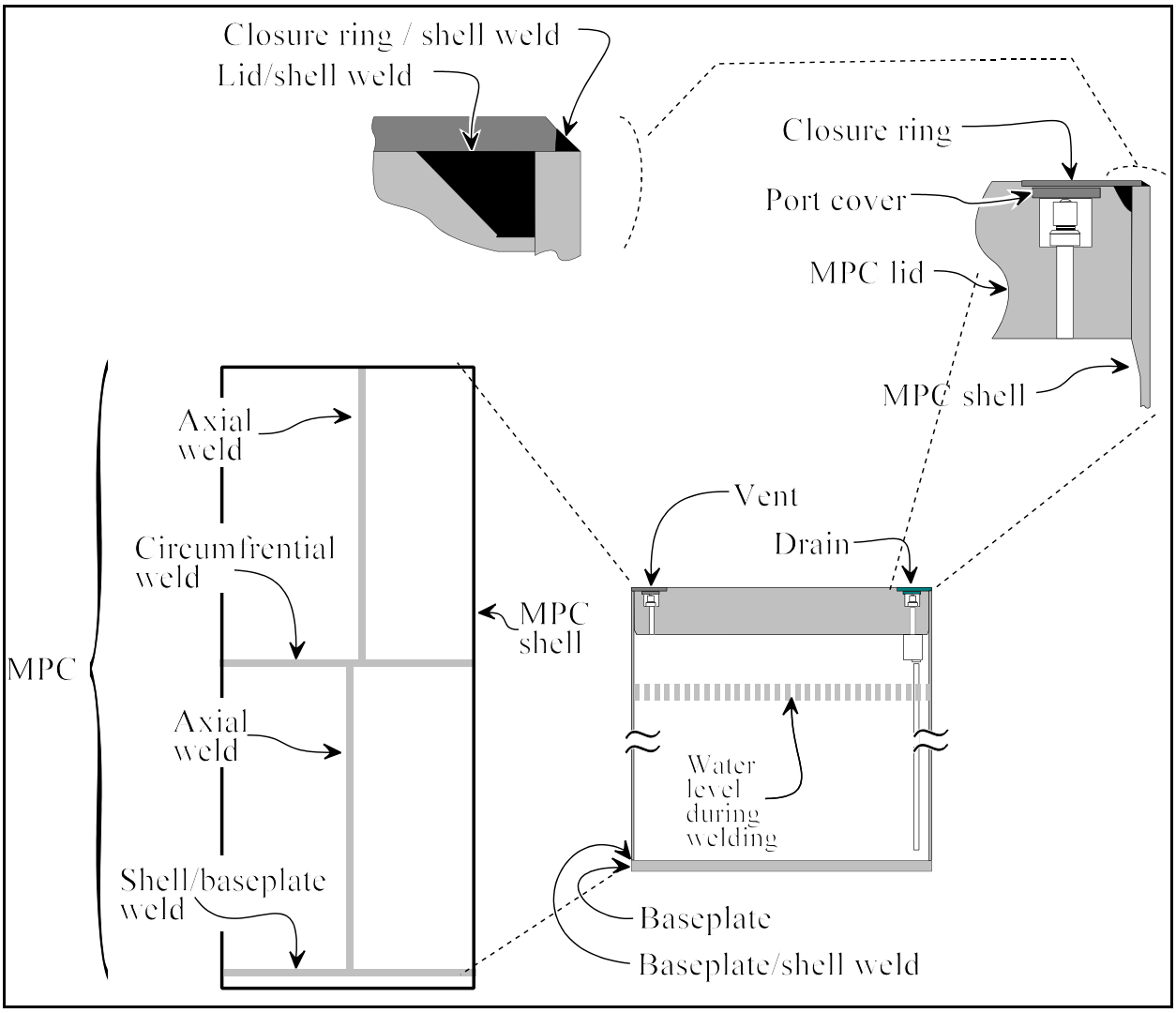

Figure B.1. Major Welds of the MPC

The MPC lid welds were not considered in the MPC failure assessments for the following reasons:

(1) The TIG process used on the lid generally produces a tougher weld than the SA weld used in the shell of the MPC.

(2) The redundancy of the lid design requires at least two welds to fail in order for MPC confinement to be compromised.

(3) The applied stresses at these locations are significantly less than the stresses in the MPC shell for all events analyzed.

B.1.2 MPC Stresses

Mechanical Loads

In the PRA, several mechanical impact accident scenarios were considered:

(1) Transfer Cask Drop onto Concrete Floor. This is a handling accident in which the transfer overpack (HI-TRAC) with the MPC inside is dropped on a concrete floor from various heights.

(2) Transfer Cask Drop onto Storage Cask. This is a handling accident in which the transfer overpack (HI-TRAC) with the MPC inside is being lowered from a height of up to 24.4 meters (80 feet) and falls on the storage overpack.

(3) MPC Drop. This is also a handling accident in which the MPC falls from a height of 5.8 meters (19 feet) when being lowered from the transfer overpack (HI-TRAC) to the storage overpack (HI-STORM).

(4) Storage Cask Drop. This is a transport accident in which the storage overpack (HI-STORM) with the MPC inside is dropped from a height of 0.30 meter (1 foot) onto concrete, gravel, and asphalt.

(5) Storage Cask Tip-Over. This is a storage accident in which the storage cask with the MPC inside is tipped over on the concrete storage pad.

The analyses used to calculate the MPC stresses for these events are described in Appendix A to this report.

The thermal analyses described in Section 4.2 indicated that steady-state conditions within the MPC under normal conditions would be attained prior to the initiation of the various handling and transfer events that move fuel out to the storage pad. These steady-state conditions are an internal pressure of 0.564 MPa (82 psi) with an MPC temperature that varies axially from 73 °C (163 °F) to 180 °C (356 °F).

It was assumed that the MPC is under normal steady-state conditions during the mechanical impact scenarios listed above. In addition, all of the fuel is assumed to be intact during these events. Fuel cladding failure would cause the internal pressure of the MPC to increase. If a mechanical impact event did cause fuel cladding failure, the resulting increase in pressure would not occur during the accident scenario. The increase in internal pressure attributable to fuel cladding failure would be a result of the mechanical loading; however, because of the extremely short duration of the impact, it would not affect the MPC internal pressure until after the mechanical loading is complete.

Thermal Loads

Only two thermal accident scenarios are considered in this PRA:

(1) Storage Cask External Fire. This is a storage accident in which the storage overpack (HI-STORM) with the MPC inside is exposed to an external fire resulting from a Gulfstream IV aircraft crash. A credible fire scenario will be less than 30 minutes. However, the analysis was performed for a fire duration of 3 hours.

(2) Storage Cask Vent Blockage. This is a storage accident in which the cooling vents of the storage overpack (HI-STORM) become completely blocked for a period of 20 years.

Under thermal loads, the only significant MPC stresses are attributable to internal pressure. Membrane stresses were calculated using the classical shell theory equations for pressurized cylinders:

$$\sigma_{axial} \equiv \frac{P \bullet r}{2 \bullet t} \tag{B.1}$$

$$\sigma_{hoop} \equiv \frac{P \bullet r}{t} \tag{B.2}$$

where: σ_{axial} = axial stress in psi
σ_{hoop} = hoop stress in psi
P = internal pressure in psi
r = MPC internal radius in inches (= 33.6875 in. or 85.5663 cm)
t = MPC wall thickness in inches (= 0.5 in or 1.27 cm)

The initial steady-state pressure of the MPC is 0.565 MPa (82 psi). Using Equations B.1 and B.2, the resulting axial and hoop stresses are 19.05 MPa (2,762 psi) and 38.1 MPa (5,525 psi), respectively.

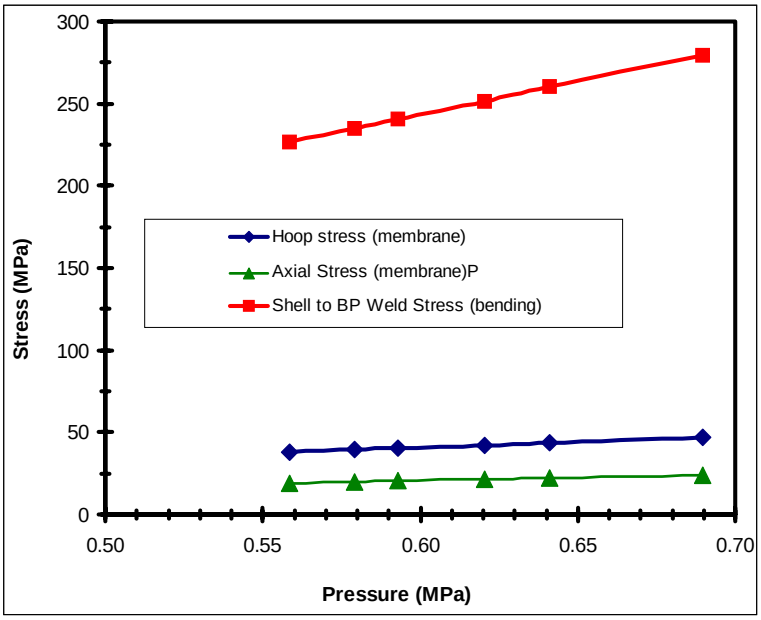

Figure B.2. MPC Stresses as a Function of Internal Pressure

The highest stress attributable to internal pressure loads occurs at the shell-to-baseplate connection. Section 3.4.4.3.1.2 of Reference B.1 analyzed the MPC stresses at various locations attributable to an internal pressure of 0.69 MPa (100 psi). These results showed that the total (membrane plus bending) stress at the MPC shell-to-baseplate connection was 303 MPa (43,986 psi). The axial membrane stress at this pressure is 23.6 MPa (3,419 psi). The difference in these values gives the bending stress acting on the shell-to-baseplate weld as 280 MPa (40,567 psi). The total stress at other pressures was assumed to be directly proportional to those at 0.69 MPa (100 psi). Therefore, at a pressure of 0.565 MPa (82 psi), the total stress at this location is only 248.7 MPa (36,068 psi). Subtracting the axial membrane stress of 19.05 MPa (2,762 psi) gives a bending stress of 229.6 MPa (33,306 psi).

The thermal accident scenarios listed above cause the MPC temperature and internal pressure to increase. The thermal analyses used to calculate the new MPC temperatures and pressures are described in Section 4.2.1.1, "Heatup Model," of the Dry Cask Storage PRA report. Figure B.2 shows the increase in axial membrane, hoop membrane, and shell-to-baseplate bending stress with increasing pressure.

B.1.3 MPC Failure Mechanisms

The following failure mechanisms were postulated for the MPC under mechanical and thermal loads:

(1) weld fracture
(2) exceeding the limit load
(3) creep rupture

All three failure mechanisms were considered for thermal events, while only weld fracture was postulated for mechanical impacts. For the purposes of this PRA, failure mechanisms are assumed to be independent. The probability of MPC failure is given as the sum of the failure probabilities from each failure mechanism.

The failure analysis for weld fracture was based on test data of Type 308 weld deposited stainless steel specimens, and specimens taken from the weldments of process water piping of nuclear production reactors constructed in the 1950s at the Savannah River Site. The mean and standard deviation of the failure strain data was calculated and adjusted for the effects of strain rate, temperature and state of stress. These results were used directly to determine the probability of weld fracture given the maximum strain calculated for each impact event. (Note that to simplify the evaluation, the adjustment for state of stress was applied to the calculated strain, rather than the failure strain.)

Failure analyses for limit load and creep rupture were conducted differently from the failure analysis for weld fracture attributable to mechanical loads. Failure models for limit load and creep rupture were created in a spreadsheet with an add-on module called @RISK® (from www.palisade.com). This module allows Monte Carlo simulations to be run in the spreadsheet by allowing values in the spreadsheet cells to be sampled from statistical distributions. The user specifies which cells are considered outputs, and the number of iterations to perform. For each iteration, the program samples values from all cells in which a statistical distribution is specified, recalculates the entire spreadsheet, and records the values in the specified output cells. The distribution of output values can then be plotted and analyzed.

Separate spreadsheets were developed for the limit load and creep rupture mechanisms. The entire MPC was modeled through a series of spreadsheets representing the different parts of the MPC. Input cells for the spreadsheets defined the material properties, flaw parameters, and applied stresses. The only inputs not sampled from statistical distributions were the applied stresses on the MPC. The statistical distributions used to describe the material properties and flaw parameters are described in Section B.1.5. The specific inputs and calculations performed in each failure model spreadsheet are described in detail in Sections B.1.6 and B.1.7. The spreadsheet cell specified as output identifies each iteration as either an MPC success or failure. This process is repeated many times in a Monte Carlo simulation. The probability of failure was calculated by dividing the total number of MPC failures by the total number of iterations performed.

The failure models used in this PRA do not attempt to predict the hole size in the MPC for a given failure probability. Any failure is assumed to create a hole in the MPC large enough to allow the particles and gases within the MPC to be released. This assumption was made because of the difficulty inherent in trying to predict the equivalent hole size produced from a particular MPC failure mode.

B.1.4 Weld Fracture Attributable to Mechanical Loads

Appendix A evaluated the structural response of the MPC for various end drop scenarios. The objective was to determine the maximum effective plastic strain (EPS) on the MPC confinement boundary for each of these scenarios. The analyses showed that the most highly stressed regions of the MPC are near the base of the cylindrical shell and in the weld joining the shell to the 2.5-inch-thick baseplate.

To determine if confinement boundary integrity is compromised, the maximum EPS in the MPC must be compared to an appropriate strain failure criterion. For a valid comparison, the conditions under which the maximum EPS is calculated, and the conditions under which the failure strain limit is measured, should be consistent. The comparison, therefore, must account for how the strain is measured, as well as the effects of strain rate, temperature and state of stress. It is the objective of this section to establish a valid basis for this comparison, and to estimate the probability of exceeding the failure strain limit for a given drop event.

Strain Measure

The LS-DYNA computer program used in the analysis for Appendix A to calculate MPC stresses and strains considers the reduction in cross-sectional area of the finite elements in the computation of stress within the element. Therefore, the program expects the user to input a true stress strain curve, which, by definition, considers the reduction in area in the computation of stress. Since the calculation of EPS within LS-DYNA is based on true strain, the failure criterion should also be based on a true strain measure.

The true strain at failure is calculated from the reduction in area (RA) within the necked-down region of a failed specimen as given in the following equation:

$$\varepsilon_t = \ell n\left(\frac{1}{1 - RA}\right) \tag{B.3}$$

where, ε_t = true strain of failure, and
RA = reduction in area

The MPC shell is fabricated from Type 304 stainless steel. (See the discussion in Section A.4.3.) Based on a review of References B.15 and B.16, a typical RA of Type 304 stainless steel at room temperature and static loading is 70%. Substituting RA equal to 0.70 into Equation B.3, the true strain at failure is 1.20 in/in or 120% strain. This value is consistent with typical true stress strain curves that can be found in Reference B.17 for Type 304 stainless steel.

Weld Metal Failure Data

In the analyses performed in Appendix A, no distinction is made between the base metal and weld metal in the MPC shell. Procurement of the weld material, which is typically Type 308 stainless steel, and fabrication of the MPC in accordance with the requirements of the ASME Code ensures that the weld strength is equal to or greater than the base metal. However, it is generally known that weld-deposited austenitic stainless steels (Type 308), although very ductile, have a tendency to be less ductile than the wrought (Type 304) product. At the high strain levels that may be encountered in beyond-design-basis events, such as severe drop impacts, this potential reduction in ductility of the deposited weld metal can be important to the structural integrity of the MPC shell.

In Reference B.18, 24 Type 308 weld-deposited metal specimens cut from fabricated weldments were statically tested at room temperature. The specimens were taken from both transverse and longitudinal orientations within the weldments. The mean value of the RA was 59.7% with a standard deviation of

9.1%. Using Equation B.3, this converts to a mean true strain at failure of 0.91 in/in. The mean true strain at failure minus one and two standard deviations are 0.71 in/in and 0.54 in/in, respectively.

In Reference B.19, the mechanical properties of archival process water system (primary coolant) piping and weld materials having approximately 6 years of service were measured. The process water system piping of the nuclear production reactors constructed in the 1950s at the Savannah River Site was composed primarily of Type 304 stainless steel with Type 308 stainless steel weld filler. Tensile properties were measured for base metal, weld metal and heat-affected zone (HAZ) materials. The test specimens represented both ASTM L-C and C-L orientations to allow comparison of the mechanical response for the cases of flaws oriented parallel and perpendicular to the pipe axis or rolling direction. The tensile properties of the archival piping material were found to be typical of recently produced commercial melts of Type 304 stainless steel piping. The values of the mean RA and standard deviation of the base metal, weld metal and HAZ material for static loading at room temperature are shown in Table B.1.

Table B.1. Reduction in Area Mean and Standard Deviation Test Results from Reference B.19

Stainless Steel Material	Mean Reduction in Area (RA)	Standard Deviation
Type 304 Base Metal	72%	9.0%
Type 308 Weld Metal	61%	10.0%
Heat-Affected Zone (HAZ)	71%	1.0%

The mean RA for the base metal of 72% in Table B.1 compares well to the typical values of 70% and 77% from References B.15 and B.16 respectively. Also, the mean RA for the weld metal of 61% and standard deviation of 10% compare well to the values of 59.7% and 9.1% cited in Reference B.18, discussed above. This data clearly shows that the 308 stainless steel weld metal is very ductile, although its ductility is slightly less than the ductility of the Type 304 base metal.

The RA data for Type 308 stainless steel weld metal at room temperature and static loading used in the evaluation herein includes all of the data in References B.18 and B.19 discussed above, as well as dynamic test data at low strain rates (0.05/sec) from Reference B.19. Combining this data of 37 tests yields a mean RA of 59.0% and a standard deviation of 9.7%. These values establish the basis for determining the probability of weld failure and assumes that the weld failure data is normally distributed.

Temperature and Strain Rate Effects

In all drop scenarios evaluated in Appendix A, the most highly stressed region of the MPC occurs within the bottom foot of the shell. (See Appendix A.) While the MPC is being moved in the HI-TRAC transfer cask, the temperature profile of the MPC shell, varies from 302 ºF at the bottom of the MPC to 445 ºF at the top (Reference B.1, Holtec HI-STORM FSAR, Table 4.5.4). The test data used to calculate the mean RA and standard deviation, discussed above, is for static loading at room temperature. Typical RA values for Type 308 weld metal as a function of elevated temperature are reported in Figure 7 of Reference B.18. The trend curve in the figure shows that at 302 ºF, the temperature at the bottom of the MPC shell, the ratio of RA at temperature to RA at room temperature is 0.90. This factor is be used to adjust the RA room temperature values to those that would be expected at the higher temperature at the bottom of the MPC.

Strain rate can also have an effect on the ductility of stainless steel weldments. Typical strain rates for the drop impact scenarios considered in Appendix A are on the order of 100/sec. Reference B.20 shows that

for strain rates of 1200/sec the ductility of stainless steel weldments deceases to about 88% of the static value. For a strain rate of 100/sec for Type 304 base metal, Reference B.15 shows that at 1,000 ºF RA is approximately 7% greater than the value at room temperature. These results are insufficient to draw any firm conclusions, but in the interest of conservatism, a strain rate reduction factor of 0.98 was selected based on the information in Reference B.20.

To account for both strain rate and temperature effects, the mean RA of 59.0% for weld metal was reduced by the factor 0.88 (0.90 x 0.98 = 0.88). This results in a mean RA of 52%, accounting for both strain rate and temperature. The standard deviation is assumed to remain the same at 9.7%. From Equation B.3, the true strain at failure of stainless steel weld metal in a uniaxial tension test, considering the effects of strain rate and temperature, can be estimated to be 0.73 in/in with a mean minus one and two standard deviations of 0.55 in/in and 0.40 in/in respectively. Table B.2 below shows the mean true strain at failure minus several standard deviations, along with the probability that the weld metal's true strain at failure is less than the tabulated value.

The probability of failure of stainless steel weld metal at the plastic strains given in Table B.2 are approximate, since the amount of test data capturing true strain at failure (or RA) of stainless steel weldments at elevated temperature and high strain rates is limited. Nonetheless, Table B.2 provides a reasonable estimate of weld failure probability in uniaxial tension at the strain rates and temperatures within the most highly stressed region of the MPC.

Table B.2. Mean True Strain at Failure minus Several Standard Deviations, and the Probability That the Weld Metal's True Strain at Failure Is less than the Tabulated Value

Standard Deviation from the Mean	True Strain at Failure (TSF) (in/in)	Probability the TSF is Less than the Tabulated Value [x < TSF]
0.0 (Mean)	0.73	0.5
0.5	0.64	0.3085
1	0.55	0.1587
1.5	0.47	0.0668
2	0.4	0.0228
2.5	0.32	0.0062
3	0.26	0.0013
3.5	0.2	0.00023
4	0.14	0.000032
4.5	0.087	0.000003
5	0.036	< 0.000001

Effect of State of Stress

For each drop scenario, the maximum EPS in the MPC shell was calculated in Appendix A. However, cracking of a stainless steel weldment cannot be determined by simply comparing the calculated maximum EPS to the true strain at failure even when temperature and strain rate have been considered. This is because the EPS was calculated from a complex three-dimensional state of stress, while the true strain at failure was derived from a one-dimensional state of stress. Unlike a one-dimensional state of

stress, a three-dimensional state of stress may constrain plastic flow in the material and lower the EPS at which failure occurs. This loss of ductility can be accounted for by the use of a triaxiality factor (TF), which is the ratio of normal stress to shear stress on the octahedral plane, normalized to unity for simple tension, as given by Equation B.4 (References B.21 and B.22):

$$Triaxiality\ Factor = \frac{\sigma_1 + \sigma_2 + \sigma_3}{\frac{1}{\sqrt{2}}\left[\left(\sigma_1 - \sigma_2\right)^2 + \left(\sigma_2 - \sigma_3\right)^2 + \left(\sigma_3 - \sigma_1\right)^2\right]^{1/2}} \quad \text{(B.4)}$$

where, σ_1 = maximum principal stress
σ_2 = intermediate principal stress
σ_3 = minimum principal stress

The reduction in ductility associated with the triaxial stress state is approximately equal to the true strain at failure in uniaxial tension divided by the TF. More precisely, the ratio of EPS at failure to the true strain at failure in uniaxial tension, which is called the ductility ratio (DR), is given by Equation B.5 (Reference B.23):

$$DR = 2^{\left(1 - TF\right)} \quad \text{(B.5)}$$

where, DR = the ductility ratio
TF = the triaxiality factor

Thus, to determine the actual strain at which weld cracking will initiate requires that either the calculated EPS or the true strain at failure be adjusted to account for the triaxial nature of the state of stress. [Note that TF = 1.0 represents uniaxial tension. TFs greater than 1.0 are produced by states of stress that constrain plastic flow, reduce ductility and result in a higher likelihood of failure for a given EPS. TFs less than 1.0 are produced by states of stress that enhance plastic flow, increase ductility and result in a lower likelihood of failure for a given EPS.]

Probability of Weld Failure

The probability that the true strain at which a weld fails is less than the calculated maximum EPS cannot be determined directly from Table B.2. To use Table B.2 to determine the probability of weld failure, the calculated maximum EPS must first be divided by the DR to adjust it for the effects of the triaxial stress state at the location where the EPS occurs. However, the location (element) where the maximum EPS occurs may not be the location most susceptible to failure. The location where the probability of failure is greatest is where the quotient of EPS divided by the DR results in the highest value. For example, in the case of the 100-foot drop of the transfer cask onto the concrete floor a maximum EPS of 0.256 in/in occurred in element 15997 on the inside surface of the MPC shell beneath the basket support, as shown in Figures A.13 and A.14. For this element, the TF is negative, indicating a very favorable state of stress, and the EPS adjusted for triaxiality is 0.13 in/in. For this lower EPS, the probability of failure decreases considerably. Thus, the element with the calculated maximum EPS does not necessarily control failure.

To determine the location where the maximum EPS adjusted for triaxiality occurs, a set of elements with high values of EPS and attributes likely to result in a high TF were selected for evaluation. For these elements, EPS, TF, DR, and adjusted EPS were calculated at each output time. This was done for the

30.5, 21.3, and 12.2 meter (100, 70, and 40 foot) drops of the transfer cask onto the concrete floor and for the 5.8 meters (19 foot) drop of the MPC into the storage overpack. For the 1.52 meter (5 foot) drop of the transfer cask onto the concrete floor and for drops of the transfer cask onto the storage overpack, the maximum EPS together with the maximum TF for a biaxial stress state of 2.0 were used to conservatively calculate the maximum EPS adjusted for triaxiality.

Transfer Cask and MPC Drop Events

For drops of the transfer cask falling onto the concrete floor, Table B.3 gives the calculated maximum EPS, the maximum EPS adjusted for triaxiality, and the probability of weld crack initiation. It is important to emphasize that the probability of weld crack initiation is calculated using the maximum EPS adjusted for triaxiality when using Table B.2. Table B.4 provides the same information for the drop of the transfer cask onto the storage overpack, and Table B.5 shows the results for the 19-foot drop of the MPC into the storage overpack.

Table B.3. Probability of MPC Weld Crack Initiation from the Drop of the Transfer Cask onto the Concrete Floor

Drop Height (ft)	Maximum EPS (in/in)	Maximum EPS Adjusted for Triaxiality (in/in)	Probability of Weld Crack Initiation (1)
5	0.024	0.048 (2)	< 0.000001
40	0.195	0.213	0.00036
70	0.24	0.285	0.0026
100	0.256	0.385	0.0196

(1) The term “weld crack initiation” or “cracking of the MPC weld” is used in place of “weld failure” or “failure of the MPC weld” to distinguish between a “crack” in the weld, that may not propagate through the entire thickness, and “failure” of the weld, which would imply a through thickness rupture of the weld and breach of the confinement boundary. When developing a weld failure criterion using uniaxial tension tests the terms failure, rupture and breach are synonymous. However, when the maximum EPS occurs on the surface of a region of high bending curvature, as shown in Figures A.14 and A.29, the initiation of a failure— a crack — does not necessarily result in a rupture or breach. Thus, some caution is required when using the word “failure” to describe what happens when a failure limit is reached at a point on the surface of a region with high curvature (strain gradient), especially when the energy input is limited.

(2) A maximum TF of 2.0 was used.

Table B.4. Probability of Weld Crack Initiation for the Drop of the Transfer Cask onto the Storage Overpack

Drop Height (ft)	Maximum EPS at Element 9421 (1) (in/in)	Maximum EPS Adjusted for Triaxiality (2) (in/in)	Probability of Weld Crack Initiation
5	0.0363	0.0726	0.000002
40	0.0601	0.1202	0.000014
80	0.0976	0.1952	0.000203

(1) See Table A.4, Note 2.
(2) A maximum TF of 2.0 was used.

Table B.5. Probability of Weld Crack Initiation for the 19-Foot Drop of the MPC into the Storage Overpack

Drop Height (ft)	Maximum EPS (in/in)	Maximum EPS Adjusted for Triaxiality (in/in)	Probability of Weld Crack Initiation (1)
19	0.456	0.623	0.282

(1) See Note 1 from Table B.3 and discussion below related to tearing of the basket support fillet welds for the 19-foot drop.

The 19-foot drop of the MPC into the storage overpack results in the highest probability (0.282) that a weld on the MPC confinement boundary will crack on impact. This result, as well as the results for the other drop events, must be viewed as a very conservative estimate of the probability of MPC confinement boundary breach or rupture. There are two reasons for this:

(1) The probability of weld crack initiation is the probability that the most highly stressed element of the six elements through the thickness of the MPC shell will fail. Because this occurs in a region of high curvature in a highly indeterminate structure, the failure of one element on the surface of the shell will result in the redistribution of internal forces to the stiffer (in bending) adjacent elements on the surface, with little of the internal forces redistributing to the lower stressed interior elements through the thickness. This makes it more likely that additional surface elements will fail, and less likely for the failure to propagate through the thickness. In addition, the process itself is contained, since the total kinetic energy is limited, as in all impact events.

(2) The maximum EPS of 0.456 in/in and the adjusted maximum EPS of 0.623 in/in result from constraint imposed on the MPC shell. This constraint is created by the discontinuous basket support "stiffeners" that terminate 3.8 cm (1.5 inch) above the MPC baseplate. The constraint on the shell imposed by the support is maintained by the 2.5 cm (1-inch) long 3.2 mm (⅛-inch) fillet weld that attaches the bottom portion of the support to the shell. Figure B.3 shows the deformation and contours of EPS in this region, and Figure B.4 shows the shear deformation and the very evident shear-lag in the elements of the support at the location of the fillet weld between Nodes 18469 and 21444. (This basket support is the same one shown in Figure A.26.) In the likely event that this weld tears during impact, the local constraint on the shell is relieved and the shell will behave locally as though it were unstiffened. A published analysis (Reference B.24) of a 7.6 meters (25 foot) drop of the MPC onto a rigid surface, in which the basket supports were not included, produced a maximum EPS of 0.21 in/ in, which is a significant reduction from the value of 0.456 in/in when the attachment welds remain intact. Thus, the potential tearing of these small attachment welds can significantly reduce the probability that a weld on the confinement boundary may crack.

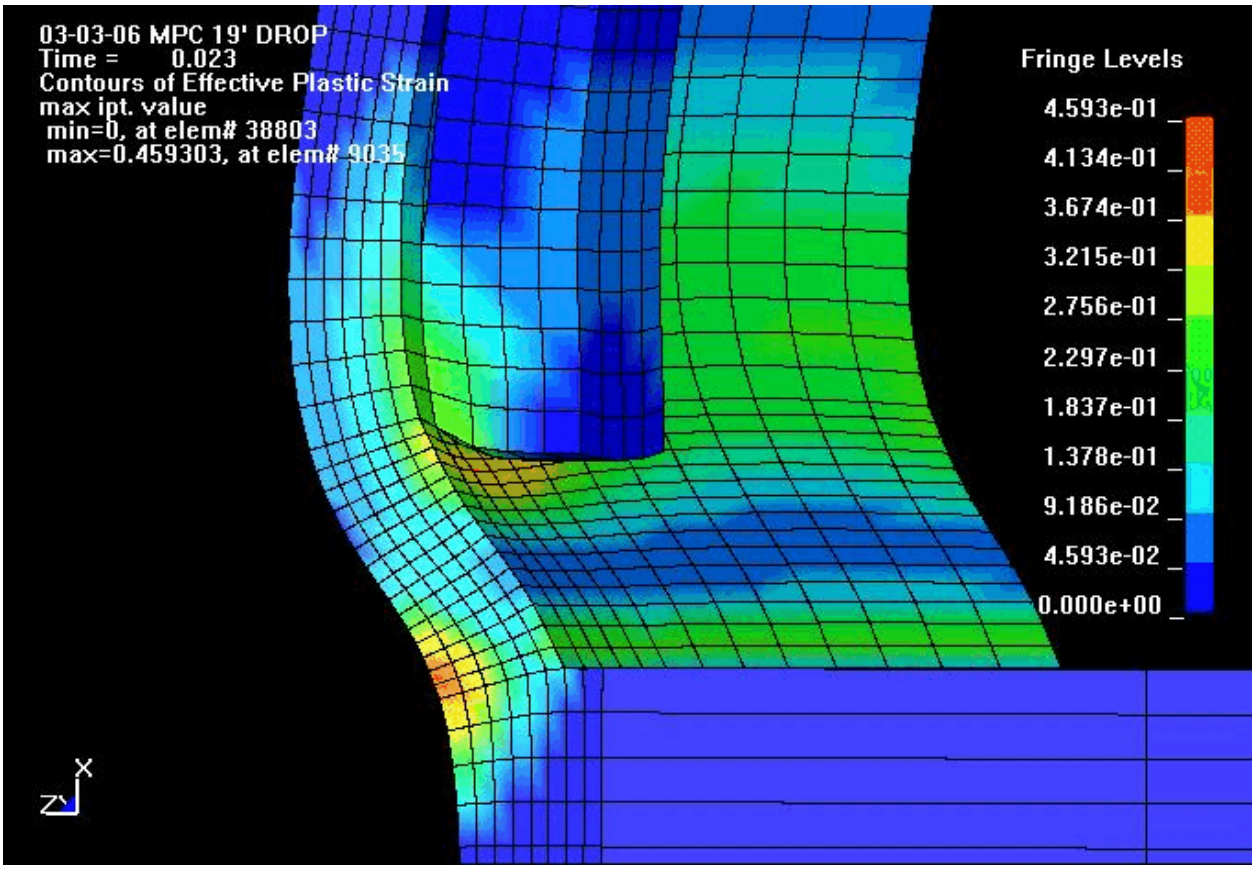

Figure B.3. Deformation and Contours of EPS in the Vicinity of the Stitch Weld Attaching the Basket Support to the Shell

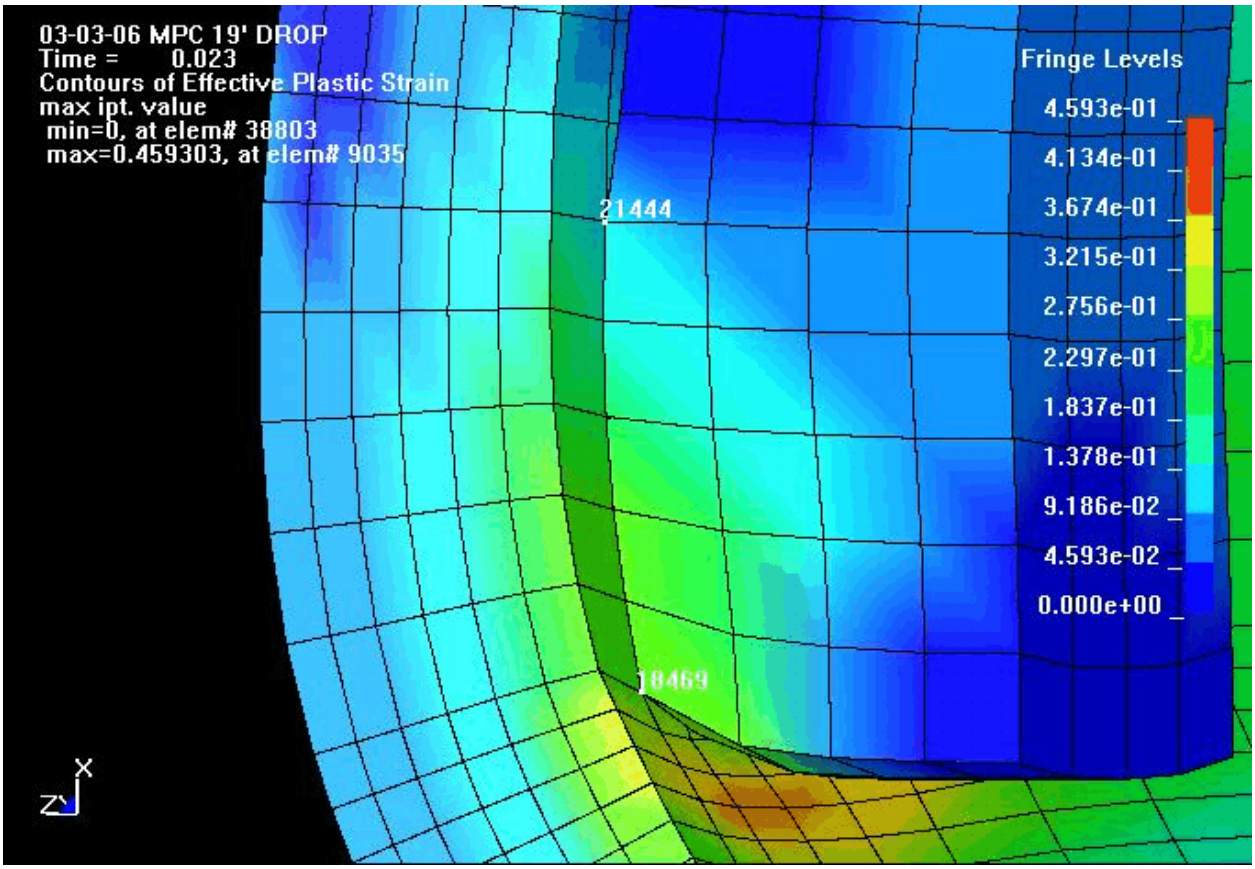

Figure B.4. Shear Deformation and Shear-Lag Are Evident in the Elements of the Support at the Location of the Fillet Weld Between Nodes 18469 and 21444

Storage Cask Tip-Over Event

The storage cask tip-over event is discussed in Section A.4.6. The maximum stresses in the MPC for this event are given in Table A.6 and come from the HI-STORM 100 SAR (Reference B.1). The maximum stress (stress intensity) is approximately 406.8 MPa (59,000 psi), which is less than the allowable stress intensity for primary membrane plus bending of 449.5 MPa (65,200 psi) for this service level. For the purpose of evaluating weld fracture, the allowable stress of 449.5 MPa (65,200 psi) is used herein. In accordance with the ASME B&PV Code, the maximum stress would have been calculated from a linear-elastic analysis, and in this case the analysis produced stresses that exceed the yield stress of 262.0 MPa (38,000 psi) at temperature (Table A.2). Therefore, the maximum stress of 449.5 MPa (65,200 psi) cannot be converted to a strain simply by dividing by the elastic modulus.

Since the weld failure criterion is based on plastic strain, the elastically calculated maximum stress must be converted to a plastic strain that could have reasonably resulted from a non-linear analysis of the same event. Also, since the "damage" that can be inflicted on the MPC during a tip-over event is energy-limited, an energy balance approach can be used to estimate the maximum plastic strain. In this approach, the strain energy per unit volume absorbed at the point of the elastically calculated maximum stress is equated to the strain energy per unit volume absorbed through elastic-plastic deformation of the material using the idealized engineering stress-strain curve in the LS-DYNA program that was used for the drop analyses.

Using this approach and the data in Table A.2, the calculated maximum plastic strain is 0.0031 in/in. Since the maximum membrane plus bending stress must have occurred on the boundary, the maximum value of the TF is 2.0. Therefore, the maximum adjusted plastic strain is 0.0062 in/in. Assuming that the maximum plastic strain occurs at one of the axial or circumferential welds, the probability of weld crack initiation from Table B.2 is less than 0.000001. This result is summarized in Table B.6.

Table B.6. Probability of Weld Crack Initiation from Storage Cask Tip-Over

	Estimated Maximum Plastic Strain (in/in)	Maximum Plastic Strain Adjusted for Triaxiality (in/in)	Probability of Weld Crack Initiation (1)
Storage Cask Tip-Over Event	0.0031	0.0062	< 0.000001

(1) See Note 1 from Table B.3.

B.1.5 Failure Analysis Inputs for Limit Load and Creep Rupture

In order to determine the probability of MPC failure for the limit load and creep rupture, distributions of the following material properties are needed at various temperatures:

(1) yield strength
(2) tensile strength
(3) creep rupture strength

In addition to the material properties, stress concentration factors are also needed.

The MPC may be constructed from several different types of austenitic stainless steels. In general, the tensile and creep rupture properties of Type 304 stainless steel tend to be more limiting regarding MPC failure than other types of austenitic steels. Therefore, yield, tensile and creep rupture strengths used in the failure analyses are based on Type 304 stainless steel. Comparisons between the material properties of Type 304 and 316 are given in the sections that follow.

Yield and Tensile Strength

The yield and tensile strength of austenitic stainless steel decreases as the material temperature increases. Figure B.5 compares representative yield and tensile strengths for Type 304 and 316 stainless steel over a wide range of temperatures (References B.2 and B.3). Even though the *required* minimum room temperature yield and tensile strengths for these two materials are identical, this figure shows that *typically* Type 316 has higher yield and tensile strengths between 24 °C (75 °F) and 816 °C (1,500 °F). Therefore, the tensile properties used in the failure analysis of the MPC are for Type 304 stainless steel.

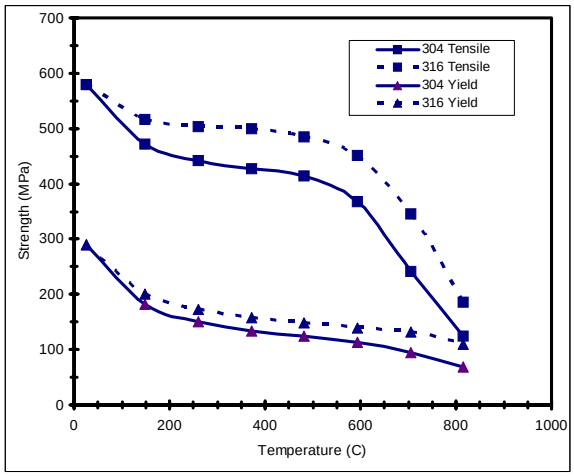

Figure B.5. Yield and Tensile Strength Behavior of Type 304 and 316 Austenitic Stainless Steels at Elevated Temperatures (References B.2–B.3)

Table B.7 describes the reduction in yield and tensile strength of Type 304 stainless steel with temperature as a fraction of the yield and tensile strength at room temperature (Reference B.3). This same reference cites mean room temperature yield and tensile strengths for this material as 254 MPa (36,900 psi) and 578 MPa (83,900 psi), respectively. The standard deviations are 44 MPa (6,400 psi) for yield strength and 30 MPa (4,300 psi) for tensile strength.

Best estimate yield and tensile strengths at various temperatures were determined using these reduction ratios and room temperature properties. Table B.7 lists these best estimate values at temperatures up to 871 °C (1,600 °F).

The ASME Code places minimum allowable yield and tensile strengths for this material at temperatures up to 427 °C (800 °F). These minimums are also shown in Table B.7. At temperatures above 427 °C (800 °F), the minimum allowable yield and tensile strengths were determined by applying the reduction ratios to the ASME minimums at room temperature.

Table B.7. Reduction in Yield and Tensile Strengths of Type 304 Stainless Steel as a Function of Temperature

Temperature °C (°F)	Yield Strength Reduction Ratio	Best Estimate Yield Strength[1] Mpa (psi)	Minimum Yield Strength[2] Mpa (psi)	Tensile Strength Reduction Ratio	Best Estimate Tensile Strength[3] Mpa (psi)	Minimum Tensile Strength[4] Mpa (psi)
24 (75)	1	254 (36900)	207 (30000)	1	578 (83900)	517 (75000)
38 (100)	0.96	244 (35424)	207 (30000)	0.97	561 (81383)	517 (75000)
93 (200)	0.83	211 (30627)	172 (25000)	0.86	497 (72154)	490 (71000)
149 (300)	0.75	191 (27675)	155 (22500)	0.80	463 (67120)	455 (66000)
204 (400)	0.69	176 (25461)	143 (20700)	0.78	451 (65442)	444 (64400)
260 (500)	0.65	165 (23985)	134 (19400)	0.77	445 (64603)	438 (63500)
316 (600)	0.61	155 (22509)	125 (18200)	0.77	445 (64603)	435 (63100)
371 (700)	0.59	150 (21771)	119 (17300)	0.77	445 (64603)	431 (62500)
427 (800)	0.56	142 (20664)	114 (16600)	0.76	440 (63764)	425 (61700)
482 (900)	0.54	137 (19926)	112 (16200)	0.74	428 (62086)	383 (55500)
538 (1000)	0.52	132 (19188)	108 (15600)	0.70	405 (58730)	362 (52500)
593 (1100)	0.49	125 (18081)	101 (14700)	0.63	364 (52857)	326 (47250)
649 (1200)	0.47	120 (17343)	97 (14100)	0.55	318 (46145)	284 (41250)
704 (1300)	0.44	112 (16236)	91 (13200)	0.46	266 (38594)	238 (34500)
760 (1400)	0.39	99 (14391)	81 (11700)	0.35	202 (29365)	181 (26250)
816 (1500)	0.31	79 (11439)	64 (9300)	0.25	145 (20975)	129 (18750)
871 (1600)	0.2	51 (7380)	41 (6000)			

Notes:

1. Best estimate yield strengths based on reduction ratios and room temperature yield strength of 36,900 psi (Reference B.3).
2. Minimum yield strengths from 24 °C (75 °F) to 427 °F (800 °F) taken from ASME Code. Minimum yield strengths from 482 °C (900 °F) to 871 °C (1,600 °F) calculated using reduction ratios and ASME minimum at 24 °C (75 °F).
3. Best estimate tensile strengths based on reduction ratios and room temperature tensile strength of 578 MPa (83,900 psi) (Reference B.3).
4. Minimum tensile strengths from 24 °C (75 °F) to 427 °F (800 °F) taken from ASME Code. Minimum tensile strengths from 482 °C (900 °F) to 871 °C (1,600 °F) calculated using reduction ratios and ASME minimum at 24 °C (75 °F).

Figure B.6 shows the decrease in the best estimate and minimum tensile properties of Type 304 stainless steel at increased temperatures. The minimum allowable tensile strengths are very close to the best estimate values. Above 427 °C (800 °F) this difference increases. For the yield strengths, the difference between the minimum and best estimate values slowly decrease at higher temperatures.

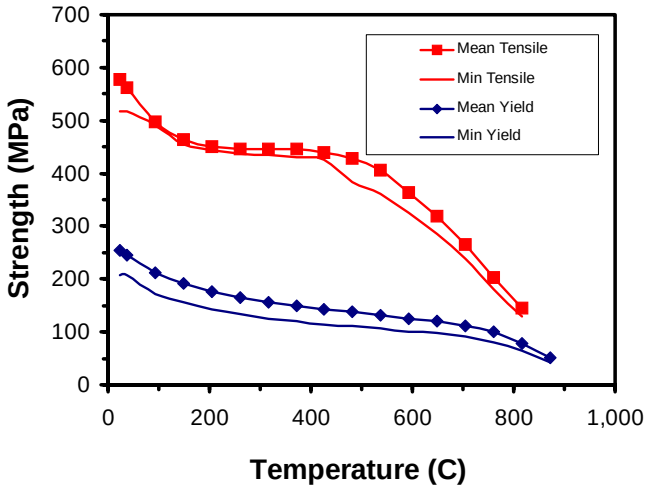

Figure B.6. Yield and Tensile Strength Behavior of Type 304 Austenitic Stainless Steels at Elevated Temperatures (Reference B.3)

It was assumed that both the yield and tensile properties of Type 304 stainless steel at any given temperature could be described by a normal distribution with a mean equal to the best estimate value at that temperature. In addition, the standard deviations defined above were assumed to apply at all temperatures. Tensile properties at temperature between those listed in Table B.7 were calculated by interpolation.

Type 304 stainless steel base metals are typically welded using Type 308 as the weld filler metal. The minimum required room temperature yield strengths and tensile strengths are identical for both of these materials. Table B.8 lists some elevated temperature tensile properties for Type 308 austenitic stainless steel.

Table B.8. Tensile Properties for Type 308 Stainless Steel at Elevated Temperatures

Temperature °C (°F)	Yield Strength MPa (Psi)	Tensile Strength MPa (Psi)
482 (900)	310 (45,000)	444 (64,400)
593 (1100)	261 (37,800)	301 (43,700)
649 (1200)	222 (32,200)	239 (34,700)

Comparing Tables B.7 and B.8 shows that the expected weld material (Type 308) is expected to have superior tensile properties to that of the base metal (Type 304). Therefore, the properties listed in Table B.1 can conservatively be used to describe the MPC welds and plates.

Creep Rupture Strength

Creep rupture strength of Type 304 stainless steel was compiled from data in the open literature (References B.2 – B.7). It should be noted that this creep rupture data is not comprehensive. The time and temperature conditions for this data were converted to the Larson-Miller parameter (Reference B.7):

$$LarsonMiller \equiv T \bullet (C + \log(t_r)) \qquad \text{(B.6)}$$

where: T = temperature in °R (= °F + 459.67)
C = constant (18 for austenitic stainless steel)
t_r = time to rupture in hours

Figure B.7 shows the stress at creep rupture data plotted as a function of this Larson-Miller parameter for Types 304, 316, and 308 austenitic stainless steels. For a given Larson-Miller parameter value, Type 316 tends to have a higher creep rupture stress. The data for Type 304 and 308 are similar. Therefore, the creep rupture data used for the MPC failure analysis is based upon Type 304 material properties. This data is used to model both the plate and weld material properties.

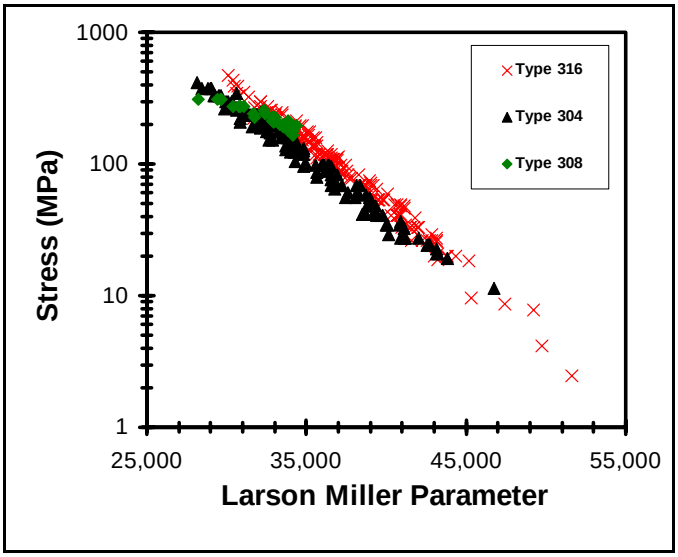

Figure B.7. Creep Rupture Properties of Type 304, 308, and 316 Austenitic Stainless Steels (References B.2 – B.7)

Figure B.8 is typically how creep rupture data is presented. However, for the purposes of developing a creep rupture model, the Larson-Miller parameter is needed as a function of the applied stress. Figure B.7 shows the Larson-Miller parameter plotted as a function of the log of applied stress for only Type 304 materials. The data was fit to a line with an R^2 value of 0.98. The equation of this line has a slope of -11,032 and a y-intercept of 81,404. The best fit, 95% upper bound, and 95% lower bound trend lines are also shown in Figure B.8.

At a given stress, there is some variability in the Larson-Miller parameter required to cause creep rupture of Type 304 stainless steel. It is assumed that this variability in Larson-Miller parameter is normally distributed about a mean value given by the best-fit line described

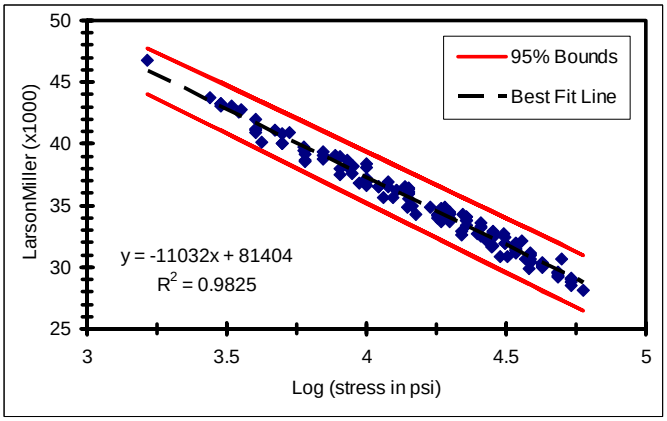

Figure B.8. Best Estimate and Bounding Larson-Miller Parameters as a Function of Log (Stress) for Type 304 Austenitic Stainless Steel

above. It is also assumed that the 95% bounds represent 2 standard deviations about this mean value. Therefore, both the mean and standard deviation of the Larson-Miller parameter vary with the applied stress.

Flaw Distribution

An analysis of the MPC welds was performed using the PRODIGAL computer code to obtain flaw distributions for the failure analyses. The PRODIGAL code is described in several of the references listed at the end of this report (References B.8–B.11). These references also describe a number of applications of the code to nuclear pressure vessels and piping. Other references describe studies that have collected data on observed flaws in welded construction and have compared the numbers and sizes of the observed flaws with predictions made with the PRODIGAL code (References B.12 and B.13).

The PRODIGAL code is an expert system model that simulates the occurrence of flaws in nuclear grade welding. An additional aspect of the model is the simulation of the radiography and dye-penetrant inspections performed to detect flaws so that defective welds can be rejected and/or repaired. The focus of PRODIGAL is on crack-like flaws that have the potential to impact structural integrity. Specific limitations of the model are that it excludes structurally benign flaws such as pores and rounded slag. The model does not address certain inspections such as UT and leak testing. It was designed to predict the expected defect distributions in an average weld but does not include a consideration of uncertainties or the expected weld-to-weld variations.

PRODIGAL outputs the size, number, and location of flaws per meter of weld. The total number of flaws per meter of weld with a depth greater than a given percentage of weld thickness is shown in Figure B.9. This figure also distinguishes between surface breaking and embedded flaws in the weld. The results show that MPC welds have more embedded flaws than surface breaking flaws. The largest flaw predicted by PRODIGAL is approximately 80% of the weld thickness.

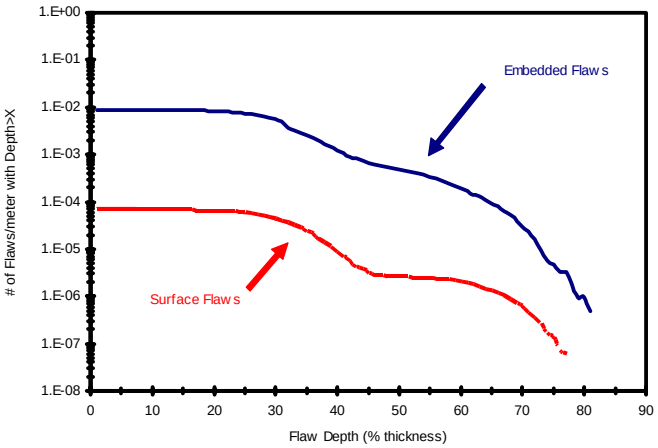

Figure B.9. Prodigal Flaw Distribution Results for MPC Welds: Total Number of Flaws with Depth Greater than a Given Depth

There are six shell welds in each MPC. This includes four axial welds, one circumferential weld, and one shell-to-baseplate weld. The length of two axial welds on each side of the MPC is 4.77 meters (15.65 feet). These two axial welds are modeled as one continuous weld extending the entire height of the MPC. The length of the circumferential and shell-to-baseplate weld is 5.46 meters (17.9 feet) each. The total number of flaws in each of the MPC welds can be calculated by taking the PRODIGAL results and multiplying by these weld lengths. There are approximately 0.04 flaws per axial weld extending the entire height of the MPC. The circumferential and shell-to-baseplate welds each have approximately 0.05 flaws per weld. In other words, 1 in 25 (0.04) axial welds will contain a flaw while 1 in 20 (0.05) circumferential or shell-to-baseplate welds are expected to contain a fabrication flaw.

If a flaw is present in an MPC weld, the location of the flaw is also based on PRODIGAL results. The flaws in the MPC welds were separated into three locations, inner surface breaking, outer surface

breaking, and embedded. Analysis of PRODIGAL results showed that 98.44% of the flaws were expected to be embedded, 0.83% were inner surface breaking, and 0.73% were expected to be outer surface breaking.

Given a flaw in a particular location, a probability distribution of flaw depths was determined as follows. In the PRODIGAL analysis, 1,000,000 meters of weld were simulated. The PRODIGAL output for a given flaw depth was multiplied by 1,000,000 meters to give the number of simulated flaws of that flaw depth. Summing these values for all flaw depths gives the total number of simulated flaws. The probability of obtaining a flaw of a given depth was calculated by dividing the number of simulated flaws of that depth by the total number of simulated flaws. This process was performed for inner surface breaking flaws, outer surface breaking flaws, and embedded flaws. The resulting probability distributions are shown in Figure B.10. The most likely flaw depth present in these welds is approximately ⅓ of the wall thickness. This is expected, since the flaw depths predicted by PRODIGAL are a function of the size of the welding bead and the welds are fabricated in three passes.

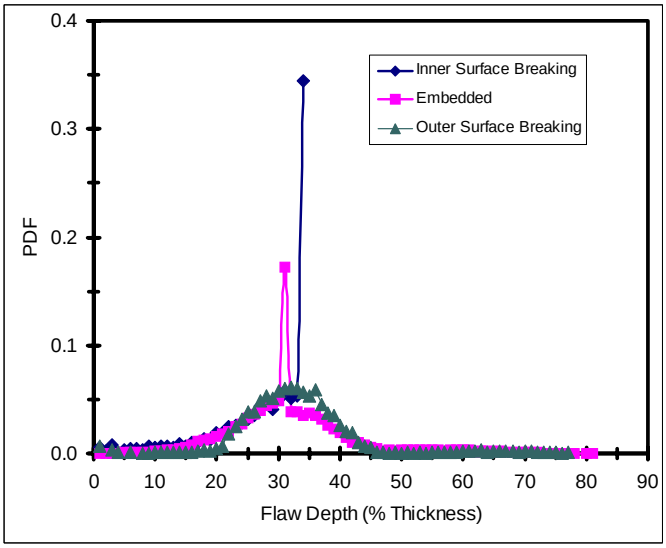

Figure B.10. Probability Distributions of Flaw Depth for MPC Welds Based on PRODIGAL Results

For a given flaw location and depth, PRODIGAL also provides a range of flaw aspect ratios (flaw length/depth). PRODIGAL reports these aspect ratios in 14 bins ranging from less than 2 to greater than 14. A probability distribution of aspect ratios was determined for each flaw depth and location based on these results. An example of the aspect ratio probability distribution is shown in Figure B.11 for an embedded flaw with a depth of 31% of the weld thickness. The probability of the last bin (>14) is much larger than the other bins in this histogram because this bins includes the entire tail of the distribution representing all flaws with an aspect ratio greater than 14.

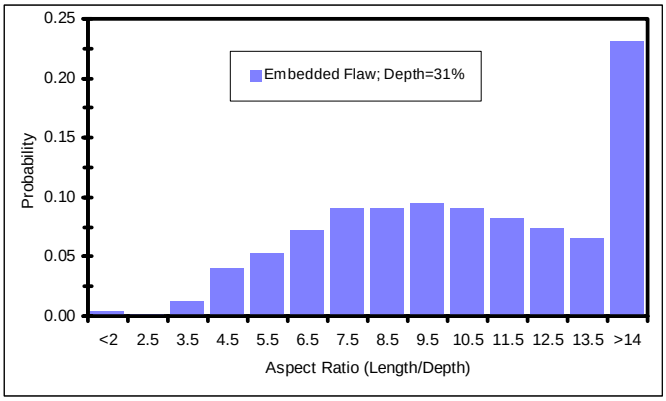

Figure B.11. Distribution of Aspect Ratios for an Embedded Flaw with a Depth of 31% of the Weld Thickness

Stress Concentration

A stress concentration is present at the shell-to-baseplate weld because of the discontinuity formed where the MPC shell and baseplate connect. The maximum stress concentration occurs at the surface and quickly approaches a value of 1 away from the shell surface. The equation used to estimate this stress concentration is as follows:

$$C = \left[1 + 0.5\left(\frac{r}{r+x} \right)^2 + 2.5\left(\frac{r}{r+x} \right)^4 \right] \quad \text{(B.7)}$$

where: C = bending stress concentration in the shell-to-baseplate weld
r = fillet radius (taken as 0.0254 cm or 0.01 inch)
x = depth from the shell surface

This equation is based on the stress distribution for a circular hole of radius, r, in a plate under tension, where the maximum stress concentration factor has been increased to 4 in order to be more representative of a small radius fillet.

For the shell-to-baseplate weld, the bending stress at a given thickness location was determined by multiplying the nominal bending stress by this stress concentration.

B.1.6 Limit Load Model

A flow stress model was also used to predict MPC failure. Failure occurs if the applied membrane stress attributable to internal pressure equals or exceeds the flow stress of the material:

$$\sigma_{flow}^{membrane} \equiv \frac{(\sigma_{yld} + \sigma_{uts})}{2} \quad \text{(B.8)}$$

where: σ_{flow} = flow stress
σ_{yld} = yield strength
σ_{uts} = tensile strength

The Level D stress limits in this material for membrane plus primary bending as specified in Section III of the ASME Code is 150% of the primary membrane limit. Using the above definition for flow stress as the primary membrane limit, the membrane plus bending stress limit is given below:

$$\sigma_{flow}^{membrane+bending} \equiv 0.75 \bullet (\sigma_{yld} + \sigma_{uts}) \quad \text{(B.9)}$$

At a given temperature, the applied stresses were calculated using the equations in Section B.1.2. The yield and ultimate tensile strengths of the material were sampled so the critical flow stress values could be determined. If the circumferential or axial stresses of the MPC were greater than the membrane flow stress, failure was predicted. Similarly, if the bending and membrane stress of the MPC shell-to-baseplate exceeded the membrane plus bending flow stress, failure was also predicted. If either of these limits was exceeded, the entire MPC was considered failed.

Again, the probability of failure attributable to exceeding critical flow stress was calculated by performing Monte Carlo simulations at various temperatures. The probability of MPC failure was defined as the number of MPC failures divided by the total number of iterations.

The sampled values were correlated such that if a mean plus 1 standard deviation value of yield stress was sampled then a mean plus 1 standard deviation tensile strength was sampled. The yield and tensile strengths sampled in this model were allowed to fall below the minimum values defined in Table B.1. Even with the yield and tensile strengths below the minimum allowables, the limit load model never contributed to failure for any of the heat-up scenarios.

B.1.7 Creep Rupture Model

The methodology used to predict creep rupture of the MPC is based on the model developed by Argonne National Laboratory for creep rupture of steam generator tubes (Reference B.14). In this model, the structure accumulates a fraction of creep damage after exposure to any specific time/temperature/stress condition. If the sum of these creep damage fractions exceeds 1, failure is predicted. In equation form, this failure criteria is as follows:

$$\int_0^{t_f} \frac{dt}{t_r(T,\sigma)} \equiv 1 \qquad \text{(B.10)}$$

where: $t_r(T,\sigma)$ = time to cause rupture at temperature, T, and stress, σ
dt = time spent at temperature, T, and stress, σ
t_f = total time

The above description applies to unflawed structures. If cracks are present, the above failure criteria is modified by multiplying the stress in an unflawed structure by an appropriate magnification factor, m_p:

$$\int_0^{t_f} \frac{dt}{t_r(T,\, m_p \cdot \sigma)} \equiv 1 \qquad \text{(B.11)}$$

The stress magnification factors for part through axial and circumferential flaws are given below. For axial flaws, the magnification factors are given by Equations B.12:

$$m_p \equiv \frac{1-\alpha \bullet \frac{a}{m \bullet t}}{1-\frac{a}{t}} \tag{B.12a}$$

$$\alpha \equiv 1+0.9 \bullet \left(\frac{a}{t}\right)^2 \bullet \left(1-\frac{1}{m}\right) \tag{B.12b}$$

$$m \equiv 0.614 + 0.481 \bullet \lambda + 0.386 \bullet \exp(-1.25 \bullet \lambda) \tag{B.12c}$$

$$\lambda \equiv \frac{1.82 \bullet c}{\sqrt{r_{mean} \bullet t}} \tag{B.12d}$$

where: m_p = magnification factor
a = flaw depth
c = flaw length
t = MPC shell thickness (= 0.5 in. or 1.27 cm)
r_{mean} = mean radius of MPC (= 33.9375 in. or 86.2 cm)

For circumferential flaws, the magnification factors are given by Equations B.13:

$$m_p \equiv \frac{1}{\left[m+\left(\frac{\theta}{\pi}\right) \bullet \left(1-\frac{a}{t}-m\right)\right]} \tag{B.13a}$$

$$m \equiv \frac{1-\frac{a}{t}}{1-\frac{a}{N \bullet t}} \tag{B.13b}$$

$$N \equiv 1+0.2 \bullet \left(\frac{\theta}{\pi}\right)^{0.2} \tag{B.13c}$$

where: a = flaw depth
θ = one half angular length of flaw
t = MPC shell thickness = 0.5 in (1.27 cm)

The probability of creep rupture failure as a function of temperature was determined as follows. The MPC stresses at any time-temperature condition were determined using the equations in Section B.1.2. For this stress, the Larson-Miller parameter required to cause creep rupture was sampled from the distribution described in Section B.1.5. Given this temperature and Larson-Miller parameter, the time required to cause creep rupture failure, $t_r(T,\sigma)$, can be determined. The incremental creep damage is calculated by dividing the actual time spent in these conditions, dt, by the time needed to cause creep rupture, $t_r(T,\sigma)$. This procedure is repeated for the next time-temperature-stress condition. If, at the temperature of interest, the summation of creep damage fractions is greater than 1, MPC failure is predicted.

Over time, the heat load in the cask would slowly drop. This heat reduction would cause a corresponding reduction in MPC temperature and internal pressure. This effect was not modeled in the thermal analyses, so it was assumed that the internal heat load remained constant for the entire 20-year license period of the cask.

Monte Carlo simulations were performed on MPCs to determine the probability of creep rupture failure. A simulated MPC consisted of both flawed and unflawed regions. The flawed regions consisted of the axial welds, one circumferential weld and one shell-to-baseplate weld. The unflawed regions were made up of the MPC shell plates. The creep rupture analysis assumed that all flaws were located on the weld surface. If any of the regions were predicted to fail, the entire MPC was counted as a failure. The probability of MPC failure is the number of failures divided by the number of simulations performed.

B.1.8 Results

Mechanical Loads

Table B.9 shows the probability of the failure of a single finite element (i.e., the probability of weld crack initiation) through the thickness of the MPC shell for (1) the drop of the transfer cask onto the concrete floor from 30.5, 21.3, 12.2, and 1.52 meters (100, 70, 40, and 5 feet); (2) the drop of the transfer cask onto the storage overpack from 24.4, 12.2, and 1.5 meters (80, 40, and 5 feet); (3) the drop of the MPC into the storage overpack from 5.8 meters (19 feet); and (4) the storage cask tip-over event. As discussed in Section B.1.4, the probability of a single element failure through the thickness of the shell is not the same as the probability of a breach of the confinement boundary. However, for the purpose of this PRA, the probability of a single element failure through the thickness will be conservatively equated to the probability of a breach.

Table B.9. Summary of the Probability of MPC Weld Crack Initiation for Various Impact Events

Event Scenario	Impact Surface (Target)	Drop Height (ft)	Probability of Weld Crack Initiation
Transfer Cask Vertical Drop	Concrete Floor	5	< 0.000001
		40	0.00036
		70	0.0026
		100	0.0196
	Storage Cask	5	0.000002
		40	0.000014
		80	0.000203
Drop of MPC into Storage Overpack during Transfer Operations	Storage Overpack Pedestal	19	0.282
Storage Cask Tip-Over	Concrete Pad	NA	< 0.000001

[1] This value should be <0.000001. See Table A.4, Note 2.

Thermal Loads

The creep, limit load, and fracture models were used to analyze the MPC failure probability for the external fire and blocked vent accident scenarios. Table B.10 shows the MPC temperature and pressure conditions for these events.

Under normal steady-state conditions, the bulk MPC internal pressure is 0.565 MPa (82 psi). The MPC temperature varies with axial location as shown in Figure B.12. In this figure, height is measured from the base of the storage overpack such that the bottom of the helium gas and fuel rods are at a height of 0.67 meter (2.2 feet). The minimum temperature of 73 °C (163 °F) occurs at the shell-to-baseplate weld at the bottom of the MPC. The maximum MPC temperature of 180 °C (356 °F) is located at the top of the MPC. Even though the axial weld temperature varied between these two extremes, the failure analyses assumed a uniform temperature equal to the maximum value. Even if these conditions were maintained for the full 20-year license period of the cask, the failure analysis shows that no MPC failures are expected.

If the storage cask was exposed to an external fire for 3 hours, as a result of a Gulfstream IV aircraft crash, the MPC pressure will increase to 0.634 MPa (92 psi). However, as mentioned in section B.1.2, a credible fire scenario will be much less than 30 minutes. As a result, the values resulting from the 3-hour fire analysis are very conservative. The MPC temperature will also increase ,as shown in Table B.10 and Figure B.12. Since creep failure is a “time at temperature” phenomenon, it was assumed that the 3-hour fire occurred after the 20-year license period of the cask. Even under these conditions, the failure analysis shows that no MPC failure is expected.

Table B.10. MPC Temperature and Pressure Conditions Following External Fires and Blocked Vent Scenarios

Quantity, SI Units (U.S.)	Normal Steady-State Conditions	3-Hour Fire	100% Vent Blockage, No Fuel Rupture	100% Vent Blockage, 50% Fuel Rupture
Internal Pressure, **MPa (psi)**	0.565 (82)	0.634 (92)	0.745 (108)	0.9 (130.5)
Maximum Temperature in Axial Weld, **°C (°F)**	172 (342)	352 (666)	283 (542)	283 (542)
Temperature of Circumferential Weld, **°C (°F)**	133 (271)	331 (628)	279 (534)	279 (534)
Temperature of Shell to Baseplate Weld, **°C (°F)**	73 (163)	335 (635)	206 (403)	206 (403)

If all four cooling vents become blocked, the MPC temperatures will increase to new steady-state values shown in Table B.10 and Figure B.12. The bulk MPC pressure would become 0.745 MPa (108 psi). The results in Appendix C, "Response of Fuel to Loads," show that for vent blockage, some of the fuel within the cask is expected to fail. This will result in an increase in MPC pressure, which is not considered in the thermal analysis. Table 4.4.14 of the HI-STORM SAR (Reference 1) shows the normal MPC pressure with no fuel failure as 0.496 MPa (72.0 psi).[4] Assuming 10% and 100% fuel rod rupture, these pressures increase to 0.517 MPa (75.0 psi) and 0.704 MPa (102.1 psi), respectively. These represent pressure increases by factors of 1.042 and 1.418, respectively. Interpolating between these values gives an MPC pressure increase of 1.208 for the case of 50% fuel failure. Results of the thermal analysis performed for this PRA show MPC pressure of 0.745 MPa (108 psi). Increasing this value by a factor of 1.208 results in a pressure of 0.9 MPa (130.5 psi). The failure analysis of the vent blockage scenario assumed this bulk internal pressure to take into account the increased pressure from fuel failure. These results are shown in Table B.10. The failure analyses show that even after 20 years of vent blockage and 50% fuel failure, no MPC failures are expected.

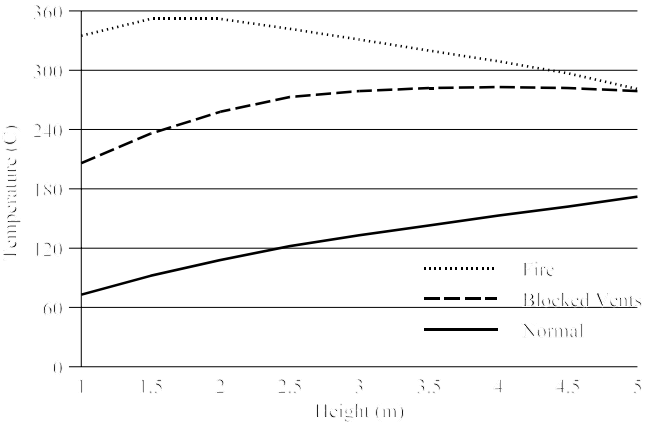

Figure B.12. MPC Wall Temperatures as a Function of Axial Height

4 Gauge pressures listed in the HI-STORM SAR (Reference 1) converted to actual pressures.

B.2 References

B.1. HOLTEC International, "HI-STORM Final Safety Analysis Report," HI-2002444, Revision 1, Marlton, New Jersey, September 6, 2002.

B.2. American Iron and Steel Institute, "High-Temperature Characteristics of Stainless Steels," Publication No 9004, Nickel Institute, Washington, DC, 1979.

B.3. Smith, G.V., "An Evaluation of the Yield, Tensile, Creep, and Rupture Strengths of Wrought 304, 316, 321, and 347 Stainless Steels at Elevated Temperatures," ASTM Data Series DS 5S2, American Society for Testing and Materials, West Conshohocken, Pennsylvania, 1969.

B.4. Klueh, R.L., and D.A. Canonico, "Elevated Temperature Tensile Strength and Microstructure of a Weld-Overlaid Type 304 Stainless Steel Forging," *Symposium on Elevated Temperature Properties of Austenitic Stainless Steels*, June 24–28, American Society of Mechanical Engineers, 1974.

B.5. National Research Institute for Metals, "Data Sheets on the Elevated-Temperature Properties for Base Metals, Weld Metals, and Welded Joints of 18Cr-8Ni Stainless Steel Plates," NRIM Creep Data Sheet No 32A, Tokyo, Japan, 1995.

B.6. Vacari, J.A., "Standard Wrought Austenitic Stainless Steels," *Materials Engineering*, Reinhold Publishing Company, December 1974.

B.7. Conway, J.B., *Stress-Rupture Parameters: Origin, Calculation and Use*, Gordon and Breach, Science Publishers, New York, New York, 1969.

B.8. Chapman, O.J.V., "Simulation of Defects in Weld Construction," Reliability and Risk in Pressure Vessels and Piping, ASME PVP Vol. 251, pp. 81–89, American Society of Mechanical Engineers, New York, New York, 1993.

B.9. Chapman, O.J.V., M.A. Khaleel, and F.A. Simonen, "A Simulation Model for Estimating Probabilities of Defects in Welds," ASME PVP Vol. 323, pp. 375–391, "Fatigue and Fracture," Volume 1, American Society of Mechanical Engineers, New York, New York, 1996.

B.10. Chapman, O.J.V., and F.A. Simonen, "RR-PRODIGAL: Model for Estimating the Probabilities of Defects in Reactor Pressure Vessel Welds," NUREG/CR-5505, U.S. Nuclear Regulatory Commission, Washington, DC, 1998.

B.11. Chapman, O.J.V., M.A. Khaleel, F.A. Simonen, and D.O. Harris, "A Method for Estimating the Probabilities of Defects in Piping Welds," ASME PVP Vol. 386, pp. 127–144, "Probabilistic and Environmental Aspects of Fracture and Fatigue," American Society of Mechanical Engineers, New York, New York, 1999.

B.12. Schuster, G.J., S.R. Doctor, and F.A. Simonen, "A Methodology for Determining Fabrication Flaws in a Reactor Pressure Vessel," *Proceedings of ASME-JSME International Conference on Nuclear Engineering*, ICONE4, Volume 1, Part A, "Basic Technological Advances," pp. 187–194, American Society of Mechanical Engineers, New York, New York, 1996.

B.13. Schuster, G.J., S.R. Doctor, and A.F. Pardini, "Validation of Reactor Pressure Vessel Fabrication Flaws," *Proceedings of NDE Damage Assessment Workshop*, October 6–7, 1997, Electric Power Research Institute, La Jolla, California, 1997.

B.14. Majumdar, S., W.J. Shack, D.R. Diercks, K. Mruk, J. Franklin, and L. Knoblich, "Failure Behavior of Internally Pressurized Flawed and Unflawed Steam Generator Tubing at High Temperatures: Experiments and Comparison with Model Predictions," NUREG/CR-6575, U.S. Nuclear Regulatory Commission, Washington, DC, March 1998.

B.15. Holt, J., H. Mindlin, and C. Ho, *Structural Alloys Handbook*, Purdue University, Center for Information and Numerical Data Analysis and Synthesis (CINDAS), West Lafayette, Indiana, 1996.

B.16. Peckner, D., and I. Bernstein, *Handbook of Stainless Steel*, McGraw-Hill, Columbus, Ohio, 1977.

B.17. *Atlas of Stress-Strain Curves*, Second Edition, American Society of Metals, Material Park, Ohio, 2003.

B.18. Ward, A., and Blackburn, L., "Elevated Temperature Tensile Properties of Weld-Deposited Austenitic Stainless Steels," *ASME Journal of Engineering Materials and Technology*, American Society of Mechanical Engineers, New York, New York, July 1976.

B.19. Stoner, K., R. Sindelar, and G. Caskey, "Reactor Materials Program: Baseline Material Property Handbook — Mechanical Properties of 1950s Vintage Stainless Steel Weldment Components," TN: 89-023-A-1, WSRC-TR-91-10, Westinghouse Savannah River Company, Aiken, South Carolina, April 1991.

B.20. Lee, W., C. Lin, C. Liu, and C. Cheng, "The Effects of Strain Rate and Welding Current Mode on the Dynamic Impact Behavior of Plasma-Arc-Welded 304L Stainless Steel," Metallurgical and Material Transactions, Volume 35A, May 2004.

B.21. Davis, E., and F. Connelly, "Stress Distribution and Plastic Deformation in Rotating Cylinders of Strain-Hardening Materials," *ASME Journal of Applied Mechanics*, American Society of Mechanical Engineers, New York, New York, March 1959.

B.22. Manjoine, M., "Ductility Indices at Elevated Temperature," *Transactions of ASME*, American Society of Mechanical Engineers, New York, New York, April 1975.

B.23. Manjoine, M., "Creep-Rupture Behavior of Weldments," *Welding Journal: Research Supplement*, Vol. 61, No. 2, American Welding Society, Miami, Florida, February 1982.

B.24. Singh, K.P., J. Zhai, "Multi-Purpose Canister: A Bulwark of Safety in the Post-9/11 Age," *International High-Level Radioactive Waste Management Conference*, Las Vegas, Nevada, 2003.

APPENDIX C
FUEL RESPONSE TO LOADS

APPENDIX C
FUEL RESPONSE TO LOADS

C.1 Fuel Response to Mechanical Loads

C.1.1 Fuel Rod Buckling

For cask vertical drop accidents, the fuel rods in the assemblies are analyzed as long, slender columns with intermediate supports provided by the assembly's spacer grids. Since the section of the fuel rod between the bottom two spacer grids supports the weight of the entire rod, only this section of the rod is typically analyzed. For this segment, the critical buckling load, α_{cr}, is given by Equation C.1 from Reference C.1:

$$\alpha_{cr} = \frac{\pi^2}{\ell^2} \frac{E_c I_c}{\left(W_c + W_f\right)} \qquad \text{(C.1)}$$

where: α_{cr} = critical inertia load magnitude for rod buckling (g)
ℓ = axial length of the fuel rod between two neighboring transverse spacer grids
$E_c I_c$ = flexural rigidity of the cladding tube column
W_c = total weight of the fuel rod cladding
W_f = total weight of the fuel pellets in the fuel rod

Under static and quasi-static loading, where load duration is relatively long, unrestrained lateral buckling and cladding failure (rupture) can be considered synonymous. By contrast, for dynamic impact events, where load duration may be on the order of only a few milliseconds, exceeding the critical buckling load will not, by itself, cause failure of the cladding. Rather it is the combination of load and load duration that determines whether the cladding reaches its failure strain. However, regardless of whether the analysis is static, quasi-static, or dynamic; whether the fuel is bonded or unbonded to the cladding; or whether the fuel is in granular or solid form, all (100%) of the fuel weight must be included in the buckling process (Reference C.1).

Table C.1 lists the specifications of fuel rods in BWR 7x7, 8x8, and 10x10 assemblies that could be loaded into the MPC at a BWR site. Table C.1 also lists the specifications of a fuel rod in a PWR 15x15 assembly. Even though a PWR assembly would not be contained in an MPC at a site, it was selected to illustrate the methodology for fuel response to drop impact, because PWR fuel rods are generally more vulnerable to impact events than BWR fuel rods (Reference C.5). This can be seen by comparing the static buckling loads of the fuel rods in Table C.1. Therefore, to bound the BWR assemblies, a PWR 15x15 fuel rod was used to illustrate the methodology.

C.1.2 Methodology and Modeling

The peak g loads imposed on a fuel rod from the vertical drop scenarios considered in the PRA far exceed the elastic buckling load of the fuel rods in the assemblies listed in Table C.1. Therefore, to determine the strain ductility demand on the fuel cladding, the inelastic buckling capacity of the fuel rods must be considered. The approach taken here is to analyze the fuel rod as an elastic-plastic beam-column with initial curvature under dynamic impact. Failure of the fuel rod is determined by comparing the maximum strain in the cladding to a strain limit based on experimental data.

Table C.1. BWR 7x7, 8x8, and 10x10 Fuel Bundle Parameters Used to Calculate Buckling Loads for Vertical Drop Scenarios

Rod Array	**BWR 7x7**	**BWR 8x8**	**BWR 10x10[1]**	**PWR 15x15**
Fuel Length, in (m)	144 (3.66)	144 (3.66)		154 (3.91)
# Spacers	7	7		8
Fuel Rod Length between spacers, in	19.62 (0.50)	19.62 (0.50)		20.5 (0.52)
Modulus, Psi (Pa)	9.8×10^{6} (6.79×10^{10})	9.8×10^{6} (6.79×10^{10})	9.8×10^{6} (6.79×10^{10})	9.8×10^{6} (6.79×10^{10})
Thickness, in (m)	0.035 (8.89×10^{-4})	0.035 (8.89×10^{-4})		0.0265 (0.0007)
Outer Radius, in (m)	0.285 (0.00724)	0.247 (0.00626)		0.215 (0.005)
Inner Radius, in (m)	0.250 (0.00635)	0.212 (0.00537)		0.189 (0.004)
Cross-Sectional Area, in^2 (m^2)	0.059 (3.8×10^{-5})	0.050 (3.25×10^{-5})		
I (Cladding Moment of Inertia), in^4 (m^4)	.00211 ($8.8\times10-^{10}$)	.00133 (5.53×10^{-10})		0.00068 (2.83×10^{-10})
Cladding Weight, lbf (N)	1.98 (8.82)	1.70 (7.55)		7.011[2] (31.19)
Fuel Weight, lbf (N)	9.60 (42.70)	7.46 (33.18)		
P_{cr} (Critical Buckling Load), lbf (N)	531.09 (2362.42)	333.72 (1484.45)	138.00 (613.86)	
α (Critical Buckling Load), g (g)	46 (46)	36 (36)	24 (24)	22 (22)

[1] Missing information is proprietary.

[2] Total fuel rod weight.

Analysis Approach

Since the impact event entails the interaction of potentially hundreds of rods, their spacer grids, tie plates, fuel spacers, basket, cask, and target under dynamic loading, the necessity for computational efficiency can be achieved by modeling a single fuel rod, as was done in some previous studies (References C.5 and C.8). Therefore, an explicit finite element analysis model of a single fuel rod with lateral displacement constraints was used to study the inelastic behavior of a fuel rod under dynamic impact loads. The LS-DYNA model used herein was initially developed by Pacific Northwest National Laboratory (PNNL) and the NRC staff (Reference C.3) to study the behavior of fuel rods under the hypothetical accident conditions described in Title 10, Part 71, of the *Code of Federal Regulations* (10 CFR Part 71), and was adapted by the NRC staff to the target characteristics of the drop scenarios evaluated in the PRA.

The model used in this evaluation is based on the following assumptions:

(1) All individual rods of a fuel assembly displace with the same deformed shape. This suggests that the single rod response is characteristic of all rods and can be studied independently. The center fuel rod in the assembly is considered representative of the typical response of the cross-section of rods through the whole assembly.

(2) All bending deformations occur in a single plane, although an actual assembly could exhibit bending deflections and/or twisting within the fuel compartment. This assumption also allows only half of the fuel rods to be modeled.

(3) The three-dimensional (3-D) finite element model uses a shell element to model the mass and stiffness properties of the cladding cross-section, but no comparable representation of the fuel was included. This assumption, which is consistent with standard fuel rod buckling analysis, provides a realistic conservative representation of the fuel by discounting any contribution of the fuel pellets to the fuel rod's flexural rigidity, but, at the same time, including 100% of their mass contribution by lumping fuel mass at each shell node of the cladding. An accurate account of the pellet-to-cladding interactions would be difficult to quantify considering the limited information available. However, to overcome unrealistic ovalization of the open cross-section, nonlinear single degree-of-freedom springs were included to represent a Hertzian-type contact between the cladding and the fuel during lateral deformation.

(4) Spent fuel rods will typically exhibit deviations from straightness after exposure to a neutron flux (Reference C.5). For rods mounted within an assembly using spacer grids, the unsupported sections of rod tend to bow out as a result of the assembly's position in the core and the fuel rods location within the assembly (i.e., proximity to a moderator rod, etc. Accordingly, a small amount of rod bowing was introduced to facilitate computation. (See discussion below.)

(5) The spacer grids are composed of a small array of leaf springs that hold the rods within the assembly. The spacer grid springs are assumed to provide lateral support to the fuel rods with a prescribed nonlinear force-deflection curve. No rotational support is accounted for, and the grids cannot slide axially relative to the rod.

(6) The cask was included in the model to capture the fuel rod and cask dynamics. This was achieved by defining a point mass to represent the cask (equal to the total physical mass of the transfer overpack and MPC divided by the total number of fuel rods accommodated in the cask).

(7) The target stiffness is modeled with a cask-to-ground spring defined by a constant force-deflection curve whose magnitude is determined through an iterative process to match the deformation characteristics of the MPC baseplate for each drop scenario.

Model Geometry and Details

Figure C.1 illustrates the single fuel rod model, which is composed of a single fuel rod, a lumped cask mass, springs representing the spacer grids, contact surfaces representing the basket compartment wall, and a spring representing the target stiffness (cask-to-ground/impact limiter). Several views of the actual finite element mesh are shown in Figure C.2. In this figure, the views shown are (a) the entire model, (b) top of rod with basket compartment walls and spacer grid spring, (c) top of rod with fuel pellet springs, and (d) bottom of rod with nodes representing the cask and target (impact limiter).

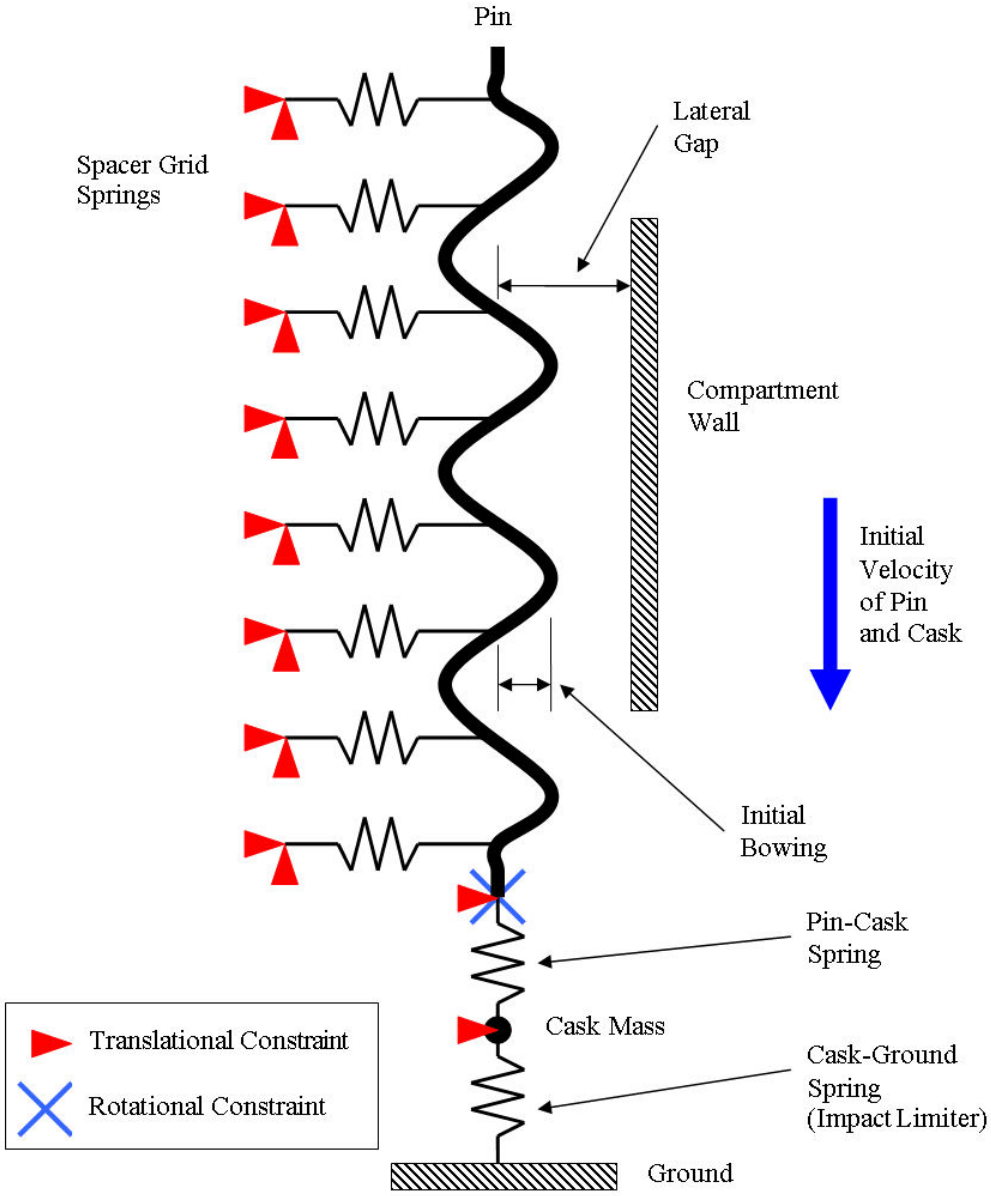

Figure C.1. Single Fuel Rod Model

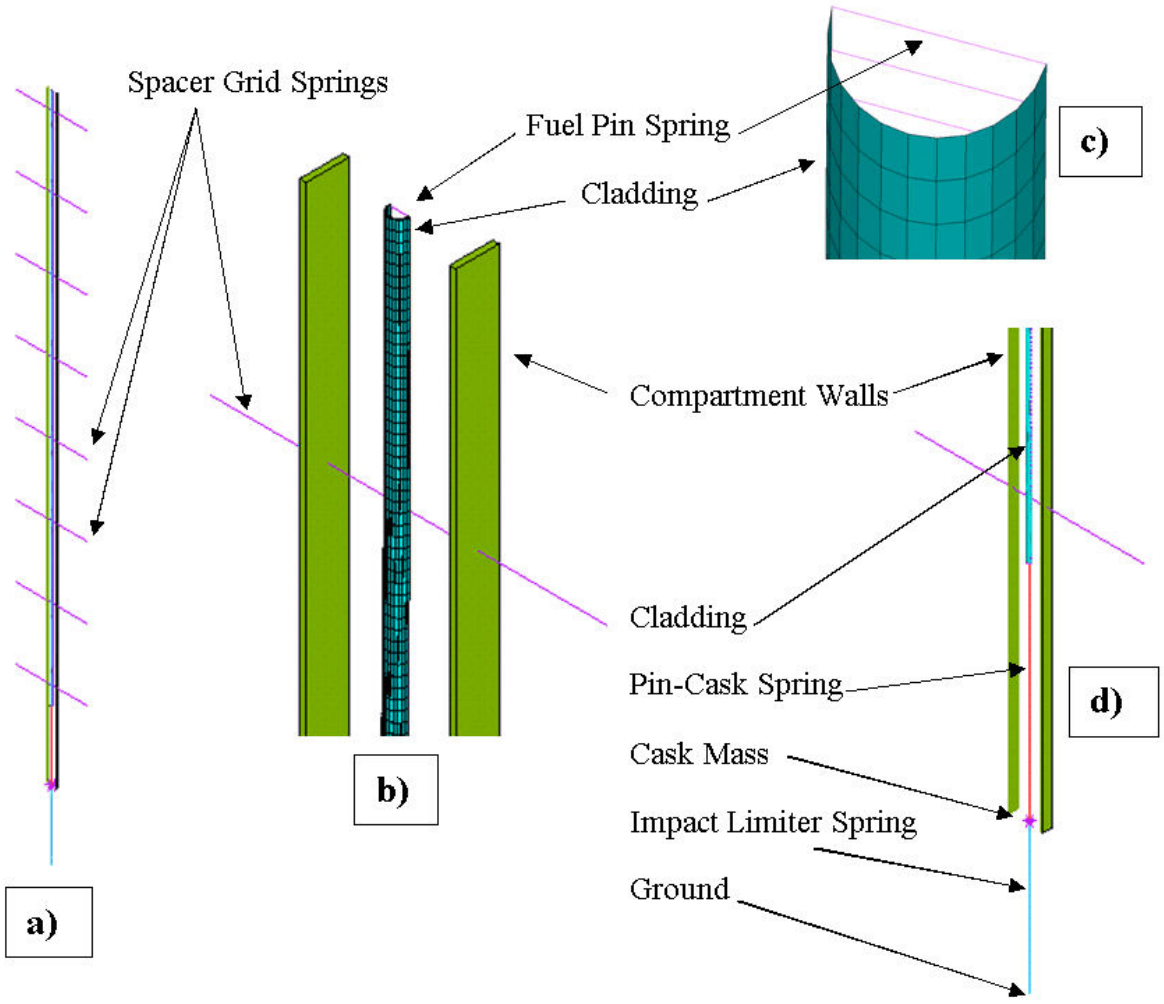

Figure C.2. Single Rod Model Showing (a) the Entire Model, (b) Top of Rod with Basket Compartment Walls and Spacer Grid Spring, (c) Top of Rod with Fuel Pellet Springs, and (d) Bottom of Rod with Nodes Representing the Cask and Target (Impact Limiter)

The typical fuel assembly rod is composed of cylindrical fuel pellets within a tubular cladding material that has reinforced end thimbles and an internal spring to minimize gap between the pellets at all times. The rod was modeled using shell elements with appropriate thickness and diameter to represent the cladding, and included about 20,000 elements and 10,000 nodes. The shell element sizing provided sufficient resolution to accurately capture the stress state, as demonstrated through sensitivity studies.

Fuel Rod

The rod was modeled with an initial bow geometry of 0.25 mm (0.010 inch) between the spacer grids. The bow between grid spacers was calculated from the overall assembly bow based on the guidance in Reference C.7. It was assumed that the rod had an initial constant curvature in these sections. At the rod ends, it was assumed that they had no initial rotation and that this condition would exist as a result of the constraint provided by the upper and lower tie plates.

Grid Spacers

The spacer grids are arrayed structures that provide intermediate support to the fuel rods in the assembly. The grids are composed of small leaf springs that ensure proper spacing of the rods in the assembly array. The grids were assumed to provide lateral support to the rod at eight intermediate locations (Figure C.1) according to the fuel geometry considered. This contribution was represented by sets of compression-only springs attached to each side of the cladding cross-section. These springs behave such that a lateral rod deflection will compress one spring and generate a compressive force, while the spring on other side is unloaded to simulate loss of contact.

Fuel Compartment

Deflection of the fuel rods during an impact event will lead to rod-to-rod and rod-to-compartment wall contact. For an assembly with all rods deforming identically, the outer rods will be the first to contact the compartment walls. Additional deformation causes the next set of rods to seat against these outer rods. This stacking continues until all rods are compressed against the compartment wall. To implement this behavior in a single rod model, the total lateral distance over which a rod could deform must be determined. The gap was determined by considering the rod diameter, number of rods, and compartment width to determine the total free space in which the center rods in an assembly could unilaterally deform, which in the case of the PWR 15x15 assembly was 3.0 cm (1.2 inch). The compartment walls were then modeled as rigid planes fixed in space at the proper lateral gap (Figure C.2). Contact elements were implemented to automatically capture contact between the cladding and the compartment walls.

Rod-Cask-Target Interaction

The cask and target stiffness (impact limiter) contribute significantly to rod dynamics. To include the effects of cask mass on system dynamics, the cask was modeled as a point mass. A compression-only spring was then used between the rod bottom and the cask. A second compression-only spring was then used to simulate the target stiffness and ground contact, where the ground was assumed to be rigid. This model construction permitted the system to impact the target surface; however, any rebounding and loss of contact between the rod and the cask or the cask and the ground would be captured.

Material Properties

Cladding

The temperature-dependent mechanical properties for the Zircalloy cladding material were obtained from PNNL data on high-burnup fuels published in Reference C.4. Since fuel rod buckling under vertical impact is expected to initiate at the bottom of the assembly where the fuel is coolest, a uniform temperature of 572 °F (300 °C) was assumed for the rod. It was also assumed that the high-burnup fuel had been irradiated to a neutron flux (fluence) of 12×10^{25} n/m^2 and would be subjected to a strain rate during buckling of 10/s. The following material property estimates correspond to these conditions:

- Elastic Modulus = 11.0×10^6 psi
- Yield Strength = 92.4×10^3 psi
- Yield Strain = 0.0084 in/in
- Tangent Modulus = 14.5×10^4 psi
- Poisson's Ratio = 0.40

Fuel Pellet Spring

To simulate the fuel pellet's ability to limit gross cladding ovalization when the cladding cross-section is subjected to high bending curvature, the fuel pellet was modeled as an equivalent spring. The force-deflection curve for this spring was adapted from the solution of an elastic cylinder compressed between two plates under diametrical Hertzian contact as given in Roark (Reference C.9).

Grid Spacer Spring

The force-deflection curves for the spacer grid springs were taken from Reference C.5. The curves represent elastic deformations from a number of coupled events that take place during the lateral movement of fuel rods in an assembly, including (1) compression of the spacer grid leaf spring, (2) compression of the spacer grid frame, (3) buckling of consecutive spacer grid cells, and (4) crushing of the fuel rod cross-section. The spacer grids at the top and bottom of the assembly are attached to the end plates and, consequently, are stiffer, so they are represented by a different curve.

Cask-Ground Spring

The cask-ground spring represents the behavior of the target impacted by the cask. This is the major source of energy absorption in the system. The target (impact limiter) is characterized by constant force deflection curve, where the force magnitude is determined through an iterative process to approximately match the deformation characteristics of the displacement time-history of the MPC baseplate for each drop scenario. Since 30.5 cm (1 foot) is the most frequent height from which a cask could be dropped, it is selected to compare the actual MPC baseplate displacement time-history to the displacement time-history used in the fuel rod buckling model. For the 30.5 cm (1 foot) drop, Figure C.3 shows the displacement time-history response of five nodes evenly spaced along the top of the baseplate from the centerline of the MPC baseplate to the MPC shell. For comparison, Figure C.4 shows the displacement time-history of the cask node in the fuel rod buckling model for the 30.5 cm (1 foot) drop.

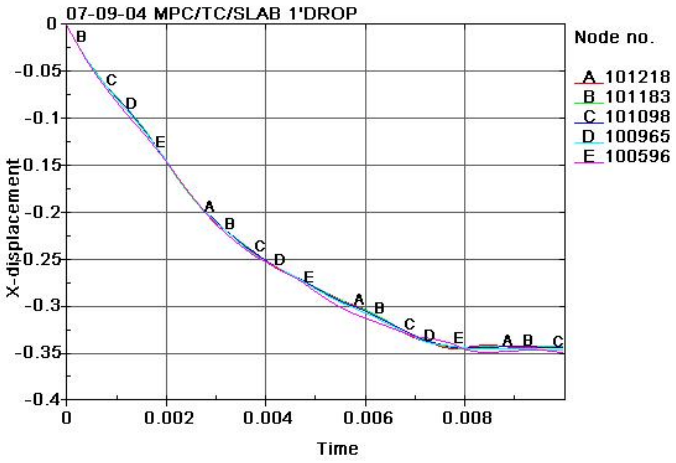

Figure C.3. Displacement of MPC Baseplate Nodes for 1-Foot Drop

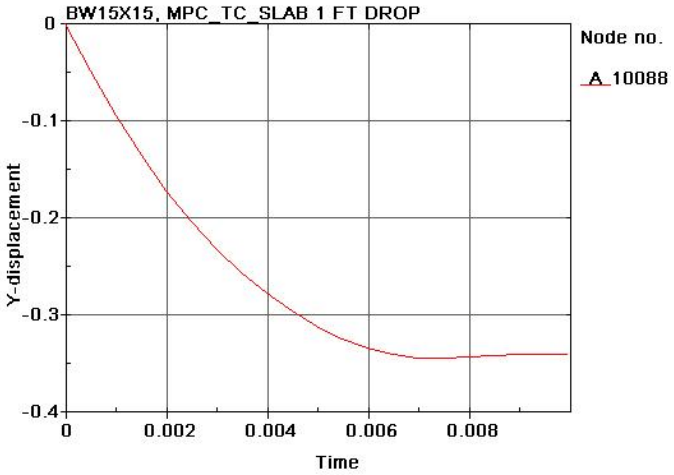

Figure C.4. Displacement of Fuel Rod Model Cask Node for 1-Foot Drop

Boundary and Initial Conditions

The boundary and initial conditions for the model are summarized below:

(1) Out-of-plane translations and rotations were constrained along the symmetry plane of the rod.

(2) In-plane rotation and lateral translation was constrained at the bottom of the rod. This is based on the assumption that the rods will likely be "jammed" into the bottom tie-plate and restrict rotation and lateral translation.

(3) Vertical translation only was enforced for the rod-cask spring, cask, and cask-ground spring.

(4) All translations were fixed at the free ends of the spacer grid springs.

(5) All translations were fixed at the ground surface.

(6) An initial velocity of corresponding to the drop height was applied to the rod and cask nodes.

Fuel Rod Internal Pressure

After a fuel assembly has been exposed to a neutron flux and burned for high-burnup durations (>45 GWd/MTU), internal rod pressures attributable to fission gas generation can range from 1,000 to 2,200 psi (6.89 to 15.16 MPa). A pressure loading of 1,400 psi (9.65 MPa) was applied to the inner cladding surface to simulate the effects of this fission gas generation. This was applied as a preload to the system using a stress initialization procedure prior to solution of the impact event.

C.1.3 Fuel Rod Response and Buckling Behavior

Table C.2 lists the maximum principal strain in the cladding for each drop height evaluated. For the drop of the transfer cask (TC) onto the concrete floor, additional drops of 6.1 and 15.2 meters (20 and 55 feet) were added to the standard drop heights of 0.3, 1.5, 12.2, 21.3, and 30.5 meters (1, 5, 40, 70, and 100 feet) in order to highlight transitions in buckling behavior or differences in response due to target stiffness.

The results show that the cladding yield strain of 0.0084 in/in is not exceeded until drops of the transfer cask are in the range of 6.1-12.2 meters (20–40 feet). The results also show that target stiffness has a significant influence on cladding strain. For example, the 6.1-meter (20-foot) drop of the TC on to the concrete floor results in a strain less than yield. However, the 5.8-meter (19-foot) drop of the MPC into the storage overpack, which is a much harder impact, produces cladding strains that are ten times greater than yield. This is because the buckling modes resulting from these two impacts are completely different, as will be illustrated later in the discussion.

Figures C.5 and C.6 show the response of the fuel rod for the 6.1-meter (20-foot) drop at the time when the maximum principal strain in the cladding is reached. Because the material response is entirely elastic and because of the interaction with the grid spacer springs, the maximum response occurs between the 5^{th} and 6^{th} grid spacers during the elastic rebound phase. The maximum lateral displacement of 3.0 cm (1.2 inch) is equal to the maximum allowable displacement imposed by the basket compartment wall as can be seen in the displacement plot in Figure C.7. It can also be seen from Figure C.6 that no flattening of the rod occurs as it touches the wall.

Figures C.8 and C.9 show the response of the fuel rod for the 12.2-meter (40-foot) drop at the time when the maximum principal strain in the cladding is reached. As expected, the maximum lateral displacement of 3.0 cm (1.2 inch) is equal to the maximum allowable displacement imposed by the basket compartment wall, but a slight flattening of the fuel rod against the compartment wall can be seen in Figure C.9.

Table C.2. Maximum Principal Strain in the Cladding for Each Drop Height Evaluated

Event Scenario	Impact Surface (Target)	Drop Height (ft)	Maximum Principal Strain (in/in)
Transfer Cask Vertical Drop	Concrete Floor	1	0.0043
		5	0.0062
		20	0.0072
		40	0.011
		55	0.025
		70	0.037
		100	0.052
MPC Drop into Storage Overpack	Storage Overpack Pedestal	19	0.09

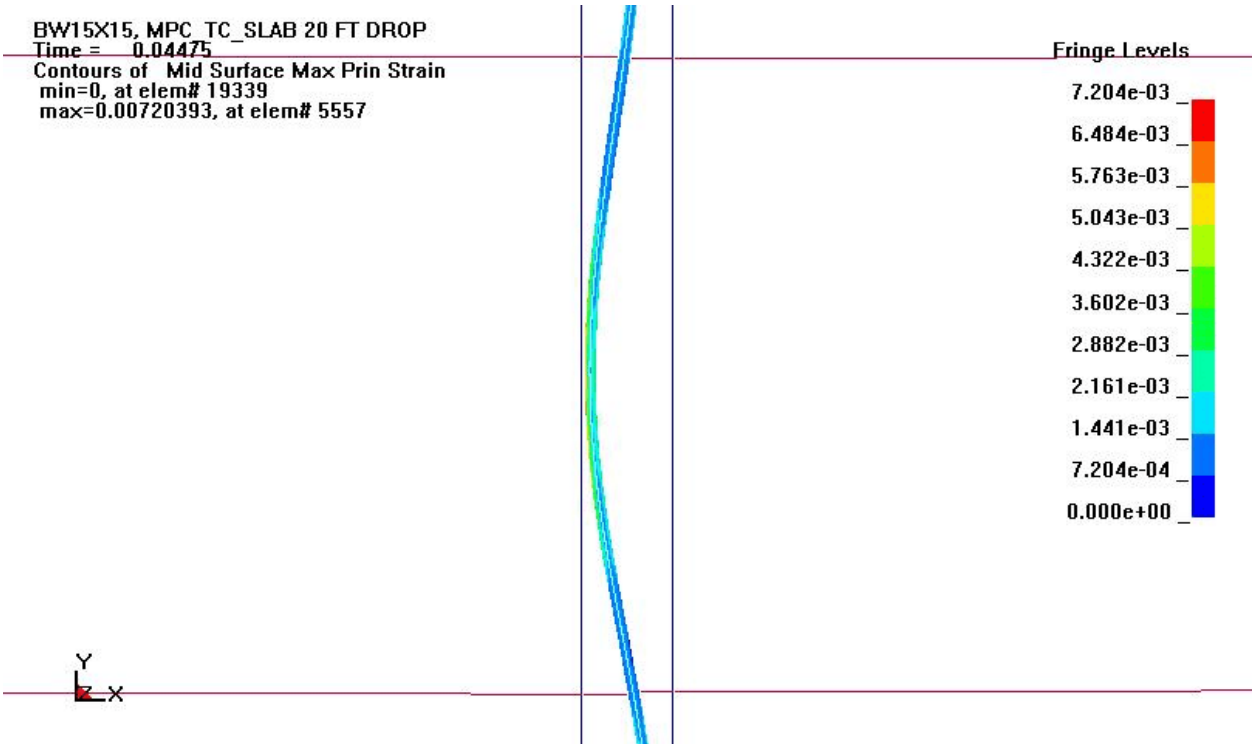

Figure C.5. Maximum Principal Strain at Time of Maximum Response (20-Foot Drop)

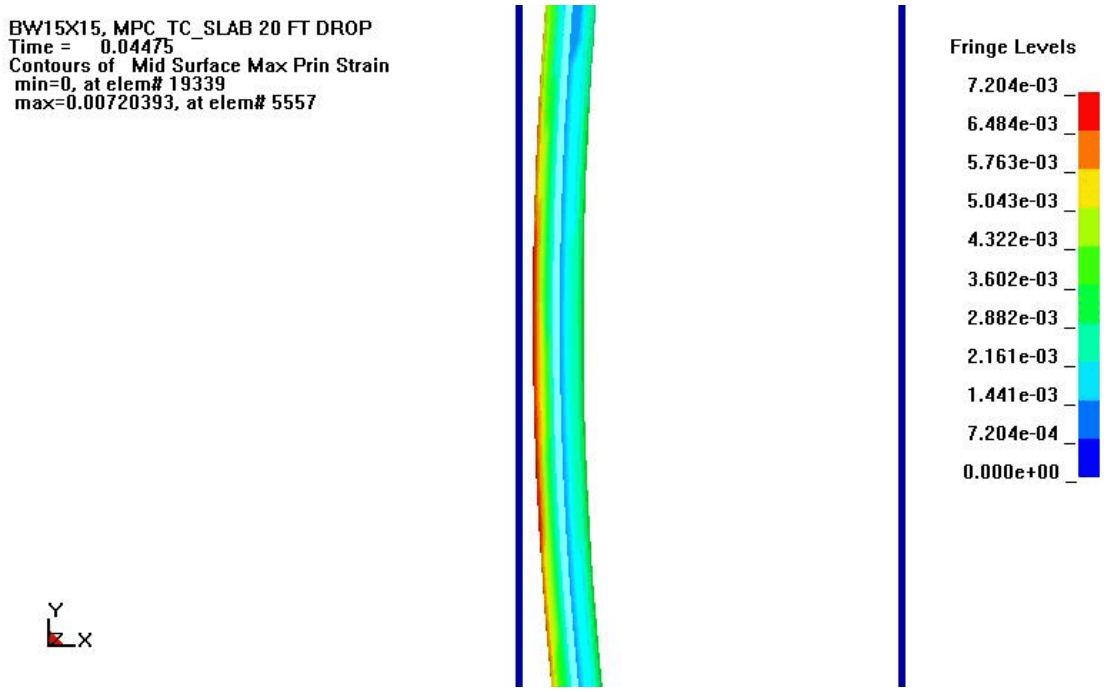

Figure C.6. Maximum Principal Strain at Time of Maximum Response (20-Foot Drop)

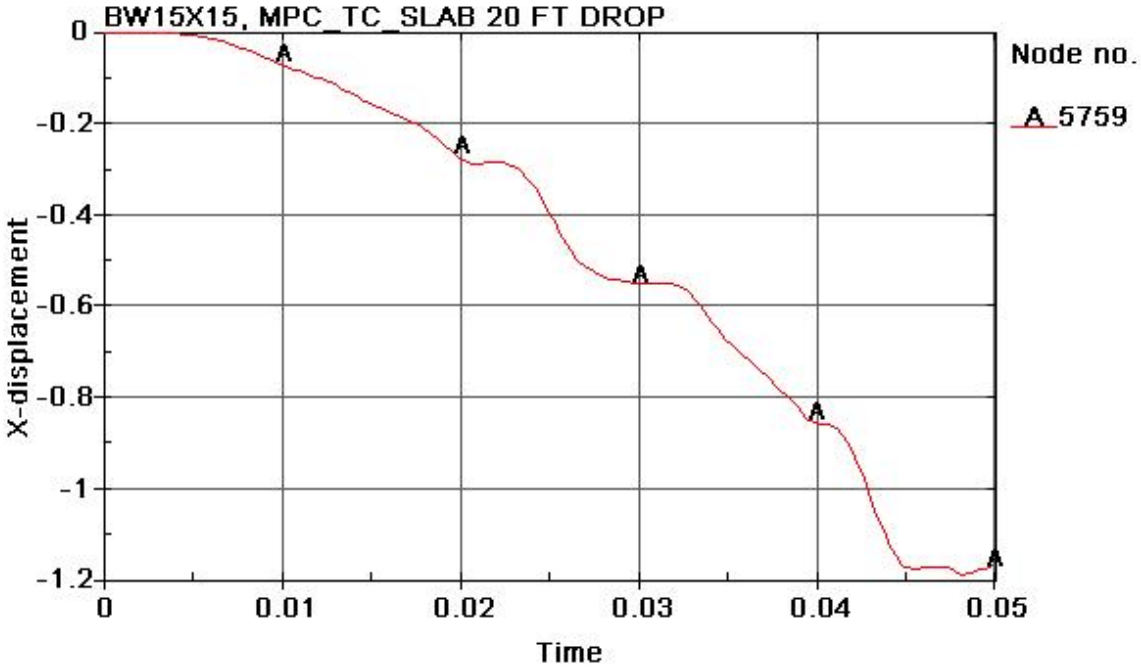

Figure C.7. Fuel Rod Lateral Displacement at Point of Maximum Response (20-Foot Drop)

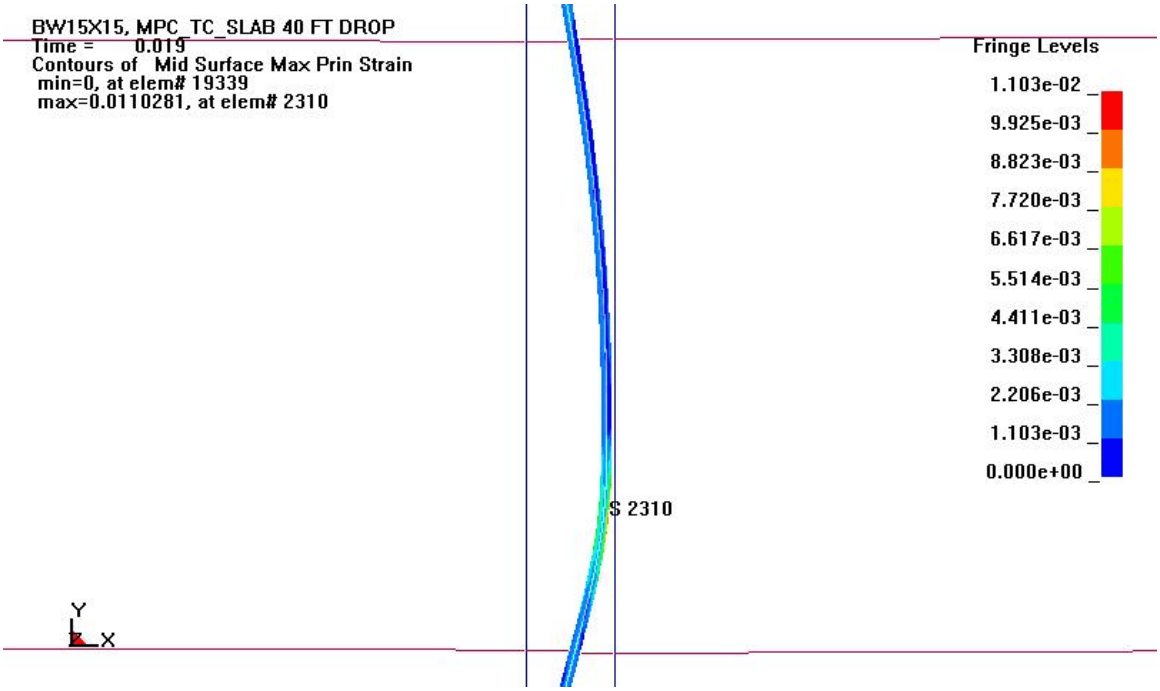

Figure C.8. Maximum Principal Strain at Time of Maximum Response (40-Foot Drop)

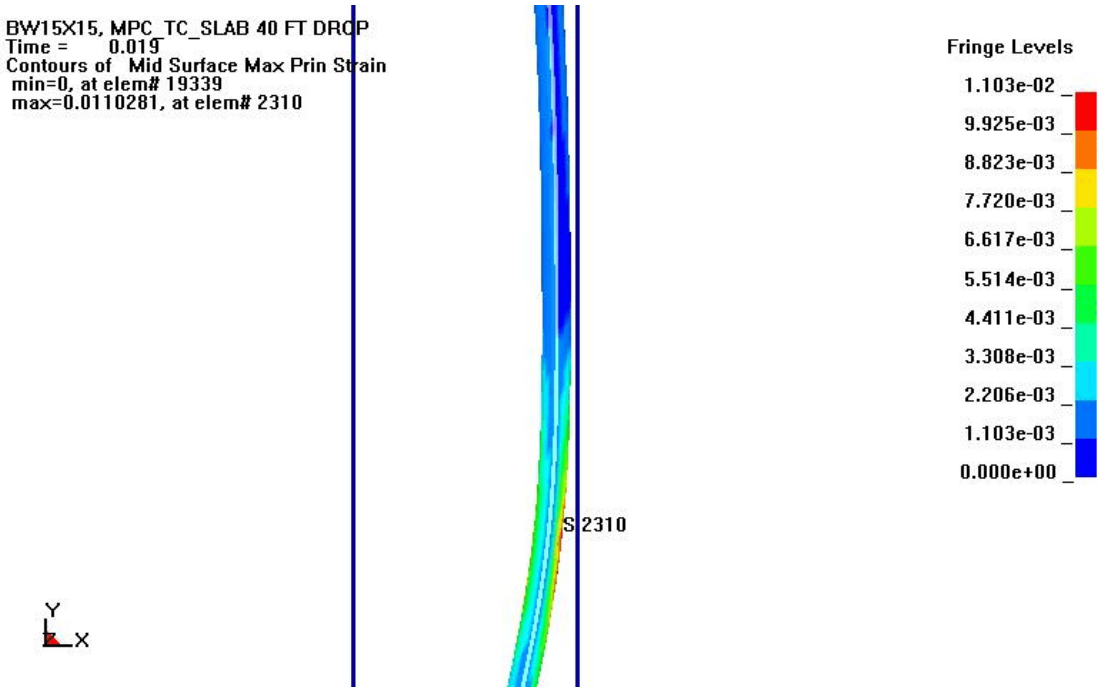

Figure C.9. Maximum Principal Strain at Time of Maximum Response (40-Foot Drop)

Contrast the 15.2-meter (40-foot) drop response with the response for a 16.8 meter (55-foot) drop. Figures C.10–C.12 show the progression of lateral deformation up to the maximum response at three different times (16.0, 16.5, and 17.0 msec) for the 16.8 meter (55-foot) drop, and Figure C.13 shows the response over two grid spacers at 17.0 msec. Figure C.14 shows the extreme flattening of the rod against the compartment wall and the concentration of curvature at the location where the rod loses contact with the wall. Figure C.15 is the same as Figure C.14, with the exception that it shows the longitudinal (meridional) strain. The response for the 21.3 and 30.5 meter (70 and 100 foot) drops are similar.

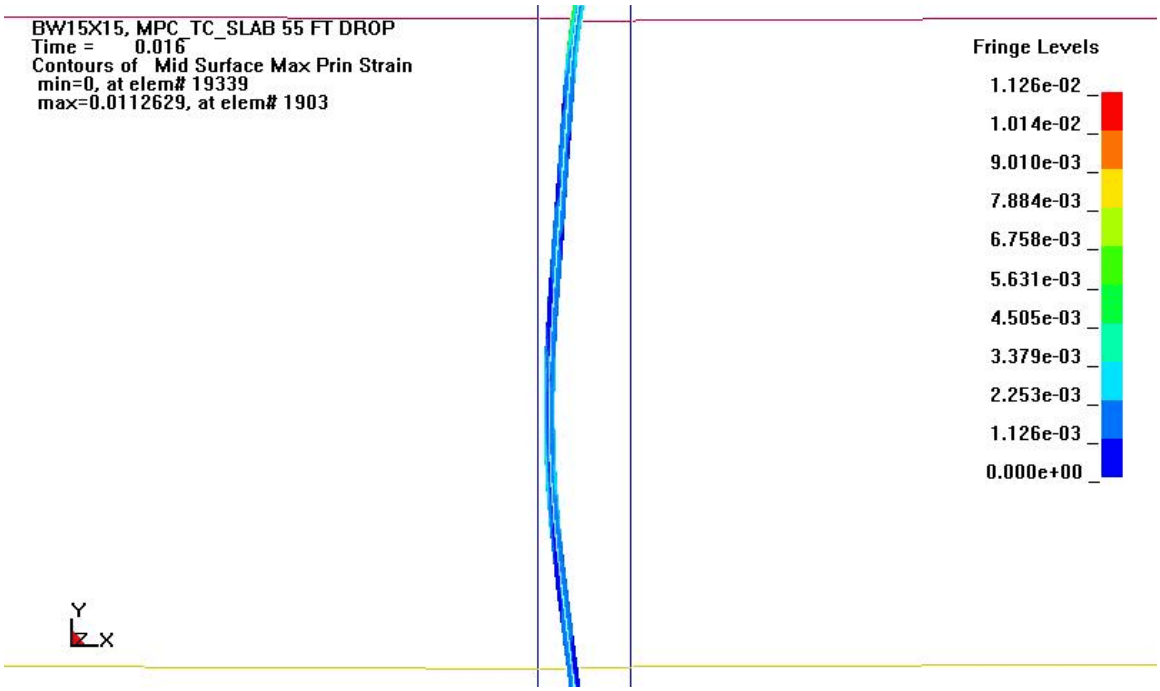

Figure C.10. Maximum Principal Strain at 0.0160 seconds (55-Foot Drop)

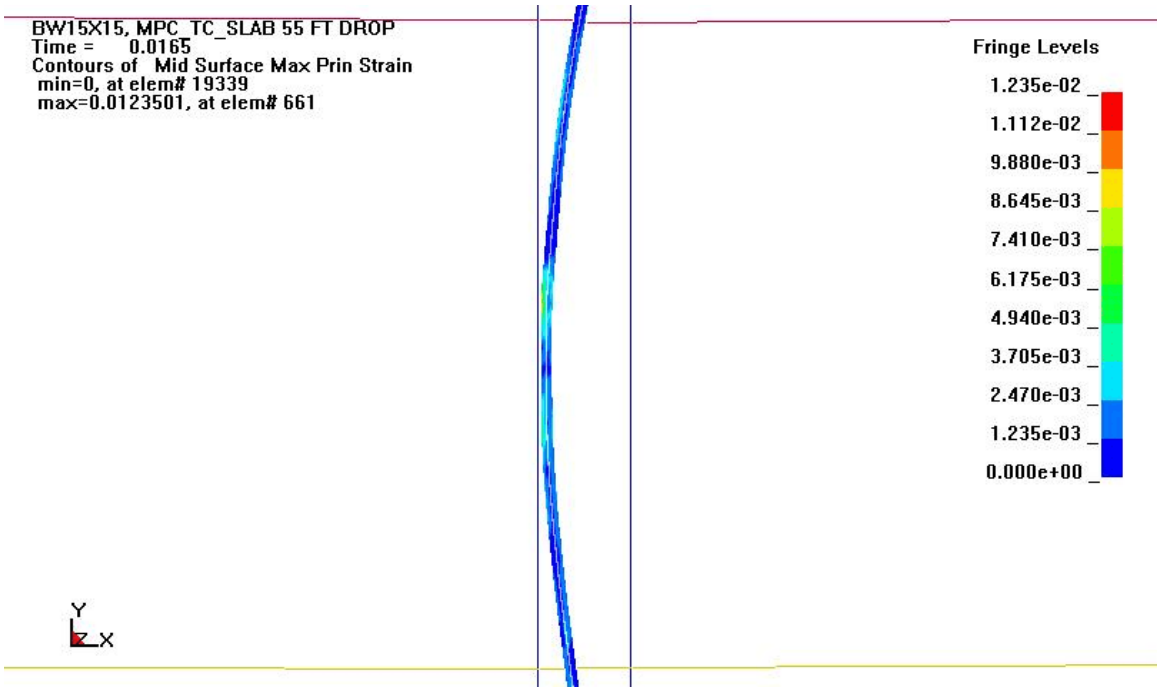

Figure C.11. Maximum Principal Strain at 0.0165 seconds (55-Foot Drop)

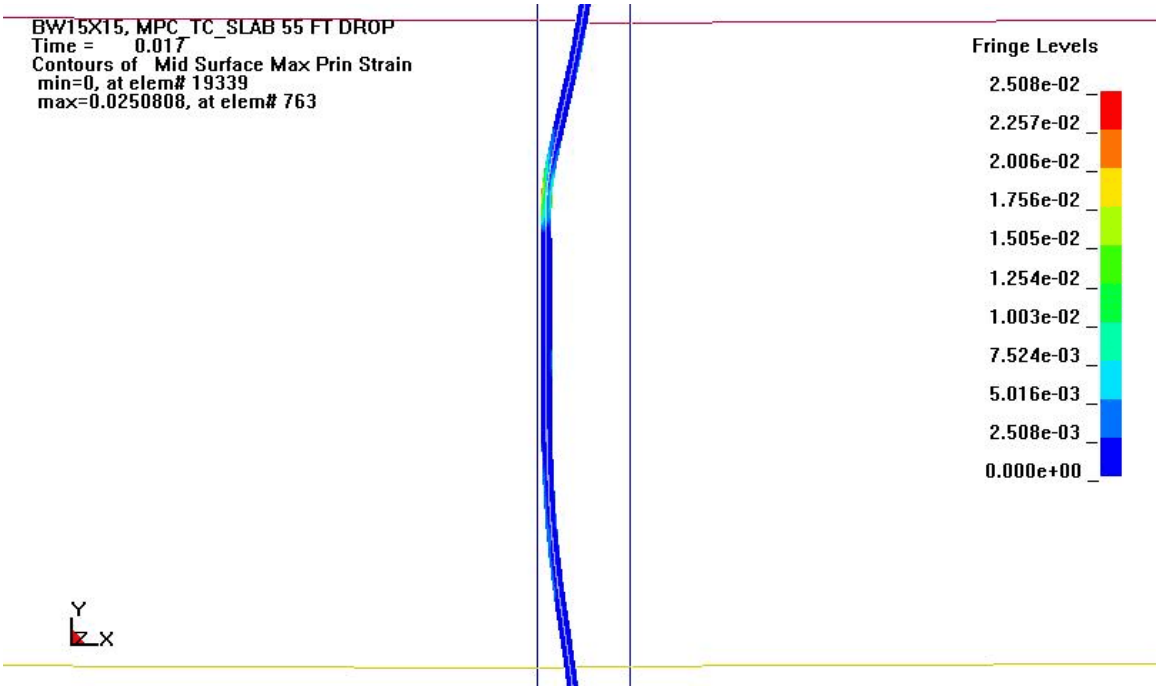

Figure C.12. Maximum Principal Strain at 0.0170 seconds (55-Foot Drop)

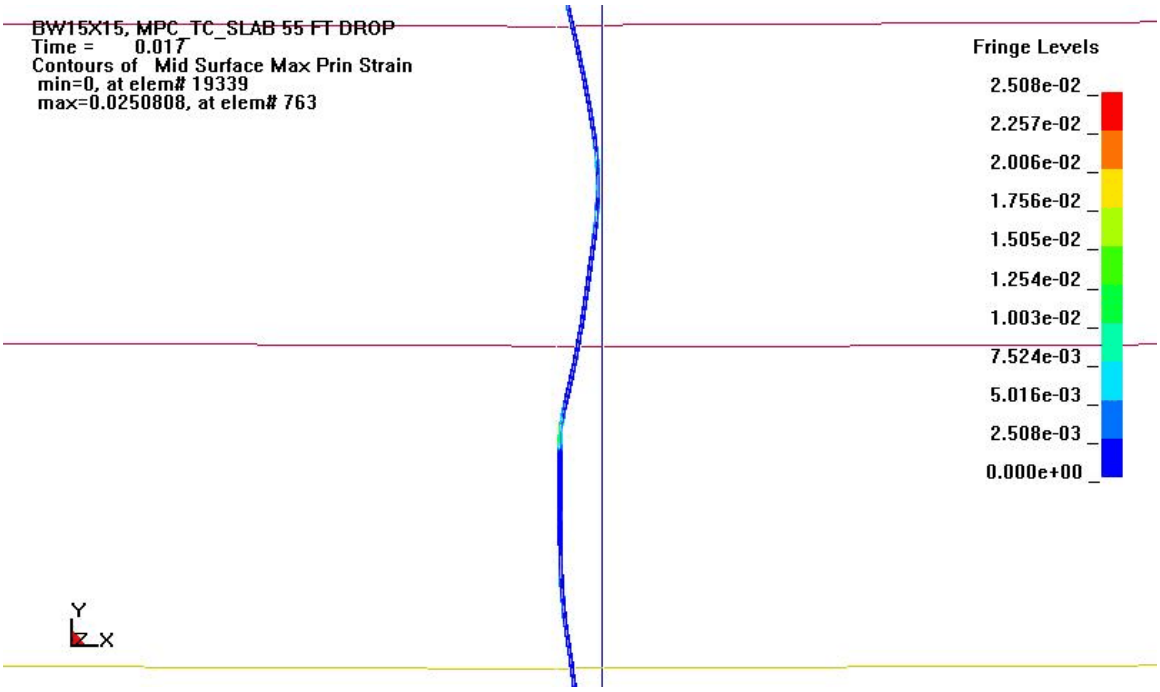

Figure C.13. Maximum Response Shown Over the Span of Two Grid Spacers (55-Foot Drop)

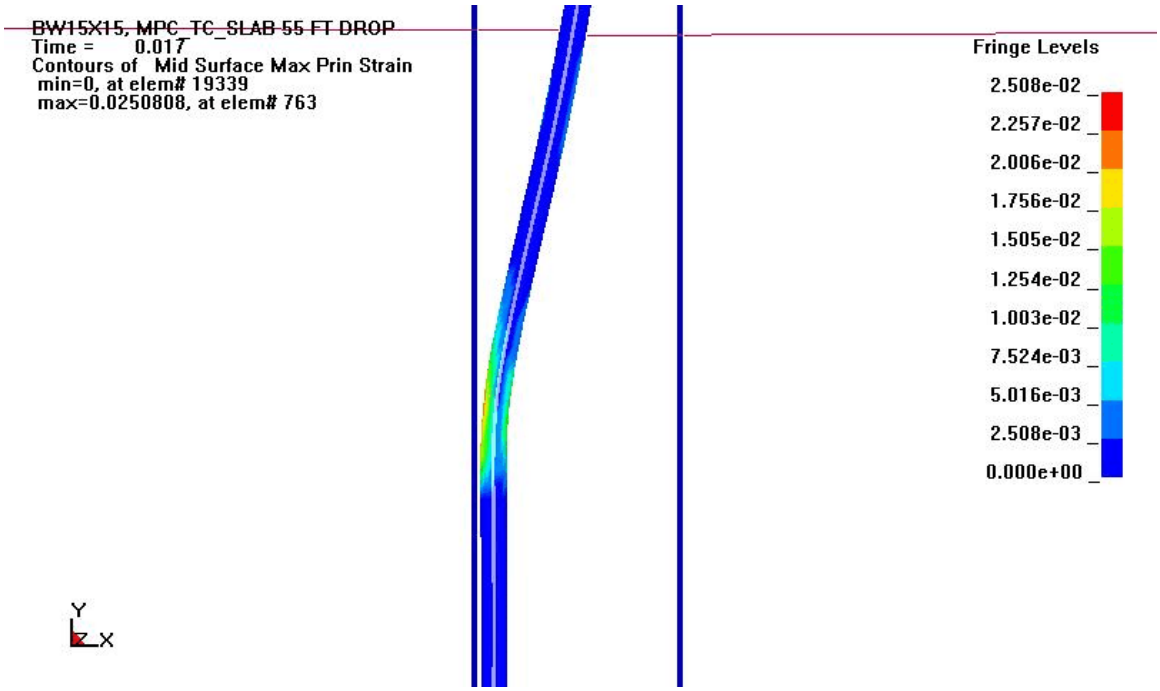

Figure C.14. Extreme Flattening of the Rod Against the Compartment Wall and Concentration of Curvature at the Location Where the Rod Loses Contact with the Wall (55-Foot Drop)

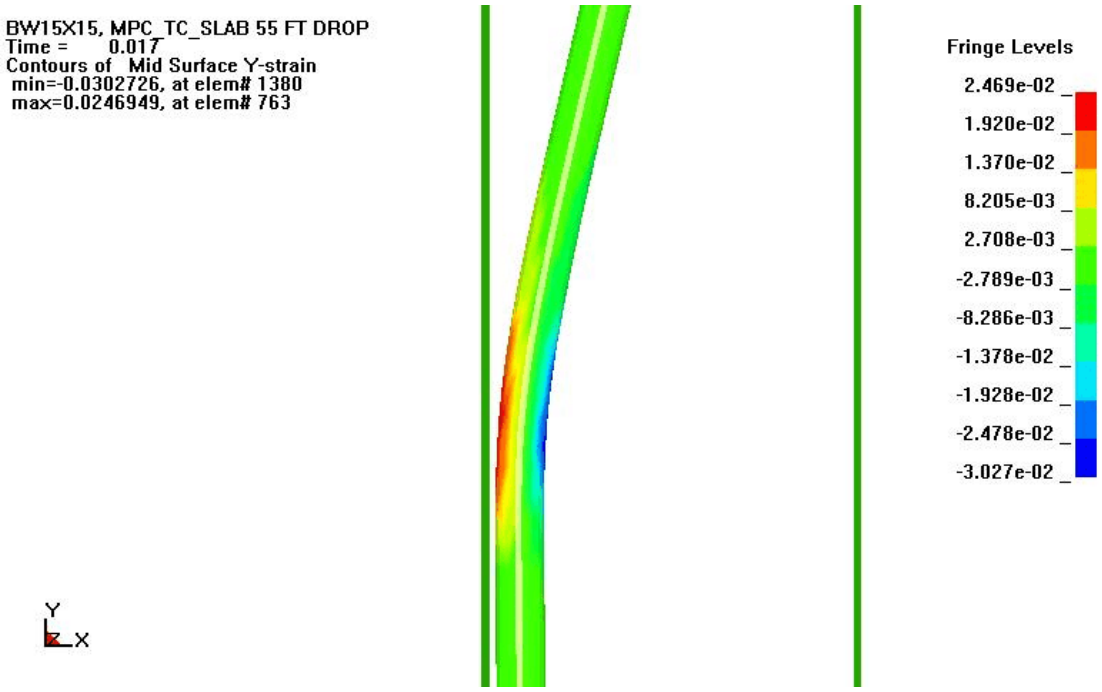

Figure C.15. Closer View of Figure C.14 Showing the Longitudinal Strain Distribution (55-Foot Drop)

The response of the fuel rod for the 5.8-meter (19-foot) drop of the MPC into the storage overpack exhibits completely different behavior than the transfer cask drops onto the concrete floor. Figure C.16 shows the global behavior just prior to the time of maximum response. Figures C.17 and C.18 are closeup views showing the maximum principal strain and the distribution of longitudinal stress at the time of maximum response. The buckled shape is indicative of the classic response of a rod that is unrestrained laterally when impacting a rigid surface (Reference 10). It is clear that the location of the grid spacers does not matter, because the short wavelength mode of buckling is so dominant that it overrides the flexible lateral resistance of the grid spacers and the lateral bow. As can be seen this free mode of buckling has a much shorter half-wavelength than the distance between grid spacers.

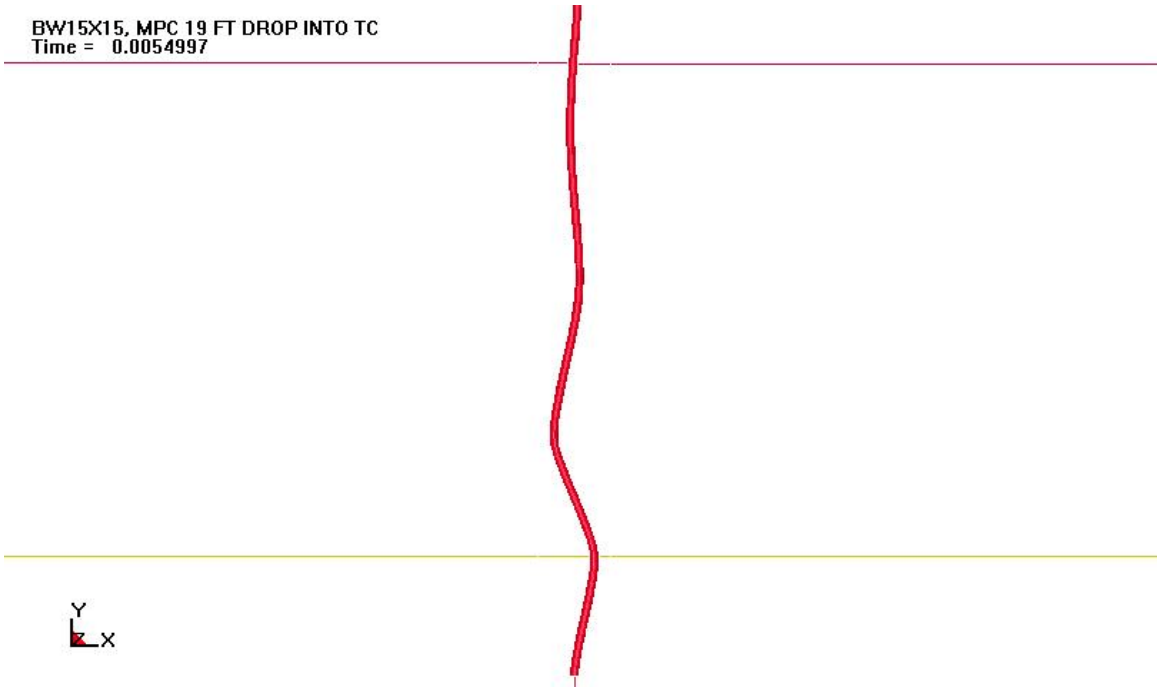

Figure C.16. Buckling Response at the Rod Bottom End Just Prior to the Time of Maximum Response (19-Foot Drop of MPC into Storage Overpack)

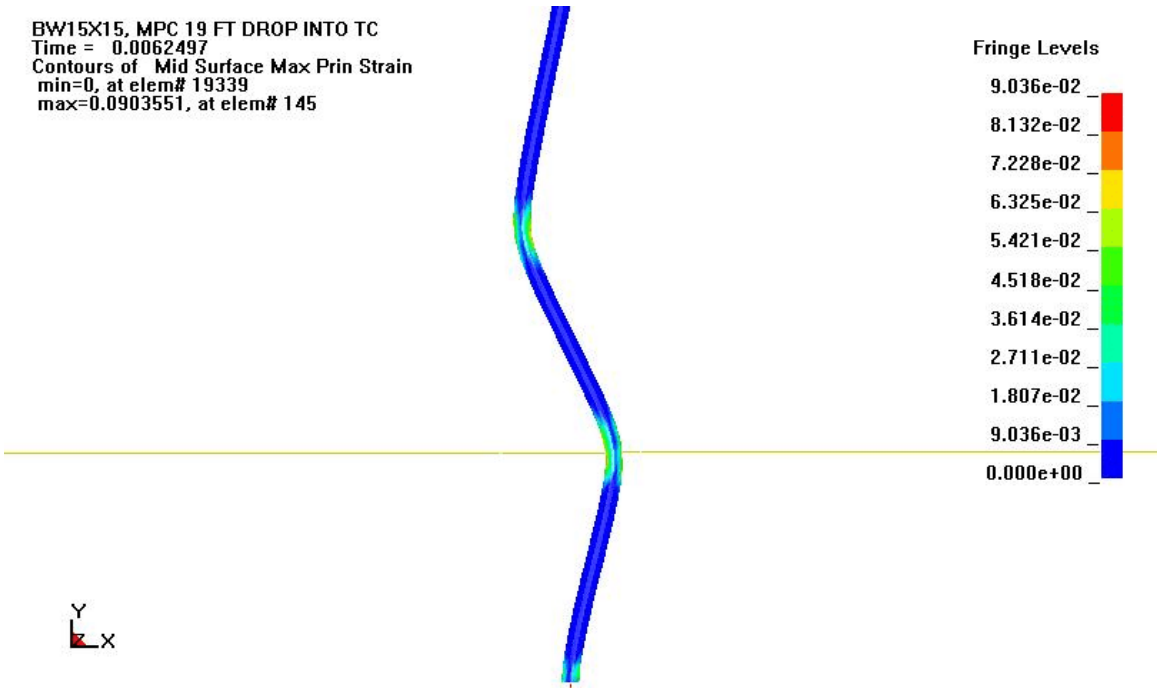

Figure C.17. Maximum Principal Strain at Time of Maximum Response (19-Foot Drop)

Figure C.18. Longitudinal Stress Distribution at Time of Maximum Response (19-Foot Drop)

C.1.4 Fuel Rod Cladding Failure

The cladding strain at failure (rupture or breach) of high-burnup fuel, which is fuel with a burnup greater than 45 GWd/MTU, is expected to range from 1.0% to 3.0%. For the purpose of the PRA, the lower value of 1.0% strain is selected as the strain limit.

Appendix D of the PRA shows that the particulate release fraction from a spent fuel rod is a function of three variables: (1) the fraction of the fuel rim layer that fractures, (2) the percentage of particulate entrained by gasses during release, and (3) the number of tears (breaches) per rod. In addition, the fraction of the rim layer fractured and the number of breaches per rod are, in turn, functions of the g loads experienced by the fuel and the severity of the buckling that takes place during a given drop.

In a full-blown PRA each of these variables would be associated with a probability distribution and sampled as part of an overall simulation. However, because of the level of effort inherent in such an approach, Appendix D simplifies the methodology by recommending an upper bound value for release fractions to be used in the consequence analysis. This, in turn, simplifies the effort here in Appendix C by not requiring an estimate of the number of breaches per rod, but only whether or not the rod breaches at all. Also, since the analysis of fuel rod failure is based on a single pin model, it will be assumed that when one rod fails, all rods fail, although this is very unlikely.

For each drop height, Table C.3 lists the maximum principal strain in the cladding, the failure strain limit and whether or not fuel cladding breach occurs based on that limit strain.

Table C.3. Likelihood of Fuel Cladding Breach for Various Drop Scenarios

Event Scenario	Impact Surface (Target)	Drop Height (ft)	Maximum Principal Strain in Cladding (in/in)	Strain Limit Selected for High Burnup Fuel	Fuel Cladding Breach
Transfer Cask Vertical Drop	Concrete Floor	1	0.0043	0.01	No
		5	0.0062	0.01	No
		20	0.0072	0.01	No
		40	0.011	0.01	Yes
		55	0.025	0.01	Yes
		70	0.037	0.01	Yes
		100	0.052	0.01	Yes
	Storage Overpack	5	-1	na	No
		40	-1	na	Yes
		80	-1	na	Yes
MPC Drop into Storage Overpack	Storage Overpack Pedestal	19	0.09	0.01	Yes

(1) This drop was not evaluated for cladding response. Results for the transfer cask drop onto the concrete floor from the same height were used to determine cladding breach.

C.2 Fuel Response to Thermal Loads

The thermal analyses described in Section 4.2.3 of this report calculated the temperature of the fuel cladding for both the external fire and blocked vent scenarios. For these accident scenarios, fuel response is determined by comparing the calculated cladding temperatures to the temperature limits as discussed in Section 4.2.3. The long-term normal and short-term accident temperature limits for Zircalloy cladding are 400 °C (752 °F) and 570 °C (1,058 °F), respectively.

In the case of an external fire, the short-term temperature limit is used because the fire duration is only 3 hours. In the vent blockage scenario, the long-term normal temperature limit is used because vent blockage is assumed to occur for 20 years for the purpose of the PRA only.

C.2.1 Results of Fuel Response to Thermal Loads

The thermal analyses performed for this PRA show that under normal steady-state conditions the bulk MPC pressure is 0.565 MPa (82 psi) and the average fuel temperature is only 179 °C (354 °F). If the storage cask is exposed to an external fire for 3 hours the pressure increases slightly to 0.634 MPa (92 psi). Figures C.19 and C.20 plot the distribution of maximum cladding temperatures following a 3-hour fire. Figure C.19 shows the maximum cladding temperature as a function of axial height while Figure C.20 shows the maximum cladding temperature as a function of radial position from the cask center. The axial height is measured from the base of the overpack such that the bottom of the fuel rods is at a height of 0.67 meter (2.2 feet). Also shown in these figures is the 570 °C (1,058 °F) short-term temperature limit. These figures clearly show that the cladding temperature limit is not exceeded. Therefore, no fuel failures occur if the storage cask is exposed to an external fire for 3 hours. [Note that cladding failure would not be expected to occur until cladding temperatures reached 750 °C (1,382 °F.]

For the vent blockage scenario, the MPC pressure and cladding temperature are also expected to increase. For the purpose of this PRA, the assumption is made that vent blockage occurs for the entire 20 year license period of the cask. Under these conditions, the MPC pressure will eventually reach a new steady-state value of 0.745 MPa (108 psi).

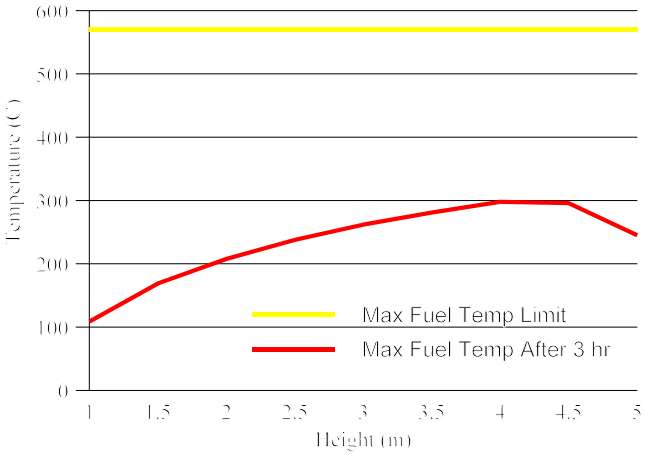

Figure C.19. Maximum Fuel Temperature as a Function of Axial Height after a 3-Hour External Fire

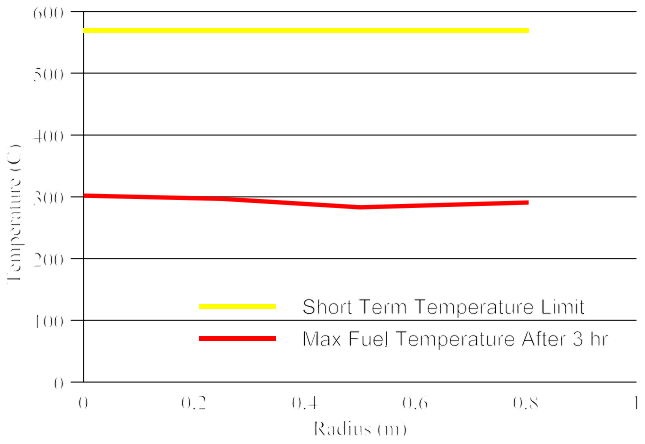

Figure C.20. Maximum Fuel Temperature as a Function of Radius after a 3-Hour External Fire

Figure C.21 shows the maximum cladding temperature as a function of axial height after steady-state vent blockage. Again the axial height is measured from the base of the overpack such that the bottom of the fuel rods is at a height of 0.67 meter (2.2 feet). Figure C.22 plots the maximum cladding temperature as a function of radial position after vent blockage. These figures also show that some of the fuel within the cask will exceed the normal long-term temperature limit of 394 °C (742 °F). The fraction of fuel rods that exceeds this temperature limit can be estimated as follows. The dashed line in Figure C.22 represents a polynomial fit (trend line) to the radial temperature distribution data. The equation of this polynomial fit is as follows:

$$T_{Fuel} = -294.53 \bullet x^2 + 68.731 \bullet x + 462.01 \qquad [C.2]$$

where: T_{fuel} = Maximum fuel cladding temperature in °C
x = Radial distance from cask center in meters

The fit to the data is excellent with an R^2 value of 0.994.

Based on this equation, all fuel rods located within a radius of 0.615 meter (2.02 feet) of the cask center will have a maximum cladding temperature that exceeds the zircalloy normal long-term temperature limit. The circular area associated with these failed fuel rods is 1.19 m^2 (12.79 ft^2). The cross-sectional area of the entire MPC interior is 2.37 m^2 (25.5 ft^2). The fraction of fuel rods that exceeds the temperature limit is estimated by taking the ratio of these two areas. Using this procedure, the fraction of fuel expected to exceed long-term temperature limits under blocked vent conditions is 0.5.[5]

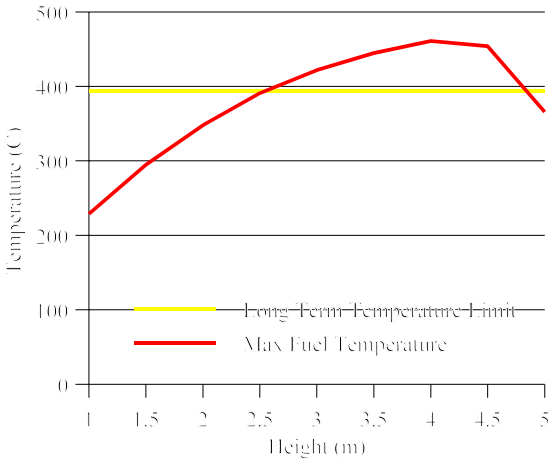

Figure C.21. Maximum Fuel Temperature with Vent Blockage as a Function of Axial Height

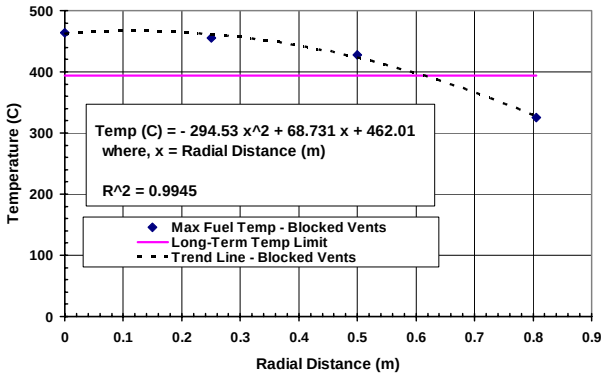

Figure C.22. Maximum Fuel Temperature as a Function of Radius After Vent Blockage and Zircalloy Normal Long-Term Temperature Limit

5 One component of determining the rod stress is the gas expansion attributable to increased temperature. At least half of the gas in the plenum is usually not the hottest part of the rod. Therefore, the stress will not be as high as if the rod was at a uniform temperature. Calculations for creep, resulting in the 400 °C (752 °F) temperature are based on a uniform temperature. Thus, the calculation is a conservative over-prediction of the rod failure rate.

C.3 References

C.1. Bjorkman, G.S., "The Buckling of Fuel Rods under Hypothetical Accident Conditions," *Proceedings of PATRAM 2004*, Berlin, Germany, September 2004.

C.2. HOLTEC International, "HI-STORM Topical Safety Analysis Report," HOLTEC Report HI-951312, Revision 8, Marlton, NJ, 1999.

C.3. Adkins, H.E., B.J. Koeppel, and D.T. Tang, "Spent Nuclear Fuel Structural Response When Subject to an End Drop Impact Accident," *Proceedings ASME/JSME Pressure Vessels and Piping Conference*, PVP-Vol. 483, American Society of Mechanical Engineers, New York, New York, 2004.

C.4. Geelhood, K.J., and C.E. Beyer, "Mechanical Properties of Irradiated Zircalloy," *Transactions of ANS Winter Meeting*, Vol 93, American Nuclear Society, Washington, DC, November 2005.

C.5. Sanders, T.L., K.D. Seager, Y.R. Rashid, P.R. Barrett, A.P. Malinauskas, R.E. Einziger, H. Jordan, T.A. Duffey, S.H. Sutherland, and P.C. Reardon, "A Method for Determining the Spent-Fuel Contribution to Transport Cask Containment Requirements," SAND90-2460, Sandia National Laboratories, Albuquerque, New Mexico, 1992.

C.6. U.S. Nuclear Regulatory Commission, "Buckling of Irradiated Fuel Under Bottom End Drop Conditions," ISG 12, Rev. 1, Washington, DC, 1999.

C.7. U.S. Nuclear Regulatory Commission, "Buckling of Irradiated Fuel Under Bottom End Drop Conditions" ISG 12, Rev 2 (DRAFT), Washington, DC, 2006.

C.8. ABB Combustion Engineering, Inc., "Fuel-Assembly Behavior Under Dynamic Impact Loads Due to Dry-Storage Cask Mishandling," EPRI-NP-7419, prepared for Electric Power Research Institute, Palo Alto, California, 1991.

C.9. Roark R.J., *Formulas for Stress and Strain*, 5th Ed., McGraw-Hill, New York, New York, 1975.

C.10. Jones, N., *Structural Impact*, Cambridge University Press, Cambridge, England, 1989.

APPENDIX D
METHODOLOGY TO DETERMINE SOURCE TERM FOR A DRY STORAGE CASK

APPENDIX D
METHODOLOGY TO DETERMINE SOURCE TERM FOR A DRY STORAGE CASK

D.1 Introduction

Should a cask containing spent nuclear fuel be impacted by a projectile or strike a hard surface, the potential exists for radioactive material to be released from the cask if the magnitude of the impact is large enough to breach the cask and disrupt the fuel rods. The extent of the release will depend on the magnitude of the impact, the characteristics of the payload of the cask, the configuration and environment of the cask, and the physical details of the cask. This section will present a model to evaluate the fraction of material released from a breached cask, and discuss the variability of the input parameters required to exercise the model. The release fractions for a particular cask and payload, derived by the methodology will be given.

D.2 Methodology

A severe enough impact on the cask will fail a fraction of the fuel rods (F_{rods}) and make their contents available for release. A portion of this available material will be released from the rod to the cask environment (F_{RC}). Part of the inventory that has been released to the cask will be transported through the breach in the cask to the environment (F_{CE}). The fractional release from the cask (F_{rel}) can be approximated by the following equation:

$$F_{rel} = F_{rods} \times F_{RC} \times F_{CE} \quad \text{(D.1)}$$

The fuel rods can have radionuclides on the cladding surface in the form of solid Chalk River Unidentified Deposits (CRUD), inside the fuel rod as gases and volatile fission products, and within UO_2 fuel grains as both solids and gases. Because of the different physical forms of the radionuclides, Equation D.1 must be analyzed separately for each radionuclide or group of similar radionuclides. Since long-duration fires are not considered in this evaluation, and the maximum design storage temperature of the fuel is 400 °C (752 °F), transport of fission products, such as Cs in the form of CsI that has a melting point >600 °C (1,112 °F), as condensable vapors will not occur, the radionuclides in spent fuel were assigned to one of the following three chemical element groups (k=1 to 3): noble gases, particulates, and CRUD. For each of these three groups, the inventory of each radionuclide that might be released from a breached cask to the atmosphere (the source term ST_i for radionuclide I) can be calculated as the product of the release fraction $F_{rel,k}$ for the chemical element group k to which the radionuclide belonged and the inventory I_i of that radionuclide in the cask. Thus, we have the following relationship:

$$ST_i = \sum_{k=1}^{3} I_{ik} F_{rel,k} \quad \text{(D.2)}$$

The major difference between the current and previous models (Reference D.1) is that the current model accounts for the different properties of the rim region formed in high-burnup fuel, as well as the reduced ductility of the cladding as a result of higher burnup and hydrogen absorption. The methodology, as presented, is only applicable to impact type events (not those that result in an elevated temperature attributable to a long-duration fire). A long-duration fire may introduce volatile fission products as a new class of releasable radionuclides, add oxidation of the fuel as a release mechanism (for example oxidation of the stable RuO_2 oxide to the volatile RuO_4), change the particle size distribution, produce additional rod failures by thermal burst rupture of unfailed rods, and increase the driving force for dispersal of material.

D.2.1 Radionuclide Inventory (I_i)

The ORIGEN2 code (References D.2 and D.3) is recommended to calculate the radionuclide inventory of the fuel. Because an ORIGEN calculation provides output for more than 800 radionuclides, the number of radionuclides in the ORIGEN output can be reduced by dividing the 10-year cooled amount of each radionuclide by its A_2 value (References D.4 and D.5) and then selecting the smallest set of these normalized Curie amounts that yielded a sum greater than 99.9 percent of the sum of all of these normalized Curie amounts. This procedure reduces the ORIGEN output to a much smaller set of 12 radionuclides that are important for the estimation of radiological health effects. If fuel fresher than 10-year cooled is loaded, this list of radionuclides may change and should be reevaluated.

In addition, five radionuclides, ^{106}Ru, ^{134}Cs, ^{144}Ce, ^{147}Pm, and ^{154}Eu, available for release in most fuels should be added so that most of the fuel inventories contain the same set of radionuclides. In order to have a noble gas in the inventory, although eliminated by the A_2 screen, ^{85}Kr, the noble gas with the largest Curie amount in the ORIGEN inventory for 10-year cooled high-burnup spent boiling-water reactor (BWR) fuel, should also be added to the reduced set of radionuclides.

Finally, ^{60}Co should be added to the reduced set of radionuclides so that release of ^{60}Co attributable to the spallation of CRUD (Reference D.6) from rod surfaces could be addressed. CRUD is the deposits that form on the surfaces of spent fuel rods while the rods are in an operating reactor (Reference D.7). The properties of CRUD were extensively reviewed by Sandoval (Reference D.7). Recommendations for calculating the CRUD inventory are given in the Table D.1 below.

Table D.1. Recommendations for Calculating the CRUD Inventory

CRUD Parameter	Recommendation
Inventory	Recommended values in the Standard Review Plan bound 99% of the fuel inventory. The CRUD inventory is reduced by a factor of 10-20 if only 90% of the fuel is bounded. Recommend using inventory bounding 90% of the fuel to be realistic or calculate release as a function of the percent of fuel bounded.
Out-of-reactor time	Reduce the inventory of ^{60}Co due to decay.
Axial Distribution	CRUD does not tend to be evenly distributed along a fuel rod. The ratio of the average CRUD thickness to maximum CRUD thickness is about a factor of 2. Reduce maximum surface CRUD concentrations by a factor of 2.
Burnup	There is no apparent burnup dependence for CRUD thickness but the inventory can be scaled linearly with burnup for conservatism. Some newer fuels have very thick crud resulting from water chemistry. The influence of water chemistry should be handled as a special case.
Fuel Type	Use inventory appropriate for fuel type (i.e., BWR or PWR).

While the ORIGIN2 code gives overall inventories for the fuel, it must be recognized that the radionuclides are not evenly distributed. The spatial distribution must be accounted for due to the variation of burnup both axially along a rod, and radially within a rod. In particular, for high-burnup fuel that contains a rim region, the actinide inventory in the rim is about twice that in the body of the fuel pellet. As a result, any analysis of release fractions should consider the rim region and the body of the pellet as separate entities. The axial distribution is only important if thermal gradients in the cask make some axial rod locations more prone to fracture than others.

D.2.2 Fraction of Fractured Rods (F_{rods}) and Fracture Sites per Rod

Only a fraction of the energy imparted to the cask system during an impact will be available for rod fracture. The remainder will be absorbed during cask deformation, or used to spall CRUD and fracture the fuel within the rods.

In previous studies (Reference D.1), calculated rod strains were compared to a rod strain failure criterion in order to estimate how many rods would be failed and how many failure sites were expected along a rod. There is no definitive information on what the exact strain to failure should be, especially at high burnups. Estimates ranging from 0.25 to 4% have been proposed (Reference D.8). Although this strain to failure should be temperature-dependent, this dependence was not considered in previous studies. Another section in this report describes a method for determining rod failure (See Section 4.4).

D.2.2.1 Variation in Cladding Material and Material Properties

During irradiation, hydrogen is introduced into the cladding as a result of waterside corrosion. The preponderance of this hydrogen precipitates as circumferential hydrides in the outer third of the cladding. The mechanical properties of irradiated Zircaloy, as a function of hydrogen content, have recently been reviewed by Geelhood, et al. (Reference D.9). During the drying of the fuel after the loading of the storage cask, conditions might be suitable for reorientation of some of the hydrides from the circumferential to a radial orientation, reducing the ductility of the cladding. As fuel is driven to higher burnups, newer claddings such as M5, and Zirlo are being put into service to reduce cladding corrosion. Cladding mechanical properties appropriate to the type of cladding and hydride orientation within the cladding should be used in any calculation of the number of breached rods.

D.2.2.2 Number of Fracture Locations ($n_{tear/rod}$) and Size of Fracture

The number of fracture locations along a rod will not affect the amount of gas available to drive radioactive solid particulates from the cask to the environment since all the available gas is released irrespective of the number of sites. Since the release of fuel fines to the cask environment is a localized event, the number of fracture sites will somewhat linearly increase the release of fuel fines. An estimate of 5 tears/failed rod has been made in the past using the strain- to-failure method, and should be used as a default value, unless a more realistic value (such as calculated in Section 6.1) is supportable.

At the current time, there is no data supporting a distribution of cladding crack sizes under impact. For the purpose of this model it is assumed that cracks caused by impact are half circumferential cracks with a length to width aspect ratio of 10. For example, the cracks formed in BWR spent fuel rods with an inner diameter of 1.07 cm by rod impact with the spacer grid will respectively have lengths (l_c) and widths (w_c) of $l_c = \pi\ (d_{rod,inner}/2) = 1.7$ cm and $w_c = 0.17$ cm.

D.2.3 Driving Force for Release from Rod-to-Cask and Cask-to-Environment

Rod fracture makes two main contributions to the release of radionuclides. Unless the cladding fractures to expose the fuel pellets and fission gases, and radionuclides contained within, only CRUD is available for release. Secondly, depressurization of the rods carry gases and entrains fuel fines from the rod to the cask and contributes to the force pushing any radioactivity from the cask to the environment. When the cladding breaches, the gas contained in the rods will be added to the initial 1 to 5 atmospheres of cask inert fill gas that will be available for cask depressurization. This is a more significant contributor in PWR systems where the rods are initially filled to a higher gas pressure, and in casks only pressurized to 1 atmosphere.

D.2.3.1 Rod and Cask Depressurization

The release of small particulate residing on the internal crack network of the fuel by entrainment depends on whether, during depressurization of the rod, the gas flows predominately through the cracks in the fuel or any fuel-cladding gap that might have opened up during cool down. In addition, the rate of depressurization of a rod will depend on the hydraulic diameter of the depressurization path.

In-core measurement, at temperature, of the hydraulic diameters of average- and high-burnup spent fuel rods from the Halden Reactor show that average- and high-burnup spent fuel rods have hydraulic diameters of about 50 and 35 μm respectively (Reference D.10). At temperature, the fuel cladding gap is closed. The extent to which it opens will depend on the temperature of the fuel (i.e., the cooling time of the fuel). Estimates of the gap from photomicrographs at room temperature range from no gap to as much as a 50 μm gap. In the latter case, the hydraulic diameter and the geometric diameter of the reopened gap should be about the same and both should be substantially larger than the hydraulic diameter of the crack network in the pellets. This raises the question of whether rods will depressurize primarily through the reopened gap and only minimally through the pellet crack network. If this is the case, crack gas flow rates may be so small that particles formed on the surfaces of the cracks will not become entrained in the gas flow and, therefore, may not be released.

The depressurization time Δt of a volume V through an orifice with area A can be calculated (Reference D.11) using the following equation:

$$\Delta t = \frac{V/A}{\sqrt{\gamma\left(\frac{P_o}{\rho_o}\right)\left(\frac{2}{\gamma+1}\right)^{\frac{\gamma+1}{\gamma-1}}}}\left(\frac{2}{\gamma-1}\right)\left[\left(\frac{\rho_1}{\rho_o}\right)^{\frac{1-\gamma}{2}}-1\right] \qquad \textbf{(D.3)}$$

where $P_o/\rho_o = RT_o/MW$, $\rho_1/\rho_o = P_1T_o/P_oT_1$, $\gamma = C_p/C_v$, and P_o, ρ_o, MW, T_o, C_p, and C_v are pressure, density, molecular weight, temperature, and heat capacities at constant pressure and constant volume of the mixture of gases in the volume V respectively, R is the ideal gas constant, and ρ_1 is the density of the gas mixture in the volume into which the volume V is venting.

This equation with P_o/ρ_o replaced by RT_o/MW and ρ_1/ρ_o replaced by P_1T_o/P_oT_1 can be used to estimate the depressurization time of the cask and also of the failed spent fuel rods in this cask.

For depressurization of the mixture of He and Xe from failed rods into the interior of a cask, MW = 94.2 g/mole, $\gamma = 2.5$, $T_1 = T_o$ = cask temperature and P_o = rod pressure at temperature. V is determined by dividing the internal rod volume by the number of crack sites on the rod (See Section D.2.2.2).

Assume for the purpose of example that the gap does not open upon cooling or that the accident occurs shortly after loading and the fuel is still relatively hot. Then, $d_{h,rods} = 3.5\times10^{-3}$ cm and $A = \pi(d_{h,rods}/2)^{2}$. Even though the internal free volume of the cask is large compared to the free volume of a spent fuel rod, because the hydraulic diameter of the fuel pellets and any pellet cladding gap in the rod is only about 35 mm, the cask should depressurize much more rapidly than the rods. So, during almost all of the rod depressurization time period, the cask pressure will be 1 atm, which means that for rod depressurization, P_1 = 1 atm. Calculations using typical BWR rod parameters and internal pressures in Equation D.3 yield $\Delta t \sim 679$ sec for the depressurization time of the average failed rod in a typical cask. Using Equation D.3, it can also be shown that the assumption of rapid depressurization of the cask is also satisfied for this example.

D.2.3.2 Depressurization and Gas Flow Rates

The flow rate of gas through failed rods to cladding failures, out of failed rods into the cask fuel tubes, and through the cask fuel tubes to the location of the closure failure will determine whether entrainment of particles formed on exposed pellet surfaces, inertial impact of particles with rod spacers, and deposition of particles onto rod and fuel tube surfaces by gravitational settling and turbulent diffusion are significant.

The rate of gas flow out of a volume can be calculated using the following relationship:

$$A\ v\ \Delta t = V\ (P_i/P_f)\ (P_i - P_f) / P_i = V\ (P_i - P_f) / P_f \qquad (D.4)$$

where A is the area of the flow path, v is the linear flow velocity, Δt is the depressurization (flow) time, V is the volume of gas that depressurizes, P_i is the initial gas pressure in this volume, P_f is the pressure in the volume after depressurization, $V(P_i/P_f)$ is the volume that the gas in the volume V would occupy were it at the depressurization pressure P_f, and $(P_i - P_f)/P_i$ is the fraction of the gas in the volume V that will flow out of that volume as a result of depressurization. Rearrangement yields the following equation:

$$v = V(P_i - P_f) / (P_f\ A\ \Delta t) \qquad (D.5)$$

If particles formed on pellet surfaces by impact fracturing become entrained in rod depressurization gas flows over these surfaces, these particles could be transported from the rod through cladding failures to the cask interior. Because of the very small hydraulic diameter of high-burnup spent fuel rods, rod gas pressures should be fairly uniform throughout the rod's internal crack network until the depressurization gas flow nears a cladding failure. Thus, for flow in the internal crack network, $v = V/A\Delta t$, where A is the hydraulic cross-section. Alternatively, if rod depressurization occurs predominantly through a reopened pellet/cladding gap, a maximum value for the flow cross-sectional area is $A = \pi[(d_{rod,inner}/2)^2 - (d_{pellet}/2)^2]$. For the same BWR example as above, for flow through the internal crack network $v_{entrainment}$ =37 m/sec. Alternatively, if rod depressurization occurs predominantly through a reopened pellet/cladding gap, a minimum value is $v_{entrainment}$ = 0.021 m/sec.

Impingement of the gas stream out of the rod onto a grid spacer or adjacent rod during depressurization of the rod will determine if impaction removes particulate from the gas stream. The efficiency of particle removal by inertial impaction will depend on the relative flow rate of rod gases as they exit cladding failures ($v_{rod\ failures}$) to the velocity of the gas moving perpendicular to the breach down the rod. From Equation D.5, $v_{rod\ failures} = V(P_i - P_f)/(P_f A\Delta t)$, where $V = V_{rod\ free}$/(number of crack sites thru which the average rod depressurizes).

Because the cask depressurizes much more rapidly than the rods, when no fuel-cladding gap is present, the fuel (basket) tubes in the failed cask will be at atmospheric pressure while the particles released from failed rods are flowing through them to the location of the cask's closure failure. Accordingly, the flow velocity down the fuel tube (v_{tube}), can be calculated as

$$v_{tube} = V_{rod\ free} F_{rods} n_{rods/assembly} (P_{rod} - P_{atm})/(P_{atm} A_{tube\ free} \Delta t)$$

where $V_{rod\ free}$ = rod free volume, F_{rods} = the fraction of the rods in an assembly that fail, $n_{rods/assembly}$ = rods per assembly, P_{rod} is the rod pressure before the rod fails, P_{atm} = 1.0 atm, Δt = rod depressurization time, and $A_{tube\ free}$ equals the free cross-sectional area of a basket tube, where $A_{tube} - A_{rod} n_{rods/assembly} = (w_{tube})^2 - \pi(d_{rod}/2)^2 n_{rods/assembly}$.

D.2.4 Release from Rod to Cask Environment (F_{RC})

In high-burnup spent fuel pellets, capture of epithermal neutrons by uranium atoms in the pellet rim produces a friable layer of fuel fines on the outer surface of each pellet. Measurements indicate that the thickness of this friable rim layer (t_{rim}) in high-burnup BWR spent fuel is about 150 μm (References D.12, D.13, and D.14). PWR rods have a somewhat thinner rim at an equivalent burnup. Because the body and the rim of high-burnup spent fuel pellets have quite different morphologies (References D.12, D.15, and D.16), release of noble gases and of fuel fines from these two regions of a high-burnup pellet may be quite different. Like fresh UO_2 pellets, the body regions of high-burnup spent fuel pellets consist of sintered 10 μm UO_2 particles. In the rim layer, 0.1 to 0.3 μm subgrains are generated by the recrystallization of UO_2.

The volume of fuel pellets in a single rod and the volume of the rim layer on these pellets are given by $V_{pellets} = \pi(d_{pellet}/2)^2 L_{active}$ and $V_{rim} = \pi d_{pellet} t_{rim} L_{active}$, and thus, $V_{rim}/V_{pellets} = 4 t_{rim}/d_{pellet}$. However, the capture of epithermal neutrons, which causes the rim layer to form, doubles the concentration of radionuclides in the rim layer compared to their concentration in the pellet body (Reference D.13). For a typical BWR rod about 11.3 percent of the total radionuclide inventory in the pellets resides in the friable rim layer of these pellets and the remaining 88.7 percent of the total inventory is contained in the body of the pellets. Accordingly, for BWR rods,

$$F_{RC,k} = (0.113)(F_{rim\ release,\ k}) + (0.887)(F_{body\ release,\ k}) \quad (D.6)$$

A similar relationship can be developed for PWR fuel.

D.2.4.1 Particulate Release from the Rod to the Cask

D.2.4.1.1 Fuel Fracture

The release fraction for fuel fine particles can be estimated as follows. First, estimate the initial fraction of the UO_2 mass in a rod that is converted to fuel fines by abrasion and vibration, radiation embrittlement, and impacts. Second, estimate the fraction of fuel fines that could become gas borne. Lastly, estimate the fraction of the gasborne particles that might be trapped by particle bed filtration as a result of passage through particle beds during transport to the location of the rod failure.

The release fraction for particles is then calculated as shown in Equation D.7 below, using the fractions from the above steps for particles formed in the following locations:

(1) in the friable rim of the pellet located right next to the rod failure

(2) in the friable rims of other pellets (pellets not located right next to the rod failure)

(3) on the surfaces of the network of internal pellet cracks by abrasion, vibration, and impact fracturing

$$F_{rel,particles} = 0.113(F_{init,rim} + F_{imp,rim})\{[n_{tears/rod}F_{tear,rim}] + [F_{ent,rim}(F_{bed})]\} + 0.887\{n_{tears/rod}(F_{init,body} + F_{imp,body})(F_{bed})\}^{6} \quad (D.7)$$

where:

F_{init} = the fraction of the mass of the UO_2 fuel pellets in a rod that has been converted to respirable fuel fines by abrasion and vibration before the impact event takes place. This fraction can be calculated for either the body or the rim region.

$F_{imp,body}$ = the fraction of the mass of the UO_2 in the body of a spent fuel pellet that is converted to respirable fuel fines by brittle fracture as a result of the impacts.

$F_{imp,rim}$ = the fraction of the mass of the UO_2 in the rim layer of a spent fuel pellet that is converted to respirable fuel fines by brittle fracture as a result of the impacts.

$F_{tear,rim}$ = the fraction of the mass of the UO_2 in the rim layer that is blown out of the rod from one rod tear during rod depressurization without filtering by passage through a particle bed.

$F_{ent,rim}$ = the fraction of the mass of the UO_2 in the rim layer that is entrained in the depressurization gas flow through the rim layer-cladding gap and transported to the rod tear and then out into the cask.

F_{bed} = the fraction of the respirable particles that are not captured during flow through a particle bed.

$n_{tears/rod} = 5$ = the number of tears in an average failed rod in the cask.

D.2.4.1.2 Estimation of In-Reactor Fuel Fracture (F_{init})

During reactor operation, compression of fuel cladding (PWR fuel) and swelling and cracking of the fuel pellets in a fuel rod largely eliminates the rod's fuel-cladding gap at high burnup and creates an internal network of cracks inside of the pellets that has a cross-sectional area in the fuel column given in Table D.2. Abrasion during insertion of the pellets into the rod and vibration during reactor operation causes fuel fines to form on pellet external surfaces and also on pellet crack surfaces, especially at the pellet-pellet interfaces.

Table D.2 Free Cross-Sectional Area in Fuel Column

	PWR	**BWR**
Low-Burnup	Initial gap area less correction for 0.6% cladding creep down	Fuel cladding gap area
High-Burnup	<< LBU PWR fuel	< LBU BWR fuel

6 Note that the factors 0.1138 and 0.887 are for very high-burnup BWR fuel and will differ slightly for lower burnups or PWR fuel.

Lorenz heated lengths of low-burnup PWR fuel to burst and measured the amount and size of the particulate emanating from the burst site. The mass fraction of respirable fines in the pellet body can be estimated from the results of Lorenz (Reference D.17) and the filtering efficiency (F_{fil}) of a particle bed for respirable particles. Let

l	=	the particle bed length (cm) that provides a filtering efficiency of F_{fil} = 0.99 for respirable particles
L	=	$10l$
	=	the particle bed length (cm) that intercepts 100 percent of the respirable particles passing through that length
$V_{2(L+l)}$	=	the volume of the spent fuel pellets in a rod section with a length $2(L+l)$
$\rho_{\leq 10\ initial}$ =	$M_{\leq 10\ 2(L+l)} / V_{2(L+l)}$	
	=	the mass concentration of respirable fines in the volume $V_{2(L+l)}$
$M_{\leq 10\ 2(L+l)}$	=	the mass of respirable particles in the volume $V_{2(L+l)}$
$M_{\leq 10\ rel}$	=	the mass of respirable fines released during one of the Lorenz burst rupture release experiments
$M_{12\ in}$	=	the pellet mass in one of Lorenz's 30.5 cm (12 inch) rod test segments
ρ	=	10 g/cm^3
	=	the mass density of a UO_2 spent fuel pellet
$F_{init,body}$	=	$\rho_{\leq 10\ initial}/\rho$.

The analysis of particle release was performed (Reference D.1) using standard aerosol physics (Reference D.18) to estimate that a 0.3-cm (0.1-inch) long bed of 200 μm particles (maximum size particle released in the Lorenz experiments) would have a filtering efficiency F_{fil} = 0.99 for respirable particles. Therefore, l = 0.3 cm and L = $10l$ = 3 cm, where 2L is the length of the rod from which respirable particles escape but are filtered as a result of passage through particle beds, $2l$ is the length of the rod from which respirable particles escape with only partial (0 to 0.99) filtering (i.e., the particle bed length is too short to provide significant filtering), and $2(L+l)$ is the length of the rod beyond which no respirable particles escape. Given these definitions, we find the following relationship:

$$V_{2(L+l)}\,\rho_{\leq 10\,initial}\left[\frac{2L}{2(L+l)}(1-F_{fil})+\frac{2l}{2(L+l)}(1.0)\right]=M_{\leq 10\,rel}$$

where the coefficient 2 corrects for the fact that the lengths L and l occur on each side of the rod failure and, since the filtering efficiency (F_{fil}) = 0.99, we have the following relationship:

$$\left[\frac{2L}{2(L+l)}(1-0.99)+\frac{2l}{2(L+l)}(1.0)\right]=\frac{L(0.01)+l}{L+l}=F_{bed}$$

Lorenz calculated the release fraction for particles from a 30.5-cm (12-inch) long test rod sections as the ratio of the mass of particles released divided by the mass of UO_2 in the 30.5-cm (12-inch) long rod test section. Thus, the release fraction value of 4×10^{-6} for respirable particles, which can be derived from the results of Lorenz, equals $M_{\le 10\ rel}/M_{12\ in}$. Therefore, for the Lorenz experiments, we have the following:

$$\frac{V_{2(L+l)}\ \rho_{\le 10\,initial}}{M_{12in}}\left[\frac{L(0.01)+l}{L+l}\right]=\frac{M_{\le 10 rel}}{M_{12in}}=4\times10^{-6}$$

Now because $M_{12\ in} = \rho V_{12\ in}$ and, therefore, $V_{2(L+l)}/M_{12in} = 2(L+1)/\rho(12\ in)$, substitution and rearrangement of the preceding equation gives the following formula:

$$F_{initbody}=\frac{\rho_{\le 10\,initial}}{\rho}=4\times10^{-6}\,\frac{30.5cm}{2(L+l)}\left[\frac{L(0.01)+l}{L+l}\right]^{-1}$$

Because heating of the rod section in the Lorenz experiments caused a bulge to grow in the cladding before a 1 mm diameter hole bursts somewhere in the bulge, the unfiltered length of the rod test section is the length of the bulge, which is about 5 cm. Therefore, 2 *l* = 5 cm, *l* = 2.5 cm, and because ρ = 10 g/cm^3 and L still = 3 cm the preceding equation yields $F_{init\ body} = 2.4\times10^{-5}$. A similar calculation cannot be done for the rim region since no tests similar to Lorenz's using high-burnup fuel have been conducted to our knowledge.

D.2.4.1.2 Expressions for $F_{imp,body}$ and $F_{imp,rim}$

The DOE Handbook (Reference D.19) gives the following formula for F_{imp}, the fraction of a brittle material that is converted to respirable fines by impact fracturing:

$$F_{imp} = 2\times10^{-11}\ \rho gh = 2\times10^{-11}\ mgh/V = 2\times10^{-11}\ (E/V) = 2\times10^{-11}\rho\ (E/m) \qquad (D.8)$$

where E/V and E/m are the energy per unit volume and per unit mass of the brittle material that is subject to fracturing and the units of the leading coefficient are cm^3/erg.

Figure D.1 compares this equation [$F_{imp} = 2\times10^{-11}\rho(E/m)$] to experimental data for the impact fracturing of a variety of brittle materials including depleted UO_2 and average burnup spent fuel pellets, but no high-burnup spent fuel pellets. The figure shows that the handbook equation lies about a factor of 10 higher than the experimental data. Accordingly, in order to be somewhat conservative, for average burnup spent fuel pellets and for the body of high-burnup spent fuel pellets; the leading coefficient in the DOE Handbook equation is reduced by a factor of five, which gives

$$F_{imp} = 4\times10^{-12}\ E/V \qquad (D.9)$$

$F_{imp,body}$ can be calculated from Equation D.9, knowing the energy that is imparted to the fuel during the impact. The accumulation of noble gas atoms in the pores in the rim layer of high-burnup spent fuel causes these pores to become highly pressurized, which means that substantial amounts of energy are stored in these pores. Because increase of gas pressure with time in rim layer pores is relieved by growth of pore volumes (Reference D.12), at any instant in time, the energy stored in pores will by itself be too small to initiate growth of grain boundary surfaces by breaking of U-O bonds or by plastic deformation of pore surfaces. However, if propagation of grain boundary cracks initiated by impact fracturing is supported by the release of this stored energy, the extent of grain boundary cracking and the fraction of respirable particles generated by fracturing may both be significantly higher than the extent of cracking and respirable particle production observed for average burnup spent fuel pellets and also for the body portion of high-burnup spent fuel pellets. Consequently, when applied to the rim layer of high-burnup spent fuel pellets, the preceding equation needs to be modified to reflect release of energy stored in the pressurized gas contained in rim layer pores.

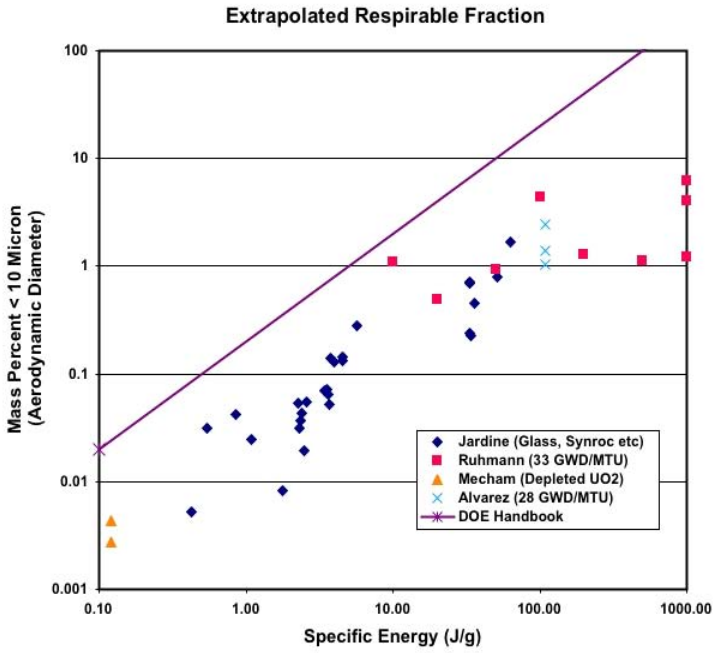

Figure D.1. Comparison of the DOE Handbook Respirable fraction equation to experimental values of the specific energy input into the brittle material

None of the material used to develop Equation D.8 was similar to the rim structure in high-burnup fuel (i.e., very fine grained material having large pores containing high-pressure gas). Using a modified Equation D.9, and making assumptions about the pore energy, one can to calculate that the rim fracture and the fracture of the body should be approximately equal. By contrast, anecdotal evidence from attempts to prepare metallurgical samples of the rim indicated that this region is much more friable than the body of the fuel. At best, it can be concluded that there is a value of high uncertainty that can range over several orders of magnitude. This uncertainty must be accounted for in any release determination. In the current study, the fraction of the rim is being allowed to fracture varies from a low equal to the same fraction as the body to a high of complete fracture.

D.2.4.1.3 Estimation of $F_{ent,rim}$

Because the friable rim layer of high-burnup spent fuel pellets is comprised of recrystallized, highly compacted, cubical UO_2 subgrains with sides between 0.1 and 0.3 μm (Reference D.13), plenum gases should not be able to cause the recrystallized rim layer to slide toward the nearest rod tear. However, if during storage the rod cladding separates slightly from the pellet rim, a small rim layer-cladding gap might open along the length of the rod. If flow through this rim layer-cladding gap during rod depressurization is significant, some particles formed from rim materials might become entrained in this flow and, if not captured by particle bed filtering, be carried out of the rod to the cask interior. In

actuality, entrainment may be insignificant, since any reopened pellet-cladding gap will be clogged with large particles formed by impact fracturing (mechanical or shock loading), i.e., the large particles will interfere with the boundary layer flow needed to entrain particles off of surfaces.

Should the conditions for entrainment occur, we have the following relationship:

$$F_{ent,rim} = R_{ent}\Delta t A_{rim} / \rho V_{rim} = R_{ent}\, \Delta t\, \pi\, d_p\, L / \rho \pi\, d_p\, t_{rim}\, L = R_{ent}\Delta t / \rho\, t_{rim} \qquad (D.10)$$

Data on the variation of entrainment rate R_{ent} with the free stream velocity of the gas flowing over the powder has been compiled for metal powders (Al, Cu, Mo, Si, and W), and Fe_2O_3. It also shows that the entrainment rates of the Tungsten (References D.20 and D.21) and of Fe_2O_3 (Reference D.22) begin to turn over at free stream velocities of 5 to 10 m sec^{-1}. Since entrainment data for UO_2 powder is not available, it was estimated ($R_{ent} = 5\times10^{-4}$ g cm^{-2} s^{-1}) by interpolating between the data for Fe_2O_3 and the data for Tungsten.

Based on the time to depressurize the rod (see Section D.2.3) and Gelbard's data, $F_{ent,rim}$ can be calculated. Sprung found that the uncertainty in the calculations led to the physically impossible entrainment fraction greater than 1. Because $F_{ent,rim}$ could not be larger than 1 but could be less, $F_{ent,rim}$ should be set to 1 to obtain a maximum release fraction. Smaller values can be assumed depending on the extent that the conditions required for entrainment are thought to prevail.

D.2.4.1.4 Estimation of $F_{tear,rim}$

If rod failure causes a plug of fuel fines to be blown out of the rod tear from the possibly friable rim layer located next to the tear, we can estimate $F_{tear,rim}$ using the following equation:

$$F_{tear,rim} = w\, \ell\, d / \pi d_p\, t_{rim}\, L \qquad (D.11)$$

where w, ℓ, and d are the final width, length, and depth of the ejected rim materials and d_p, t_{rim} and L are the diameter of the fuel pellets, the thickness of the pellets friable rim layer, and the active length of the spent fuel rod (the length of the pellet stack in the rod). For a 10 ×10 fuel d_p = 0.87 cm, t_{rim} = 150 μm = 0.015 cm (Reference D.13), and L = 369 cm. If the rod tear has a length/width aspect ratio of 10/1 and the tear length is equal to half of the circumference of a pellet, the plug length $\ell = \pi\, d_p/2$ = 1.4 cm and the plug width = 0.14 cm.

After the ejection of a rim layer plug, the depressurization flow of rod gases over the sides of the hole left by plug ejection should entrain more rim material into that flow, which will increase the final width of the total mass of rim material lost by plug ejection plus entrainment. Since the volume of rim layer material that will be lost by entrainment is given by $V_{ent} = R_{ent}\Delta t\, A_{plug\ side}/\rho$ and the width of the mass of materials entrained from one side of the hole is $w_{ent} = V_{ent}/A_{plug\ side}$,

$$w_{ent} = R_{ent}\, \Delta t/\rho$$

Material from both sides of the breach is being entrained, so 2 times w_{ent} must be added to w to get a maximum effective breach width ($w_e = w + 2\, w_{ent}$). The actual breach width might be much smaller.

Thus,

$$F_{tear,rim} = w_e \ell t_{rim}/\pi d_p t_{rim} L \quad (D.12)$$

For an atrium 10 ×10 BWR rod, $F_{tear,rim} = 2.8\times10^{-4}$.

D.2.4.1.5 Rod-to-Cask Particle Release Fractions

Values have now been developed for all of the parameters in the expression for the release fraction for rod-to-cask release of particles. Substitution of these values into Equation D.7 yields the fractional release in the respirable size range from the rod to the cask.

D.2.4.2 Rod Surface-to-Cask Release Fraction for CRUD

Because impact spallation data for CRUD is not available, consistent with the analysis performed in NUREG/CR-6672 (Reference D.1), the impact loading of the spent fuel rods was assumed to cause about 10 percent of the CRUD deposits on the surfaces of the spent fuel rods to spall. [Other estimates from Sandoval are in the same range (i.e., 15%).] Thus, the release fraction for ^{60}Co in CRUD from the rod surface to the interior of the cask was assumed to be 0.1. A cumulative number distribution for the CRUD particles that formed on the surface of a Quad Cities BWR rod was developed by examination of a Scanning Electron Microscopy (SEM) photo of the surface of this rod (Reference D.7). Conversion of this number distribution to a mass distribution indicates that about 15 percent of the total particles mass is contained in respirable particles (particles with aerodynamic particle diameters $d_p \leq 10$ μm). There are no data to indicate if the CRUD spallation fraction is independent of the particle mass. Therefore, $F_{RC,CRUD} = (0.1)(0.15) = 0.015$.

D.2.4.3 Rod-to-Cask Release Fraction for Noble Gases

The voids and the internal crack network that form in pellet bodies cause these body regions to have porosities of 5 to 10 percent (References D.13, D.14, and D.16). During reactor operation, about 8% of the noble gas atoms generated by the decay of fission products from spent fuel pellets with burnups of 55–60 GWd/MTU diffuse to particle grain boundaries and then escape to the rod free volume through the pellet's internal crack network (References D.13 and D.14). Additional fission gas will be released when the body of the high-burnup spent fuel pellet fractures but the exact amount is highly speculative. Estimates of the fission gas release upon fracturing the unrestructured material have been advanced as high as 25%.

In the rim layer, 0.1 to 0.3 μm subgrains are generated by the recrystallization of UO_2 and gas atoms in subgrain interiors migrate to subgrain boundaries, where they accumulate in micropores that were formed by clustering of lattice vacancies (References D.12, D.15, and D.16). Because distances to grain boundaries are so short in rim layer subgrains, noble gas atoms formed by fission product decay migrate efficiently to rim layer subgrain boundaries. Consequently, 90% of the noble gas atoms formed in the pellet rim layer is contained in the micropores that have formed on subgrain boundaries (Reference D.14). Once again, the release of this gas resulting from the fracture of the rim upon impact is an unknown quantity. If the rim disintegrates, as postulated by some, essentially all of the fission gas in the rim region being released is a possibility.

Accordingly, the rod-to-cask release fraction for noble gases from high-burnup spent fuel pellets was calculated as the sum of the fraction of the inventory in the pellet rim and body that is released by diffusion plus impact fracturing with each quantity weighted by the fraction of the total inventory that is contained in each region.

Fission gas is contained in three regions in a high-burnup rod: the void volume, the fuel rim, and the body of the fuel. There would be no rim in a lower-burnup rod. The size of the rim and the percentage of fission gas that is in the void volume will be a function of the burnup. Because of the neutronics in the reactor, the concentration of actinides in the rim is about twice that in the body of the fuel. Assume a fraction Z of the produced fission gas is released to the void volume during irradiation. Because of the radial temperature gradient in pellets during irradiation, the fission gas accumulated in the void volume tends to come from the hotter central body of the fuel pellet so the density of fission gases in the rim are about twice that in the central body of the pellet. (1-Z) of the fission gas will be left in the fuel column to be partitioned between the rim and the body. Let the following values apply:

ρ_R = density of fission gas in the rim region
ρ_B = the density of fission gas in the body
R_R = fraction of the rim that fractures
R_B = fraction of the body that fractures
R_{Rg} = fraction of gas released per volume of fractured rim
R_{Bg} = fraction of gas released per volume of fractured pellet body
X = fraction of the pellet volume (V) that is rim material; $V_R = X\ V$

As indicated above, $\rho_R = 2\ \rho_B$. It can be shown that the overall density of fission gas in the pellet (ρ) can be given by $\rho = \rho_B\ (1+X)$.

Let I be the total inventory of fission gas. Then, $I = I_R + I_B$, where I_R and I_B are the inventories of fission gas in the rim and body respectively.

After irradiation, the total gas inventory is given by the following equation:

$$\begin{aligned} I &= \text{gas in gap + gas in rim + gas in pellet body} \\ &= ZI + 2\ \rho_B\ V_R + (\rho_B\ V_B - ZI) \end{aligned}$$

After an impact, the rim and the body may fracture. When the cladding is breached the total gas in the gap, ZI is available for release as well as gas that is released from the grain boundaries and body of the rim and pellet body. The gas released (I_f) is given by the following equation:

$$I_f = ZI + R_R\ R_{Rg}\ 2\ \rho\ X\ V/\ (1+X) + R_B\ R_{Bg}\ [\rho\ V\ (1-X)/\ (1+X) - Z\ I]$$

Let the fraction of fission gas released from the rod after fracture to the cask be given by $R_{RCg} = I_f/I$ Since $\rho\ V = I$, R_{RCg} is given by the following equation:

$$R_{RCg} = Z + R_R\ R_{Rg}\ 2\ X\ /\ (1+X)\ + R_B\ R_{Bg}\ [(1-X)/\ (1+X) - Z\ ]$$

If typical values for high-burnup fuel, Z= 0.08 and X = 0.1, are substituted, the equation becomes as follows:

$$R_{RCg} = 0.08 + 0.18\ R_R\ R_{Rg} + 0.74\ R_B\ R_{Bg}$$

The gas release will be highly dependent on the magnitude of the event and the amount of fuel that is fractured. If it is assumed that there are 5 breach locations in the cladding, and that ±5 cm around the breach site are fractured and that 25% of the gas in the body and rim are released, the equation predicts a release of ~12% of the fission gas. This is similar to the 10% predicted by Sprung. By contrast, if it is assumed that the whole rod fractures and that 80% of the gas is released from the rim region, ~40% of the gas in the rod is released. This illustrates how the uncertainty in the fracture properties of the cladding and the rim introduce uncertainties for the driving force for the release from both the rods and the cask. Until more definitive data are available, the choice of rim fracture fraction is at the discretion of the analyst. This parameter will be varied over a range for this study.

D.2.5 Cask-to-Environment Release Fractions ($F_{CE,k}$)

After the fuel particulate and CRUD are released from the rod to the cask atmosphere, a portion will deposit within the cask and the remainder will be released from the cask in proportion to the volume of gas that is released to depressurize the cask to atmospheric pressure. The fraction of the material in chemical element group k that escapes from the cask to the environment, $F_{CE,,k}$, can be estimated using the following expression (Reference D.1):

$$F_{CE,\,k} = \left(1 - F_{deposition\ \ ,k}\right)\left(1 - \frac{p_{atm}}{p_{rod\ failure}}\right) = \left(1 - F_{deposition\ \ ,k}\right)F_{exp} \qquad \text{(D.13)}$$

where:

$F_{deposition,k}$ = the fraction of the materials in chemical element group k that is deposited onto cask interior surfaces after release to the cask atmosphere from failed rods

P_{atm} = 1.0 atm = atmospheric pressure

$P_{rod\ failure}$ = the pressure that the depressurized cask would reach upon rod failure, if release of rod gases to the environment were not occurring

F_{exp} = the fraction of the gases in the cask atmosphere that is released to the environment by cask redepressurization following rod depressurization

This equation must be used with care since it is a static approximation of a dynamic event. Two simultaneous venting events are taking place; the breached rods into the cask, and the cask to the environment. Because of the large pressure and volume differences (~50 atm and 20 cc for the rods, and a few atmospheres and 6,000 liters for the cask) the size of the leak path becomes very important. In the high-burnup rods, the leak path is governed by the hydraulic diameter that results in a very small leak path and long depressurization time. This may not be the cask for severely shattered rods or lower burnup rods. The cross-sectional area of the leak from the cask will depend on the size of the impact, and cover a wide range of sizes (Reference D.1).

If the cask depressurizes rapidly with respect to the rod depressurization, the only material available for release will be the CRUD, and rim and body particulate initially ejected from the rod. The driving force for the removal of the material from the cask will only be the temperature dependent fill gas pressure differential with the cooler environment. The release of fission gas to the cask will not play a part in the release of this material. The particulate that is removed from the rod as a result of entrainment in the gas stream will have a much small driving force to remove it from the cask, because the pressure buildup in the cask resulting from rod depressurization will be small. By contrast, if the cask depressurizes slowly with respect to the rod depressurization, the driving force will include the full pressure ($P_{\text{rod failure}}$) calculated below. In addition, the entrained material will also be swept out with this depressurization.

D.2.5.1 Fractional Release Fraction of Cask Atmosphere (F_{exp})

The fraction of the cask atmosphere released to the environment is given by the following equation:

$$F_{exp} = \left(1 - \frac{p_{atm}}{p_{rod\ failure}}\right) \quad \text{(D.14)}$$

$P_{\text{rod failure}}$ is calculated using the ideal gas law. Define the following values:

P_{rod}	=	the pressure of He and fission product noble gases in a rod at ambient conditions including fission product noble gases released by pellet fracturing
V_{rod}	=	the free volume of a spent fuel rod
n_{rod}	=	the number of moles of He plus fission product noble gases in a 10-year cooled high-burnup spent fuel rod
P_{cask}	=	the pressure of He fill gas in the cask at ambient conditions
V_{cask}	=	the free volume of the cask
n_{cask}	=	the number of moles of He fill gas in the cask
R	=	the ideal gas law constant
T	=	the average temperature of the cask interior and the spent fuel rods in the cask at ambient conditions
P_{final}	=	$P_{\text{rod failure}}$
N_{rods}	=	the number of spent fuel rods in the cask
V_{final}	=	the sum of the cask free volume plus the total free volume of the failed rods

The moles of gas in the breached rod is given by $P_{rod}V_{rod} = n_{rod}RT$. The number of mole of gas originally in the cask is given by $P_{cask}V_{cask} = n_{cask}RT$. These can be combined ($P_{final}V_{final} = n_{final}RT$) to determine the amount of gas that is pressurizing the free volume in the cask and the now-breached rods. These are given by the following equations:

$$n_{final} = F_{rods}N_{rods}n_{rod} + n_{cask}$$

$$V_{final} = F_{rods}N_{rods}V_{rod} + V_{cask}$$

Substitution yields the final pressure in the cask after rod failure but prior to rod depressurization.

$$P_{\text{rod failure}} = P_{\text{final}} = \frac{F_{\text{rods}} N_{\text{rods}} P_{\text{rod}} V_{\text{rod}} + P_{\text{cask}} V_{\text{cask}}}{F_{\text{rods}} N_{\text{rods}} V_{\text{rod}} + V_{\text{cask}}} \quad \text{(D.15)}$$

The parameters required to calculate the final cask pressure can be obtained from cask safety analysis reports, fuel rod performance reports, and so forth.

The size of the impact event will determine the size of the opening in the cask and which of the two above scenarios, or one in between, should prevail. An upper bound for release is obtained if one assumes that the rods depressurize into the cask rapidly to build up pressure before significant cask depressurization occurs. Under this scenario, Sprung used cask dimensions to calculate a final pressure in a cask of 1.5 atm, up from the initial backfill pressure of 1 atmosphere. At a final pressure of 1 atm, F_{exp} is ~33%. For the HI-STORM 100 cask, with an initial backfill pressure at temperature of ~5.6 atm, depending on the number and type of failed rods, the amount of expelled gas can range between 82 and 98%.

D.2.5.2 Deposition Mechanisms onto Cask Internal Surfaces

Because gas flow rates out of the failed rods are high, removal of particles by inertial impaction onto spacer plates or rod surface located next to cladding failures may occur, provided particle sticking probabilities per collision are significant at the particle impact speed. Those particles not sticking as a result of impaction may settle before reaching the cask opening. Because rod depressurization is slow (see Section D.2.3), gas flow velocities through the failed cask will also be slow, so particle removal during transport through the cask to the location of the cask's closure failure will occur by Brownian and turbulent diffusion to cask interior surfaces and by gravitational settling onto upward facing interior surfaces. If rod depressurization occurs through a reopened pellet-cladding gap, depressurization may not be slow (though it still may not be fast enough to make inertial processes important). Removal of the larger respirable UO_2 particles (UO_2 particles with geometric diameters close to 3.16 μm) will occur primarily by gravitational settling, while small particles, are removed primarily by Brownian and turbulent diffusion.

D.2.5.2.1 Impingement on Adjacent Rods

Sprung calculated the typical impingement distance from a rod breach to the next nearest surface for a variety of casks and concluded that in almost every instance that the largest size respirable particulate (3.16 μm diameter) released from a rod would impinge on the neighboring surface. However, the impact velocity would be so great ($> 4.3\times10^4$ cm/s) that the sticking coefficient for UO_2 particles is most likely $\leq 1\times10^{-5}$ (Reference D.23). Hardly any of the particles that impact the spacer plates will stick to the plates, and, therefore, $F_{\text{inertial impaction}} = F_{\text{surface}}F_{\text{stick}} = (1.0)(0.0) = 0.0$. Because of the uncertainty of the sticking factor, no deposition attributable to impaction is recommended.

D.2.5.2.2 Gravitational Settling

After a drop impact, there are two possible configurations of the cask: (1) a tip-over with the cask lying horizontally on its side, or (2) the cask remaining in a standing vertical orientation with the breach in the bottom weld:

(1) Horizontal: During cask depressurization, one side of each of the spent fuel assembly basket tubes in the cask, and half of the outer surface area of the spent fuel rods in each tube will be facing upward and, therefore there will be surfaces onto which particles can deposit by gravitational settling. The force on the particulate in the gas stream attributable to the gas flow is in the horizontal direction. The force attributable to gravity is orthogonal to the gas flow in the vertical direction. If the time to traverse the distance to the adjacent rod or basket surface is less than the time for the particle to be swept to the breach site, the particle can be considered to be gravitationally settled.

Under quiescent conditions, the gravitational settling velocity of 3.16 μm UO_2 particles is about 0.2 cm/sec (Reference D.24). Since the diagonal separation distance between the 10×10 fuel rods in an assembly is ~0.8 cm, it takes about 5 sec for deposition by gravitational settling of 3.16 μm UO_2 particles under quiescent conditions. This is short compared to the time required to depressurize a rod (see Section 2.3). If rod depressurization occurs through a reopened pellet-cladding gap this assumption might change. Since the flow conditions in the cask during rod depressurization are relatively quiescent, and every 3.16 μm UO_2 particle will encounter a horizontal surface in about 5 sec, removal of respirable UO_2 particles by gravitational settling will be efficient.

Under the relatively quiescent that will prevail during the passage of rod gases and fission products from rod failures to the cask closure failure, any respirable UO_2 particles not removed by inertial impaction should encounter a horizontal surface before they exit the cask. Since the sticking coefficient for 3.16 μm UO_2 particles at their gravitational settling impact speed is certainly $\geq$0.9 (Reference D.23), $F_{\text{gravitational settling}} = F_{\text{surface}}F_{\text{stick}} = (1.0)(0.9) = 0.9$.

(2) Vertical: In this configuration, both the gas stream and gravitational force are pushing the entrained particles down until they meet the first horizontal surface, which is the grid spacer with its horizontal projection of the spring surfaces, and plates. The fuel assembly is made of seven spans between grid spacers. We can assume, similar to the horizontal case, that at least 90% of the particulate settle at the grid spacer. If the cladding breaches have an equal probability of forming anywhere on the rod, 1/7 of the fractures will form in each span. If 90% of the entrained particles settle on a grid spacer, the total gravitational settling can be expressed by the following equation:

$$F_{\text{gravitational settling}} = 1 - 0.143 \times \sum_{n=1}^{7} (1 - 0.9)^n = 0.984$$

As a bounding case, breaches may not be equally distributed along the rod but may be expected to concentrate on the lower grid span. The particles will settle only on the lower end plate of the assembly and the 90% settling factor is more probable and will be used in this analysis. This analysis does not take into account the tortuosity of the path through the seal.

Similarly, after spallation from rod surfaces attributable to impact forces, CRUD particles will also be removed by gravitational settling onto cask and rod surfaces.

For both the respirable fuel and CRUD particles, the fraction of particulate that escapes the cask to the environment is given by

$$F_{CE,\,(CRUD,\,fuel)} = 0.1 \times (\text{depressurization ratio for the particular situation})$$

$F_{CE,\,(CRUD,\,fuel)}$ may range from 0.033 to 0.1 depending on the cask design and fuel loading. For the HI-STORM 100 cask, which has a depressurization ratio between 0.82 and 0.98, depending on the number of breached rods, $F_{CE,\,(CRUD,\,fuel)}$ is between 0.08 and 0.1. Since noble gases won't settle, the escape fraction is given by the following equation:

$$F_{CE,\,gas} = \text{depressurization ratio}$$

D.3 Input Parameters To Model

D.3.1 Fuel, Cladding, Cask, and Storage Environments

All of the fuel, cladding, and cask physical parameters and tolerances that are used in the model are well known although possibly hard to locate or proprietary. Although no systematic evaluation of the influence of the uncertainty or variation of these parameters on the release rate has been made, it is not suspected that parameters such as cladding, thickness, internal rod volume, etc., will have a large influence. By contrast, internal cask pressurization or cask free internal volume, for example, will probably have a large effect, as they have a large effect on the driving force from the cask cavity to the environment.

D.3.2 Fuel Performance Parameters

The changes that occur in the properties of the fuel and the cladding while in-reactor may introduce large errors into the determination of the release factors, because of the uncertainty of the database. Table D.3 identifies some of the changes in the fuel attributable to burnup and briefly describes the uncertainties introduced by these changes. No attempt has been made to quantify the degree of the uncertainties or to determine if they are significant to the risk.

Table D.3. Fuel Characteristic Changes That Occur at High-Burnup That Can Introduce Uncertainty into the Release Fractions

Burnup		
	Gap	The pellet-cladding gap closes as the burnup increases. The partitioning of the gas flow and entrainment of fuel between the rim and the body will be dependent on the gap size. Until better data on the gap at room temperature in high-burnup fuel is obtained, use of no gap in the calculations is recommended.
	Gas generation, and release	The fission gas release from the pellet to the rod void volume increases with burnup. Circa <2% at lower burnups, it may rise to 8–10% at high burnups. This additional gas is available for driving particulate from the fractured rods, and increases the pressurization of the cask resulting in more particulate release to the environment. The release from the cask is directly proportional to the release from the pellets
	Fission gas release upon fracture	The majority of the generated fission gas is trapped in the grains of the fuel pellet. This gas is available for release when the pellet fractures. There are no good measurements of the amount that is released upon fuel fracture. Sprung uses 10% release in his calculations, but release may be as high as 25% or more in the impacted fuel regions
	Rim development	At about 50 GWd/MTU average burnup or 100 GWd/MTU localized burnup, a rim forms on the exterior of the fuel pellet. The rim has a fine grain structure (submicron) and retains much of its fission gas in large pores
	Cladding mechanical properties	During irradiation, the cladding thins as a result of oxidation and embrittles as a result of irradiation and hydrogen uptake. Mechanical properties that lead to fracture will change with burnup and temperature. The number of rods that fracture and the number of fracture sites per rod will depend on the cladding mechanical properties
Cladding type		The fracture properties of the newer cladding types and newer heat treatments of older cladding types has not been well developed
Rim		
	Size	The size of the rim will increase exponentially with burnup. It is about 50% larger in BWR fuel at equivalent burnup.
	Inventory	The actinide inventory in the rim is ~twice that in he body of the fuel pellets
	Fracture during accident	Based on pore pressurization, the rim should fracture in a similar manner to the body of the pellet. Anecdotal evidence and expert opinion tends to indicate that the rim should fracture rather easily and into finer particulate than the body of the pellet. The maximum respirable fraction will occur if the entire rim was fractured into submicron size particulate. In this case, the release fraction could increase by a factor of 3. For lower energy of impact, the difference could be considerably greater because of the small fracture of the body of the fuel. No estimate of the energy input required to do this has been made and it is highly unlikely complete fracture of the rim will occur.
	Fracture in reactor	Experiments similar to Lorenz's have not been conducted on high-burnup fuel with a rim. No data are available on the fracture and particle size distribution of the rim as it comes out of the reactor as a result of thermal cycling in the reactor and subsequent handling. For this exercise, it assumed that fracture similar to that in the body of the pellet has occurred in reactor. Because of the uncertainty in the fracture of the rim during the fall, the uncertainty in this parameter may be unimportant.
	Particulate size distribution	The rim is ~10% of the fuel volume. The grains are 10–100 times smaller in diameter. Most of the rim would fracture into respirable size particulate because of the grain size.
Cask Drying		During drying, hydrides may reorient to radial direction further decreasing ductility leading to more fractures and/or more fracture sites per rod.
CRUD		
	amount	Most data is pre 1990 and based on lower burnup fuel. At that level, no burnup dependence was found; however, this may change at higher burnups. Some assemblies have shown very large CRUD deposits, enough to span fuel rods. Also, some rods are showing azimuthal dependence to CRUD distribution.
	Size distribution	It is unknown whether CRUD fractures into small particulate on the micron size range as shown in photomicrographs or stays agglomerated in flakes. If the latter, it will settle very quickly in the casks
	Spallation	10% spallation of CRUD is assumed. No data on spallation from impacts are available. Some work on thermal spallation indicates 15%. There is no technical reason that this should be the same for impacts
Fuel pellet fracture database		Little fracture size distribution data is available on irradiated fuel pellets. The DOE Handbook database seems to indicate that both glasses and ceramics fracture in a similar manner. Newer work appears to indicate that the Handbook values over predict the fraction of respirable by at least an order of magnitude.

D.4 Release Fractions to Environment

The model can be applied to any cask, and fuel loading to determine the potential release fractions for that particular situation. The model can also use ranges of input parameters and combinations, with suitable weighting factors to determine the potential range of release fractions. Based on the model, the release fractions for a HI-STORM 100 cask, containing 68 10×10 BWR fuel assemblies with a burnup of 60 GWd/MTU that is dropped 30.5, 12.2, and 1.52 meters (100, 40, and 5 feet) were calculated and tabulated in Table D.4.

Table D.4. Values of F_{rods}, $F_{RC,k}$, $F_{CE,k}$, and $F_{rel,k}$

Chemical Element Group (k)	Inventory	F_{rods}	$F_{RC,k}$	$F_{CE,k}$ **	$F_{rel,k} = F_{rods}F_{RC,k}F_{CE,k}$
Noble Gases	ORIGN	1 to 0.33	0.12 to 0.4	1	4×10^{-2} to 0.4
Particles	ORIGN	1 to 0.33	Table 5	0.1	(0.1 to 0.033) × value in Table 5
CRUD	0.72 Ci/rod*	1.0	0.015	0.1	1.5×10^{-3}

* based on 10 yr old cooled 10x0 fuel, bounding 90% of the fuel inventory

** HI-STORM 100 is pressurized to 5.6 atm at temperature resulting in 82% release. Rod breaches will increase this to 98% release of gas. Other casks may have lower values because of lower initial cask pressurizing.

$F_{RC,k}$ was calculated for the above cask and fuel for a range of $n_{rod/tear}$, rim fracture and the rim entrainment. At a minimum, the rim was assumed to fracture in the same respirable fraction as the body of the fuel. At the opposite extreme, the rim was assumed to fracture into 100% respirable fraction since the rim consists mainly of submicron grains. The entrainment ranged from zero to complete entrainment. Results are shown in Figures D.2 and D.3. At this point, a distribution should be assigned to both variables and a sampling done to obtain a most likely value and uncertainty using a probabilistic calculation. Based on these plots and others like it, four release fractions can be assigned to each drop height for the extreme values of the rim fracture and the entrainment. These are shown for a sample case in the 2×2 matrix in Table D.5 below. Other values can be obtained from the plots or by calculation but since there is currently no technical justification to chose an intermediate value for the rim fracture or entrainment, this table is made for bounding simplicity.

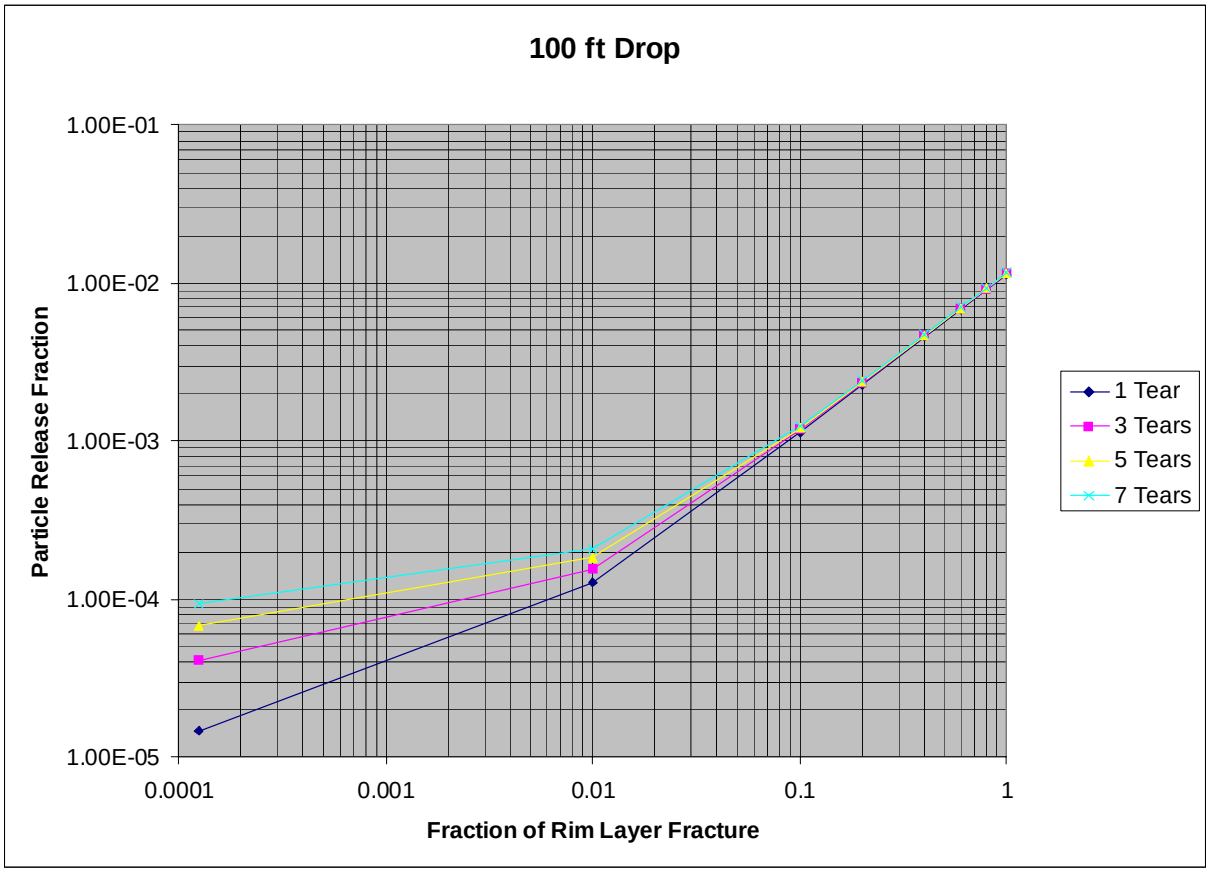

Figure D.2. $F_{RC,k}$ for 100% Entrainment of the Rim as a Function of the Number of Tears and Fraction of Rim Layer Fracture

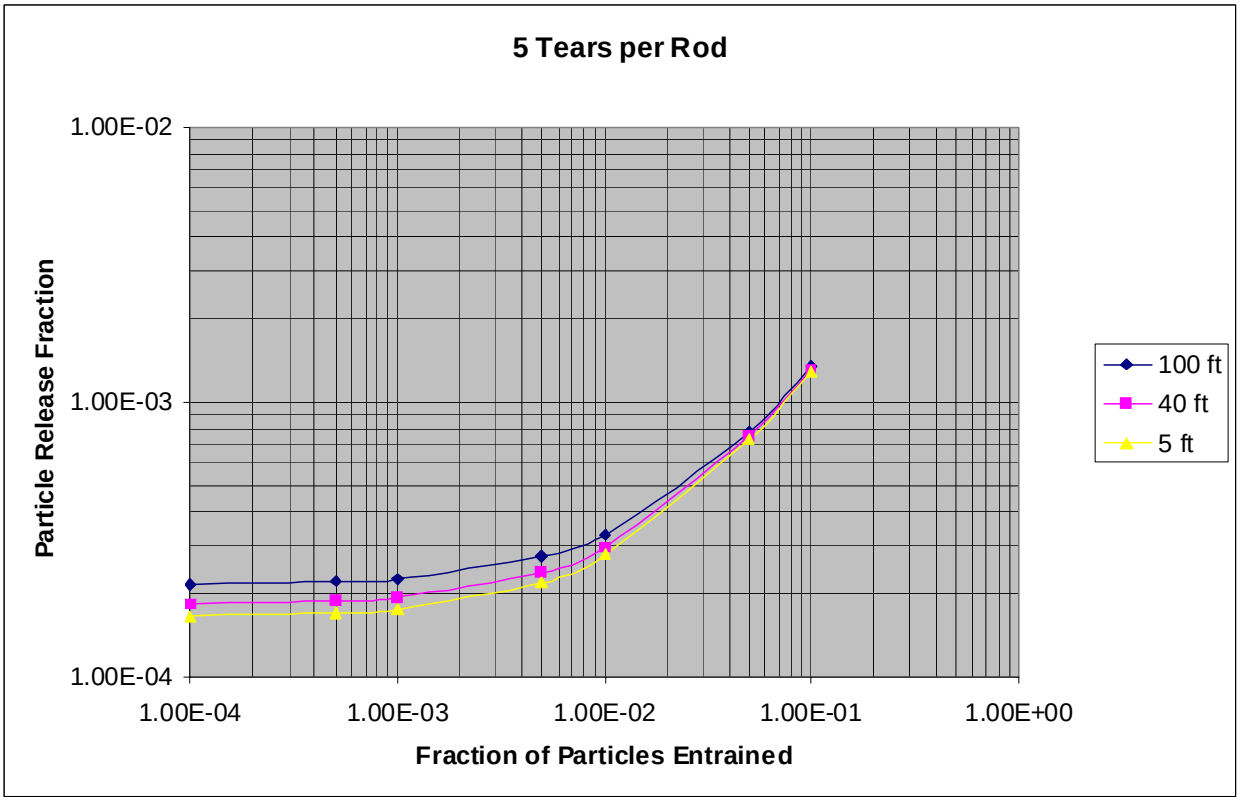

Figure D.3. $F_{RC,k}$ for 100% Rim Fracture and 5 Tears per Rod as a Function of Fraction of Particles Entrained

Table D.5. Variation of $F_{RC,k}$ with Input Parameters for 100-Foot Drop and 5 Breaches per Rod

		Entrainment, $F_{ent,rim}$	
		None = 0	Complete = 1
Rim fracture, $F_{imp,rim}$	Same as body of fuel $=1.24 \times 10^{-4}$	6.6×10^{-5}	6.8×10^{-5}
	Complete fracture = 1	2.2×10^{-4}	1.2×10^{-2}

Lacking a probabilistic calculation, a deterministic evaluation is being done in this report to illustrate the methodology. Without experimental data, it is difficult to justify the value in Table D.5 to choose for $F_{RC,k}$. Entrainment requires a fuel cladding gap for the gap to flow through and pick up rim particles. High-burnup fuel has little or no gap and, as a result the gas flow, will occur between the fractured pellet fragments. Even with a small gap, there should be sufficient gas flow to entrain the particles; therefore, full entrainment probably occurs. Because of the very limited information on rim fraction, no technical justification can be given for choosing an $F_{RC,k}$ value based on rim fracture. Plots and tables similar to Table D.5 and Figures D.2 and D.3 were constructed for a variety of drop heights and fracture sites per rod. The results are tabulated in Table D.6 below.

Table D.6. $F_{RC,k}$ for Particles

Breaches per Rod	Drop Height (ft)		
	100	40	5
1	1.5×10^{-5} to 1.1×10^{-2}	6.6×10^{-6} to 1.1×10^{-2}	3×10^{-6} to 1.1×10^{-2}
5	7×10^{-5} to 1.2×10^{-2}	3.3×10^{-5} to 1.2×10^{-2}	1.3×10^{-5} to 1.2×10^{-2}

The most conservative position is to use the highest release fraction from Table D.6, but that may be considerably higher than a realistic value. The overall release from the cask can be calculated using Equations D.1 and D.2. The values for use in these equations for this particular case of the HI-STORM cask with a 30.5 meter (100-foot) drop are given in Table D.7.

Table D.7. Values of Release Fractions F_{rods}, $F_{RC,k}$, $F_{CE,k}$, and $F_{rel,k}$*
(10-year-old cooled 10x10 Atrium fuel, 30.5 meter (100-foot) drop of a HI-STORM 100 cask, all of the rods fail with an average of 5 breach locations per rod)

Chemical Element Group (k)	Inventory	F_{rods}	$F_{RC,k}$	$F_{CE,k}$	$F_{rel,k} = F_{rods}F_{RC,k}F_{CE,k}$ respirable
Noble Gases (k=1)	ORIGEN	1	0.12	1	0.12
Particles (k=2)	ORIGEN	1	7×10^{-5} to 1.2×10^{-2}	0.1	7×10^{-6} to 1.2×10^{-3}
CRUD (k=3)	0.72Ci/rod	1	0.015	0.1	0.0015

* F_{rods} = the fraction of rods contributing to the release [1.0 (100% of the rods, see Table D.4)].
$F_{RC,k}$ = the fraction of material released from a single rod to the cask environment.
$F_{CE,k}$ = the fraction of respirable radioactive material in the cask atmosphere that is released to the environment and $F_{rel,k}$ = fraction of the radioactive material in the cask that is released to the environment in the respirable size range.

D.5 Conclusions

If the imparted energy is sufficient when a cask is dropped, a leak path can open in the cask and radionuclides released from damaged fuel. The release can be in the form of noble gases, CRUD, or fuel particulate. The driving force for release from the cask to the environment is the pressure differential between the cask cavity and the environment outside the cask.

A linear model was built to determine the release fraction of the gas, CRUD, and particulate. The model consists of four units: rod radionuclide inventory, number of rods that will breach to release material, release of material from the rods to the cask cavity, and release of material from the cask cavity to the environment. All of these components will depend on the type of cask, characteristics of the fuel loaded into the cask, and magnitude of the impact force. A brief discussion is given on the uncertainty in these input parameters. By far, the biggest uncertainties are the general fracture characteristics of irradiated ceramic UO_2 fuel, the fracture characteristics of the rim region in high-burnup fuel, the variation of mechanical properties of the irradiated cladding, and deposition characteristics of the particulate in the cask. This model has not been benchmarked against experimental data. As a result, some of the phenomena submodels such as particulate entrainment may be significantly off. In these cases, an attempt was made to determine the uncertainty introduced into the final results by varying the potential output of the submodel over a bounding range.

Output of the model was presented for a typical cask and fuel loading to illustrate the expected magnitude of the release fractions. The quantity of radioisotope released from the cask is the product of the inventory, contained in or on the rods, of that isotope in the cask times the fraction of the inventory that is released from the cask. Based on Tables D.5 and D.6 above, Table D.7 values should be used for the consequence analysis.

D.6 References

1. Sprung, J.L., et al., "Reexamination of Spent Fuel Shipment Risk Estimates," NUREG/CR-6672, U.S. Nuclear Regulatory Commission, Washington DC, March 2000.

2. Croff, A.G., "ORIGEN2: A Revised and Updated Version of the Oak Ridge Isotope Generation and Depletion Code," ORNL-5621, Oak Ridge National Laboratory, Oak Ridge, Tennessee, July 1980.

3. Oak Ridge National Laboratory, "ORIGEN2 Isotope Generation and Depletion Code," CCC-371, Oak Ridge, Tennessee, 1991.

4. International Atomic Energy Agency, Safety Series No. 7, "IAEA Safety Guides: Explanatory Material for the IAEA Regulations for the Safe Transport of Radioactive Material" (1985 Edition), 2nd Edition, Vienna, 1987.

5. *Code of Federal Regulations*, Title 49, Section 173.435 (49 CFR 173.435).

6. Hazelton, R.F., "Characteristics of Fuel Crud and Its Impact on Storage, Handling, and Shipment of Spent Fuel," PNL-6273, Pacific Northwest Laboratory, Richland, Washington, September 1987.

7. Sandoval, R.P., et al., "Estimate of CRUD Contribution to Shipping Cask Containment Requirements," SAND88-1358, Sandia National Laboratories, Albuquerque, New Mexico, January 1991.

8. Geelhood, K.J., and C.E. Beyer, "Examination of Strain to Failure Data from Irradiated Zircaloy," white paper prepared for the NRC's Spent Fuel Package Vulnerability Study, 2004.

9. Geelhood, K.J., and C.E. Beyer, "Mechanical Properties for Irradaiated Zircaloy," *Transactions*, Vol. 93, ANS Winter Meeting, Washington, DC, November 2005.

10. Vankeerberghen, M., "Recent Gas Flow Measurements in IFA-504 Rods," HWR-433, Halden Reactor Project, Halden, Norway, November 1995.

11. Bird, R., W.E. Stewart, and E.N. Lightfoot, *Transport Phenomena*, John Wiley and Sons, New York, New York, pp. 480–482, 1960.

12. Manzel, R., and C.T. Walker, "EPMA and SEM of Fuel Samples from PWR Rods with an Average Burnup of Around 100 MWd/kgHM," *Journal of Nuclear Materials*, 301:170, Elsevier, Inc., Burlington, Massachusetts, 2002.

13. Einziger, R.E., and C.E. Beyer, "Characteristics of High-Burnup Fuel that May Affect the Transportation Source Term," white paper prepared for the NRC's Spent Fuel Package Vulnerability Study, 2004.

14. Manzel, R., and C.T. Walker, "High-Burnup Fuel Microstructure and its Effect on Fuel Rod Performance," *Proc. Intl. Topical Meeting on LWR Fuel Performance*, Park City Utah, April 2000.

15. Thomas, L.E., C.E. Beyer, and L.A. Charlot, "Microstructural Analysis of LWR Spent Fuel at High Burnup," *Journal of Nuclear Materials*, 188:80, Elsevier, Inc., Burlington, Massachusetts, 1992.

16. Spino, J., K. Vennix, and M. Coquerelle, "Detailed Characterization of the Rim Microstructure in PWR Fuels in the Burnup Range 40–67 GWd/tM," *Journal of Nuclear Materials*, 231:179, Elsevier, Inc., Burlington, Massachusetts, 1996.

17. Lorenz, R.A., et al., "Fission Product Release from Highly Irradiated LWR Fuel," NUREG/CR-0722, Oak Ridge National Laboratory, Oak Ridge, Tennessee, pp. 48–80, February 1980.

18. Otani, Y., *Aerosol Science & Technology*, 10:463, American Association for Aerosol Research, Mt. Laurel, New Jersey, 1989.

19. U.S. Department of Energy, "DOE Handbook: Airborne Release Fractions/Rates and Respirable Fractions for Non-Reactor Nuclear Facilities," DOE-HDBK-3010-94, Section 4.3.3, "Free-Fall Spill and Impaction Stress," Washington, DC, December 1994, p. 4-52.

20. Iversen, J.D., "Particulate Entrainment by Wind," Project 1699, ISU-ERI-Ames-85010, Department of Aerospace Engineering, Iowa State University, Ames Iowa, Report prepared for Los Alamos National Laboratory, 1984.

21. Wright A.L., and W.L. Pattison, "Results from Simulated Upper-Plenum Aerosol Transport and Aerosol Resuspension Experiments," *Proceedings of the CSNI Specialists Meeting on Nuclear Aerosols in Reactor Safety, 4th to 6th September, 1984, Karlsruhe, FRG*, Ed. W.O. Schikarski and W. Schock, CSNI 95, KfK 3800, February 1985.

22. Fromentin, A., "Particle Resuspension from a Multilayer Deposit by Turbulent Flow," PSI-Bericht Nr. 38, Programm LWR-Sicherheit, Paul Scherrer Institute, Switzerland, 1989.

23. Beal, S.K., "Correlations for the Sticking Probability and Erosion of Particles," *Journal of Aerosol Science*, 9:455, Elsevier, Inc., Burlington, Massachusetts, 1978.

24. Reardon, P.C., G.S. Brown, and Y.R. Rashid, "On the Particle Size Distribution of Crushed Spent Fuel," *3rd International Radiological Waste Management Conference*, Las Vegas, Nevada, 1992.

APPENDIX E
CONSEQUENCE ANALYSIS

APPENDIX E
CONSEQUENCE ANALYSIS

E.1 Introduction

This appendix presents a more detailed explanation of the consequence analysis introduced in Section 6.0 for the dry cask probabilistic risk assessment (PRA). This consequence analysis assesses a severe accident scenario related to an inadvertent 30.5 meter (100-foot) drop of a HI-STORM 100 cask system during the transfer process (Reference E.1). The consequence measures chosen for this study were the mean values given by the MELCOR Accident Consequence Code System (MACCS2) for the individual risk of early fatality and the individual risk of cancer fatality within 16 km (10 miles)[7]. The value of 1.6 km (1 mile) is the measured distance from the exclusion area boundary (EAB), assumed to be 0.5 km (0.3 mile), out to a distance of 2.1 km (1.3 mile). These consequence measures were chosen to allow comparison to the NRC's quantitative health objectives for reactor accident risk. Because cask accident consequences in terms of individual risks of early fatality and cancer fatality are small, the consequence mean value calculated for individual lifetime dose commitment (the mean value of the variable known in MACCS2 as "peak dose found on spatial grid") may also be of interest. Therefore, this report includes the mean individual lifetime dose between 1.2 and 1.6 km (0.75 and 1.0 mile) as measured from the release point. Also, close-in consequence estimates are generally more dependant on the source term and evacuation timing, while consequences further away tend to be controlled by long-term relocation assumptions. The MACCS2 consequence analysis performed for this study does not consider sheltering and evacuation.

E.2 Approach

This assessment was performed using MACCS2 (Reference E.2) for a representative site. Site-specific data important to modeling a HI-STORM dry cask 30.5 meter (100-foot) drop accident scenario in the MACCS2 consequence calculation were collected and used. The important parameters/variables required to model the site are the population density/distribution and the site meteorology. The radionuclide inventory, source term (i.e., release fraction, release start time, and release duration), initial plume dimensions (related to the system geometry), and plume heat content are discussed below. Other settings and models necessary for a MACCS2 calculation (e.g., food chain model) were taken from the NUREG-1150 study MACCS2 input file prepared for the Surry Power Station. The input file is documented in Appendix C to the MACCS2 code manual and is referred to there as Sample Problem-A. Sample Problem-A was chosen because of its ready availability and previous use by the NRC in scoping studies of various types. Discussions of some of the values used for the MACCS2 calculations are given in Sections E.3 – E.11.

7 Unless otherwise stated, all consequence measures given in this appendix are mean values calculated using the MACCS2 code. The mean value in MACCS2 is defined as the average (expected) consequence over all weather trials (Reference E.2).

E.3 Dose Conversion Factor

The dose conversion factors (DCFs) used in this study are the same as those used in the NUREG-1150 study (DOSDATA.INP). The DCFs were provided by K. Eckerman from Oak Ridge National Laboratory (Reference E.3). These DCFs include definitions for 19 organs and 60 radionuclides important in reactor accidents.

E.4 Radionuclide Inventory

High-burnup spent fuel is placed inside a HI-STORM cask no sooner than 10 years after being removed from the reactor. A maximum of 68 boiling-water reactor (BWR) assemblies can be loaded in a HI-STORM cask. The inventory per cask calculated with the ORIGEN code (References E.4 and E.5) is presented in Table E.1. The analysis assumes that the spent fuel placed in HI-STORM cask for the 30.5 meter (100-foot) drop accident is a 10-year-cooled high-burnup spent fuel.

Table E.1. Dry Cask Nuclide Inventory: SNL ORIGEN 50,008 MWD/MTIHM (10-yr-cooled)

Nuclide	Bq	Ci	Nuclide	Bq	Ci
Co-60	1.61×10^{14}	3133	Pu-238	3.98×10^{15}	107440
Kr-85	2.77×10^{15}	74800	Pu-239	1.87×10^{14}	5060
Y-90	3.40×10^{16}	918000	Pu-240	3.47×10^{14}	9384
Sr-90	3.40×10^{16}	918000	Pu-241	5.23×10^{16}	1414400
Ru-106	2.92×10^{14}	7888	Am-241	1.20×10^{15}	32504
Cs-134	5.13×10^{15}	138720	Am-242m	1.97×10^{13}	532
Cs-137	5.54×10^{16}	1496000	Am-243	3.07×10^{13}	830
Ce-144	5.08×10^{13}	1374	Cm-243	3.02×10^{13}	816
Pm-147	3.37×10^{15}	91120	Cm-244	5.66×10^{15}	153000
Eu-154	4.15×10^{15}	112200			

The radionuclide inventory in Table E.1 was generated using the ORIGEN code, corresponding to an 8×8, 50 GWd/MTU, 10-year cooled high-burnup BWR spent fuel. This inventory was used to demonstrate the methodology of developing a consequence analysis. As recommended in Appendix D, specific radionuclide ORIGEN calculation should be performed for the actual spent fuel loaded inside the HI-STORM casks.

Cobalt-60 is formed in spent fuel by activation of Ni-60 in cladding, but its most important source is in the CRUD that forms on cladding surfaces during reactor operation (References E.6 – E.8). During a 30.5 meter (100-foot) cask drop impact accident, the amount of Co-60 that was formed by activation of Ni-60 in cladding will tend to remain trapped where it formed, while the Co-60 in CRUD can be released by spallation. Therefore, the Co-60 inventory in Table E.4.1 represents the CRUD inventory. The value was calculated from the Appendix D inventory of 0.72 Ci/rod for a 10×10 fuel assembly (see Table D.7). This value was assumed to be similar for the inventory used in this analysis. The value for CRUD in Table E.1 is for 64 BWR rods per assembly and 68 assemblies per cask.

E.5 Chemical Element Groups

Separate release fractions need not be developed for each element in a dry cask inventory. The releases for the cask drop accident are from mechanical means, not because of differing volatilities. Accordingly, release fractions need to be developed only for three chemical element groups: noble gases, CRUD, and particulates. Inspection of Table E.1 shows that the noble gas chemical element group contains only Kr_{85}, the CRUD chemical element group contains only Co-60, and all other elements in the canister inventory are members of the particulate chemical element group because these elements can only escape from failed fuel rods as constituents of fuel fine particles. These chemical elements groups for the 30.5 meter (100-foot) drop accident scenario, are consistent with the analysis and methodology presented in Appendix D.

E.6 Source Term

E.6.1 Release Fraction

The release fractions for the calculations are given in Appendix D. Two different source terms were evaluated. The first represents a large release, one that assumes little reduction in fuel fines escaping from the cask while the second represents a median estimate of fuel fine reduction in the escape path. Further, for those cases where filters are assumed to be operable, a reduction of a factor of 10 for particulates and CRUD has been assumed. In all cases, no credit is given for deposition within the reactor building. Table E.3 includes the release fraction for each of the consequence results analyzed.

E.6.2 Release Start Time

The MACCS2 calculation assumed that the release to the environment occurs immediately.

E.6.3 Release Duration

The release duration used in the MACCS2 consequence calculation was assumed to be 2 minutes. A methodology for estimating this value is presented in Appendix D.

E.7 Release Height

The dropped cask scenario occurs inside the reactor building. Two different release locations are possible. The first one is through vents located 50 meters (164 feet) above ground. These vents contain filters which, when operating, could reduce the release as discussed above. The second release path of radionuclides to the environment is through the stack. The opening from the stack to the environment is located at a height of about 120 meters (394 feet) from ground. Table E.3 include the release height and the reduced release fraction from filters, as applicable, for each of the consequence results analyzed.

E.8 Initial Plume Dimension

The initial plume dimensions (i.e., the plume dimensions at the release point) are determined by the width and height of the building wake. In MACCS2, the initial plume dimension is specified by the user in terms of σ_y and σ_z, which represent the lateral and vertical plume spreading from the release point respectively. To reduce the effect of plume spreading attributable to the building wake effect, it was decided to assume that the release is from a point source. This was implemented in the MACCS2 calculation by setting the dimensions of the structure releasing the radioactive material to be 4 meters high by 4 meters wide (13 x 13 feet) (i.e., approximately the cask dimension). The vertical and lateral spreading, σ_y and σ_z, is then estimated by dividing the building width and the building height by 4.3 and 2.15, respectively. These values are shown in Table E.2.

Table E.2. Plume Dimensions at the Release Point

	Point Source
structure width	4 meters (13.1 feet)
structure height	4 meters (13.1 feet)
σ_y	0.93
σ_z	1.86

E.9 Plume Heat Content

The plume heat content determines the rise of the plume in the atmosphere. The plume heat content for the dropped cask accident is expected to be approximately equal to the heat content of the spent fuel. For ten-year cooled spent fuel, the maximum decay heat load is 264 watts per assembly. The MACCS2 calculations used 18 kilowatts for 68 high-burnup fuel assemblies in a cask. The plume resulting from this release will not be hot enough to produce significant plume rise.

E.10 Population Distribution

The population distribution for the site was obtained from the SECPOP code (Reference E.9), based on year 2000 census data.

E.11 Site Weather

MACCS2 code samples from 1 year of hourly weather data to calculate offsite radiological consequences. This weather data includes wind speed, wind direction, atmospheric stability, and rainfall. The weather data file in MACCS2 format was requested and obtained from the site licensee. Because this file had some missing hourly weather data, it was modified in two ways. First, if data were missing for a number of consecutive hours, the weather of the previous day was used. Second, if data were missing for only 1 hour, either the hour before or the average of the hour before and the hour after was used. In addition, the weather data provided by the licensee did not include the mixing layer height for each season. The mixing layer height is the top of the well-mixed surface layer of air, and is used in MACCS2 to limit both buoyant plume rise and vertical dispersion. Therefore, the Sample Problem-A MACCS2 mixing heights were used in the calculation. The option used in MACCS2 to sample weather data was the weather category bin sampling. This option is typically used in MACCS2 in order to ensure adequate sampling of rain cases.

E.12 Results

Six separate MACCS2 calculations were performed. For each of the two source terms, releases at 50 meters (164 feet) with and without filter operation and at 120 meters (393 feet) were evaluated. The results are presented in Table E.3 and are mean values as calculated by MACCS2, where mean is the average (expected) consequence over all weather trials (Reference E.2). In all cases, the health impacts are small.

Table E.3. MACCS2 Consequence Calculation Results

Release Fraction			Release Height meters (feet)	Individual Risk of Prompt Fatality within 16 km (10 miles)	Individual Risk of Cancer Fatality within 16 km (10 miles)	Individual Peak Dose at 1.2–1.6 km Sv (rem)
Noble Gases	Particles	CRUD				
.12	1.2×10^{-3}	1.5×10^{-3}	50 (164)	0	3.6×10^{-4}	1.85 (185)
.12	1.2×10^{-3}	1.5×10^{-3}	120 (393)	0	2.1×10^{-4}	0.14 (14)
.12	1.2×10^{-4}	1.5×10^{-4}	50[1] (164)	0	5.2×10^{-5}	0.22 (22)
.12	7×10^{-6}	1.5×10^{-3}	50 (164)	0	4.3×10^{-6}	0.026 (2.6)
.12	7×10^{-6}	1.5×10^{-3}	120 (393)	0	2.6×10^{-6}	0.0032 (0.32)
.12	7×10^{-7}	1.5×10^{-4}	50[1] (164)	0	4.3×10^{-7}	0.0027 (0.27)

[1] Results corresponding to a release fraction with filters operable.

E.13 References

E.1. HOLTEC International, "HI-STORM Topical Safety Analysis Report," HOLTEC REPORT HI-951312, Revision 8, Marlton, NJ.

E.2. U.S. Nuclear Regulatory Commission, "Code Manual for MACCS2," NUREG/CR-6613, Vol. 1, Washington, DC, May 1998.

E.3. U.S. Nuclear Regulatory Commission, "DOSFAC2 User's Guide," NUREG/CR-6457, Washington, DC, December 1997.

E.4. Croff, A.G., "ORIGEN2: A Revised and Updated Version of the Oak Ridge Isotope Generation and Depletion Code," ORNL-5621, Oak Ridge National Laboratory, Oak Ridge, Tennessee, July 1980.

E.5. "ORIGEN2 Isotope Generation and Depletion Code," CCC-371, Oak Ridge National Laboratory, Oak Ridge, Tennessee, 1991.

E.6. Hazelton, R.F., "Characteristics of Fuel Crud and Its Impact on Storage, Handling, and Shipment of Spent Fuel," PNL-6273, Pacific Northwest Laboratory, Richland, Washington, September 1987.

E.7. Sandoval, R.P., et al., "Estimate of CRUD Contribution to Shipping Cask Containment Requirements," SAND88-1358, Sandia National Laboratories, Albuquerque, New Mexico, January 1991.

E.8. Lukic, J.D., and J.S. Schmidt, "Taming the CRUD Problem: A Utility Perspective," *Nuclear Technology*, 142:283, American Nuclear Society, La Grange Park, Illinois, 2003.

E.9. Humphreys, S.L., J.A. Rollstin, and J.N. Ridgely, "SECPOP90: Sector Population, Land Fraction, and Economic Estimation Program," NUREG/CR-6525, U.S. Nuclear Regulatory Commission, Washington, DC, September 1997.

APPENDIX F
QUESTIONS AND ANSWERS

APPENDIX F
QUESTIONS AND ANSWERS

Question 1: Why did the NRC conduct this study?

Answer 1: The spent fuel pools of commercial nuclear power plants are becoming filled with spent fuel assemblies. Because spent fuel pools were not typically designed to accommodate all the spent fuel assemblies generated during a plant's lifetime, many licensees have been removing the older spent fuel assemblies and storing them onsite in dry cask storage systems. The NRC conducted this study to develop a methodology for assessing the potential risk to the public from the storage of spent fuel in a dry cask storage system.

Question 2: How did the NRC assess the potential risk from dry cask storage systems?

Answer 2: The NRC developed and applied a methodology for performing a probabilistic risk assessment (PRA) of a dry cask storage system at a boiling-water reactor site. The PRA provides insights into the potential impact of various challenges and accidents on the dry cask storage system, as well as how the various stages of operation contribute to risk.

Question 3: What was considered in the PRA?

Answer 3: The NRC developed a comprehensive list of challenges and accidents that could impact the integrity of the dry cask storage system, and evaluated the risk associated with each of them. The NRC evaluated a number of ways casks might break from extremes in temperature and pressure. Conditions considered included earthquakes, floods, high winds, lightning strikes, accidental aircraft crashes, and pipeline explosions, as well as dropping the cask during transfer operations. In evaluating the risk, the NRC considered realistic weather conditions and a representative population distribution in the vicinity of the site.

Question 4: Did the NRC evaluate terrorism events in this study?

Answer 4: No. The NRC has evaluated the impact of various terrorism events on dry cask storage systems in separate studies. Collectively, these studies confirm the adequacy of the designs and demonstrate that they provide an acceptable level of safety. Due to the sensitive nature of the studies, they are not publically available.

Question 5: What are the results of the study?

Answer 5: The results of PRA studies are normally presented in measures such as the probability of a prompt fatality and the probability of a latent cancer fatality. The results of this study indicated that no prompt fatalities are expected. The resulting calculated risk for a latent cancer fatality is extremely small

(i.e., less than one in a trillion years). Due to the exceedingly low risk numbers calculated, the conclusion that should be reached is that cask storage systems provide a safe means to store spent nuclear fuel.

Question 6: Why are the calculated risk measures so low?

.

Answer 6: A major contributor is that dry cask storage systems are inherently passive, i.e. they do not rely on active support systems or human actions to achieve their safety function. In addition, the designs of dry cask storage systems are inherently robust from a structural integrity perspective, i.e., they are massive structures that are highly damage tolerant. To have a measurable impact on risk, the dry cask storage system would have to be breached and spent nuclear fuel would need to be disrupted and released to the environment.

Question 7: If the calculated risks from dry cask storage systems are so low, why shouldn't all the spent fuel be stored in them, as opposed to a spent fuel pool?

Answer 7: There are two reasons. Fuel that has been recently removed from a reactor must be kept in a pool for several years to cool (to remove heat generated by radioactive decay). Only after the fuel has cooled sufficiently may it be safely stored in dry casks. Therefore, spent fuel pools are necessary. Second, various studies have shown that spent fuel pools and dry cask storage systems are both safe and secure. Assuming that the aged fuel in a spent fuel pool is air cooled, similar to the dry cask storage system, and the probability of direct release from the fuel due to associated risk contributors (e.g., aircraft, seismic event) is similar, the overall risks should be comparable. Since the NRC has determined that either storage system ensures that spent fuel is stored safely and securely, the decision to move spent fuel from the spent fuel pool to dry casks is a decision for licensees.

Question 8: How can the study be used?

Answer 8: The methodology developed in NUREG-1864 can be used as a guide for performing similar PRAs for other dry cask storage systems at other nuclear power plant sites. The NRC will consider the insights from this study in our continuing efforts to improve and risk-inform the licensing and inspection activities associated with dry cask storage.

NRC FORM 335 (2-89) NRCM 1102, 3201, 3202

U.S. NUCLEAR REGULATORY COMMISSION

BIBLIOGRAPHIC DATA SHEET

(See instructions on the reverse)

1. REPORT NUMBER (Assigned by NRC, Add Vol., Supp., Rev., and Addendum Numbers, if any.)

NUREG-1864

2. TITLE AND SUBTITLE

A Pilot Probabilistic Risk Assessment of a Dry Cask Storage System At a Nuclear Power Plant

Final Report

3. DATE REPORT PUBLISHED

MONTH	YEAR
March	2007

4. FIN OR GRANT NUMBER

5. AUTHOR(S)

Gordon Bjorkman, Tze-Jer Chuang, Robert Einziger, Shah Malik, Asimios Malliakos, Jocelyn Mitchell, Carlos Navarro, Christopher Ryder, Syed Shaukat, Anthony Ulses, Ghani Zigh

6. TYPE OF REPORT

Technical

7. PERIOD COVERED *(Inclusive Dates)*

8. PERFORMING ORGANIZATION - NAME AND ADDRESS *(If NRC, provide Division, Office or Region, U.S. Nuclear Regulatory Commission, and mailing address; if contractor, provide name and mailing address.)*

Division of Risk Assessment & Special Projects
Office of Nuclear Regulatory Research
U.S. Nuclear Regulatory Commission
Washington, DC 20555-0001

Spent Fuel Project Office
Office of Nuclear Material Safety and Safeguards
U.S. Nuclear Regulatory Commission
Washington, DC 20555-0001

9. SPONSORING ORGANIZATION - NAME AND ADDRESS *(If NRC, type "Same as above"; if contractor, provide NRC Division, Office or Region, U.S. Nuclear Regulatory Commission, and mailing address.)*

Sam
e as above

10. SUPPLEMENTARY NOTES

Asimios Malliakos, NRC Project Manager

11. ABSTRACT *(200 words or less)*

As the basis for this report, the U.S. Nuclear Regulatory Commission (NRC) has developed and applied a methodology for performing a pilot probabilistic risk assessment (PRA) of a dry cask storage system at a nuclear power plant site (i.e., an independent spent fuel storage installation). This report documents the pilot PRA for a specific dry cask system (Holtec International HI-STORM 100) at a specific boiling-water reactor (BWR) site. The methodology developed can serve as a guide for performing similar PRAs in the future. The pilot study can provide guidance for assessing the risk to the public and identifying the dominant contributors to that risk. The cask system consists of a multipurpose canister (MPC) that confines the fuel, a transfer overpack that shields workers from radiation while the cask is being prepared for storage, and a storage overpack that shields people from radiation and mechanically protects the MPC during storage. The study covers various phases of the dry cask storage process, from loading fuel from the spent fuel pool, preparing the cask for storage and transferring it outside the reactor building, moving the cask from the reactor building to the storage pad, and storing the cask for 20 years on the storage pad. The study develops and assesses a comprehensive list of initiating events, including dropping the cask during handling and external events during onsite storage (such as earthquakes, floods, high winds, lightning strikes, accidental aircraft crashes, and pipeline explosions). Potential cask failures from mechanical and thermal loads are modeled. The study estimates the annual risk for one cask in terms of the individual probability of a prompt fatality within 1.6 km (1 mile) and a latent cancer fatality within 16 km (10 miles) of the site.

12. KEY WORDS/DESCRIPTORS *(List words or phrases that will assist researchers in locating the report.)*

dry cask storage system
dry cask storage operation
HI-STORM 100
probabilistic risk assessment (PRA)
multipurpose canister (MPC)
independent spent fuel storage installation (ISFSI)
dropped fuel assembly
dropped transfer cask
storage/transfer overpack
spent fuel assemblies

13. AVAILABILITY STATEMENT

unlimited

14. SECURITY CLASSIFICATION

(This Page) unclassified

(This Report) unclassified

15. NUMBER OF PAGES

16. PRICE